UC San Diego

UC San Diego Electronic Theses and Dissertations

Title

Acoustofluidic droplet generation: physical understanding and applications of jetting and atomization

Permalink

Author

Connacher, William James McDonald

Publication Date

2022

Peer reviewed|Thesis/dissertation

UNIVERSITY OF CALIFORNIA SAN DIEGO

**Acoustofluidic droplet generation:
physical understanding and applications of jetting and atomization**

A dissertation submitted in partial satisfaction of the
requirements for the degree
Doctor of Philosophy

in

Materials Science and Engineering

by

William James McDonald Connacher

Committee in charge:

Professor James Friend, Chair
Professor Olivia Graeve
Professor David Saintillan
Professor Oliver Schmidt
Professor Oscar Vasquez Mena

2022

The dissertation of William James McDonald Connacher is approved, and it is acceptable in

quality and form for publication on microfilm and electronically.

University of California San Diego

2022

DEDICATION

Dedicated to my mother, Mary McDonald, who survives through her art and through her children's contributions. Dedicated to my father, Russell Connacher, who developed my work ethic and anti-fragility without which I would certainly not have completed PhD school.

EPIGRAPH

We take other men's knowledge and opinions upon trust; which is an idle and superficial learning. We must make them our own. We are just like a man who, needing fire, went to a neighbor's house to fetch it, and finding a very good one there, sat down to warm himself without remembering to carry any back home. What good does it do us to have our belly full of meat if it is not digested, if it is not transformed into us, if it does not nourish and support us?

—Montaigne

The answers you get depend on the questions you ask.

—Thomas Kuhn

TABLE OF CONTENTS

LIST OF FIGURES

LIST OF TABLES

ACKNOWLEDGEMENTS

Thank you to my supervisor, Prof. James Friend, for taking a chance on an applicant with less than outstanding academic performance. He allows and encourages his students to think deeply about what research they would prefer to work on and why, with uncommon emphasis on the "why." We are not just taking in funding and spitting out publications in James' group we have a goal in mind. This is not an easy task for a principal investigator and he has taken great time and effort to identify and support projects that are impactful and that his students want to work on. He also makes room for mistakes, nonlinearity, and simple human nature in his group and has cultivated a welcoming and safe working environment. I hope he continues to enjoy success and progress while also enjoying life.

Thank you to my committee for their guidance and their commitment to education. Of all the classes I have taken in my life, Prof. David Saintillan's fluid mechanics was [a close second] in terms of rigor, pedagogy, and comprehensive understanding. I have had an enriching experience working with Prof. Friend and with Prof. Oscar Vasquez-Mena on research projects, which involved both technical discussions and more philosophical chats about the nature of science and academia. I have learned from Dr. Olivia Graeve not just in the classroom, but also in the context of her fantastic outreach programs. Her work to increase STEM matriculation from the Hispanic community and strengthen the bond between people in the USA and Mexico through science is an inspiration and I have been happy to volunteer my time for this effort. I am grateful to Prof. Oliver Schmidt for taking the time to discuss a new research idea at a late stage in my graduate school career and I hope that I will be able to, at the very least, inspire a future student to take up the corresponding work.

I have had a good deal of mentorship outside of the faculty during graduate school and I thank all the following people. I needed a different style of mentorship than could be provided by my supervisor alone and I was struggling mightily until Dr. Jeremy Orosco joined our group. I will continue to struggle, because that's how I know I'm taking on appropriate challenges, but with

Chapter 1, in part, is a reprint of the materials as it appears in Lab on a Chip, 2018. William Connacher, Naiqing Zhang, An Huang, Jiyang Mei, Shuai Zhang, Tilvawala Gopesh, and James Friend. "Micro/Nano Acoustofluidics: Materials, Phenomena, Design, Devices, and Applications" Lab on a Chip 18.14 (2018): 1952-1996. The dissertation author was the primary investigator and author of this paper.

Section 1 of Chapter 2, in full, is a reprint of the materials as it appears in Physical Review Letters, 2020. William Connacher, Jeremy Orosco, and James Friend, "Droplet Ejection at Controlled Angles via Acoustofluidic Jetting", Physical Review Letters 125.18 (2020): 184504. The dissertation author was the primary investigator and author of this paper.

Section 2 of Chapter 2, in full, has been submitted for publication of the material as it may appear in IEEE Transactions on Aerospace and Electronic Systems, 2022. Amihai Horesh, William Connacher, and James Friend. "Acoustothermal phase change of fluids for thrusters", IEEE Transactions on Aerospace and Electronic Systems, 2022. The dissertation author was the secondary investigator and author of this paper.

Section 1 of Chapter 3, in part, is a reprint of the materials as it appears in Lab on a Chip, 2020. An Huang and William Connacher, Mark Stambaugh, Naiqing Zhang, Shuai Zhang, Jiyang Mei, Aditi Jain, Sravya Alluri, Vincent Leung, Anushi Rajapaksa, and James Friend, "Practical Microcircuits for Handheld Acoustofluidics", Lab on a Chip 21.7 (2020): 1352-1363. The dissertation author was the co-primary investigator and author of this paper.

Section 2 of Chapter 3, in full, is a reprint of the materials as it appears in Journal of Video Experiments, 2020. Aditya Vasan, William Connacher, and James Friend. "Fabrication and Characterization of Thickness Mode Piezoelectric Devices for Atomization and Acoustofluidics", JoVE (Journal of Visualized Experiments) 162 (2020): e61015. The dissertation author was the secondary investigator and author of this paper.

Section 3 of Chapter 3, in part, is a reprint of the materials as it appears in Lab on a Chip, 2020. An Huang and William Connacher, Mark Stambaugh, Naiqing Zhang, Shuai Zhang,

Jiyang Mei, Aditi Jain, Sravya Alluri, Vincent Leung, Anushi Rajapaksa, and James Friend, "Practical Microcircuits for Handheld Acoustofluidics", Lab on a Chip 21.7 (2020): 1352-1363. The dissertation author was the co-primary investigator and author of this paper.

Section 1 of Chapter 4, in full, has been submitted for publication of the material as it may appear in Chaos, Solitons and Fractals, 2022. Orosco, Jeremy, William Connacher, and James Friend. "Identification of weakly- to strongly turbulent three-wave processes in a micro-scale system", *Chaos, Solitons and Fractals*.

Section 2 of Chapter 4, in full, has been submitted for publication of the material as it may appear in Physical Review E, 2022. William Connacher, Jeremy Orosco, and James Friend, "Modal analysis of capillary wave turbulence", Physical Review. The dissertation author was the primary investigator and author of this paper.

Appendix A, in full, is a reprint of the materials as it appears in Medical Devices & Sensors, 2020. Aditya Vasan, Reiley Weekes, William Connacher, Jeremy Sieker, Mark Stambaugh, Preetham Suresh, Daniel E. Lee, William Mazzei, Eric Schlaepfer, Theodore Vallejos, Johan Petersen, Sidney Merritt, Lonnie Petersen, James Friend, Acute Ventilation Rapid Response Taskforce (AVERT), "MADVent: A low-cost ventilator for patients with COVID-19," Medical Devices & Sensors 3.4 (2020): e10106. The dissertation author was the secondary investigator and author of this paper.

VITA

2014	B. S. in Engineering Physics, University of California, Berkeley
2018	M. S. in Materials Science and Engineering, University of California, San Diego
2022	Ph. D. in Materials Science and Engineering, University of California, San Diego

PUBLICATIONS

Connacher, William, et al. "Micro/nano acoustofluidics: materials, phenomena, design, devices, and applications", *Lab on a Chip* 18.14 (2018): 1952-1996.

Connacher, William, J. Orosco, J. Friend, "Droplet Ejection at Controlled Angles via Acoustofluidic Jetting", *Physical Review Letters* 125.18 (2020): 184504.

Connacher, William, A. Huang, et al., "Practical Microcircuits for Handheld Acoustofluidics", *Lab on a Chip* 21.7 (2020): 1352-1363.

Connacher, William, Jeremy Orosco, and James Friend. "Modal analysis of capillary wave turbulence", *Physical Review E. in preparation*

Orosco, Jermey, William Connacher, and James Friend. "Identification of weakly- to strongly turbulent three-wave processes in a micro-scale system", *Chaos, Solitons and Fractals. in preparation*

Connacher, William, Seungbae, Oscar Vasquez Mena, and James Friend. "An implantable ultrasound powered calcium sensor with QLED output signal", *in preparation*

Horesh, Amihai, William Connacher, and James Friend. "Acoustothermal phase change of fluids for thrusters", *IEEE Transactions on Aerospace and Electronic Systems submitted*

Vasan, Aditya, William Connacher, and James Friend. "Fabrication and Characterization of Thickness Mode Piezoelectric Devices for Atomization and Acoustofluidics", *JoVE (Journal of Visualized Experiments)* 162 (2020): e61015.

Friend, James, et al. "Acoustic wave atomizer." U.S. Patent Application No. 16/632,303.

Vasan, Aditya, et al. "MADVent: A low-cost ventilator for patients with COVID-19", *Medical Devices & Sensors* 3.4 (2020): e10106.

Gopesh, Tilvawala, et al. "Vacuum exhasusted isolation locker (VEIL) to reduce inpatient droplet/aerosol transmission during COVID-19 pandemic", *Infection Control and Hospital Epidemiology* 43.1 (2022): 105-107

Ashdown, Christopher P., et al. "Pulsed Low-Frequency Magnetic Fields Induce Tumor Membrane Disruption and Altered Cell Viability", *Biophysical Journal* (2020).

ABSTRACT OF THE DISSERTATION

Acoustofluidic droplet generation:
physical understanding and applications of jetting and atomization

by

William James McDonald Connacher

Doctor of Philosophy in Materials Science and Engineering

University of California San Diego, 2022

Professor James Friend, Chair

Ultrasonic waves generated by piezoelectric devices produce forces on fluids and particles that can be controlled to produce useful functions. The research field of acoustic microfluidics has developed fundamental understanding of these forces and demonstrated some useful functions, but it has yet to break through into industry and commercial use. We describe acoustic radiation force and acoustic streaming as well as some less common forces and review piezoelectric materials. Then we review some fundamental work in fluid mixing, translation, jetting, and atomization. Particle manipulation will also be briefly touched on, but it is not the focus. Instead, the focus of our work has been on producing droplets of liquid in air, either one at a time via jetting or many

at a time via atomization

We present a focused surface acoustic wave system in order to investigate the fundamental physics of jetting and to explore the possibility of some applications. We show that jetting must account for surface tension effects. Acoustic streaming is well understood to be the driving force behind jetting and its amplitude and direction are not dependent on surface tension in most literature because it is typically considered far from a deformable interface. However, jetting to produce a droplet is fundamentally an interfacial phenomenon and we show quantitatively how it should be accounted for in order to control droplet ejection angles. Our experimental system uses only two transducers, but it is not hard to imagine a system with four transducers that could control droplet ejection in two dimensions. This capability could be useful in printing by reducing the amount that the printing head has to translate. With this same focused surface acoustic wave device we demonstrate how frozen liquid can be melted and subsequently atomized. We also demonstrate a through-hole liquid supply that allows for continuous atomization and show that the angle control, similar to the jetting case, is possible with atomization. These capabilities could be useful as a thruster for small spacecraft.

One of the major reasons that acoustic microfluidics has not achieved widespread use is that the equipment required to drive the devices is prohibitively complicated, bulky, and expensive. We produced a hand held system to drive high frequency ultrasound devices and demonstrate its use for several typical applications. We provide all the necessary information to recreate these systems to promote adoption by other labs and entrepreneurs. Our primary application for this system is in nebulization and atomization of liquid, which could be useful for pulmonary drug delivery, agriculture, or fuel injection. We describe in detail how to fabricate the thickness mode devices that we use to produce atomization at large flow rates in our lab. We then show how these devices have been integrated with the driving system to produce a truly hand-held high-frequency nebulizer.

The fundamental physics of atomization is far more complicated than that of jetting, but

we have made contributions here as well. It is currently our hypothesis that acoustic radiation sets up a standing wave pattern in the liquid volume based on its initial shape and then a feedback loop between the two leads to an initial set of capillary waves (work that Shuai Zhang will soon publish). At larger power acoustic streaming may also play a role, but regardless the capillary waves become turbulent before the onset of atomization. For high-frequency forcing, these capillary waves occur at very short time-scales and very small length-scales so that it has been difficult to study them directly, but we have developed a new and unique experimental capability, high-speed digital holographic microscopy. We describe capillary wave turbulence regimes available in our system and show evidence for finite domain effects and strong nonlinearity. We also show quantitatively how energy transfers between time and length scales with increasing power input.

Chapter 1

Introduction: Acoustofluidics

The problems and promise of microfluidics have served to motivate researchers for over twenty-five years. Small volumes, fast processing, dynamic control, low costs, and hand-held devices compete with numerous difficulties in actuation, manipulation, and eventual integration into practical devices [7]. The goal is to replace each step in a macro-scale process with a micro-scale counterpart and then to seamlessly integrate these parts without compromising the advantages, all embodied by integrated devices that can be used by non-experts. In 2014, Sackmann *et al.* [8] raised the question: *Why hasn't microfluidics seen widespread adoption?* Becker [9] noted five years prior to that, in 2009, that the success of any new discipline hinges upon a "killer application", and that microfluidics still lacked one. In the eight years since, much has been accomplished in the discipline, with Becker [10] and others finally expressing a cautiously optimistic outlook.

However, an answer overlooked by many researchers is that much of the benefit of microfluidics is lost when actuation still must rely on an external bench-top pneumatic pump connected by a tangle of tubes—for example, the first figure in Whitesides' review [7]. Such a system is difficult to operate by an expert in a laboratory, let alone a non-expert with a hand-held version. Biological assays represent one of the most important applications for lab-on-a-chip

devices, yet requires mixing—difficult via traditional microfluidics where laminar flow is difficult to overcome and diffusion is glacially slow. Passive mixers [11] offer solutions in some cases, but require complex architectures. A good argument was put forth by Collins *et al.* [12]: relying on spatially and temporally distant means of pressure reduces the dynamic control one has over microfluidic processes. Finally, Sackmann *et al.* [8] point out that macro-scale technologies have likewise been advancing and, in order to compete, microfluidics must do better than simply matching the performance of larger technology for the same tasks, a sort of *red queen* [13] evolutionary problem in developing and applying microfluidics technology. In this review, we will show that the actuation of fluids and particles via acoustic waves can overcome these hurdles and help fulfill the promise of microfluidics.

Vibration as a means to manipulate particles within fluids (and gases) has interested the scientific community since the work of Chladni *et al.* [14], Faraday *et al.* [15], and Kundt *et al.* [16]. Fluid actuation by acoustic waves is complex in analysis but simple in practice, with little hardware required to operate, and offers large actuation forces and force gradients. The seeds of acoustofluidics date from two centuries ago, and acoustics was considered a classic discipline as early as the 1960's. Few new areas of research had developed in acoustics until a recent and dramatic resurgence as a result of interesting results at small scales (*see* reviews on microscale acoustofluidics from Friend *et al.* [17], Ding *et al.* [18], Yeo *et al.* [19], and more recently Destgeer *et al.*[20]).

While some of the effects discussed in this review were known by Chladni, Faraday, Kundt, and their contemporaries, the acoustic devices available to them and fellow researchers until the 1960's were inadequate for small-scale applications. They were either underpowered, providing little more than laboratory curiosities like "quartz wind" [21], or generated ultrasound with wavelengths at centimeter to meter length scales from relatively large, inefficient, and strongly heating transducers. These devices brought with them a collection of side effects from cavitation to weak acceleration unfortunately incompatible with micro/nano-scale fluidics.

Notably, the phenomenon of surface acoustic wave (SAW) propagation on a substrate was first reported by Lord Rayleigh in 1885 [22], but these were only properly produced with the maturation of microfabrication to form interdigital transducers (IDTs), thin finger-like electrodes formed upon a piezoelectric substrate as described by White and Voltmer in 1965 [23]. Many of the most recent reports in micro/nano acoustofluidics have relied on SAW generation at tens to hundreds of MHz, which was not possible prior to IDTs and reduces the acoustic wavelength to a scale compatible with microfluidics. There is an ancillary effect that is arguably far more significant. Because the particle velocity in typical acoustic devices is limited to around 1 m/s regardless of size or frequency due to the limitations in material integrity, selecting higher operating frequencies allows a concurrent increase in particle acceleration, to as much as 10^8 m/s^2. It is this very large acceleration that is responsible for many of the observed effects in acoustofluidics.

In this review, we first examine the piezoelectric materials that underpin this transformation in micro/nano-scale fluidics and then describe the basic device architecture used to generate acoustic waves before reviewing the most recent developments in the field. We explore mixing, manipulation of particles, translation, jetting, and atomization in sessile drops, and then consider mixing, pumping, and particle and drop manipulation in closed channels. Nanoscale phenomena are examined as a new direction of work, and the review closes with coverage of an important observational technique, laser Doppler vibrometry.

1.1   Piezoelectric Materials and Electro-acoustic Waves

Microscale acoustofluidic actuation relies on the generation of acoustic waves in piezoelectric materials. The well-known *direct piezoelectric effect* generates electric charge upon the application of mechanical stress in certain materials; the generation of mechanical strain from the application of an electric field is the *inverse piezoelectric effect* [24]. Atoms or molecules present in the solid lattice structure of the material are either ions in the typical case [25, 26] or have

strong polarization—a separation of dissimilar charges, forming an electric dipole—in the case of some piezoelectric polymers such as poly-vinylidene fluoride (PVDF) [27, 28]. In single crystal piezoelectric media formed from ions, the ions exhibit miniscule, thermodynamically favorable misalignment that forms dipoles over each unit cell of the crystal material. This misalignment tends to be identically oriented throughout the crystal, and so its effect accumulates for each repeated unit in the crystal as *polarization*, growing to become physically significant and present in a natural state as *remanent polarization* [29]. Polycrystalline piezoelectric material exhibits similar behavior, though the orientation of the "misalignment" is unique to the *domains*, one or more of which are present in each crystal grain that forms the material [30]. An extremely large voltage is applied to polycrystalline piezoelectric material in the desired polarization direction for a few minutes to several hours while immersed in an inert fluid [31, 32] in order to reorient the polarization of each of these domains to generally lie along a particular direction. This step is necessary to form a useful piezoelectric coupling effect in any such media that lacks remnant polarization.

Piezoelectric materials have long been used to generate and detect acoustic waves. Rochelle salt and quartz were employed in the first large-scale application of piezoelectrics to acoustically detect submarines during World War I [33]. The earliest medical applications were for ultrasonic imaging of tissues in medicine [34, 35]. High-power ultrasound has been applied in industrial mixing and cleaning, applications familiar to most researchers [36, 37]. Other common uses include non-contact sensors and range-finders [38, 39]; more recently, local harvesting of energy from motion to eliminate or reduce the need for batteries have driven innovative use of piezoelectric materials [40]. The simplest of all these piezoelectric ultrasonic devices tend to be driven at resonance via planar electrodes on both faces of a flat and thin piezoelectric element, itself polarized from one to the other planar electrode. These may be sandwiched into a rod to form a Langevin transducer [41], and rarely other modes of vibration are used, usually to generate more complex motion necessary for actuators or motors [42, 43]. Regardless of the

application, the waves generated by piezoelectric media was generally limited to bulk acoustic waves (BAW) until the advent and broad acceptance of IDTs [23], which enabled high frequency SAW. The demonstration by White and Voltmer of spatially periodic thin-film metal electrodes on a piezoelectric quartz bar to produce a traveling SAW was broadly taken up by the electronics industry for use in signal processing at frequencies ranging from 10 MHz to 1 GHz. "True" SAW or Rayleigh waves are confined within three to four wavelengths of the surface of the material. Leaky SAW (LSAW) [44], Love waves [45], Bleustein-Gulayev waves [45], surface skimming bulk waves (SSBW) [46], and surface transverse waves (STW) [47] are generally categorized as pseudo-SAW (PSAW), may have some limited applications in acoustofluidics, but mainly lie outside the scope of this review.

In order to generate high frequency acoustic waves, a panoply of piezoelectric materials have been used over the last 50 years. Polycrystalline piezoelectrics can be fabricated in more and simpler ways and have greater electromechanical coupling coefficients than single crystalline piezoelectrics, implying a greater ability to transform energy from one form to the other. However, single crystal materials have higher quality factors, and lower damping than polycrystalline materials, and so the choice of material in a given application is not straightforward [48]. Single-crystal piezoelectric media are however generally compatible with microfabrication facilities whereas, for example, lead zirconate titanate (PZT) [49], the most common polycrystalline ceramic piezoelectric material, is not. Furthermore, PZT is toxic, with significant excess lead oxide present along the grain boundaries [50], and facing regulations that aim to eliminate it from use [51]. There have been some successes in eliminating lead while retaining good performance from polycrystalline ceramics, most notably those derived from potassium sodium niobate (KNN) [52]. The granular nature of polycrystalline piezoelectrics limits their use to relatively low frequencies ($O(1$ kHz–1 MHz)) due to the finite size of the grains and domains within the material that strongly interact with the generation and propagation of acoustic waves at greater frequencies to generate heat [53]. Though some researchers over the years have synthesized

polycrystalline ceramic piezoelectric materials with submicron grain size in an aim to increase the useful frequency range to 100 MHz or more [54], these materials have not been widely employed. The likely reason is the existence of single crystal materials that operate at high frequencies (O(1 MHz–1 GHz)) with superior characteristics.

The materials most popularly used to make SAW devices include quartz, lithium tantalate (LT, $LiTaO_3$) and lithium niobate (LN, $LiNbO_3$). Others include gallium arsenide (GaAs), cadmium sulfide (CdS), zinc oxide (ZnO), lithium tetraborate ($Li_2B_4O_7$), and langasite ($La_3Ga_5SiO_{12}$) [55]. All piezoelectric materials are anisotropic, and because these choices are especially so, the type of wave generated from them is strongly dependent on the material orientation. White and Voltmer [23] used a Y-cut, Z-propagating quartz plate. Shortly after, in the late 1960's Bell Laboratories were credited for the development of lithium tantalate (LT) and lithium niobate (LN) which exhibit significantly stronger electromechanical coupling coefficients than quartz [56, 57]. Due to its exceptionally high coupling coefficient relative to other single crystalline materials for SAW, LN has become ubiquitous for this application. Typically, wafers are obtained by growing a boule (*see* Fig. 1.1) of LN from a seed crystal with the desired orientation, which is cut into wafers of the required thickness.
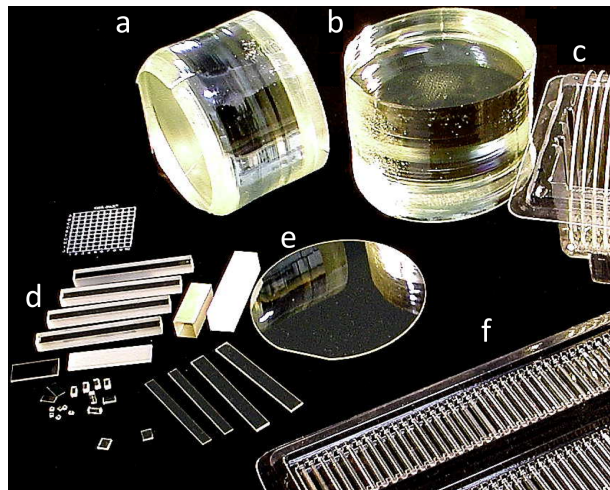
Figure 1.1: (a, b) A boule of lithium niobate, (c,e) with wafers and (d,f) other shapes cut for typical applications. *Image provided by Precision Micro-Optics, MA, USA.*

Initially, SAW devices were designed so that waves propagated along the symmetric crystal axes. Later on, as enhanced properties along different rotated cuts were discovered, these cuts gained popularity in various applications. In particular, the Y-cut, Z-propagating orientation of LN (YZ LN) was extensively used for SAW filters requiring Rayleigh waves. Due to the dependence of wave velocity on the propagation direction in an anisotropic material like LN, waves in rotated cuts propagating in a direction not aligned with a principal axis in the material translate laterally in a phenomena known as *beam steering* [58]. With further studies, particularly the works of Takayanagi *et al.* [59] and Slobodnik *et al.* [60], the 131° Y-rotated cut of LN was found to have exceptional electromechanical coupling and low beam steering and became widely used. However, this cut exhibited spurious parasitic waves, and in 1976 Shibayama [1], determined that the 127.86° Y-rotated cut reduced the generation of these parasitic waves and consequently had the highest electromechanical coupling coefficient and lowest insertion loss. The 127.86° Y-rotated X-propagating cut of LN (128° YX LN) became the most popular and widely accepted orientation for applications requiring Rayleigh waves. Other cuts of LN have even higher electromechanical coupling coefficients, but these produce spurious modes and beam steering that preclude them from applications requiring "true" SAW. Among the other cuts, the 36°, 41°, and 64° Y-rotated cuts are the most popular. Table 1.1 lists some of the best-known cuts of LN and their electromechanical coupling constants, where $K^2 = 2\Delta v/v = 2\left(v_f - v_m\right)/v_f$. Here, v_f is the wave velocity in the free substrate and v_m is the wave velocity measured along a short-circuited plane.

Evidently, the 41° and 64° YX cuts of LN have higher electromechanical coupling coefficients than the 128° YX, however, these generate PSAW and not "true" SAW/Rayleigh waves. Cuts that produce non-Rayleigh SAW have been used to make SAW resonator filters [61] (64° YX) and delay lines for liquid sensors [62] (41° YX) among other applications.

The majority of research conducted with SAW for microfluidics has utilized 128° YX LN. Recently, there have been some studies which demonstrate the use of X-cut LN [63]. Materials

Table 1.1: Commonly used cuts of LN and their corresponding electromechanical coupling coefficients and velocities. Reproduced with permission from Shibayama *et al.* [1], Campbell [2], Ciplys *et al.* [3], Soluch *et al.* [4] and Hickernell *et al.* [5]

Cut	$2\Delta v/v$ (%)	Velocity (m/s)
YZ [3]	4.82	3488
ZX [3]	0.53	3798
ZY [3]	2.25	3903
XY [3]	3.58	3748
20° XY [4]	1.6	3727
120° XY [4]	4.1	3403
XZ [3]	5	3483
YX [3]	1.54	3769
36° [2] YX	16.7	4802
41° YX [5]	17.2	4752
64° YX [5]	10.8	4692
128° YX [1]	5.3	3992

most commonly used in acoustofluidics are anisotropic in nature due to their crystal structure. The 128° YX and *X*-cut LN, for example, can generate SAW of the same frequency and amplitude only in one direction. Any veering from the primary propagation direction is affected by beam steering and changes in frequency and electromechanical coupling coefficients. Kurosawa [64] demonstrated this for a two-axis motor made using the 128° YX LN wafer, showing that the vibration displacement and velocity were 200% higher in the *X*-axis propagation direction compared to the *Y*-axis propagation direction. In order to overcome the anisotropic nature of the substrate, Guo *et al.* [65] and Devendran *et al.* [66] demonstrated perpendicular IDT pairs at 45° to the *X*-axis to create an orthogonal standing wave of the same frequency. However, the issue of *beam steering* remains. The superior electromechanical coupling present along the X axis and the unmatched wave velocities along the X and Y axes contribute to wave propagation with a lateral component. As a result, high frequency SAW devices made using LN substrates are limited to a single direction for acoustic wave propagation if optimal performance is desired.

Acoustic Wave Measurement

A laser Doppler vibrometer (LDV) is an interferometer that uses the Doppler effect to measure vibrations. When light encounters a moving surface, the reflected light incurs a frequency shift depending on the velocity of the surface and the wavelength of the light. In an LDV, the laser is split into a reference beam, directed straight to the photodetector; and a measurement beam, which reflects off the vibrating surface before being combined with the reference beam at the photodetector. This superposition creates a modulated signal, thus revealing the Doppler shift in frequency (*see* Fig.1.2. Signal processing and analysis provide the vibrational velocity and displacement of a point on the surface in the direction normal to the surface. The in-plane motion can be measured using a different configuration where two measurement beams impinge on a spot with an angle between them, thus yielding interference fringes, though other methods exist[67]. As well, the LDV can be operated in scanning mode so that sequential measurement at many points reveals the vibrational motion of a portion of the surface with desired resolution. These and other advances are covered by [68] and a more recent review was published by [69].
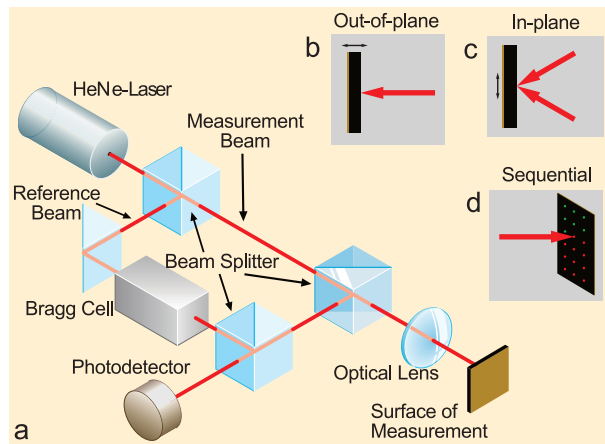
Figure 1.2: a) The interaction of the reference and measurement beams to produce a Doppler shift at the photodetector in this configuration of a Polytec laser Doppler vibrometer. b) Out-of-plane vibration measured by a single beam normal to the surface. c) In-plane vibration measured by two beams aimed at the same point with an angle between them. d) Sequential measurement, which is used to obtain the vibration of the surface in phase.

The LDV has been extensively used in aerospace [70], automotive [71], and hard disk

drive[72] industries, and for land-mine detection [73]. The technology has also been broadly accepted for use in microelectromechanical systems (MEMS) applications [74]. In the context of acoustofluidics, the LDV is well-suited to measure and characterize vibrational motion in the solid surfaces of devices. While the primary aim is usually the determination of the resonance frequencies and mode shapes of the devices (*see* Fig.1.3, the LDV can also be used to identify the type of waveform obtained: Lamb, SAW, BAW, Love, etc. The piezoelectric coefficients (as discussed in Section 1.1) of materials used in acoustofluidics can also be measured with remarkable accuracy [75]. Due to the high frequencies and small amplitudes involved (especially in SAW), measurement of the vibration driven velocity has been vital for analytical validation which would otherwise be impossible at the micro/nano scale. This capability has been particularly useful for characterization of nanofluidic devices[76] and cantilevers for atomic-force microscopy (AFM) [77]. The technology can also be applied to identify vibrations on fluid surfaces[78] and even in air flow [79]. This capability has been helpful in studying fluid atomization and particularly in confirming the absence of the well-known Faraday wave response at half the excitation frequency [80].
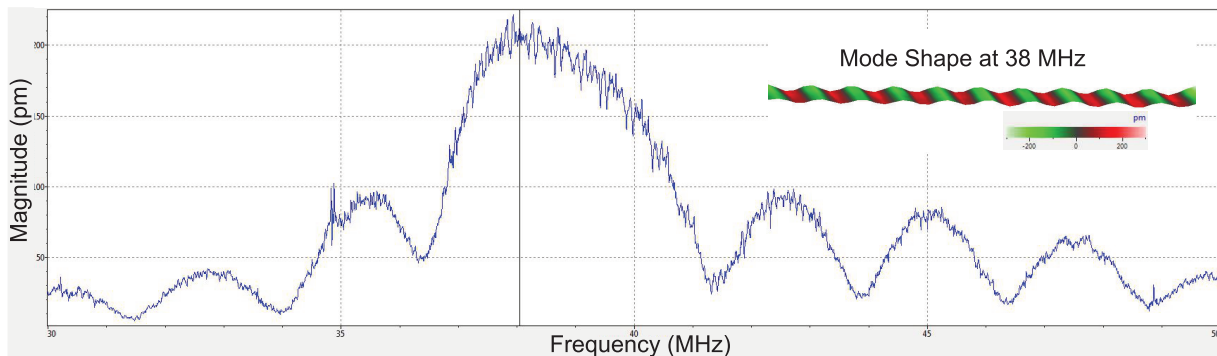
Figure 1.3: The resonance mode of a SAW device is revealed by this graph of amplitude vs frequency at a single point over an averaging period while the device is driven with a multi-frequency signal. Once this resonance is known, a sequential measurement over a region of the surface while the device is driven a the resonance frequency reveals the vibration mode, SAW in this case.

The technology has some limitations and prevailing issues. The choice of interferometer

design has important implications for the sensitivity and measurement range of the LDV, especially in scanning mode. For example, the Sagnac design is inherently more mechanically stable than others due its lack of moving parts (more detail on this topic was provided by Tachizaki[81]). Non-ideal behavior of the interferometer has been known to lead to significant error when measuring small displacements. This and other sources of error, particularly alignment-based error, are covered by Siegmund [82]. Unwanted light waves can interfere with the desired interaction between the reference and measurement beams—known as three-wave interference—but the artifacts of this can be predicted [83]. The vibration of rotating objects and the in-plane motion can likewise be measured, but the setup is relatively complex [84].

Digital holographic (DH) microscopy has been investigated as an alternative to LDV. Data from a high density of points can be obtained simultaneously using DH but, so far it lacks the ability to provide continuous (non-stroboscopic) measurements at frequencies greater than 1 MHz. [85] provide a good introduction to the interested reader. He highlight two new papers in this area as indications of what may follow in the future. [86] demonstrate the ability to measure three dimensions of displacement in acoustic waves traveling in a solid simultaneously using three-color DH. Typically, particle tracking is accomplished by optical videography and particle image velocimetry (PIV), but [87] have applied DH to track particles in 3D that are moving under acoustophoresis. In the future, digital holography may enable new insights into previously well studied acoustofluidic phenomena.

1.2   Electrode Design

Most acoustofluidic devices use either very simple thickness mode transducers are photolithographically patterned IDTs, which sometimes require complex micro-fabrication. Below we highlight two notable exceptions. Rezk *et al.* proposed a low cost alternative to photolithographic IDT fabrication. Aluminum foil electrodes were simply cut with scissors and clamped in

place on a LN substrate to produce a Lamb wave device capable of producing flow in a channel, mixing in a drop, and atomization from a drop [88]. It is likely that this type of electrode will significantly reduce performance due to poor electrical and mechanical contact, but may still be useful for some applications where cost and complexity are extremely limiting. Another alternative to expensive microfabrication was demonstrated by [89] in the form of patterned conductive liquid, but this method was able to produce IDTs for SAW rather than Lamb waves. Nam fabricated channels in PDMS taking the negative shape of the intended IDT design and these were then filled with eutectic gallium indium. Azimuthal flow was achieved at 162 mW and colored dye could be mixed with a viscous, 25% glycerin solution within 1 second using 578 mW of power.

The substrate thickness is an important factor in IDT design, as it determines the minimum frequency of the SAW. Most suppliers provide 500 μm thick wafers, and the Rayleigh SAW is known to extend 4–5 λ into the substrate. This places a lower limit on the frequency suitable to form true Rayleigh SAW of about 40 MHz. Using frequencies below this value cause the acoustic wave to penetrate all the way through the substrate to the other side forming, alongside Rayleigh SAW, spurious Lamb waves that can shed energy through the back side of the substrate into its mounting and affecting the wave propagation and device performance. This is not merely a theoretical problem, as we have seen (in unpublished work) strong fluid transport in 20 MHz shear-horizontal SAW (SH-SAW) devices that should show no fluid transport at all. The 36° Y-rotated, X-propagating lithium tantalate cut used in this case also generated Lamb waves that appeared to be responsible for the confusing observations.

More importantly, much of the literature reports the generation of SAW at frequencies well below 40 MHz without noting or apparently being aware that this problem could arise. In our case, we were forced to use 20–30 MHz SAW for many years due to limitations of our laser Doppler metrology equipment, and fortunately this problem no longer exists.

In order to realize full miniaturization and widespread adoption, SAW microfluidics will

require high power efficiency. Winkler *et al.* laid out the most important efficiency drains in these devices and proposed engineering solutions[90] (*see* Fig. 1.4). They covered optimal electrical impedance through IDT design, use of unidirectional IDTs, passive matching circuits, passivation and electrical shielding for submerged devices, and choice of wavelength based on geometry. Many of these solutions were utilized in a recent paper[91] demonstrating an atomization specific device, which will be discussed in section 1.4.5.

Heating occurs in acoustofluidics since energy must inherently be dissipated on chip in order to produce fluid and particle motion and resistive heating can be minimized or controlled but never eliminated. This is sometimes considered an issue (e.g. evaporation in digital microfluidics), but can be controlled to support additional functionallity. Shilton *et al.* described the progress made in studying and using acoustofluidic heating, for example in PCR, in their paper on controlling and optimizing this phenomena [92]. Drops could be reliably heated to a stable temperature up to 12 degrees above room temperature within 3 seconds. The temperature increase was precisely controlled by the frequency and power. This heating was decoupled from the spurious resistive heating due to the IDT.

Straight IDTs

SAW are typically generated by applying an oscillating electrical signal matching the resonant frequency of the IDT. This signal translates into an acoustic wave via the inverse piezoelectric effect as described earlier. In the literature, frequencies in the range 1 MHz–1 GHz have been used in the study of acoustofluidics, which correspond to wavelengths between 200 and 4 μm for the case of 128 $^{\circ}$ YX LN, implying a range of feature sizes of 50 to 1 μm. These feature sizes are typically microfabricated by photolithography and lift-off [93].

The first and simplest IDTs[23] consisted of straight rectangular metal bars—referred to as fingers—deposited onto the surface of a piezoelectric substrate and alternately connected on either end to contact pads or "bus bars" as pictured in Fig. 1.5. This structure creates an array of
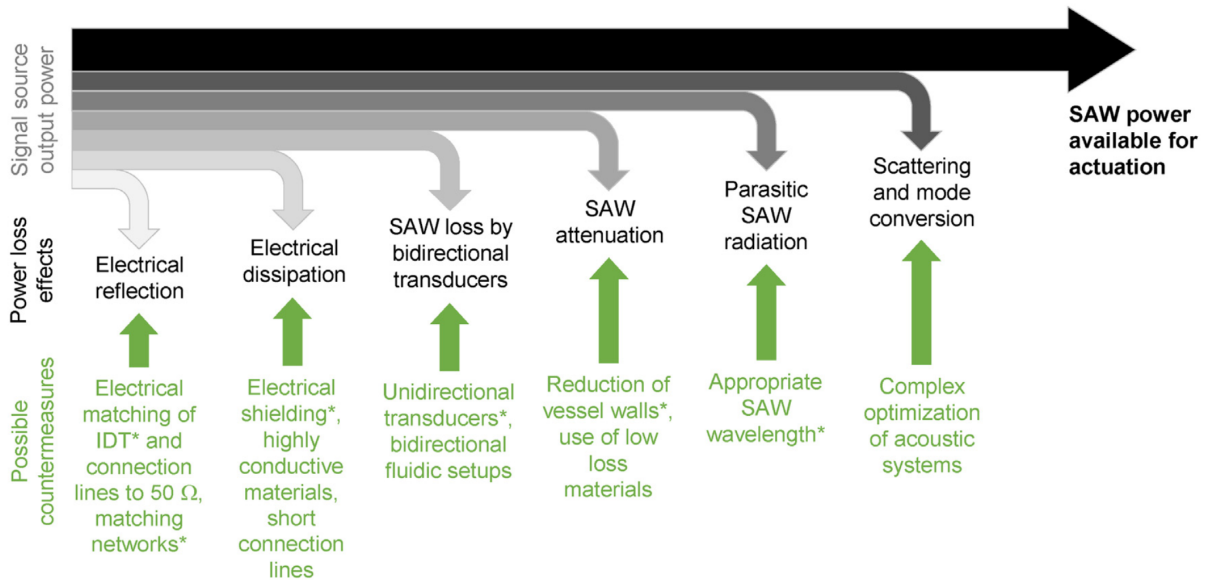
Figure 1.4: Power drains in typical SAW microfluidic devices along with proposed engineering solutions. Reprinted from [90]

electric fields of alternating direction between the transducer finger pairs that in turn create, via the inverse piezoelectric effect, alternating regions of compressive and tensile strain in the substrate. Each finger pair thus produces displacement in the substrate that oscillates with the electric field and radiates a SAW [23]. The periodicity of the finger pairs defines the wavelength of the resulting SAW (λ_{SAW}) such that the distance from one finger to the next is $\lambda_{SAW}/4$. The surface wave velocity (v_R) depends on the material properties of the substrate, the propagation direction, and the thickness of the IDT. Consequently, the center frequency ($f_r = \omega/2\pi = v_R/\lambda_{SAW}$) of a given device is determined by the choice of substrate, propagation direction, and IDT design [6, 23].

The thickness of the metal film that comprises the IDT, h, is typically chosen so that the film thickness ratio $h/\lambda_{SAW} \approx 1\%$ so as to strike a balance between the efficient transmission of electric current in thicker films and the lower mass present upon the substrate for thinner films. Excessively thin films can cause premature finger failure and localized heating from ohmic losses [94], while excessively thick or heavy films can reduce the resonance frequency of SAW in the IDT region compared to the surrounding region that have no fingers, unintentionally producing

an acoustic cavity. Slightly thicker films, $h/\lambda_{\text{SAW}} \approx 1\%$, are optimal in most cases for reflectors, structures that appear similar to IDTs but act to reflect the SAW on the piezoelectric surface to form an acoustic cavity or improve the device's efficiency. The details of IDT finger design, and the closely related details of SAW reflector design, are provided in substantial detail in Morgan *et al.*[95] and references therein.
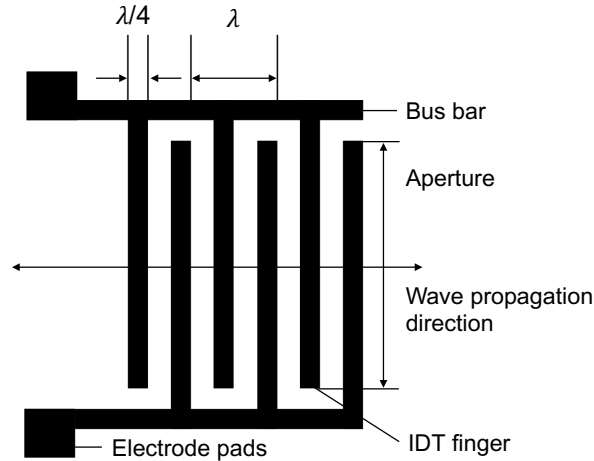
Figure 1.5: A SAW device consisting of comb-like interdigital transducers (IDT fingers), bus bars, and electrode pads on a piezoelectric substrate (e.g. 128–YX LN). The resulting traveling wave propagates as shown (perpendicular to the fingers), which can be observed using a laser Doppler vibrometer (LDV). The periodicity of the finger pairs defines the wavelength of the resulting SAW, λ_{SAW}.

As the SAW propagates through subsequent finger pairs, the wave is diffracted, creating a near-field region of largely parallel wavefronts known as the Fresnel region. The far-field region, where the SAW is broadly diffracted along major and minor lobes, is known as the Fraunhofer region. To minimize diffraction losses, the aperture of the IDT must be contained within the Fresnel region. For design purposes, a Fresnel parameter (F) is defined as $F = 4\lambda_{\text{SAW}}D_F/a^2$ where a is the aperture width (shown in Fig. 1.5 and D_F is the distance from the IDT edge. To remain within the Fresnel region, the aperture should be selected such that $F < 1$.

The efficiency of a SAW device is commonly linked to its quality factor [96], $Q = f_r/\triangle f$, where $\triangle f$ is the width of the resonant peak in frequency space measured at one-half the peak's
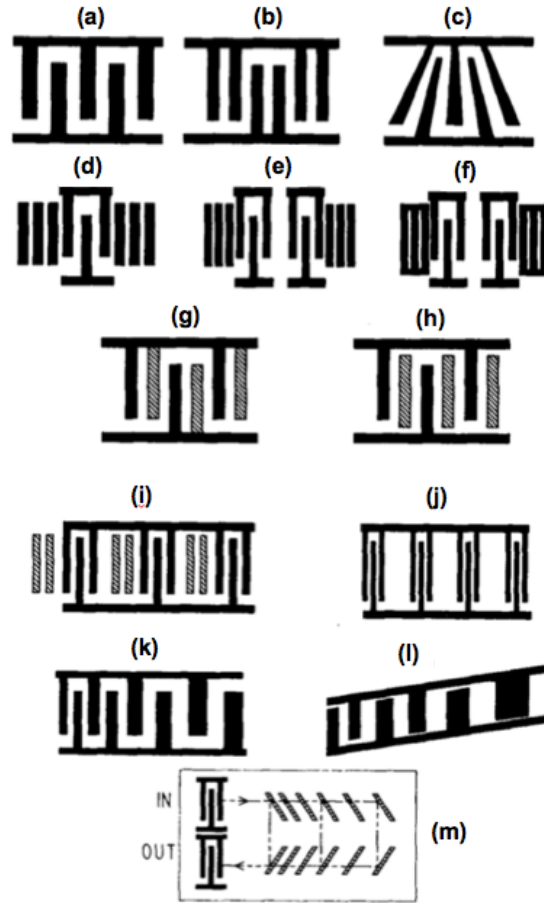
Figure 1.6: Common IDT designs for SAW devices: (a) single electrode IDT, (b) double electrode IDT, (c) slanted-finger IDT (SFIT) on collimating substrate shown with exaggerated tilt, (d) one-port resonator, (e) two-port resonator with open-circuited reflection-grating elements, (f) two-port resonator with short-circuited reflection-grating elements, (g) double-metalization single- phase unidirectional transducer (SPUDT), (h) floating-electrode SPUDT,(i) Lewis-type SPUDT,(j) "conventional" comb-filter, (k) chirped IDT, (i) chirped IDT for slanted-array compressor (SAC), and (m) geometry of a reflective array compressor using etched-groove reflectors. Reprint permis. Campbell (1989) [2].

highest amplitude. The quality factor is influenced by dielectric losses of the piezoelectric materials, loading effects, ohmic losses, and acoustic leakage to the substrate. The number of finger pairs (N_p) of a SAW IDT is an important parameter partially due to its effect on the quality factor [95]. The other aspect that drives the choice of the number of finger pairs in a SAW IDT is the effective piezoelectric coupling coefficient of the substrate, which can be defined in terms of

the change of SAW velocity from an open-circuit configuration to a short-circuit configuration, divided by one-half of the average of that velocity, $2\Delta v/v$. The greater the coupling, the greater the amount of energy that can be transduced in the IDT to mechanical output as a SAW. The amplitude of the SAW increases with N_p up to a material dependent limit, but the bandwidth is likewise reduced. In signal processing applications, optimizing N_p is a complex procedure [95]. However, when the primary concern is transduction power alone, typical in acoustofluidics, the constraints are simpler. For example, the bandwidth must only be suffcient to allow the device to be driven by signal generation and frequency response analysis equipment.

Optimization begins by defining the electrical admittance ($Y_t(\omega)$) of the IDT, which is dominated by capacitance (C_t), conductance ($G_a(\omega)$), and susceptance ($B(\omega)$), as in $Y_t(\omega) = G_a(\omega) + j(\omega)B(\omega) + j(\omega)C_t$. The equivalent circuit therefore consists of three components in parallel. When a voltage (V) is applied to the transducer, the power that is absorbed and produced are respectively defined as

$$P_a = \frac{1}{2}G_a V^2 \tag{1.1}$$

and

$$P_s = \frac{1}{4}\omega\varepsilon_\infty a N_p^2 \left(\frac{\triangle v}{v}\right)\left(\frac{\sin(x)}{x}\right)^2, \tag{1.2}$$

where ε_∞ is the capacitance per period of a unit-aperture, single electrode transducer, which depends on the substrate. At a certain frequency, the susceptance becomes negative and begins to counteract the capacitive term. When these terms cancel out, the admittance becomes real and directly corresponds to a resistive load, and also corresponds to the most efficient operation of the IDT. This occurs when the following equations are satisfied: $N_p = v\pi Q_t/2\triangle v$ and $\triangle f/f_r = 1/N_p$. Therefore, N_p=21 for a single electrode IDT, as in Fig. 1.6(a), with a bandwidth of 0.05, while N_p = 26 for the double electrode IDT with a bandwidth of 0.038 on 128° YX LN (*see* Fig. 1.6 (b)).

Figure 1.6 depicts other commonly used IDT designs to fit different design requirements. The double electrode IDT (*see* Fig. 1.6(b)) eliminates the in-phase reflections produced by

standard, single electrode IDTs by producing 180° phase shifted reflections that cancel out. The electrode sampling frequency changes from $2f_r$ to $4f_r$. Ma *et al.*[97] presented a self-aligned method to fabricate double electrode IDTs. The slanted-finger IDT (SFIT) (*see* Fig. 1.6(c)) is used to generate a wide-band response filter. The maximum angle that can be achieved depends on the coupling coefficient of the substrate. For example, the limit for a YZ LN substrate is 7° due to beam steering losses. The chirped IDT (*see* Fig. 1.6(k)) has a linear gradient in finger spacing that allows it to resonate at a wide range of frequencies, allowing the excitation of SAW at different wavelengths by tuning the input signal. Another common method of reducing SAW efficiency loss due to in-phase reflection is by adding reflectors, as shown in Fig. 1.6 (d), (e), and (f). The reflectors are typically the same size as the fingers and are offset by one wavelength from the fingers. Finally, to decrease the reflection loss from a source or finite impedance, a single-phase unidirectional transducer (SPUDT) design is used to cancel out those reflections (Fig. 1.6(g)-(i)) [98, 2]. Normally waves radiate in both directions from an IDT, but SPUDTs radiate in only one desired direction, towards the right in Fig. 1.6.

Focused IDTs

Compared to the designs described in Fig. 1.6, focused IDTs (FIDTs) can generate SAW with higher intensity by laterally focusing the SAW energy towards the main axis of the IDT, producing what is called a higher beamwidth compression ratio, $\eta_c = W_b/w$, where W_b is the -3 dB transverse bandwidth and w is the equivalent aperture of the FIDT. They have been utilized in many applications, such as signal processing convolvers [99, 100, 101], storage correlators [102], and time-Fourier transformers [103]. High intensity acoustic fields can also be generated, and thus enhance the acoustic-electric effect in order to manipulate electron-hole pairs in GaAs quantum wells [104]. Later in this review we will see examples of their use in acoustofluidic devices.

The FIDTs were first introduced by Kharusi *et al.* in 1972 [105]. They proposed a

structure that consisted of a series of identical curved fingers, so-called conventional circular-arc-shaped FIDTs (*see* Fig. 1.7(a)), which focus the waves into a narrow rectangular region along the *X* propagation axis. They discovered that the degree to which the waves were focused and the focal length depended on the anisotropy of the substrate. Their results matched Cohen *et al.*'s finding[106] that the focal length is given by $R_f/(1-2b)$, where R_f is the finger curvature and *b* represents the anisotropy of the substrate material ($b = 0$ for an isotropic substrate). In addition, they emphasized that the focusing properties of conventional circular-arc-shaped FIDTs do not improve as N_p is increased. Therefore, this type of FIDT was suggested to not be used on a highly anisotropic material, such as LN. In the 1980s, [107] calculated the amplitude field of circular-arc-shaped FIDTs on YZ LN and confirmed that the acoustic energy could be focused into a long, narrow region about the propagation axis on a substrate with high anisotropy (*see* [107], Fig. 3). Their results showed the beam compression ratio to be about 3% at a distance farther than R_f, which coincided with their experimental data. An important discovery in their work was that the actual focal point for SAW generated from a given set of fingers in the FIDT did not correspond with the geometric focal point. The anisotropy of the substrate typically causes the actual focal point for the SAW to lie up to two times farther away from the IDT than the geometric focal point.

More recently, an alternative FIDT design was investigated by [108, 109] consisting of a series of concentric fingers (*see* Fig. 1.7(b)) that focus the waves to a single spot. These concentric-arc-shaped FIDTs produce higher SAW intensity and beamwidth compression ratios than the conventional circular-arc-shaped FIDTs. The intensity of the SAW is proportional to N_p^2—much stronger than the N_p dependence of a straight IDT with an equivalent aperture. So as N_p increases, concentric-arc FIDTs display a stable amplitude field and better focusing characteristics while the conventional circular-arc FIDTs become unsteady. Moreover, increasing the curvature of the arc does not increase the amplitude, but it does increase the compression ratio, according to Wu *et al.*'s data.
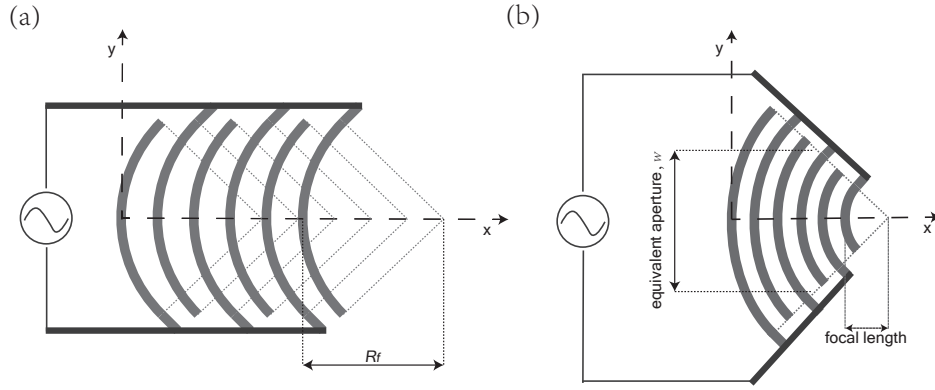
Figure 1.7: Commonly used FIDTs designs: (a) conventional circular-arc structure (characterized by R_f as curvature of transducer finger) and (b) concentric circular-arc structure (characterized by w as equivalent aperture). It shows clearly that the concentric design focuses to a point instead of a narrow region, resulting in better focusing property.

Like the traditional FIDT design, modified circular-arc FIDTs exhibit an actual focal point farther away than the geometric focal point due to the anisotropy of the material, as was discussed earlier in the section. Positive values of b in $R_f/(1-2b)$ tend to defocus the transducer, while negative values of b bring the focal plane closer toward the transducer. [110] experimentally showed that a concentric-circular FIDT focused to a point $\sim$1.7 times farther than the geometric center (*see* Fig. 1.8 (d)). This agreed with earlier work in which [109] measured the amplitude vs propagation distance of various configurations of concentric FIDTs and concluded that the actual focal length was $\sim$1.5–1.8 times greater than the geometric focal length. Work done earlier by Kharusi *et al.* [105] recognized this phenomena and suggested another type of FIDT design, the group-velocity surface shape. This type of shape, as its name indicates, consists of points tracked by the end of the energy velocity vector and ensures that waves are focused to a single point despite the dependence of wave velocity on propagation direction in an anisotropic material. The group-velocity surface pattern would become identical to the circular-arc pattern in the case of an isotropic surface. Further investigation by Wu *et al.* [108, 109] revealed that this shape is indeed a superior focusing structure, producing a higher intensity and beam compression ratio than the concentric circular-arc shape. An efficient application of this group velocity design was
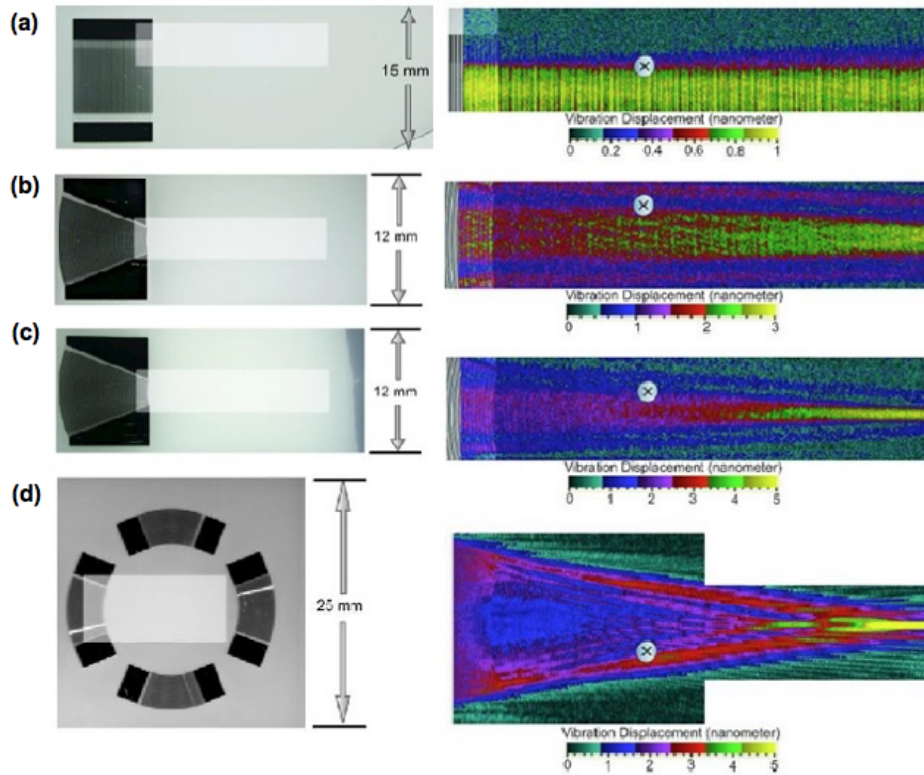
Figure 1.8: The distribution of SAW displacement on a LN substrate of different IDT designs at a center frequency of 30 MHz: (a) straight SPUDT, (b)&(c) focusing elliptical SPUDTs with approximate eccentricities of 0.616 & 0.831 respectively, and a (d) focusing circular SPUDT. It shows that the displacement of the SAW produced by straight SPUDT is uniform on the substrate, a line parallel to the propagation direction for the elliptical SPUDTs, and a single point with a circular SPUDT. Reprint permis. Shilton (2008) [110].

reported by Laude *et al.* [111], as they constructed the IDTs in an fully annular shape following the wave surfaces for *Y* cut and *Z* cut LN. The generated SAWs were experimentally proven to greatly overcome the anisotropy of the piezoelectric substrates and converge to an intense spot at the center.

Besides curved and annular shape of FIDTs, there are more advanced designs worth mentioning. Riaud *et al.* [112] proposed an IDTs array (IDTA), which consisted of 32 unidirectional slightly curved IDTs placed along the wave surface of the substrate to compensate for beam steering. By tuning the input signal of each IDT using the inverse filter method [113], the IDTA was reported to be able to not only focus the waves at an arbitrary position, but also generate

swirling SAWs, with an even higher intensity at the center. Later on, an alternative design, called the single spiraling IDTs, was introduced by the same group[114], *see* Fig. 1.9, which encoded the SAWs like a hologram and induced acoustical vortices when there was fluid on the surface. Applications of these SAW devices will be further discussed in subsection 1.4.2.
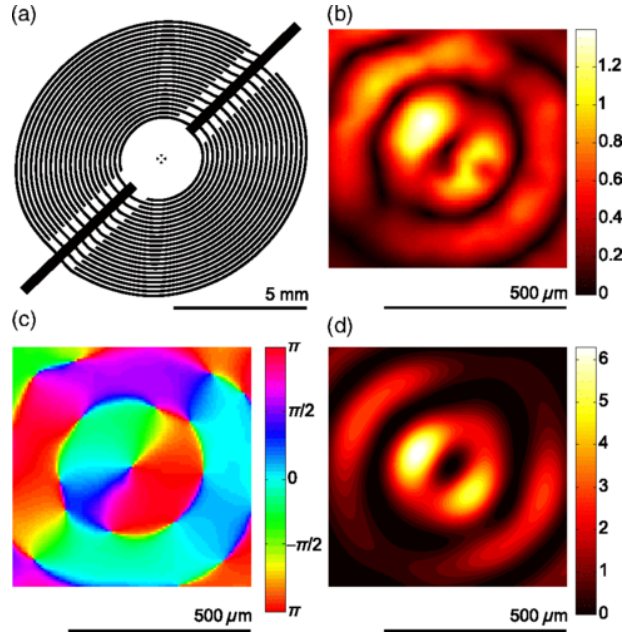
Figure 1.9: (a) Single spiraling IDTs design. (b) Experimental substrate vertical vibration amplitude (max amplitude 1.4 nm$_{pp}$ at 7 V$_{rms}$). (c) Experimental substrate vertical vibration phase. (d) Calculated potential well from experimental data (max height 6.3 fJ). Figures are reprinted with permission from Riaud (2017) [114]. Copyright (2017) American Physics Society.

Efforts have been made to visualize the amplitude field generated by FIDTs. Tan *et al.* [115] were able to directly visualize SAW using smoke particles with a mean diameter of 250 nm. The large transverse surface accelerations generated by SAW carry these particles aloft to relatively low vibration regions (*see* Fig. 1.10). Furthermore, Shilton *et al.* [110] showed SAW propagation patterns generated on a 128° YX LN surface for a straight SPUDT, concentric-elliptic SPUDTs with various eccentricities, and a concentric circular SPUDT by scanning the surface with an LDV (*see* section 1.1. Their results (*see* Fig. 1.8) offer clear visual evidence that curved IDT fingers focus SAW while straight SPUDTs do not. However, the smoke particle method allows measurement in larger frequency and amplitude ranges and does so in a shorter time

compared to LDV visualization. Rambach *et al.* [116] recently introduced another rapid and simple method of visualization using a wetting fluid film on the piezoelectric substrate, where film deformation was induced by acoustic radiation pressure causing a visible contrast between excited and non-excited areas. This method not only makes visualization of the sound path possible, but also possibly exposes the crystal anisotropy and SAW velocity.
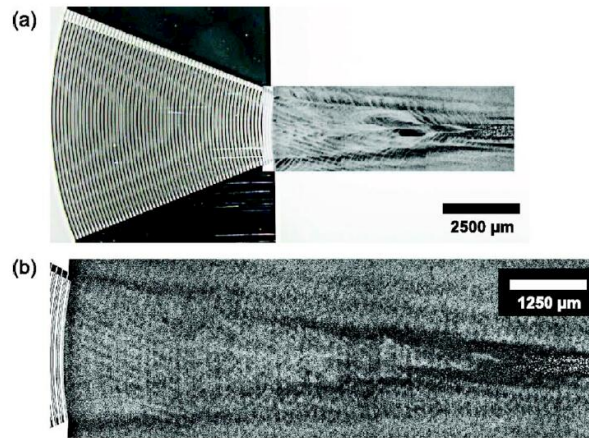
Figure 1.10: Visualization of SAW generated by FIDT with 250 nm sized smoke particles placed on the substrate after (a) 15 s exposure, and (b) after 30 s exposure. The distribution of pattern is achieved by the large transverse surface acceleration that carries the particles aloft to relatively quiescent regions nearby via acoustic streaming. Figures are reprinted with permission from Tan (2007) [117].

The above contributions have allowed FIDTs to be widely employed in acoustofluidic applications where their high intensity and greater bandwidth compression ratio can be utilized. Sessile drop translation and merging, particle concentration and mixing, and cell sorting have all benefited from the use of FIDTs due to their ability to maximize the proportion of acoustic energy that results in efficient acoustic force gradients and acoustic streaming.

1.3   Principles of Operation

Surface acoustic waves propagate upon single crystal piezoelectric substrates with weak attenuation. Upon encountering a fluid on the surface (*see* Fig. 1.11), SAW "leaks" into the
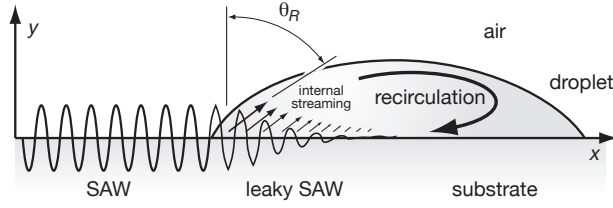
Figure 1.11: Sketch of a SAW acting on a small sessile drop. The acoustic energy is diffracted into the fluid at the Rayleigh angle, θ_R, leading to internal streaming in the small fluid volume, which drives recirculation. Adapted from [118]

fluid, forming sound that propagates in the fluid and acting to quickly attenuate the SAW in the substrate. The mechanism of the acoustic energy attenuation is balanced by viscous attenuation and dialative dissipation. This can be described as: $\frac{\partial W}{\partial t} + \nabla \cdot J = \rho_0 v_o[bu_0 \cdot \nabla u_0 - u_0 \cdot \nabla \times \nabla \times u_0]$, where W is the acoustic energy density, J is the energy flow, $\nabla \times \nabla \times u_0$ describe the viscous attenuation, and $u_0 \cdot \nabla u_0$ describe the dialative dissipation.

The sound, a progressive longitudinal acoustic wave, travels through the liquid at a Rayleigh angle $\theta_R = sin^{-1}(v_l/v_R)$ [119], where v_l and v_R represent the speed of sound in the liquid and the speed of the Rayleigh SAW upon the solid substrate, respectively. For example, for the case of SAW traveling from 128° YX LN into water, $v_l =$1485 m/s and $v_R = $ 3965 m/s, results in $\theta_R = 22°$.

Generally, the acoustic wave will turn into the media with a slower acoustic velocity, analogous to Snell's law. It is important to remember, however, that modal conversion can occur, allowing acoustic waves to travel across interfaces even when the Snell's law prediction suggests total internal reflection would occur, as explained in [120] where modal conversion from longitudinal acoustic waves (sound) in a fluid to Lamb waves in a superstrate are found. Furthermore, SAW likewise will leak into viscoelastic solids, particularly those typically used in microfluidics like polydimethylsiloxane (PDMS). While SAW devices can be used in enclosed microfluidics devices that employ PDMS, it is best to minimize the area of PDMS bonding to the piezoelectric substrate over the region carrying the SAW. Inexpensive alternatives to PDMS are possible to mitigate this problem, especially via the use of ultraviolet-sensitive, low-viscosity

epoxies for layer bonding [121].

The length along the surface of the piezoelectric substrate over which a Rayleigh wave decays by a factor of e due to the leakage of SAW into the fluid to transmit sound is the attenuation length $\alpha^{-1} \propto 1/f$: [119]

$$\alpha^{-1} = \frac{\rho_s v_R \lambda_{\text{SAW}}}{\rho_f v_l}, \tag{1.3}$$

where ρ_f and ρ_s are the densities of the fluid and the solid respectively, v_l is the speed of sound in the fluid media and $v_R = f\lambda_{\text{SAW}}$ is the Rayleigh wave phase velocity. The sound wave in the fluid, on the other hand, propagates uniaxially at the Rayleigh angle[122] and has a distinctly different attenuation length, $\beta^{-1} \propto 1/f^2$:

$$\beta^{-1} = \frac{\rho_0 v_l{}^3}{4\pi^2 f_{\text{SAW}}^2 \left(\frac{4}{3}\mu + \mu'\right)}, \tag{1.4}$$

where f_{SAW} is the SAW frequency and μ and μ' are the shear and bulk viscosities of the fluid, respectively. Values of the solid and fluid attenuation lengths in the LN-water system were measured by Dentry *et al.* [6] and are listed in Table 1.2.

Table 1.2: Attenuation length of the SAW surface displacement at the LN and water interface, expressed as α^{-1} (*see* Eqn. 1.3) and attenuation length of the sound in water, expressed as β^{-1} (*see* Eqn. 1.4). Reproduced with permission from Dentry (2014) [6].

f_{SAW}(MHz)	α^{-1}(mm)	β^{-1} (mm)
19.7	2.4	120
54.2	0.87	16
122	0.39	3.1
240	0.19	0.80
490	0.097	0.19
936	0.046	0.052

Attenuation of the sound in the fluid induces a momentum flux responsible for the formation of steady state fluid flow: acoustic streaming [123, 122]. Acoustic streaming can be crudely classified depending on the acoustic path length permitted in the fluid and the location

of viscous attenuation. Schlichting streaming is the result of viscous shear attenuation near the solid-fluid boundary [124] and Eckart streaming is the result of sound attenuation in the bulk of the fluid [21]. Rayleigh streaming arises from Schlichting streaming [22]. Further details on the types of streaming, their respective characteristics, and previous studies are summarized in Table 1 of the review by Friend *et al.* [17]. In cases where a free fluid surface is present, the nature of streaming and how it causes fluid transport is slightly more complex [125]. In later sections, we will explore how streaming produces fluid and particle motion.

Particle behavior in acoustofluidic systems is typically controlled by the following forces: direct and indirect (Bjerknes) acoustic radiation forces, viscous Stokes drag, van der Waals forces, and electrostatics and electrodynamics. The latter two, van der Waals and electrically-driven forces, tend to be negligible in acoustofluidics, though there have been reports of combining these phenomena to achieve results not possible with acoustics alone. The direct SAW radiation force under a traveling wave was derived by King[126] and is expressed as:

$$F_{rt} = 2\pi\rho_0 A^2 \left(\frac{kr}{2}\right)^6 \left[\frac{1 + \frac{2}{9}\left(1 - \left(\frac{\rho_0}{\rho_p}\right)^2\right)}{2 + \left(\frac{\rho_0}{\rho_p}\right)^2}\right] \tag{1.5}$$

where r is the particle radius, $k = \omega/v_R$ is the wavenumber of SAW, A is the amplitude of the incident wave, ρ_0 is the liquid density, and ρ_p is the particle density. On the other hand, the radiation force under a standing wave is expressed as [127]:

$$F_{rs} = \left(\frac{\pi p_0^2 r^3 \beta_w}{2\lambda_{SAW}}\right)\left(\frac{5\rho_p - 2\rho_0}{2\rho_p + \rho_0} - \frac{\beta_c}{\beta_w}\right)(\sin(2kx)) \tag{1.6}$$

where p_0 is the acoustic pressure, x is the position of the particle, λ_{SAW} is the wavelength of SAW, and β_c and β_w are the compressibility of the particle and the surrounding fluid, respectively. Notice that the radiation force is proportional to r^6 for a traveling wave, but only proportional to r^3 for a standing wave. However, the reader should consult more recent literature by Bruus [128],

26

Lauga [129], and Marston [130] to properly take into account fluid and particle compressibility and other important effects. We finally note that acoustic radiation interacts with surfaces in a more complicated way, demanding care in its treatment [131].

The stream-wise drag experienced by a particle of radius r can be approximated by the Stokes drag equation, $F_D = 6\pi\mu r v_D$, where v_D is the velocity difference between the surrounding fluid and the particle. Finally, the Bjerknes force, an interparticle force arising from the scattering of the incident acoustic wave can be used to describe the interparticle interactions between bubbles [132] or compressible particles [133, 134, 135, 136]. The Bjerknes force is defined as:

$$F_B = 4\pi r^6 \left[\frac{(\rho_p - \rho_0)^2 \left(3\cos^2\theta - 1\right)}{6\rho_0 r^4} U^2 - \frac{\omega^2 \rho_0 (\beta_c - \beta_w)^2}{9L^2} p_0{}^2 \right] \tag{1.7}$$

where U is the particle velocity amplitude, L is the distance between two particles, θ is the contact angle between the fluid and particle, and p_0 is the acoustic pressure amplitude.

1.4   Fluid Manipulation in Sessile Drops

Sessile drops rest on top of a surface and have been successfully actuated by electrowetting, SAW, and even light using special photoresponsive surfaces [137], forming virtual walls using optical illumination of photoelectric layers [138, 139]. The dominant application of these technologies is in biological assays. The reader is referred to the review by Haeberle *et al.* for a comparison of these and other methods for microfluidic lab-on-a-chip platforms [140]. However, none of the other methods are capable of all the types of actuation described in this section.

Both acoustic streaming within the drop and acoustic radiation force on the free surface of the drop can be induced using SAW. Traveling SAW (TSAW) and standing SAW (SSAW) dominate the literature, but other acoustic modes are also useful in select situations. However, we note that acoustic waves in solids are not easily isolated so that unintended modes are often

present. These waves, whether SAW or not, deliver sound into a sessile drop at the Rayleigh angle as described in Section 1.3, as long as the wave propagates from a region without the fluid to a region where the fluid is present. In general, the effect of the acoustic wave in the drop depends on the properties of the original wave in the substrate, the properties of the fluid, and the geometry of the drop. We break down manipulation into four regimes: mixing, translation, jetting, and atomization. For each regime, we highlight recent work regarding the basic understanding of the phenomena as well as recent advances in the associated applications. After mixing we pause to consider particles in sessile drops.

1.4.1   Mixing

Acoustic streaming at the Rayleigh angle produces recirculation in a stationary sessile drop (*see* Fig. 1.11). Almost fifteen years ago, Wixforth *et al.* [141] described the idea of an acoustically-actuated, miniaturized digital droplet lab on a chip, including sessile drop transport and internal mixing with recirculation. The primary internal flow promotes mixing in the drop, but is not generally helpful for other applications such as particle concentration as will be explained in Section 1.4.2. Li *et al.* [118] demonstrated that an azimuthal flow with a vertical component can be induced in a sessile drop from asymmetric SAW exposure on a LN substrate, driving vortical flow about a tilted axis [142]. They [118] provided several designs for generating asymmetric SAW as illustrated in Fig. 1.12.

Improvements have been made in producing internal flow in drops by exploring other types of acoustic waves. Shilton *et al.* [110] explored circular and elliptical FIDTs in a similar asymmetric exposure arrangement. Elliptically focused SAW produced more intense streaming and thus stronger primary internal flow while circularly focused SAW produced stronger azimuthal flow, concentrating the SAW power to a single small region of size comparable to the SAW wavelength, accentuating the effects of the asymmetric droplet placement.

Theoretical work on acoustic streaming, which induces mixing in sessile drops, was

undertaken by Nyborg in the 1960s who suggested that the nonlinear hydrodynamic term due to the Navier-Stokes momentum equation could be neglected [143]. He argued that streaming and the resulting fluid velocity were both second order phenomena and thus the above term was fourth order and negligible. In the 1970s, Lighthill argued that the nonlinear term was only negligible for slow streaming [122]. Shiokawa followed Nyborg's use of an effective body force for calculating streaming velocity in the theory following his experimental work on manipulation of sessile drops using acoustic streaming [144]. Both authors neglect viscosity and argue that the attenuation, which is fundamental to streaming, comes mostly from refraction of the wave at the solid/fluid interface rather than from viscous attenuation.

Most modern numerical work on streaming has closely followed Shiokawa's procedure including a 3D simulation of low power mixing performed in 2010 by [145]. They include the nonlinear hydrodynamic term, but continue to neglect viscosity. They experimentally measured the SAW amplitude as a function of input power and separately measured the streaming velocity as a function of input power. Then, in their numerical calculation, they determined streaming velocity in three spatial dimensions as a function of SAW amplitude and correlated these results to their experiments using a fitting relationship between the two measured quantities. The numerical and experimental results illustrate some simple flows in relatively large drops (30 uL) under relatively low power (up to 0.025 W).

In contrast, Vanneste *et al.* [146] contributed a numerical formulation of acoustic streaming that incorporates viscous attenuation. They derive three contributions to the resulting mean flow: internal Eulerian, boundary Eulerian, and Stokes drift. They point out that without viscous dissipation (as formulated above) Reynolds stress and the pressure gradient are balanced and there can be no mean flow generated in the interior. Instead of using the effective body force in the averaged momentum equation, they use an averaged vorticity equation due to Eckart [21]. The authors are able to apply their results to a variety of geometries, but their solutions are only in two dimensions. Importantly, neither of these two numerical simulations accounts for acoustic

29

radiation force and the reflections that result from a finite boundary.
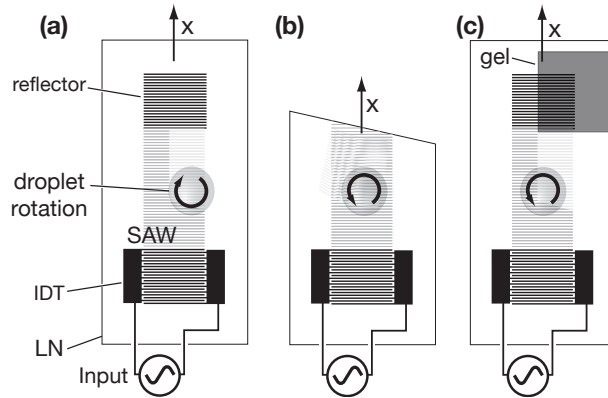
Figure 1.12: Three methods used to produce azimuthal flow via asymmetric SAW actuation. (a) Symmetry is broken offsetting the drop from the center line, (b) Asymmetry is generated from the angled edge of the LN substrate, and (c) Asymmetry is generated by absorbing SAW in one region, while reflecting them in another.

In 2014, [147] were able to produce *poloidal* flow using a simplified transducer, a pair of L-shaped electrodes that generate Lamb waves. Poloidal flow only occurred above a critical frequency that was found to be dependent on the diameter of the drop. Lamb waves occur in the bulk of the substrate so their attenuation is different from that of SAW, but the concept is the same. The acoustic streaming-driven primary internal flow from the Lamb wave becomes poloidal flow only when both the acoustic energy impinges radially from all sides and the attenuation length of the Lamb wave in the substrate is less than the radius of the drop as in Fig. 1.13. Since the attenuation length is dependent on frequency, the existence of a critical frequency is due to the necessity of this attenuation length being less than the drop radius for the poloidal flow to exist.

At the same time, Riaud *et al.* [148] described a more complicated acoustic wave that they claim allows greater control over the internal flow. They suggested the use of helical waves (Bessel beams) to generate cyclone-like flow with both poloidal and toroidal streamlines. Theoretically, the shape of vortices in the fluid can be controlled by the boundary conditions of the fluid and the properties of the helical acoustic waves. Specifically, the axial vorticity is controlled by the acoustic field while the azimuthal vorticity is controlled by the boundary conditions. This result
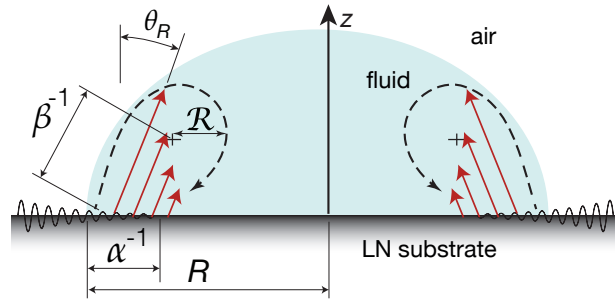
Figure 1.13: Poloidal flow is set up in a sessile drop due to the chosen ratio of drop radius, R, to recirculation length, $\mathcal{R}$, which depends on β, α, and θ_R. Corrected and adapted with permission from [88] Copyright (2014) American Chemical Society.

is analogous to the conclusions drawn above regarding internal flow produced by asymmetry and different wave-forms [149]. Riaud *et al.* argue mathematically that these effects are decoupled. This implies that the variables can be independently chosen to produce desired internal flows. They also observed a curious phenomena: fluid flowed *away* from the acoustic energy source when the acoustic beam-width was small compared with the width of the fluid boundary, but flowed *toward* the source when the beam was confined. The authors call these repeller and attractor vortices respectively. The helical acoustic waves used to produce these flow effects can be generated using inverse filtering techniques. In fact, in another paper they [63] demonstrate the production of "swirling SAW" by an array of IDTs; in a more recent paper, they [150] also use these waves for particle manipulation.

Riaud *et al.* [151] also investigated the effects of viscosity on acoustic streaming flow, showing that it strongly affects the Eckart streaming in the bulk of the sessile drop and therefore should be considered even though it is absent from the velocity expression obtained by a balance of acoustic attenuation and fluid shear. This is an important improvement upon the traditional perspective perhaps best espoused by Lighthill *et al.* [122]: viscosity is crucial to acoustic streaming, yet its specific value is said to not affect the streaming characteristics. This work expands on the simulations by Vanneste *et al.* described earlier. They reproduced experimentally observed flow patterns in sessile drops actuated by SAW with hydrodynamic simulation and were

able to show how this relates to the acoustic field. They found that the acoustic field that drives streaming is dominated by a small number of caustics despite the presence of a chaotic field (this chaotic field was quantified earlier by Shilton in the context of flow in microfluidic wells [152]). In the case of a sessile drop on LN they use scaling to reduce the problem to dimensionless numbers for surface attenuation and bulk attenuation that may be used to predict flow patterns in new situations.

One of the major advantages of sessile drop microfluidics is the extremely small sample volumes that are possible. Recently, Shilton *et al.* [153] were able to shrink the size of sessile drops while maintaining control of the flow for mixing, and Miansari *et al.* [76] were able to crudely manipulate 10 fℓ droplets in a nanoslit using SAW.

Generally, these devices are operated below a critical input power necessary to translate the sessile drop across the substrate. This critical power depends on the contact line pinning of the drop, in turn dependent upon the wetting properties of the fluid/surface combination; for example, [149] report the critical power for their arrangement to be 700 mW. Once identified for a given system, this critical power level represents the upper practical limit for inducing mixing, flow, or internal manipulation within the droplet.

1.4.2   Particle, Colloidal, and Cell Manipulation in Sessile Drops

The manipulation of micro-scale objects in fluid by SAW relies on both the acoustic streaming-induced flow described in the previous section and the acoustic radiation force and other forces introduced in section 1.3. Acoustic streaming depends upon the properties of the acoustic wave generated by the source and by the geometry and fluid properties of the drop. The size, density relative to the fluid, and compressibility of the particles determine the effectiveness of acoustic radiation forces upon them.

Concentration, separation, or isolation of target particles are typical needs in biochemical analysis. For dilute samples, an effective collection procedure for the targeted particles can

significantly reduce the amount of fluid handling [154]. Particle concentration helps to minimize measurement noise and improve detection sensitivity. Acoustic forces can be used to non-invasively position, concentrate, or fractionate particles. In something of a scientific curiosity, standing waves were first identified by the concentration of suspended particles at acoustic pressure nodal or antinodal planes in a fluid by Kundt and Lehmann in 1874 [155]. However, the process was slow, with concentration requiring at least several minutes. Recently, researchers have used SAW devices to accelerate and otherwise improve concentration, separation, and centrifugation.

The position of the particles in sessile drops vary with the drag force and acoustic radiation force applied to the particles. Destgeer *et al.* investigated four regimes of particle position[156]. A droplet with $R > \alpha^{-1}$ has reduced potential for symmetrical vortices. Droplet size and SAW attenuation length also determine whether the acoustic radiation field produces standing waves or traveling waves in the case of counter-propagating IDTs. If $R > \alpha^{-1}$, then TSAW is generated from each side of the drop. If $R < \alpha^{-1}$, then standing waves are set up in the portion of the drop where overlap occurs.

As described in Section 1.4.1, Li produced azimuthal flow in a sessile drop. This type of flow allows particles to be rapidly concentrated at the center of the drop due to shear-induced migration. It is important to note that concentration was only observed in a range of applied power between 150–450 mW while dispersion was observed on either side of this range. This intermediate range of SAW power represents a Goldylocks state below which streaming does not overwhelm particle concentration and above which the particles are transported [118]. Li showed that bio-particles remained viable and were concentrated to within 10% of the drops volume under asymmetric SAW actuation. These results show promise for use in conjunction with bio-sensors in order to reduce the sensitivity requirements among other applications.

Wilson *et al.* introduced a method using phononic superstrates to achieve programmable complex fluid manipulation on-chip [157]. The phononic structures can produce filter and

waveguide effects by scattering and reflecting the SAW without fabricating multiple IDTs on the substrate. They chose a square array of circular holes made in a silicon wafer via dry-etch photolithography and demonstrated centrifugation of 10 μm polystyrene beads and blood cells in a droplet using either a filter-based design or a waveguide-based design. This technique may be useful in certain specialized applications where a single SAW device could be used for multiple types of manipulation depending on the superstrate, which could be switched out as desired. Later on, [112] claimed an improved result from a set of 32 IDTs patterned in a circle and driven by a programmable circuit in order to effectively drive planar waves. They demonstrated droplet division, merging, and atomization with the platform. Moreover, they later demonstrated particle manipulation and positioning through careful control of the signals input into the IDTs [114].

As mentioned earlier FIDTs can improve fluid actuation in SAW devices. Shilton found that a concentric circular-arc SPUDT was capable of concentrating particles in microliter drops in under 1 second, which is an order of magnitude faster than the straight SPUDT [110].

[158] have claimed that the conclusions made by Rezk *et al.* about their poloidal flow, Lamb wave device are incorrectly based entirely on acoustic streaming flow without due consideration of the acoustic radiation force. The experiments by Rezk included only one droplet size (1.5 mm) and single particle size (5 μm), whereas those by Destgeer included a range of particle sizes and droplet volumes, while both researchers varied frequency. Rezk claimed that shear-induced migration caused concentration within the poloidal vortex (*see* Fig. 1.15). Destgeer found that particles were only concentrated when a parameter representing the balance of radiation force to drag force, $\kappa = \pi d_p f_{LW}/c_f$, was greater than unity (*see* Fig. 1.14(a)). Here d_p is the particle diameter, f_{LW} is the frequency of the Lamb waves, and c_f is the speed of sound in the fluid. They were able to accurately predict which combinations of particle size and frequency would result in concentrated rings (*see* Fig. 1.14(b)). However, [158] failed to take shear migration into account, important in forming such a ring. It may be that poloidal flow is a necessary, but not sufficient condition for concentration in a ring shape, which requires radiation force. The studies agreed

that increasing the frequency, and thus reducing the attenuation length in the substrate, moved the concentrated ring towards the perimeter of the drop. Regardless of the precise mechanism, these studies show that particles can be reliably concentrated to a narrow ring at a tunable radius in a sessile drop without the need for microfabricated IDTs.
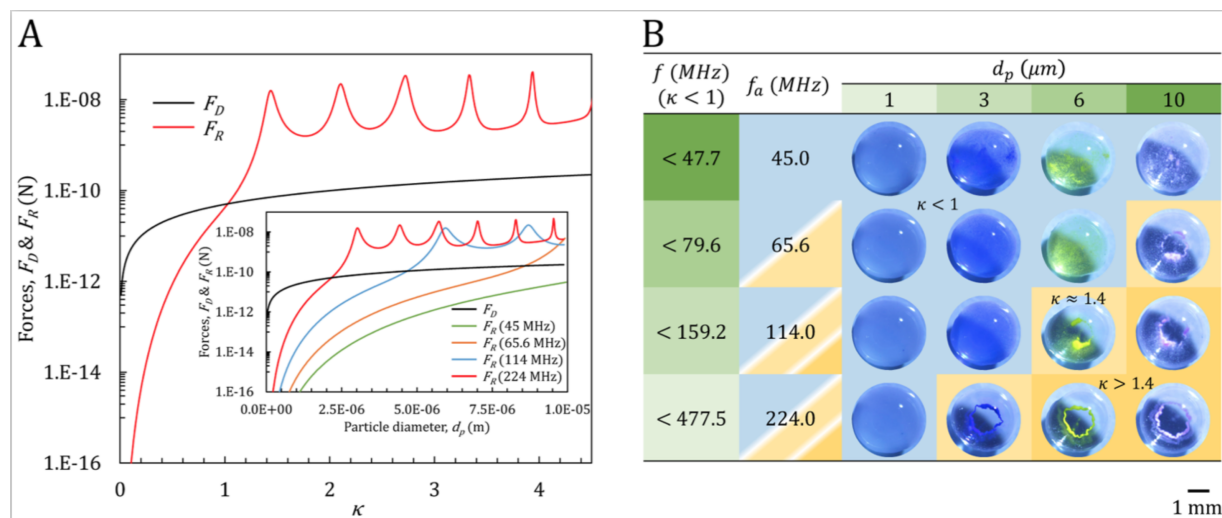
Figure 1.14: A) Force vs κ, where F_D is the drag force and F_R is the radiation force. Notice that F_R overtakes F_D at $\kappa = 1$. The inset shows the similar Force vs drop size relationship for various frequencies. B) Each image corresponds to a frequency, drop size pair and the values of κ for each pair are indicated to show that ring formation occurs for $\kappa > 1$, where radiation force dominates drag. Reprinted (adapted) with permission from G. Destgeer, B. Ha, J. Park and H. J. Sung, *Analytical Chemistry*, 2016, **88**, 3976–3981. Copyright 2016 American Chemical Society.

Other researchers have also played with this balance between flow forces induced by streaming and direct radiation force in order to separate particles. [159] were able to efficiently separate and align different sized particles within a drop using SSAW. They fabricated two opposing IDTs with different resonance frequencies on a 128° YX LN substrate in order to set up a periodic distribution of pressure nodes. [160] demonstrated using a 20 MHz device that relatively small particles (2 μm) for which drag force dominates were concentrated in the bulk of the drop, while large particles (30 μm) for which radiation force dominates were driven to the periphery. In their experiments, the large particles were concentrated to the free surface of the droplet within 3 seconds under 400 mW of power (*see* Fig. 1.16). [161] used slanted IDTs
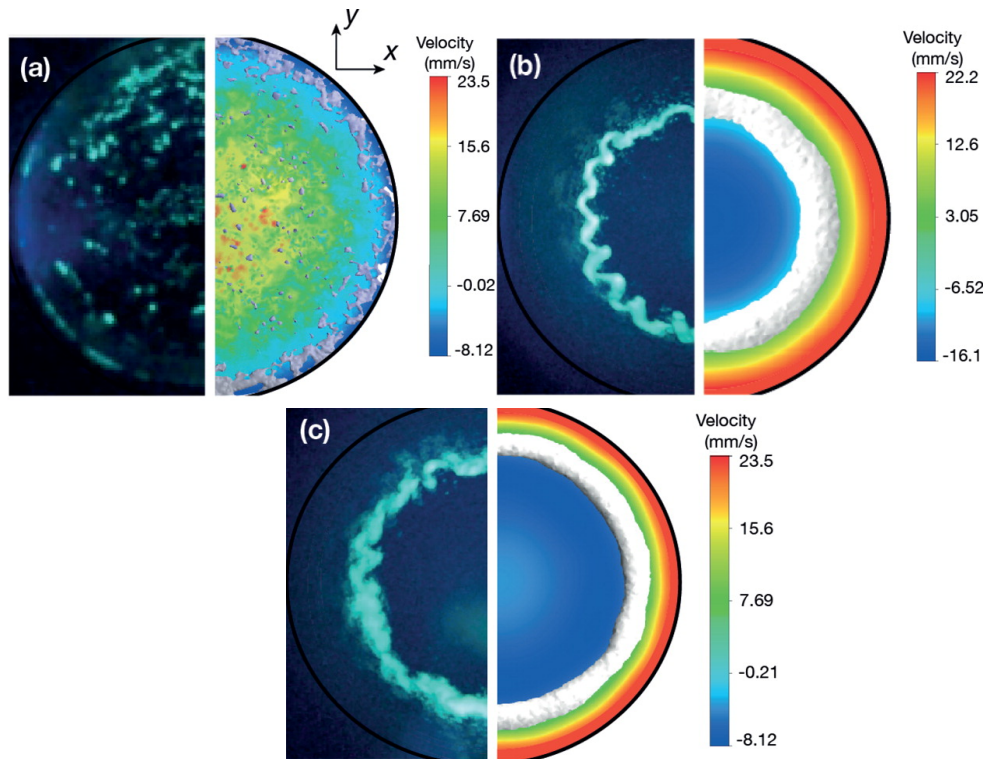
Figure 1.15: Experimental images (left) compared to finite element analysis predictions of fluid velocity (right) for a sessile drop actuated by Lamb waves. a) At 25 MHz no vortex is formed. b) At 157 MHz a clear vortex is formed and the particles collect at the lowest shear area. c) At 225 MHz the vortex and particle ring shift towards the perimeter due to a shortened attenuation length. Adapted with permission from A. R. Rezk, L. Y. Yeo and J. R. Friend, *Langmuir*, 2014, **30**, 11243–11247. Copyright 2014 American Chemical Society.

to generate SAW at multiple frequencies from a single device, which allowed them to separate particles according to their size due to the dependence of radiation force on both frequency and particle size. [162] later demonstrated particle separation by density using TSAW to generate acoustic streaming inside a droplet. Drag, buoyancy, and gravity forces effect particles to varying degrees based on their density relative to the carrier fluid. As a consequence, when the density of the fluid was between that of the two particles, the high density particles (red beads) were accumulated in the center of the droplet while the low density particles (green beads) were enriched at the periphery. The separation shown was achieved in 3 seconds using 200 mW of power.

The coffee-ring effect is used extensively in stationary sessile drop platforms [163]. [164]
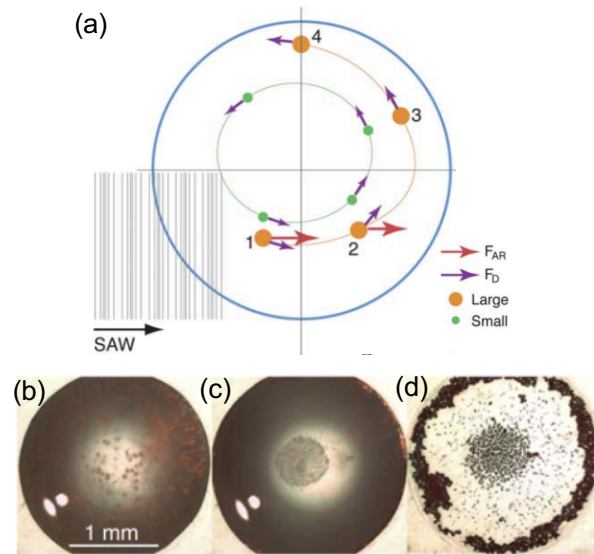
Figure 1.16: (a) Larger particles (the size of which are frequency dependent) are dominated by radiation force with the drag force playing a smaller role on the overall particle trajectory. The larger particles in position 1 are driven toward the free surface of the droplet. The effect of acoustic streaming at positions 1-4, however, causes the particles to circulate within a portion of the droplet before they reach the periphery near position 4. The smaller particles recirculate within the droplet until they concentrate in the center under the influence of drag. From experiment: (b) Initially the pollen and synthetic particles were suspended homogeneously throughout the entire droplet. (c) After 3 s, the pollen particles concentrated in the center of the droplet, and are hence separated from the synthetic particles, which concentrated along the periphery of the droplet. (d) The two species remain separated even after the droplet is fully evaporated after 1 min. Printed with permission[160] from The Royal Society of Chemistry.

combined this technique with low frequency SSAW to control evaporative self-assembly of particles from a drop placed on a variety of superstrates. Under uncontrolled circumstances, particles in evaporating drops are pulled towards the contact line by convection. They showed that SAW actuation could trap particles within capillary wave nodal circles and/or SSAW nodal lines and thus prevent this so called "coffee-ring effect." This technique does not require modification of the fluid, particles, or surface involved (unlike other methods). However, in light of the above paragraph on Destgeer's work, it must be noted that their technique does require compatibility between frequency and drop size in order to set-up standing wave nodes. Fig. 1.17 shows how particles were uniformly deposited in a disc rather than concentrated in a ring near the contact line when SAW were used.
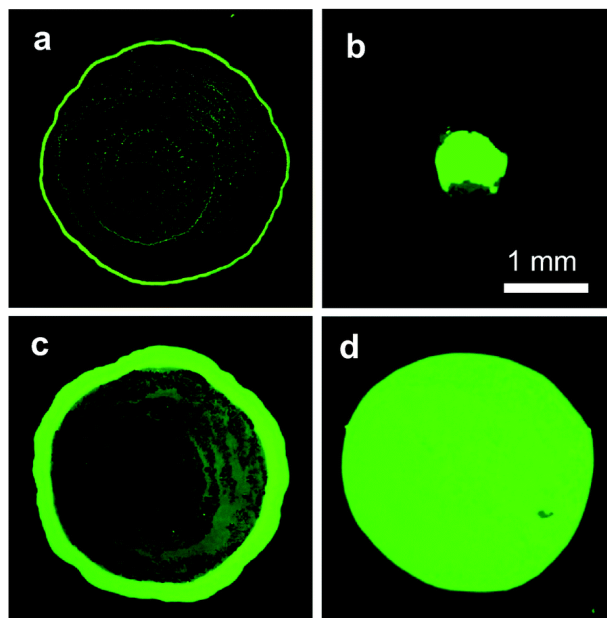
Figure 1.17: The coffee-ring effect is suppressed in a sessile drop containing 2 μm particles when actuated with SSAW. a) An undisturbed drop with 0.1% volume fraction of particles. b) A similar drop actuated by 9.7 MHz SSAW. c) An undisturbed drop with 2.5% volume fraction. d) A similar drop actuated by 20 MHz SSAW. All images are post-evaporation. Printed with permission[164] from The Royal Society of Chemistry.

Many other biological assay processes can be enhanced by the use of SAW. Cellular spheroids are useful in diagnostics and drug testing since they resemble the structure and functional performance of in vivo tissue [165]. A SAW-driven centrifugation approach was reported to enhance the assembly of cellular spheroids in a micro well plate by [166]. Acoustic radiation was coupled through a fluid on a LN substrate into the micro well plate placed on top of the SAW device. Centrifugation was driven via acoustic streaming generated by SAW. In this technique microcentrifugal flow in the micro wells—a result of geometric asymmetry—aggregates the cells as a precursor to spheroid formation. Kurashina also used ultrasound-generated vortices in well plates to agglomerate cells and reported that spheroids formed by ultrasound were fifteen times larger than without the ultrasound in low cell binding plates [167].

The influence of flow on particle uptake rates of cells has been studied using SAW-generated acoustic streaming [168]. Acoustic streaming was used to mimic blood flow conditions

for cell culturing and the results show that in relatively high shear conditions, particle uptake rates of cells are much lower.

[169] studied the influence of 132 MHz focused SAW on the adhesive properties of red blood cells that had been affected by malaria and treated with glutaraldehyde (a common disinfectant used in hospitals) but were nonetheless healthy. The detachment behavior of cells initially adhered to the piezoelectric substrate were observed during exposure to acoustic streaming at various values of input power. The results show that healthy red blood cell membranes translate across the substrate before detachment. Rolling and flipping behaviors are observed for treated and malaria-infected cells. Malaria-infected cells also strongly reattached to the surface in the process. Detachment rates for healthy red blood cells were larger than the modified cells. Adhesive properties of cells have also been utilized to sort cells (HEK293 and A7r5 for example) using acoustic streaming flow [170].

In addition to cell manipulation, SAW has been used to manipulate smaller bio-particles. [171] reported a method to sense micro-RNA, which have potential applications in the early detection of cancer, with greatly reduced sample volumes by lysing exosomes with SAW. Exosomes are much smaller than most cells and the acoustic radiation force and electric field produced by SAW is uniquely suited to their lysis.

1.4.3 Translation

The primary application for sessile drop translation is planar microfluidic lab-on-a-chip platforms. Transport in microfluidics is conventionally achieved by pumping in continuously filled channels, but it can also be achieved with sessile drops using SAW. With this approach, drops are isolated from their surroundings and require smaller volumes, though evaporation can become an issue [172]. The SAW input power must exceed a threshold that arises due to contact line pinning and contact angle hysteresis, which must be overcome in order to translate the drop. These concepts are well explained in a review of surface science by Gao *et al.* [173].

Wixforth *et al.* [174] first demonstrated drop translation using a combination of TSAW and patterning of the surface wettability. Renaudin *et al.* then explored the effects of surface wettability treatments on the power necessary to translate a 2 μL drop [175]. It is important to point out that they used X-cut LN rather than the more common 128° YX LN, which have different coupling coefficients. On bare LN, which is hydrophilic, the drop required 1.6 W and after a hydrophobic treatment it required only 0.56 W. They found that predictable movement required a surface patterned path, but bare LN paths lead to inefficient movement and clearly, hydrophobic paths would lose drops to the surrounding area. In 2007, Tan approached the problem in a slightly different way using elevated teflon strips (10 μm thin) on bare LN[117] (*see* Fig. 1.18). This technique regained the translation efficiency while avoiding the predictable movement problems encountered by Renaudin *et al.* by using a slightly raised surface to isolate the intended path rather than surface treatment.
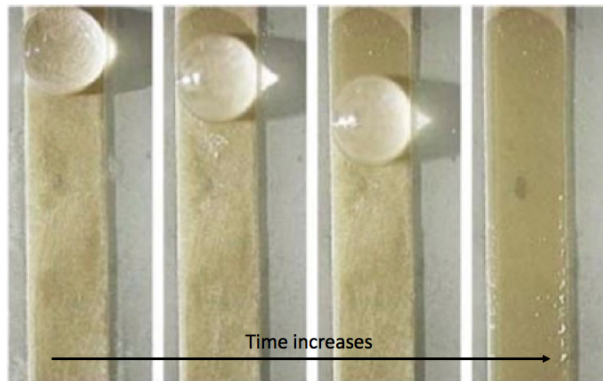
Figure 1.18: A water droplet being translated on a 10 μm thick hydrophilic Teflon path atop a LN substrate via a TSAW. Adapted with permission[117] from The Royal Society of Chemistry.

Because the acoustic and hydrodynamic response time-scales are radically different, input signal modulation can be used to improve translation efficiency. Both Renaudin *et al.*[175] and Tan *et al.*[117] employed duty cycles in their signals. Renaudin *et al.* found that, at a certain pulse duration, the displacement per pulse was constant with respect to increases in drop volume so that greater efficiency is possible with short pulse width modulation. Baudoin *et al.*[176] presented a modulation of the SAW by Rayleigh-Lamb inertial-capillary frequencies that reduces the power

required for translation by a factor of two. Modulation may also be useful for mixing, jetting, and atomization.

In 2010, Brunet *et al.*[177] numerically and experimentally explored the effects of surface displacement amplitude, drop volume, and viscosity on drop translation. The drop experienced internal flow, asymmetric deformation at the Rayleigh angle, vertical, free-surface oscillations and translation. They observed, as expected, that a minimum amplitude was required for translation, but this minimum did not seem to depend at all on drop volume. In the same set of experiments, varying the amplitude at a fixed volume revealed an asymptotic drop velocity maximum whose value depended on the choice of volume.

There was also a velocity maximum as the volume was varied at fixed amplitude, but this maximum occurred at the same volume regardless of which amplitude was chosen. We can understand this by noting that attenuation of SAW in the substrate indicates how much energy is absorbed by the drop. Maximum velocity occurs when the drop/surface interface is at least as long as α^{-1}. Drops larger than this do not absorb more energy, but gain excess mass and thus move slower.

This study highlights the importance of considering both radiation pressure and streaming. Radiation pressure becomes important when the acoustic beam reaches the drop's free surface before being attenuated. Thus, the size of the drop relative to β^{-1} determines in part the effect of radiation pressure. Brunet observed vertical oscillations in the drops at frequencies and amplitudes (referring to the fluid oscillation not the solid displacement) that correspond to inertial-capillary vibration modes (similar to Rayleigh-Lamb as exploited by Baudoin above). In their interpretation, the free-surface deforms upward due to radiation pressure, but this deformation simultaneously reduces the effect of radiation pressure so that capillary forces pull the drop back down and the cycle repeats. Viscosity had the obvious effect of decreasing the translation speed, but it also reduced oscillations. Since viscosity increases attenuation it reduces radiation pressure and increases streaming. Clearly radiation pressure is critical for translation and for deformation of

41

the free surface.

A drop can also spread as a thin film towards a SAW source as shown by Rezk *et al.*[178] (and recently explored by Morozov *et al.* [179]). This phenomena was observed (regardless of fluid type) when the contact angle was small enough (requiring surface treatment in some cases) to produce a region at the edge of the drop where Rayleigh streaming dominated over Eckart streaming. They derived a constant velocity film front by neglecting Eckart streaming and applying appropriate boundary conditions for the region near the contact line. Their derivation matched with experiment across various frequencies, viscosities, and substrate velocities without employing an empirical fitting parameter as shown in Fig. 1.19. The data is separated by streaming Reynolds number $\mathrm{Re}_s = \rho_f U \lambda_{\mathrm{SAW}}/4\pi\mu$, where ρ_f is the fluid density and U is the particle velocity of the surface. This thin film phenomena was utilized by Collins *et al.* for atomization, which will be covered in Section 1.4.5.

Additional functionality is required if planar SAW microfluidics are to live up to their promise as a lab-on-a-chip platform. The ability to stop, merge, and split drops as well as increased speed are valuable for future devices.

In 2012, Travagliati *et al.*[180] introduced a new tool to effectively detect when a drop has reached its desired location. They drove a drop via SAW towards a cavity with a certain resonance. When the drop entered the cavity, the resonance of the cavity shifted, causing the SAW to be reflected and thus halting the drop.

In the same year, Ai *et al.*[181] applied the concept of focused SAW to translation. They showed that a circular FIDT was able to translate a drop placed just outside its focal distance approximately 5 times faster than a straight IDT under the same power, frequency, and drop size. Though not in strict contradiction, this calls into question the maximum volume-dependent velocity of drops as amplitude is increased described by [151]. Within the focal distance the speed was still 3 times faster and all drops, regardless of location, moved toward the focal point. They suggested that this phenomena may be useful in merging drops.
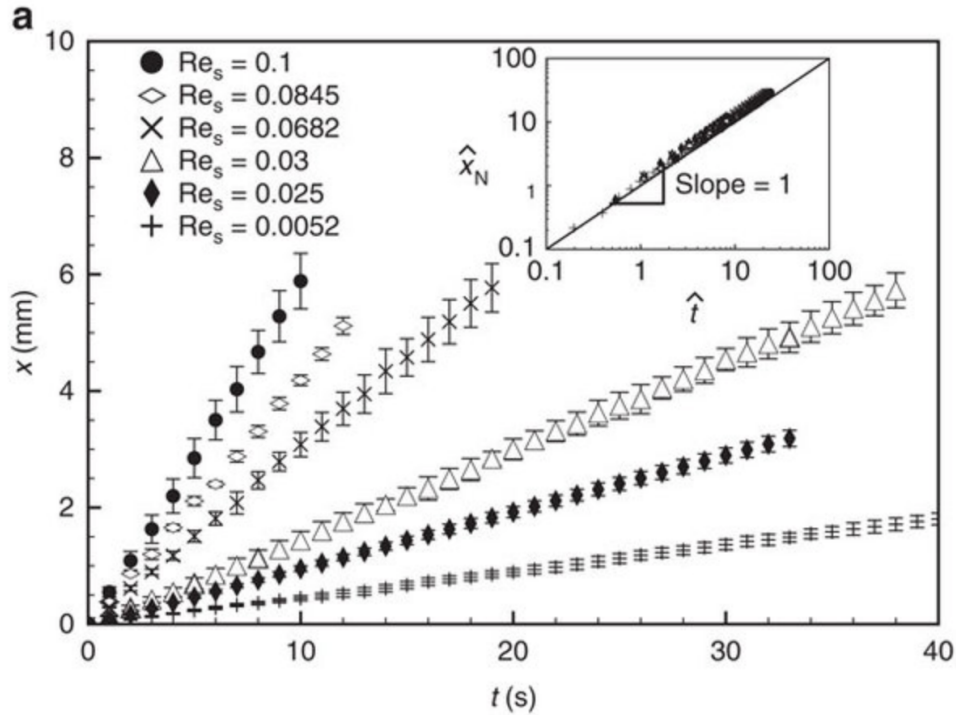
Figure 1.19: Experimental results of film front displacement, X, versus time, t, indicating constant velocity for various values of Re_s. The inset shows the same data with X and t normalized based on the derived film evolution equation showing agreement between theory and experiment. Adapted by permission from Macmillan Publishers, Ltd. [178], copyright 2012.

Indeed, Collignon *et al.*[182] achieved merging by this phenomena, but splitting required a more complex mechanism. A two-part signal (*see* Fig. 1.20(a)) was produced that first initiated internal rotation and then elongated the drop towards a necking event. Rotational flow due to the first part was critical to suppress jetting behavior allowing sufficient injection of momentum without ejecting the drop. From there a balance of capillary force and drainage due to necking causes the drop to split as seen in Fig. 1.20(c). Collignon *et al.* performed the task with a range of fluids and obtained a non-dimensional number to predict the capillary bridge effect that ultimately splits the drop; the Ohnesorge number, $Oh = \mu/\sqrt{\rho_f \gamma R_0}$ describes the balance of inertial and viscous stresses, where R_0 is the radius of curvature of the neck. In Fig. 1.20(b) we see that splitting occurs in a narrow band at a critical Oh value. We will return to this concept of capillary bridge hydrodynamics in the next section describing the application of jetting to extensional

rheometry.
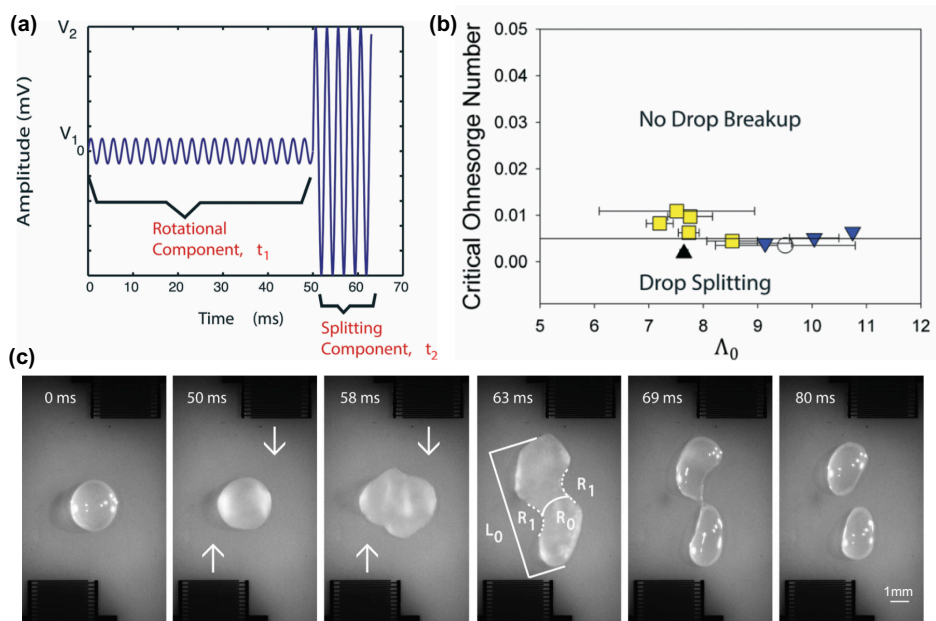
Figure 1.20: (a) The waveform of a single pulse used to split a sessile drop via counter-propagating offset SAW. The low-amplitude phase, applied over a period t_1, provides the initial energy for stretching the drop while avoiding jetting. The second, high-amplitude phase is applied over a much shorter duration t_2 comparable to the inertial time scale to rapidly elongate the drop. (b) The relationship between Oh and a dimensionless aspect ratio (Λ_0), showing the collapse of data points representing successful splitting events to a critical value of Oh. (c) A sequence of photographs depicting a successful splitting event with counter-propagating SAW indicated by arrows. Reproduced[182] with permission from The Royal Society of Chemistry.

Though many practical milestones have been reached with regards to sessile drop translation, much of the underlying physics has not been completely explained. Bussonniere *et al.* recently illuminated some of the physics by studying the oscillation, displacement, and contact line dynamics via a high speed camera [183]. They found that displacement of the rear and front contact lines alternately occur during each cycle as seen in Fig. 1.21. This revelation builds on the work of Brunet and fits intuitively within the context of regimes. The vertical oscillation could reasonably transition to jetting when inertia overcomes the capillary forces. They suggest an explanation for the maximum speed observed by Brunet (when varying amplitude). The speed is given by the product of the net drop displacement per oscillation cycle and the frequency of

these oscillations. And, while the displacement is linear with the amplitude of drop deformation, the frequency is nonlinear with the amplitude due to hydrodynamic effects. We will encounter a similar concept in the atomization section. It is currently unclear how this explanation could account for increased speed under focused SAW.
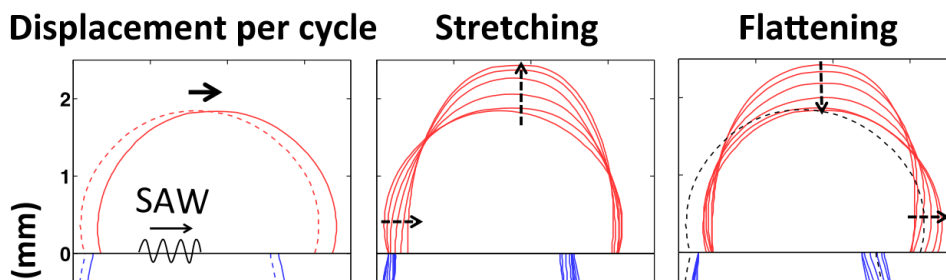
Figure 1.21: Oscillation of a sessile drop causing displacement of the rear contact line during stretching followed by displacement of the front contact line during flattening. The pair constitutes one cycle. Reprint permis. Bussonnière (2016) [183].

Droplet transportation using SAW helps to integrate different reaction processes on the same chip. For example, polymerase chain reaction (PCR), which is a DNA segment amplification process developed in the 1980s [184]. This method is critical for DNA sequencing (*see* Section 2 of Yeo and Friend's review for more on this topic[185]). Three main reactions happen at different temperatures in the PCR process: denaturation, annealing, and elongation. After the DNA is amplified, the solution must be hybridized to check the results. Guttenberg *et al.*[172] developed a microfluidic device to direct the reaction of DNA, a primer, and the necessary nucleotides within a sessile drop. Surface treatments define the paths of the drops and resistance heaters are integrated into the surface to promote reaction. They demonstrated successful PCR with only 200 nL drops. With the precise control of droplet translation, PCR and hybridization can be done with the same device.

SAW generated droplet translation also provides a promising, efficient way to seed cells in an external matrix with uniform distribution, an important step in tissue engineering. Cells seeded in bio-compatible, bio-degradable scaffolds have been used to recover defective tissue [186, 187]. [188] reported the use of SAW to seed cells into a scaffold made of polycaprolactone (PCL) in

2007. A droplet containing cells was placed between the scaffold and the SAW source so that the droplet was driven into the scaffold in 10 s. Later, [189]studied cells seeded in a scaffold using micro-computed tomography and found it possible to ensure a homogeneous distribution of infused cells. They also observed proliferation of the seeded cells during a fourteen-day continuous culturing study, confirming their viability after exposure to SAW radiation.

1.4.4 Jetting

In general, jetting occurs at a fluid-fluid interface when inertial pressure overcomes surface tension, which tends to maintain the interfacial shape. The well-known Weber number, We is a good metric for this balance; We $= \rho_f u^2 L_c / \gamma$, where L_c is the characteristic length, u is the fluid velocity, and γ is the surface tension. Viscosity, which intuitively should factor into this balance, is not present in We, but is indirectly expressed via the fluid velocity. More viscous fluids will derive less inertia from a given stimulus. Fluid velocities high enough to overcome surface tension, which increases for smaller fluid geometry, typically require a nozzle so that sufficient inertia can be generated. SAW is capable of producing very large surface accelerations, which translate into fluid velocity for a drop placed directly on the surface, thus eliminating the need for a nozzle.

The interaction between acoustic waves, elastic solids, and liquid drops to produce jets and satellite droplets is very complex [190]. Tan *et al.* attempted to elucidate the phenomenon by focusing SAW from two counter-propagating, FIDTs into various sized drops sitting upon Teflon coated LN [191]. This setup provided a stable drop location and high intensity, which promote jetting over other sessile drop phenomena such as internal flow and translation. Standing wave actuation produced an axisymmetric jet, which was assumed cylindrical. Vertical inertia generated by the focused SAW lead to elongation of the drop and eventually to a break-up event once a threshold input power was exceeded. Below this size dependent threshold, only vibration of the drop was observed (similar to that observed by Bussonniere *et al.*[183]) and above the

threshold a Rayleigh-Plateau instability resulted in multiple droplets per jet.

They showed that the various jetting regimes corresponded to a modified jetting We as seen in Fig. 1.22, where u was replaced by the jet velocity (U_j) and L_c was replaced by the jet radius. They were also able to predict experimental values of U_j for various fluids, graphed in Fig. 1.23, by modifying the momentum balance derived by Eggers *et al.* [190] for the case of acoustic streaming. It is critical to note that jetting only seems to occur during a pulse of SAW energy, either at the onset of the signal or during a pulsed signal. This was convincingly shown by Wang *et al.*[192] in a detailed, high speed video study of a sessile drop.
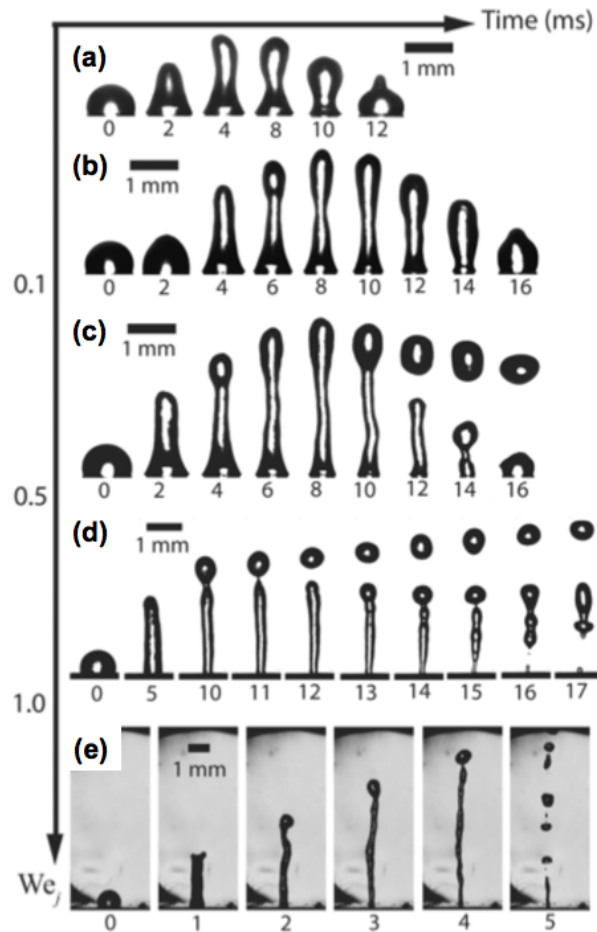
Figure 1.22: Jetting behavior according to We$_j$ (on the vertical axis) from an investigation by Tan in 2009. Regimes involving (a) & (b) drop elongation, (c) pinch-off of a single droplet, and (d) & (e) jet breakup to form multiple droplets are depicted. Reprinted figure with permission [191]. Copyright (2009) by the American Physical Society.
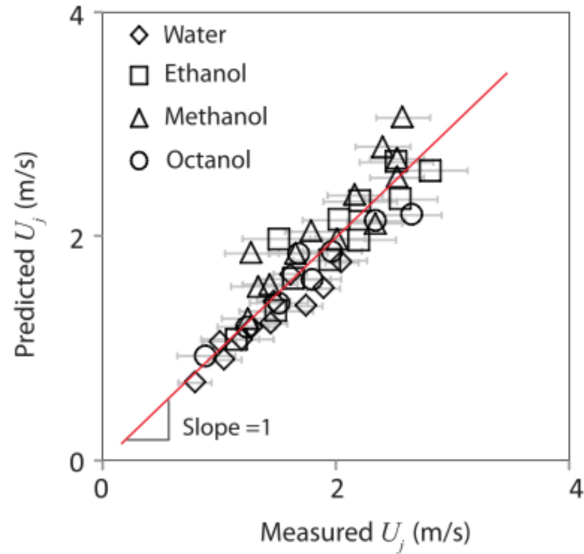
Figure 1.23: Comparison of the jet velocities, U_j, predicted by a momentum balance for acoustic streaming with measured values for various liquids. Proximity to the red line with unit slope indicates good agreement between measurement and prediction. Reprinted figure with permission [191]. Copyright (2009) by the American Physical Society.

Though largely unrecognized in the field, the jetting of fluids using SAW has been applied to extensional rheometry to great effect. Much of rheometry relies on the generation of shear flow in order to observe the diffusion of stress through layers of fluid as one or more fluid layers are caused to slide relative to each other. Another approach is to employ shear-free extensional flows in which normal stresses develop from contraction in two spatial dimensions and stretching in the third. Unlike shear flows, extensional flows are irrotational, implying that any fluid parcels of appreciable aspect ratio will be aligned but will not be caused to rotate, thus fluid parcel alignment will remain constant at steady state. Therefore, measurements in extensional flows qualitatively reveal information regarding fluid behavior down to the molecular-scale.

Creating valid and controlled extensional flow has always been a challenge for rheologists. Filament-stretching extensional rheometry[193] (FiSER) and capillary break-up extensional rheometry[194] (CaBER) are previously developed extensional rheometry techniques; both involve creating thin filaments from sample drops. In FiSER, a liquid sample is placed between two end-plates and the plates are then moved apart at a controlled rate. In CaBER, on the other

hand, the plates are rapidly separated to a fixed distance and then held stationary forming a liquid bridge that is allowed to neck and break-up under capillary forces. In either case, the tendency of the cylindrical column of liquid to neck due to capillary stresses is resisted by viscous, and in the case of viscoelastic fluids, elastic stresses. The evolution of the profile of the thinning filament with time is governed by these forces. The flow and the local strain rate at the middle of a thin filament in uniaxial extension can be related to the change in the filament's radius.

Both FiSER and CaBER have been successfully applied to Newtonian and non-Newtonian fluids alike, but it is difficult to test fluids with viscosities less than 100 mPa·s, thus notably excluding aqueous solutions [194]. CaBER requires the initial end-plate opening time to be as short as possible, but typical apparatus require more than 50 ms to open the gap and form the filament. The primary difficulty is that mechanical operation can induce perturbations that seed inertio-capillary instabilities and thus hasten break-up. As a result low viscosity fluids tend to break-up before the filament is formed. Furthermore, relatively large sample sizes are required for both techniques (D=6 mm). Large sample sizes increase the relative effects of gravity on the filament causing it to sag towards the bottom. This produces asymmetric fluid flow around the mid-filament region.

SAW burst extensional rheometry (SAWBER) addresses the above issues in order to make low viscosity fluids accessible to stress and strain measurement in extensional flow [195]. It combines the concept of CaBER with the novel idea of using a burst of SAW energy to create the liquid bridge. This improvement reduces the time required to create a liquid bridge by an order of magnitude (1.5 ms as opposed to 50 ms) and reduces the necessary sample sizes by a factor of two (diameter of 3 mm as opposed to 6 mm). These qualities allow reliable data collection from extensional flows of fluids at viscosities close to that of water. As an added benefit, the use of SAW eliminates the need for mechanical components, which require more maintenance and are less reliable.

The technique involves an arrangement similar to that used by [191] (as described above).

49

Energy from a pair of FIDTs generates momentum flux calibrated to elongate a drop of fluid that bridges a gap between the LN substrate and an opposing parallel surface. The SAW burst enables creation of stable liquid bridges which then thin under the action of capillary forces, generating extensional flow at the necking plane. Using high speed videography and image processing, the dynamics of the break-up can then be analyzed. The use of SAWBER was extended for two distinct studies, one involving suspensions of motile microbes[196] and the second for copper nanowire suspensions in aqueous polymer solutions [197]. In the later, viscosities between 3 mPa·s and 37.2 Pa·s were used thus demonstrating that the technique extends the viable range to much lower viscosities while maintaining the high range. In the former, McDonnell *et al.* was able to show that microbes that move by pulling tend to increase the effective viscosity of a fluid while microbes that push tend to decrease it. These studies form the tip of the iceberg in terms of complex low viscosity fluid behavior that could be illuminated using SAWBER.

1.4.5 Atomization

Atomization has received abundant attention in recent years due both to its interesting physics and many important applications. In SAW devices, it tends to occur at higher power inputs than do the phenomena discussed so far. Atomization produces a continuous flow of many small droplets in a tight size distribution and much of the research is undertaken to optimize and predict the relevant parameters. The underlying mechanism of SAW atomization is still not completely clear, but several studies on the effects of viscosity, input frequency, fluid geometry, and acoustic amplitude have been recently completed. There have also been advances made in the engineering of devices necessary to reliably produce SAW atomization at lower input powers.

It was posited early on that the mechanism of droplet production was somehow linked to capillary waves on the free surface of the fluid. In 1962, Lang used a piezoelectric transducer to induce acoustic waves in thin films and bulk, contained fluids [198]. He was able to show a link between capillary wavelength, λ_c and droplet size by varying the applied piezoelectric

excitation frequency, f. In Kelvin's equation $\lambda_c^3 = 2\pi\gamma/\rho_f f_c$, λ_c is dependent on the capillary wave frequency, f_c. Lang assumed that f_c was equal to $f/2$ based on work by Faraday and others [199, 200, 201] and found that the capillary waves followed this modified Kelvin's equation and that the median drop diameter was a constant factor, 0.34, of λ_c when f was between 10–800 kHz. It is important to note that these experiments were not done using SAW and sessile drops and that the capillary wave observation was done at a different acoustic amplitude than the droplet production and sizing.

Kurosawa *et al.* created the first SAW atomization devices much later[202, 203] but used the same modification of Kelvin's equation to predict the resulting droplet size—they used $f/2$ in place of f_c and allowed for an empirical fitting constant. However, the fitting constant they found was 3.8 rather than 0.34. They suggested that the difference was due to the large surface vibration amplitudes in their study compared to those in Lang *et al.* but another important consideration is that they used 10–40 MHz acoustic waves as opposed to 10–800 kHz. Many ideas later investigated more rigorously were mentioned by Kurosawa *et al.* They noticed that atomization occurred more readily from a thin film than from a drop, the atomization rate increased linearly with input power above an initial threshold and then reached a maximum, and the resulting droplet size distribution had multiple peaks.

More than 10 years later, Qi *et al.*[204] confirmed the involvement of capillary waves in mechanisms of atomization. Qi used LDV to determine the frequencies of both acoustic waves in the substrate and capillary waves in the free surface of the drop. The size of the resulting droplets was measured using an aerodynamic particle spectrometer. The authors showed that the correct frequency to use in Kelvin's equation for droplet size prediction is in fact f_c and they defined equations for this frequency dependent on the the mechanism at play. If internal viscous damping dominates then Eqn. 1.8 holds, but if inertial forcing dominates then Eqn. 1.9 holds.

$$f_c \sim \frac{\gamma}{\mu R} \tag{1.8}$$
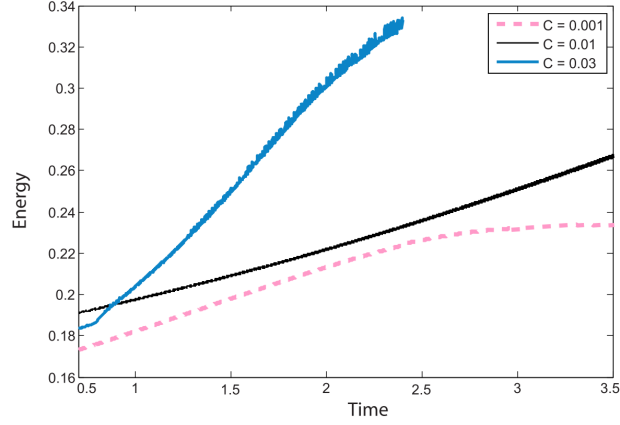
Figure 1.24: Interfacial energy vs time for 3 values of C_a (written as C in the figure) from a numerical study of atomization. There is an inflection near $C_a = 0.01$, which is close to the critical value predicted for the onset of atomization. Reprinted[204] with the permission of AIP Publishing.

$$f_c \sim \left(\frac{\gamma}{\rho_f R^3} \right)^{1/2} \tag{1.9}$$

They determined experimentally and numerically that Eqn. 1.8 applies in drops while Eqn. 1.9 applies in thin films near the viscous boundary layer thickness, $\delta = (\mu/\rho_f 2\pi f)^{1/2}$. They were able to predict the droplet size to reasonable accuracy in both glycerol and water in both the drop and thin film geometries. In drops, they observed at least two distinct mechanisms of droplet production corresponding to two distinct sizes. The drop deformed asymmetrically about the Rayleigh angle (as observed in translation studies by Brunet and others in the field) forming a wave crest that pinched off during a whipping motion producing a large droplet. Smaller droplets were produced from axi-symmetric, roughly cylindrical jets with diameter $\sim \lambda_c$.

In their numerical work they defined an acoustic capillary number,

$$C_a = \frac{\rho_f (2\pi f)^2 A^2 L \cos^2(\theta_R)}{\varepsilon \gamma}, \tag{1.10}$$

that describes the ratio of applied acoustic stress to capillary stress, where A is the SAW amplitude, and ε is the aspect ratio (height over length (H/L), which is assumed to be small for thin films).

They predicted a critical acoustic capillary number, through fluid dynamic numerical simulation, above which the surface will destabilize and produce atomized droplets. Their critical number was close to the value at which an inflection in the interfacial energy vs time graph occurs (*see* Fig. 1.24). It seems clear that the droplet size depends on the capillary wave frequency while the onset of atomization that produces said droplets may be predicted by the capillary number. Much more work is needed to test this and other methods of predicting the onset of atomization.

Qi *et al.* [204] observed a broadband low-frequency response in the free surface of the fluid, but did not investigate the effect of substrate displacement amplitude on this response. Tan *et al.* [205] explored this topic by performing similar experiments at multiple amplitudes and performing a more complex numerical simulation. They introduced an acoustic Reynolds number,

$$\text{Re}_a = \frac{\rho_f u_1 \lambda_f}{2\pi(\mu' + 4\mu/3)},\tag{1.11}$$

to distinguish between the fast streaming, high amplitude regime ($\text{Re}_a > 1$) and the slow streaming, low amplitude regime ($\text{Re}_a < 1$). In Eqn. 1.11, u_1 is the first order fluid velocity and λ_f is the wavelength of sound in the fluid. They used the successive approximation method, which limited their numerical results to the low amplitude regime where nonlinear effects are small. However, they were able to show that, in this regime, the capillary wave response has a fundamental resonance frequency equal to f plus additional superharmonics. The amplitude of the free surface vibrations also was comparable to that of SAW in the substrate. They were able to investigate the high amplitude regime with experiments and found that the f_c response was broadband and reached orders of magnitude lower frequencies than f. No hint of the $f/2$ subharmonic Faraday response was found. They also determined that in thin films irradiated by TSAW the capillary wavelength is related to λ_{SAW}, but in drops irradiated by SSAW it corresponds to λ_f.

Building on both the thin-film transport work described in Section 1.4.3 and the advances in droplet size prediction just described, a paper by Collins *et al.* [206] further strengthened
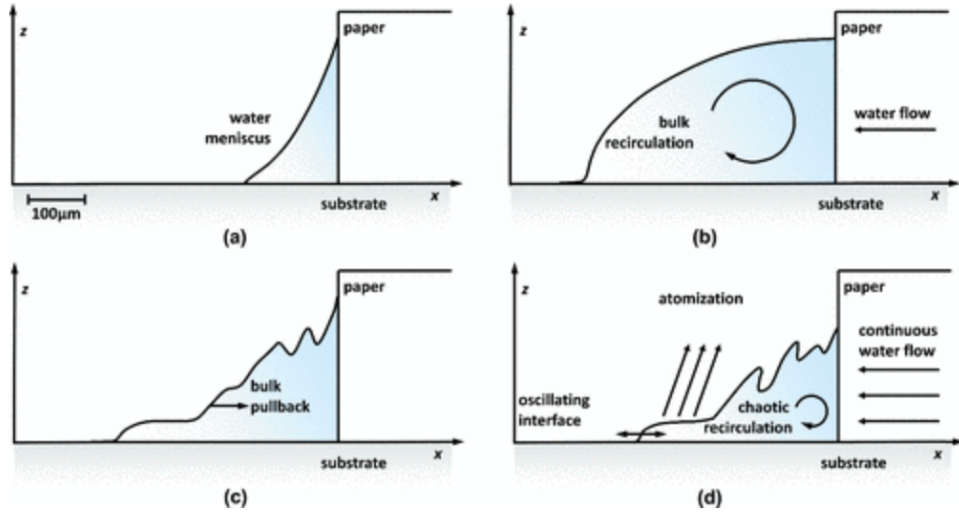
Figure 1.25: Dynamic behavior of fluid supplied via a paper wick to a TSAW source. (a) Before application of TSAW. (b)Bulk liquid is drawn out by initial surface vibrations. (c) After a transient, the bulk retreats back into the wick leaving a thin film of quasisteady geometry estimated by Collins. (d) Atomization occurs from the thin film, which competes with and is periodically obscured by the bulk. Reprinted figure with permission [206]. Copyright (2012) by the American Physical Society.

the case for atomization from thin films. They investigated the dynamics of thin-films of water drawn from a paper wick onto a LN substrate (their observations are illustrated in Fig. 1.25). They theorized that the height of the thin-film produced during TSAW actuation depends on acoustic resonance modes and can be estimated by a balance between acoustic radiation intensity and capillary stress. Local energy minima occur at $h = n\lambda_f \cos(\theta_R)/8$ ($n = 1,3,5...$) according to this theory and they found the experimental value in this case to be $h = 7\lambda_f \cos(\theta_R)/8$. They also produced numerical results predicting the length and height of the films based on including radiation pressure and streaming in the Navier-Stokes equations. These results showed a dependence of the film length on an acoustic Weber number $We_a = \rho A^2 \omega^2 L/\varepsilon\gamma$. This lead to an adjustment to the droplet size prediction based on the instability wavelength established by Qi *et al.* in 2008 [204] yielding,

$$D \sim \frac{\gamma H^2}{\mu L^2} \frac{We_a^{2/3}}{f},$$
(1.12)

54

where *L* is the lateral dimension of the fluid volume (parallel with the substrate) and *H* is the vertical dimension of the fluid volume. They confirmed the validity of Equ. 1.12 in experiments at a range of SAW power and frequency (*see* Fig. 1.26b) and obtained the well-known trimodal distribution as seen in Fig. 1.26a.
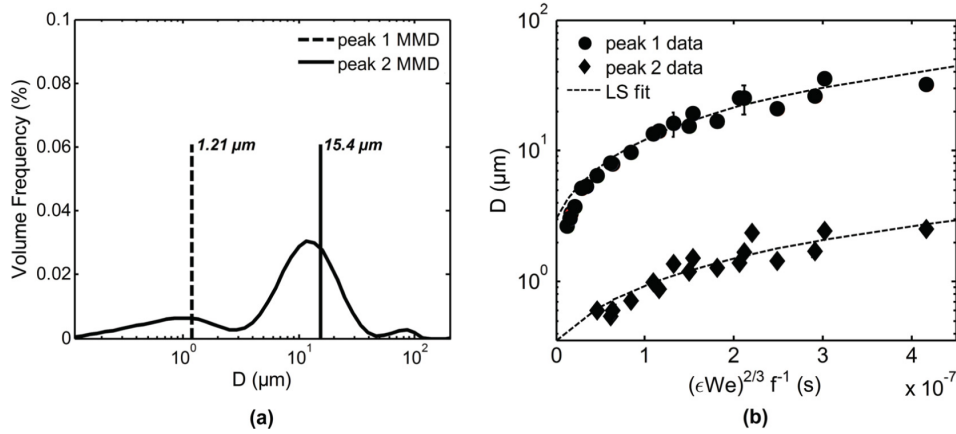
Figure 1.26: (a) Distribution of drop sizes during atomization from a thin film in an experiment using 22 MHz SAW at 5.2 W. The two highlighted peaks represent drops that were observed to originate from the thin film, while the third peak at the far right originated in the bulk fluid. Distributions at other frequencies and powers were qualitatively similar. (b) A graph of the drop diameter vs $(\varepsilon We_a^{1/3})^2 f^{-1}$ for the two thin film peaks highlighted in (a). Noting that the *y*-axis is a log scale, this agreement verifies the validity of eqn. (1.12). Reprinted figure with permission [206]. Copyright (2012) by the American Physical Society.

Recently, Wang *et al.* [192] confirmed that droplet size is more correctly predicted by the mechanism dependent capillary stress balance put forth by Qi *et al.* leading to eqn. (1.12), than by the modification of Kelvin's equation put forth by Lang. Similar to Tan *et al.* [205], they experimented with a single 20 MHz device while varying the applied power, which is proportional to the substrate displacement amplitude. At high power they observed the trimodal distribution, but in this study of sessile drops, the largest volume contribution was from the largest droplets (*see* Fig. 1.27) whereas the middle mode was largest in the above study of thin films.

The authors were able to record the atomization process over time with high speed video. This further revealed that the largest drops occur first followed by the medium drops and finally, after most of the original drop volume was removed, the smallest droplets. Qi *et al.*, they

emphasize that the fluid geometry and length scale largely determine the atomization mechanism. Their paper claims that each peak in the size distribution corresponds to a distinct mechanism, which in turn corresponds to a distinct geometry/scale. Large drops are produced from acoustic radiation pressure on the fluid interface leading to extension, whipping, and pinch off, medium drops from capillary waves due to Eckart streaming in the bulk, and small drops from capillary waves due to Schlichting streaming in the viscous boundary layer. However, no evidence is offered beyond video observation that these are the specific mechanisms at play. They conclude that drops cannot be atomized without jetting occurring first to decrease the height of the fluid geometry, but we have already seen that the distribution in droplet size can be shifted towards the smaller modes in thin films. Further control of fluid geometry may allow even better mode selection.
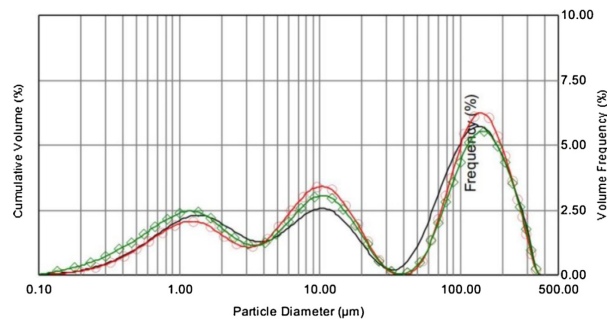
Figure 1.27: Trimodal distribution of droplet sizes during atomization from a sessile drop at 4.2 W and 20 MHz (each curve represents a separate trial). Notice which peak dominates in this distribution from Wang compared to the distribution from Collins in Fig. 1.26. Reprinted[192] with permission from Elsevier.

Relatively high power is required for atomization, but (as was common with translation) modulation of the input signal can reduce the power requirement. In a 2014 paper by Rajapaksa *et al.* [207], amplitude modulation, rather than pulse width modulation as used by Kurosawa [202], was demonstrated to reduce the input power while maintaining relatively high atomization rate, small droplets, and a narrow size distribution. This concept takes advantage of the difference in time scale between the hydrodynamic fluid response and the acoustic forcing. The modulation

frequency was chosen to avoid damage to biological particles, which they also demonstrated in the paper, so that it could be used in applications. Droplet size was seen to increase with input power as expected based on eqn. (1.12). However, size also changed based on the frequency of modulation with a peak at 1 kHz. More work is needed to clearly explain this dependence. At the power demonstrated, 1.5 W, devices could be powered by small batteries so that they can be miniaturized as has been desired for SAW microfluidics for some time.

Another path to more efficient atomization has been suggested in a recent paper by Rezk *et al.* [208]. Hybrid acoustic waves with bulk and surface components may prove to be synergistic in contrast to the current understanding of Lamb waves as spurious in SAW devices. However, this concept has not yet been convincingly demonstrated.

It is known that the excitation frequency of a SAW device, f_{SAW}, does not change the substrate particle velocity, but recently f_{SAW} has been shown to affect other aspects of sessile drop manipulation. In a paper by Dentry *et al.*, the authors modify Lighthill's turbulent jet model to allow its successful application to low excitation powers and explain the effects of frequency variation between 20–946 MHz on acoustic streaming velocity and distribution [6].

Their modification [122] included a finite source of acoustic energy and replaced turbulent dissipation with viscous dissipation. Experimentation with SAW devices fabricated with a range of resonant frequencies agreed well with this theoretical model. The maximum streaming velocity as well as the distance from the source at which this maximum occurred were recorded with the aid of fluorescent particles as the input power was varied. The maximum velocity increased with power, but the beam shape was independent of power. They emphasized the importance of the attenuation length of the acoustic beam in the fluid, β^{-1}, on streaming. They found that β^{-1} decreased with increasing frequency, thus increasing the power density within the beam. From this the authors deduced that the streaming velocity is proportional to frequency squared. They pointed out that when normalized for the frequency-dependent source area (dependent on attenuation of SAW in the substrate), there were two distinct regimes(*see* Fig. 1.28). At

low frequency, streaming velocity increases with the square of the frequency as they originally deduced, but at high frequency, it increases with the square root. The practical upshot of this finding is that, above 100 MHz, increased frequency gives diminishing returns in streaming velocity and thus must be balanced with the fabrication costs of such devices.
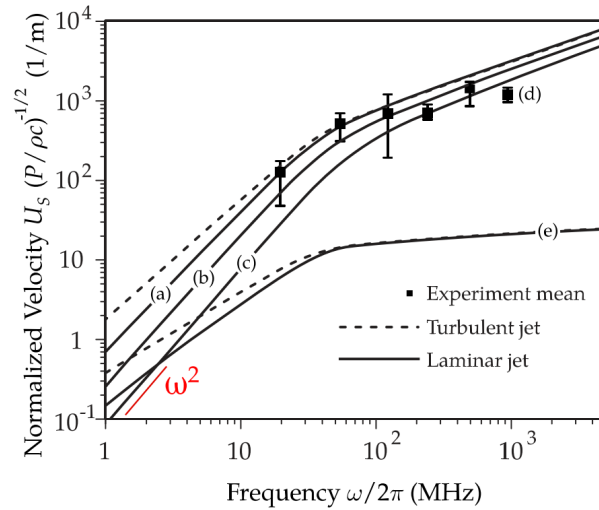
Figure 1.28: Streaming velocity versus applied frequency. In Dentry's laminar jet model (solid curve): at low frequency, streaming velocity increases with the square of the frequency, but at high frequency, it increases with the square root. As beam power is decreased at a fixed frequency((a) 10 mW, (b) 1 mW, (c) 0.1 mW) the streaming velocity is reduced. Experimental values (square dots) agreed fairly well with both models (Lighhill's turbulent jet model in dashed curve). (d) Indicates a lower than expected experimental data point at 936 MHz due to practical limitations (velocity could not be measured at its peak location). (e) Indicates an alternate normalization of the 10 mW data incorporating the frequency-dependent source area. Reprinted figure with permission [6]. Copyright (2014) by the American Physical Society.

The delivery of fluid to the substrate is vital to produce continuous atomization. Also, in light of the above work showing the dependence of droplet size, distribution, and the onset of atomization on the geometry of the sessile drop, fluid delivery becomes even more important. In a 2015 paper, Winkler *et al.* [209] suggested that the best way to produce reliable atomization devices at manufacturing scale was to supply the fluid to the SAW in the form of a thin film at the periphery of the acoustic beam. This strategy avoids the complexities of Eckart streaming in favor of Schlichting streaming within the boundary layer, which as described above produces

more reliable atomization. It also removes potentially damping structures from the acoustic beam path as the film is drawn into the path by the mechanism explained earlier by Rezk *et al.* [178] However, we note that the damping issue can be mitigated by using more rigid structures bonded with a UV-epoxy as demonstrated by Langelier *et al.* [121].

Winkler claims that this fluid supply approach avoids the jetting regime before the onset of atomization. It is accomplished by fabricating a microchannel from SU-8, a common photoresist used in microfabrication, adjacent to the beam. This avoids the uncertainty of a wick or capillary, which imposes non-thin-film fluid boundary conditions (as was observed by Collins and evident in Fig. 1.25). It is an improvement upon the idea of a capillary slit originally used by Kurosawa [202, 4].

In experiments with SSAW from 65 MHz IDTs, Winkler *et al.* showed that droplet size increased with fluid supply rate, since it is related to the height of the film, in agreement with eqn. (1.12). In these devices, as opposed to those used by Wang *et al.* [192], they found that large drops only weakly contributed to volume removal. This indicates that they successfully avoided jetting in favor of atomization. The middle peak of the three mode droplet size distribution dominated the volume removal and increasingly so at higher supply rates. This agrees with the claim that Eckart streaming produces the medium size droplets while Schlichting streaming produces the smallest droplets. Peak locations were at the same order of magnitude between distributions obtained by Collins [206], Winkler [209], and Wang [192]. This agreement suggests that there is some consistent set of mechanisms at play in SAW atomization.

Building on the 2015 paper describing an SU-8 microchannel fluid supply system, Winkler *et al.* [91] studied the effect of various placements of the channel outlet as well as the flow rate in SSAW devices. The best atomization behavior was observed when the fluid was supplied just outside the aperture of the SSAW region. Any closer and the effect of the microchannel's presence within the acoustic beam becomes large and farther away the fluid geometry is less controllable. They determined that the stability of continuous atomization is critically dependent on the ratio

of power to flow-rate (*see* Fig. 1.29). On the other hand, they showed that the resulting drop size could be tuned within a single device by choosing the power (this agrees with the work by Collins to incorporate We_a into the equation for drop size prediction). Importantly they were able to achieve atomization without initial oscillation and jetting due to the precise nature of the fluid supply system.
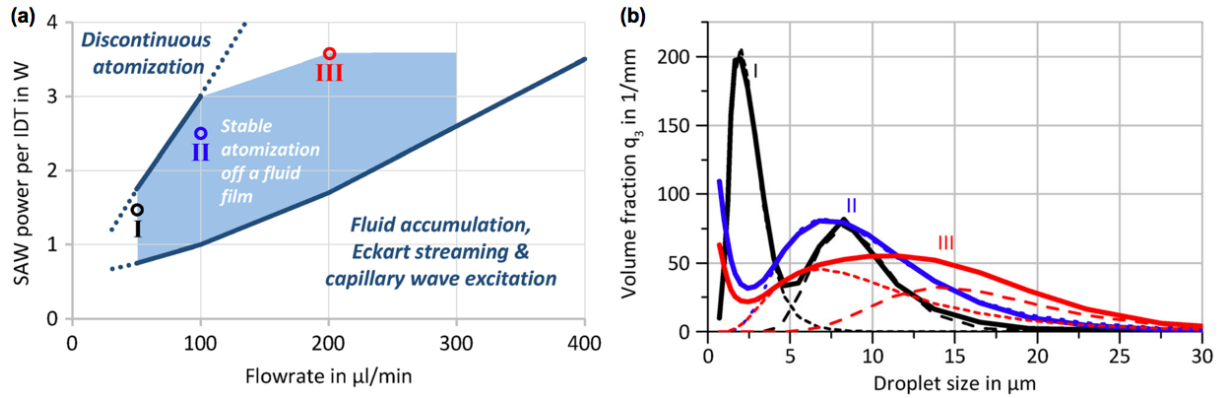
Figure 1.29: (a) An experimentally determined stability graph where a high power to flow-rate ratio leads to occasional dry-out and a low ratio leads to accumulation of fluid. (b) Droplet size distributions corresponding to points indicated on the stability graph show that droplet size can be tuned by changing the power and flow-rate while maintaining their ratio within the stable region. Reprinted from [91]

Viscosity is another important parameter that has recently been investigated in more detail. In a 2015 paper, Guo *et al.* [65] varied the glycerol content in droplets atomized from ZnO/Si SSAW devices designed for frequencies 12–65 MHz. Though ZnO requires higher powers, the effect of viscosity should be analogous in LN devices. They observed the same sequence of stages leading to atomization and the three mode droplet size distribution described in many of the above experiments. They also note that droplet size decreased with increasing excitation frequency, but at the cost of increased power required for onset of atomization. The highest frequency devices, requiring the highest power, also tended to produce more jetting before the onset of atomization. Unsurprisingly an increase in viscosity required a large increase in input power to achieve atomization at a given frequency. Additionally, at a certain viscosity, atomization could not be achieved even with increased power. As the frequency was increased the maximum

atomizable viscosity decreased.

The authors pointed to increased viscous damping of acoustic energy leading to reduced streaming velocity, but offered no detailed explanation of the observed behavior. Curiously, the authors retained a fudge factor and used the excitation frequency as opposed to f_c in calculating droplet size though they sited Qi *et al.* [204]. However, the measured values agreed reasonably well with calculated values leading to the conclusion that their fudge factor was appropriate for this frequency range.

A similar study was done by Winkler *et al.* more recently with LN SSAW devices in the 40–120 MHz range [210]. Fluid was supplied at the edge of the acoustic beam path of a SSAW by a capillary tube and syringe pump. They found the standard trimodal droplet size distribution at low viscosity, while as viscosity is increased the distribution accumulates to a single peak. They suggested that this effect was due to the limited ability for secondary and tertiary vibration modes to generate droplets at high fluid viscosity. They also observed that the dominant peak moved to smaller droplet sizes and itself became narrower (more monodisperse) as viscosity was increased. Additionally they found that increased viscosity reduced the range of frequencies at which the fluid could be atomized, as well as the atomization rate, and the height reached by the resulting mist. Again, no detailed mechanistic explanation was offered for the observed phenomena suggesting that more work is needed.

Some critical advances in applications have been enabled due to the above progress in acoustofluidic atomization.

Evaporation-induced self-assembly (EISA) is an important nanofabrication technique first introduced by Brinker *et al.* in 1999 [211]. Friend *et al.* demonstrated that SAW atomization could be used to produce nanoparticles (from a PCL acetone solution in this case) by EISA [212]. Particle aggregates of 150–200 nm were formed in each droplet atomized from the fluid/air interface and were collected in a container filled with surfactant solution. The size of particle aggregates was largely determined by the volume of PCL contained in each droplet.

Transmission electron microscopy (TEM) images revealed that each aggregate was composed of many 5–10 nm particles. Friend *et al.* suggested that these formed due to spatial non-uniformities at the evaporation surface leading to phase separation and nucleation (similar processes have been demonstrated[213, 214]). The particle size was correctly predicted via Gibbs free energy minimization thus validating this suggestion. The advantage of using SAW for this application is that the particle aggregate size can be tunned by the frequency of the device since frequency controls droplet size in SAW atomization. Additionally many other solvent-solute combinations can be used to create other kinds of nanoparticles. Large molecules or other compounds could also be encapsulated within the particles.

SAW in conjunction with electrostatic deposition has been developed to fabricate thin films and coatings, but this technology requires high frequency and power to atomize high density solutions or those with strong inter-particle bonding. A recent paper by Choi *et al.* integrated electrohydrodynamic atomization (EHDA) with SAW to accomplish atomization of these solutions at lower frequency and power [215]. The authors were able to produce sub-micron size droplets that were unprecedented with EDHA alone without exceeding the operating frequency that would be required for atomization of these fluids by SAW alone (20 MHz). The reduction in frequency of the SAW device was made possible because fluid was supplied to the SAW as small droplets (on the order of 1 μm) rather than as large 1 mm order drops. The authors confirmed the usefulness of the technique by depositing high quality ZnO and two conductive polymers as well as fabricating a high performance humidity sensor.

Solution deposition of lanthanum and zirconium on nickel tungsten substrates is a common method of producing superconducting thin films, but current mechanisms of spraying the solutions require mechanical parts and nozzles and lack a tight size distribution with small droplet sizes. A recent paper by Kirchner *et al.* proposed to replace these methods with SAW atomization [216]. One of two buffer solutions (either water or propionic acid based) was applied using SAW atomization followed by a typical heat treatment to produce the desired superconducting thin

film layer. The resulting films were highly crystalline, homogeneous, and dense, but suffered discontinuities due to poor surface wetting and/or uneven evaporation. This application is therefore promising but requires further work.

Vuong *et al.* presented a possible replacement technology for pipette tips [217]. Pipettes are often inaccurate due to the adhesive forces between the liquid and the tip, especially in the case of depositing liquid onto superhydrophobic surfaces. In this paper, the fluid was instead atomized into a container with a hydrophobic internal surface. The amount of dispensed fluid was precisely weighed before being perturbed in the container to form it into a single drop. The volume of the resulting drops was linear with the operation time of the atomization device.

SAW atomization can also be used to cool a surface by distributing sub-micron size droplets of an evaporative fluid as demonstrated by Ang *et al.* [218] SAW technology is well suited to compact electronic device cooling since it can be miniaturized and provides enhanced heat flux removal due to smaller droplets and thus quicker vaporization. This nozzleless technique also limits the chance of device failure due to clogging, which is common in various nozzle based atomizers. In this paper, cooling was also enhanced by an optimized concentration of copper oxide nanopowder, which lead to increased surface area once deposited on the surface to be cooled thereby allowing greater outward heat flux.

Nebulization provides a quick, non-invasive method for drug delivery with mild, limited side effects. Alvarez, Friend, and Yeo first described a method of generating monodisperse aerosols via SAW atomization for drug delivery [219]. They demonstrated insulin aerosols of 3 μm diameter, within the size range known to be optimal for absorption into the lungs. The technique was shown to be effective (80% delivery efficiency) in delivering a model asthma drug to a twin-stage impinger lung model [220]. SAW nebulization has also been shown to be compatible with an antibody treatment [221] and a plasmid DNA vaccine [222]. Paper represented a cheap and generic carrier for such bio-fluids and SAW atomization has been shown to work well with fluid laden paper samples [223].

The detection of bio-molecules can be enhanced by the integration of SAW nebulization. Heron *et al.* [224] used SAW to nebulize peptide solutions and demonstrated that mass spectroscopy (MS) performed on the resulting ions provided similar results to matrix assisted laser desorption ionization (MALDI) and electrospray ionization (ESI) depending on the mode of operation of the SAW device. Yet, this device still required a high voltage between the substrate and the MS inlet. Ho *et al.* [225] developed a device without this requirement by utilizing the surface electric field present on all SAW devices. Huang showed that SAW nebulization produces ions with lower internal energy (vital for MS) than does ESI [226] and later improved the performance (higher ion intensity) of a mass spectrometer by incorporating two SAW IDTs to produce smaller, more monodisperse droplets at a higher volumetric flow rate than their previous design [227]. The ion intensity produced by ESI is still typically higher than that produced by this double-IDT SAW device, but there are fewer limits on the samples and no high-voltage source as is required for electrospray.

1.5   Conclusions

Acoustic waves can be generated at the surface of a piezoelectric material by passing an electrical signal through electrodes deposited on the surface. The crystal structure, propagation direction, and wave mode are important considerations when choosing a substrate and electrode system for the fabrication of new acoustofluidic devices. The combination of interdigital transducers on lithium niobate has become most popular in the field due to relatively high coupling coefficients, transparency, biological and microfabrication compatibility, and the ability to produce efficient, predictable surface acoustic waves at high frequency. Acoustic energy couples into a fluid placed on the surface of such devices producing both acoustic streaming and an acoustic radiation force. The wave at the interface between fluid and substrate is attenuated over a characteristic length and the wave in the fluid attenuates over another distinct characteristic

length.

We discussed how these phenomena have been used to actuate sessile drops in four ways: mixing, translation, jetting, and atomization. Flow can be generated in the altitudinal or azimuthal plane and can be manipulated to achieve poloidal and other more complicated flows by the choice of fluid properties and the design of IDTs. These flows, in addition to acoustic radiation and other forces, can be used to manipulate particles in sessile drops in order to perform a wide range of processes necessary for lab-on-a-chip applications. Selective concentration, separation by size or density, and convective mixing can all be achieved rapidly on very similar if not identical platforms at low power and, furthermore, the drops can then be controllably translated, combined, and separated on the same surface. The combination of these capabilities makes SAW microfluidics very attractive for biological assays, and especially so since SAW has been proven harmless to many bio-particles and organisms in the necessary power and frequency ranges.

The mechanism of flow is acoustic streaming via viscous attenuation, but the mechanism of translation is very likely a combination of streaming and radiation pressure on the free-surface that deforms the drop so that it oscillates vertically and moves in an inchworm-like fashion. At increased power, these oscillations can be extended to form liquid jets with predictable break-up events. This phenomena has been successfully applied to extensional rheology, but there is a lack of other jetting applications in the literature though the potential exists (e.g. ink-jet printing). The mechanism underlying atomization is much less clear. The prediction of droplet size has improved, but not to the point of confirming the mechanism on which the theory is based. It is clear, however, that the mechanism and droplet size is critically dependent on the geometry of the fluid. Atomization has applications outside of biological assays like pulmonary drug delivery, materials fabrication, surface cooling, and others and this list will certainly grow in the future as control over atomized mists via acoustic actuation continues to improve. Both internal flow and translation of drops—as well as jetting and atomization—can be enhanced by the use of specialized IDT designs (e.g. FIDTs) and signal modulation. These two parameter spaces have

not been fully explored and future work in this vein could reveal new and improved microfluidic capabilities.

We also evaluated acoustofluidics in closed channels—the platform where most traditional microfluidics occurs. Mixing in traditional microfluidics is difficult due to low Reynolds numbers, but SAW and BAWs are used to easily mix fluids. Bubbles and sharp edges can be incorporated to enhance and expand this capability. Fluid pumping can be achieved via acoustic counterflow or via tightly confined acoustic streaming, and has been demonstrated in closed circuits in both glass and PDMS. Particles have been manipulated in many ways including: concentration, separation, focusing, sorting, and patterning. Techniques based on both standing and traveling SAW were presented and most techniques are easily tunable based on the frequency of the acoustic waves. In addition, drops of a second, immiscible fluid can be formed, split, and merged within channels. This type of lab-on-a-chip platform combines the small volumes and discrete nature of planar sessile drop microfluidics and the simple, evaporation-free operation of continuous channel microfluidics. Acoustofluidcs also offers particle motion control along the length of a channel and capture and release of particles from micro-wells. Clearly there is a large and expanding set of capabilities related to acoustic actuation in closed channels, which again makes SAW microfluidics attractive for biological assays.

Finally we presented the relatively less developed, but exciting field of acoustically actuated nanofluidics. Carbon nanotubes can be oriented with SAW and they have also been presented as an ideal platform for nanoscale fluid flow. Early work has shown that very fast pumping rates, mixing, femtoliter drop manipulation, and nanoparticle separation are possible. The underlying mechanisms and potential applications remain to be explored.

Micro-scale acoustofluidics retain all the features of traditional microfluidics with many added benefits. The resulting devices are inherently simple to operate since they rely on electrical signals. And they have low power requirements that allow the possibility of self-contained, hand-held devices. This field also offers novel functionality beyond mimicking existing lab scale

processes, which increases incentive for further development and eventual commercial adoption.

However, it is also important to recognize the limitations of this technology. There are a few examples of integrated systems that incorporate acoustofluidics in academia, and even fewer examples in industry despite the fundamental and proof of concept progress that we've outlined in this review. We believe this is due to a lack of interdisciplinary groups that contain both microfluidics experts and acoustics experts. Similarly, there have not been enough resources dedicated to developing the circuit design knowledge necessary to drive acoustofluidic devices, which have a unique set of circuit requirements. Devices typically operate between 50-3000 mW and 5-200 MHz and tunable frequency and power output is often desired. We expect these challenges to be overcome in the near future, but there a several inherent limitations of which the reader should be aware. In many of the applications given in this review, other technologies can produce superior performance in ideal situations. For example, electrospray produces smaller more monodisperse droplets than does acoustic atomization, which leads to higher performance in mass spectrometers, but the acoustofluidic devices would be cheaper and easier to use. Similarly optical tweezers can manipulate particles at a smaller length scale than acoustic tweezers, but require more expensive equipment and restrict the application space due to heating. Many acoustofluidic devices rely at least in part on streaming which only occurs when acoustic waves are attenuated. Thus acoustofluidic devices are inherently limited by attenuation. For this reason acoustofluidic technologies are not well suited for large volume applications. For example, though mixing in sessile drops has been shown to be effective, it would be ineffective to use acoustic waves to mix a liter of fluid.

We hope that the information assembled here inspires those outside the field to consider integrating acoustofluidics into their own research and helps experts and newcomers to the field to gain perspective on its development.

1.6 Index of symbols

α^{-1} length along the surface of the solid over which a Rayleigh wave decays by a factor of e due to the emission of leaky SAW into the fluid

β^{-1} distance that the longitudinal sound wave travels in the fluid before decaying by a factor of e

β_c compressibility of particles

β_w compressibility of fluid

δ viscous boundary layer thickness

Δ_f width of the resonant peak

ε aspect ration

ε_∞ capacitance per period of a unit-aperture, single electrode transducer

γ surface tension

λ_{SAW} wavelength of the SAW

λ_c capillary wavelength

λ_f wavelength of sound in the fluid

$\mathcal{R}$ recirculation length

μ shear viscosity of the fluid

μ' bulk viscosity of the fluid

ω angular frequency

ρ_0 density of the fluid

ρ_p particle density

ρ_s density of the solid

θ contact angle between a liquid and a solid

θ_R Rayleigh angle

$2\Delta v/v$ coupling coefficient of the substrate

a aperture width

A amplitude of SAW

b anisotropy of the substrate material

$B(\omega)$ susceptance

C_t capacitance

Ca capillary number

D instability wavelength

D_F distance from the IDT edge

d_s	effective focal spot size of an FIDT	f	applied piezoelectric excitation frequency
F_{rs}	SAW radiation force under a standing wave	F_{rt}	SAW radiation force under a traveling wave
f_{SAW}	frequency of the SAW	F_B	Bjerknes force
f_c	capillary wave frequency	F_D	Stokes drag force
f_r	resonance frequency	$G_a(\omega)$	conductance
H	vertical dimension (height)	$j(\omega)$	imaginary part of ω, angular frequency
k	wavenumber of SAW	k_0	propagating wave vector
L	lateral dimension (length)	L_c	characteristic length
N_p	number of finger pairs	Oh	Ohnesorge number
p_0	acoustic pressure	P_a	power that is absorbed
P_s	power that is produced	Q	quality factor
r	particle radius	R	drop radius
R_f	radius of the finger curvature	Re_a	acoustic Reynolds number
Re_s	streaming Reynolds number	t	time
U	amplitude of particle velocity	u	fluid velocity
u_1	first order fluid velocity	V	voltage
V_{pp}	peak-to-peak voltage	v_D	velocity difference between the surrounding fluid and the particle
v_l	speed of sound in the liquid	v_R	phase velocity for Rayleigh wave in solid
W	width of the channel	w	equivalent aperture of FIDT
W_b	-3 dB transverse bandwidth	We	Weber number
We_j	jet Weber number	x	position along the IDT fingers
X	film front displacement	y	position along the channel width

$Y_t(\omega)$ electrical admittance z effective focal length shifts

1.7 Acknowledgement

This chapter, in part, is a reprint of the materials as it appears in Lab on a Chip, 2018. William Connacher, Naiqing Zhang, An Huang, Jiyang Mei, Shuai Zhang, Tilvawala Gopesh, and James Friend. "Micro/Nano Acoustofluidics: Materials, Phenomena, Design, Devices, and Applications" Lab on a Chip 18.14 (2018): 1952-1996. The dissertation author was the primary investigator and author of this paper.

Chapter 2

Focused surface acoustic waves for fundamental physics and applications

2.1   Droplet ejection at controlled angles via acoustofluidic jetting

We study the nozzle-free ejection of liquid droplets at controlled angles from a sessile drop actuated from two, mutually opposed directions by focused surface acoustic waves with dissimilar parameters. Previous researchers assumed that jets formed in this way are limited by the Rayleigh angle. However, when we carefully account for surface tension in addition to the driving force, acoustic streaming, we find a quantitative model that reduces to the Rayleigh angle only when inertia is dominant, and suggests larger ejection angles are possible in many practical situations. We confirm this in demonstrating ejection at more than double the Rayleigh angle. Our model explains the effects of both fluid and input parameters on experiments with a range of liquids. We extract, from this model, a dimensionless number that serves as an analogue for the typical Weber number for predicting single droplet events.

2.1.1 Introduction

Acoustofluidic jetting, droplet ejection without an orifice from a sessile parent drop by surface acoustic wave (SAW) actuation [191], requires deeper physical understanding to gain quantitative control. There are exciting applications [228, 197, 229], including swifter printing by replacing nozzle translation with ejection angle control. Ejection angle control physics are unexplored, with only modest control previously achieved via variation of acoustic power from opposite sides of a sessile drop [230]. The driving force of the phenomenon, acoustic streaming, has been well studied [231]. Tan et al. studied vertical jetting using now typical devices [191] (Fig. 1(a)) producing two counter-propagating SAW. Interdigital transducers (IDTs) produce SAW that "leaks" energy into liquid as longitudinal sound waves. These propagate at the Rayleigh angle, θ_R measured from vertical (Fig. 1(b)), to produce momentum flux driven streaming from viscous attenuation [122]. The value of $\theta_R = \sin^{-1}(c_l/c_r)$ is determined by the mismatch in velocity between that of the surface acoustic wave, c_r, and that of the sound wave in the liquid, c_l.

The current assumption for ejection angle control is flawed because it fails to account for surface tension. Streaming forms a Gaussian jet at θ_R in a fluid half-space [6]. In sessile drops, however, interfacial forces must be considered. Castro et al. assumed that jetting from a single IDT SAW source occurs strictly at θ_R [230] as reported by Shiokawa et al. [232]. This limits the range of the ejection angle, defined by θ_e from the vertical, to between $-\theta_R$ and $+\theta_R$ from the vertical when using two parallel IDT SAW sources. For water and SAW on lithium niobate, $\theta_R = 22°$. With demonstrated control so far limited to $\theta_e = \pm15°$, this assumption seems reasonable, especially without quantitative modelling [230].

However, experimentation reveals that the ejection angle θ_e can be much *larger* than θ_R. Droplets eject from one SAW source at the "limiting angle" $\theta_e = \theta_R = 22°$ only when the vibration velocity is large. The ejection angle θ_e becomes larger than the Rayleigh angle θ_R (Fig. 2.2) when the vibration velocity is reduced. This contradicts the assumption that θ_R limits θ_e and demands a more complete description. Figure 2.2 demonstrates that a balance between
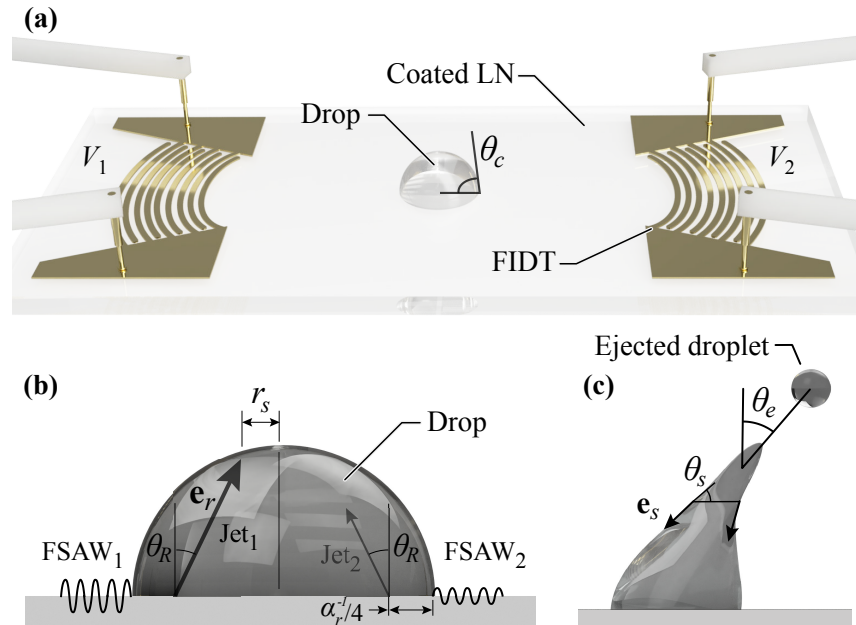
Figure 2.1: (a) Typical acoustofluidic jetting devices consist of two focused IDTs (FIDTs). A sessile drop with a given volume is confined to the SAW focal region by a hydrophobic coating that is applied everywhere except this region. The resulting contact angle, θ_c, depends on the size of the region. A voltage, V_i, signal with burst duration t is delivered to each FIDT. (b) A stationary sessile drop is deformed by acoustic streaming when SAW leaks in at the Rayleigh angle, θ_R, while (c) surface tension resists deformation according to eqn. (2.3) resulting in an ejected droplet at θ_e.

inertia and surface tension yields asymptotic dynamics: when inertia dominates, droplets eject near θ_R, but when surface tension dominates, droplets eject at significantly greater angles.

Why does surface tension change the ejection angle, θ_e, rather than directly oppose inertia? Recalling the classic text by de Gennes et al. (*see* Supplemental Material for a helpful analog) [233], surface tension produces a force per unit length tangent to the fluid interface and opposing surface area generation. In our system (Fig. 1(b)), generally the fluid interface does not align with inertia, thus surface tension modifies θ_e. This explains why Shiokawa et al. observed jetting at the Rayleigh angle: (i) the hydrophobic surface made it a special case where the fluid interface *was* nearly perpendicular to inertia and (ii) a large inertia was used, which dominated surface tension.

We are also interested in which parameters produce a single droplet rather than zero or
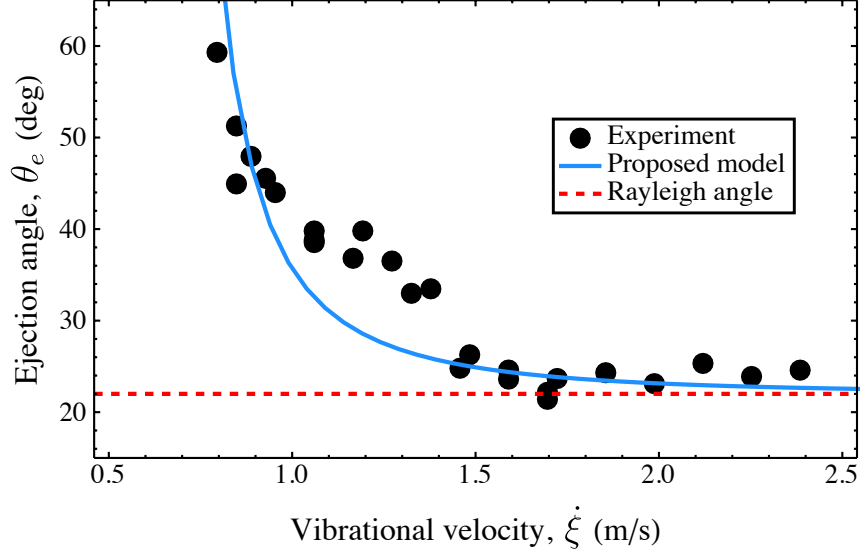
Figure 2.2: As vibrational velocity, $\dot{\xi}$, due to one FIDT is increased, θ_e approaches θ_R *from larger angles*. This result is at odds with the assumption in the literature that θ_R is the upper limit. Instead, it appears to be the *lower* limit in the case of a single IDT SAW source. Our proposed model (*see* text) provides a fuller understanding of these physical trends when two SAW sources are considered.

multiple. Tan et al. acknowledge surface tension's role in opposing inertia and define a Weber number, $\mathrm{We}_j \equiv \frac{\rho_l U_j^2 R_j}{\gamma}$, distinguishing zero, one, or multiple droplet jetting events. However, $\mathrm{We}_j = 1$ does not align with experimental single-droplet ejection conditions. The definition also requires advance knowledge of the jet velocity, U_j, and jet radius, R_j, precluding ejection *prediction*. Castro et al. defined [234] $\mathrm{We}' \equiv \frac{VI\Delta t}{\pi \gamma L^2}$, without explicit consideration of the acoustofluidic physics. Rayleigh, Plateau, and others have thoroughly studied droplet formation—Eggers provides two elucidating reviews [235, 236]—but the majority of this research involves an orifice or nozzle. It is therefore unsurprising that We_j relies on U_j and R_j; typical Weber numbers use orifice-dependent length scales and fluid velocities entering the nozzle, each typically defined by the researcher in droplet break-up studies. In our case, the corresponding choices are not obvious. A dimensionless number based on physics and dependent only on input parameters is still needed to make predictions.

We propose a quantitative model for ejection angle prediction from force vector sum-

mation: streaming, surface tension, and gravity. Furthermore, we control θ_e beyond $40°$ across fluid parameters, sessile geometries, and signal parameters [237]. We finally provide a properly balanced, predictive Weber-like dimensionless number.

2.1.2 Experiment

Typical jetting devices as in Fig. 2.1 are set up so that signal and sessile drop parameters are well controlled while θ_e is measured. Sessile drops are pipetted onto a hydrophilic region bound by a hydrophobic coating. The hydrophilic region radius, r, dictates the contact angle, θ_c measured from horizontal, for a given volume, V [238]. For the experiments in Fig. 2.2 a single voltage signal burst is applied to one FIDT at its resonance frequency, f. In the remainder of the experiments, a signal is simultaneously supplied to two opposing FIDTs, each with independently controlled peak-to-peak voltage, V_{pp}, and burst duration, t. We measured the focal spot vibrational velocity, $\dot{\xi}$, for each V_{pp} [239] using laser Doppler vibrometry (Polytec UHF-120). We define the use of two different voltage values in the two signals as the *vibrational velocity ratio method* (Fig. 2.3); the signals are otherwise identical. We define the use of two different burst durations in the two signals as the *duration ratio method* (Fig. 2.4); in this approach, the signals start simultaneously and are otherwise identical, only differing by the time at which they finish. We record each jetting event (Photron Fastcam Mini UX100) at 5000 fps and measure θ_e in post-processing (ImageJ and MATLAB) [240, 239]. Water and aqueous mixtures of glycerol and propylene glycol [239] provide varied viscosities, densities, and surface tensions (See Fig. 2.5).

Though we investigate their effects, our study is not focused on θ_c and f. Doubling f from 40 to 80 MHz produces negligible changes in θ_e [239]. However, varying θ_c from $60°$ to $100°$ strongly affects achievable θ_e ranges, with the largest θ_e range when $\theta_c = 75°$ [239]. We also note a strong effect on ejected droplet number from θ_c—more than from V [241]. Henceforth, we fix $\theta_c = 75°$ and $f = 40$ MHz to enable thorough investigation of other θ_e dependencies.

We investigate a four-dimensional parameter space (Fig. 2.6) to experimentally determine

the null, single, and multiple droplet ejection regimes. Vibrational velocity ratio and duration ratio are important since each controls θ_e. We also choose average vibrational velocity, $\bar{\dot{\xi}} = (\dot{\xi}_1 + \dot{\xi}_2)/2$, and average duration, $\bar{t} = (t_1 + t_2)/2$, since these control total energy input. In each subspace, two parameters were kept constant at values known by the experimenter to produce single droplets while the remaining parameters were varied.

2.1.3   Physical model

We estimate θ_e via force summation acting on the sessile drop: acoustic streaming, surface tension, and gravity. The acoustic streaming acceleration vector is given by

$$A_s = \frac{\pi v_a^3 f \beta}{2 c_l^2} \, e_r, \tag{2.1}$$

a modified version of the one presented by Tan et al. [191], where $v_a = \dot{\xi} e^{-\alpha_l y}$ is the particle velocity due to the passage of the acoustic wave and explicitly dependent upon the vibration velocity $\dot{\xi}$, e_r is a unit vector along the acoustic wave propagation direction in Fig. 2.2, and β is the nonlinearity coefficient [242]. Note y is measured along e_r. Acoustic wave absorption by the fluid is described by the length along the substrate over which the leaky Rayleigh wave amplitude attenuates by an exponential factor, $\alpha_r^{-1} = \frac{\rho_s c_r^2}{\rho_l c_{lf}}$ [119]. The longitudinal sound wave within the fluid has a distinct attenuation length, $\alpha_l^{-1} = \frac{\rho_l c_l^3}{4\pi^2 f^2(\frac{4}{3}\mu + \mu_b)}$ [122], where ρ_l and ρ_s are the density of the liquid and solid, respectively, f is the driving frequency, and μ and μ_b are the dynamic and bulk viscosity, respectively. Each FIDT produces a longitudinal acoustic wave propagating at θ_R from its side of the parent drop (Fig. 1(b)). Summing these two contributions predicts the angle of the combined acoustic streaming jet,

$$\hat{\theta}_e = \arctan\left[\frac{(t_1 A_{s1} - t_2 A_{s2})\tan\theta_R}{(t_1 A_{s1} + t_2 A_{s2})}\right], \tag{2.2}$$

representing the *conventional* model for the droplet ejection angle from past literature [230]. Note that eqns. (2.2) and (2.5) have been rewritten in terms of the vibrational velocity ratio, $\dot{\xi}_1/\dot{\xi}_2$, and the duration ratio, t_1/t_2, for use in Figs. 2.3, 2.4, 2.5, and 2.6. Without a fluid interface, eqn. (2.2) is valid, but for sessile drops, it poorly predicts experimental droplet ejection (Figs. 2.3 and 2.4).

We revise the model on the hypothesis that surface tension is responsible for the observed discrepancy. We derive the surface tension term by noting that it acts at the point where streaming jets intersect the drop interface (Fig. 1(b)). This defines a circle of radius r_s [243], whose circumference gives the force due to surface tension at this point, $\gamma 2\pi r_s$, applied at the local angle of the fluid interface, θ_s [244] measured from the horizontal (Fig. 1(d)). This force divided by the parent drop mass is the surface tension acceleration,

$$D_{st} = \frac{\gamma 2\pi r_s}{V\rho_l}e_s,\tag{2.3}$$

where e_s is a unit vector pointing along the fluid surface as shown in Fig. reffig:1fidt. The forces do not generally act over the same time period. Streaming acts over burst durations t_1 and t_2, but surface tension and gravity act from initial interface deformation to droplet pinch-off,

$$t_{df} = \frac{r - (\alpha_r^{-1}/4)}{\sin(\theta_R)v_a} + \sqrt{\frac{\rho_l r_s^3}{\gamma}}.\tag{2.4}$$

The second term in eqn. (2.4) is the characteristic timescale [236], which estimates the time for breakup to occur after column formation. The first term characterizes time taken for column formation, estimated as the distance from the streaming origin to the intersection with the opposite streaming vector divided by v_a. Notice that the jet originates a distance from the three-phase contact line (Fig. 1(b)) due to beam displacement, sometimes called the *Schoch length* and explained by Bertoni and Tamir [245]. We estimate this quantity based on high speed imaging as $\alpha_r^{-1}/4$. Equation (2.4) matches high speed observations to an accuracy equivalent to observation accuracy in a representative sample of experiments. And, finally, we note that gravity acts

vertically downward with the standard value.

The sum of acceleration vectors produces a prediction of the droplet ejection angle [246],

$$\theta_e = \arctan\left[\frac{(t_1 A_{s1} - t_2 A_{s2})\sin\theta_R}{(t_1 A_{s1} + t_2 A_{s2})\cos\theta_R - t_{df}(D_{st}\sin\theta_s/4 + g)}\right]. \tag{2.5}$$

Note that the horizontal contributions from surface tension cancel out, so that we are left with only the net vertical. The shape of the sessile drop changes over time, necessitating a time-averaged acceleration due to surface tension. The initial, maximum value, D_{st} (eqn. (2.3)), decays over time with decreasing radius, r_s. High-speed image sequences reveal that r_s decreases cubically, producing the time-averaged value $D_{st}/4$ [247, 239].

In addition to θ_e, these accelerations facilitate definition of a dimensionless number for predicting whether zero, one, or multiple droplets will eject. If the ratio [246],

$$\Upsilon = \left[\frac{(t_1 A_{s1} + t_2 A_{s2})\cos\theta_R}{t_{df}(D_{st}/4 + g)}\right] \tag{2.6}$$

is greater than one, a droplet is ejected. Once the balance has tipped towards inertia-dominated behavior, experimental data suggest a secondary threshold beyond which multiple droplets are ejected.

2.1.4   Discussion

Both methods of ejection angle control are effective and both are well described by our model, eqn. (2.5). Average vibrational velocity and average duration influence the number of droplets as expected (Fig. 2.6), but they also influence θ_e (Fig. 2.3). This is because, as in Fig. 2.2, the strength of streaming relative to surface tension affects θ_e, and streaming depends on both duration (t_i in eqn. (2.5)) and vibrational velocity ($\dot{\xi}$ in eqn. (2.1)). Our proposed model translates this qualitative observation into quantitative understanding.
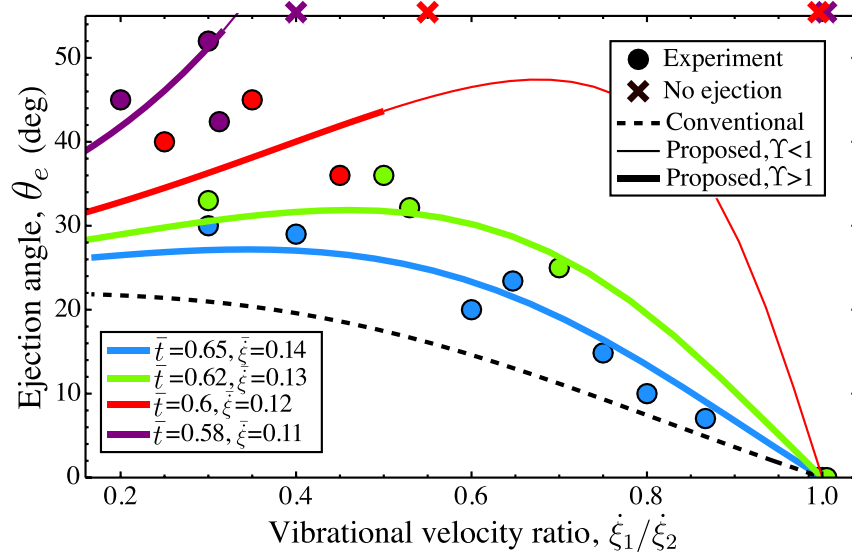
Figure 2.3: In order to control θ_e to $\approx 45°$ with the vibrational velocity ratio, the average vibrational velocity, $\bar{\bar{\xi}}$, and average duration, $\bar{t}$, must be adjusted. Our proposed model, eqn. (2.5), explains the experimental results with greater fidelity than the conventional model, eqn. (2.2), and also indicates which parameter values will produce the desired angles. Notice that greater inertia (increasing $\bar{t}$ or $\bar{\bar{\xi}}$) moves the proposed model closer to the conventional model, confirming as in Fig. 2.2 that inertia-dominated ejection is limited to θ_R, but θ_e can be much greater with substantial surface tension. Thick lines indicate droplet ejection is predicted via eqn. (2.6), while thin lines indicate no ejection is predicted.

Ejection angles up to $45°$ are demonstrated with both methods, but the control parameters must be adjusted in order to achieve this with the vibrational velocity ratio method. This is readily understood in light of our model, as no single curve in Fig. 2.3 contains the full range, $0 - 45°$. Consulting eqns. (2.5) and (2.1), this results directly from nonlinear dependence on v_a with corresponding nonlinear curves in Fig. 2.3, and linear dependence on t_i with a corresponding linear curve in Fig. 2.4. These dependencies also influence droplet formation regimes—Fig. 6(a,b) has vertical contours while Fig. 6(c,d) has nonlinear contours. The linear nature of the duration ratio method may provide better control in applied settings.

Figure 2.6 clearly indicates agreement between experiment and the single droplet regime at $\Upsilon = 1$, whereas other definitions require empirical threshold calibration [191]. Similarly, beyond $\Upsilon = 2$ ejection events reliably contain multiple droplets, a threshold which is not built
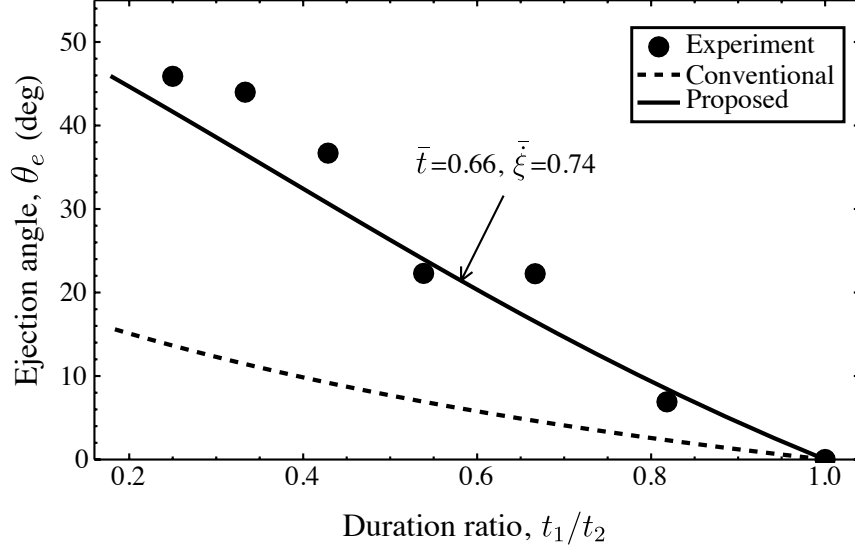
Figure 2.4: The duration ratio method achieves ejection control to $\approx 45°$ with a fixed parameter set. Our proposed model, eqn. (2.5), explains the experimental data better than the conventional model, eqn. (2.2), by accounting for surface tension and gravity. Notably, ejection angle is nearly a linear function of duration ratio, an attractive feature in the context of potential applications, and in distinct contrast to the highly nonlinear relationship present between vibration velocity ratio and ejection angle observed in Fig. 2.3.

into eqn. (2.6). Between single and multiple droplet regimes, a transition regime appears at $1.5 < \Upsilon < 2.0$.

Our proposed model accurately predicts θ_e for multiple fluids without relying on any *ad hoc* fitting parameters (Fig. 2.5) for a majority of the fluids and input signals chosen. There is an apparent offset between experiment and model in Fig. 5(a); there may be an experimental error here since the deviation is consistent in magnitude and direction but absent in most other cases. Jetting higher viscosity fluids requires higher energy input via larger vibrational velocities and/or burst durations. They are more difficult, in practice, to eject at large angles. These features are captured in our proposed model simply by accounting for inherent fluid parameters, leading to reliable mean estimates of observed phenomena. In polymer solutions for 3D printing applications there is an interesting topic for future research. The viscosity behavior of such non-Newtonian liquids could be determined using SAW-based rheometery[197] and applied to our model. After initial validation, our model could predict polymer droplet jetting angles given only fluid property
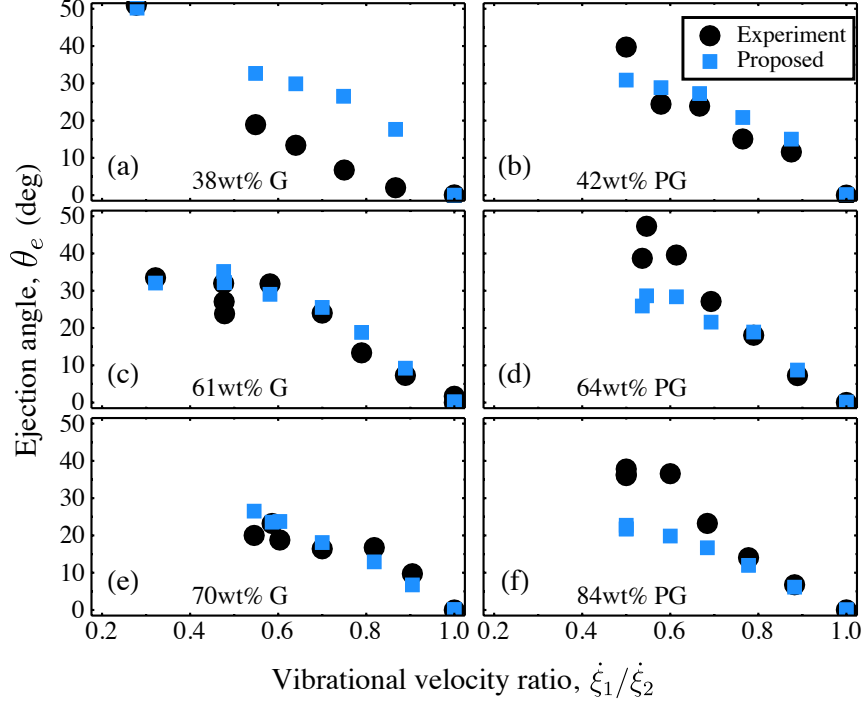
Figure 2.5: Aqueous mixtures of glycerol (G) and propylene glycol (PG) were jetted using the vibrational velocity ratio method. As in Fig. 2.3, $\bar{t}$ and $\bar{\bar{\xi}}$ were adjusted as needed to obtain desired angles. For clarity, we only plot model points necessary for comparison with experiments. Equation (2.5) takes fluid parameters into account, predicting ejection angle without need for *ad-hoc* empirical fitting parameters.

data on the polymer solutions.

The validity of eqn. (2.1) for streaming is corroborated by an alternative method starting with the streaming velocity calculated by a form of Lighthill's turbulent jet model modified by Dentry [6]. A simple Newtonian calculation determines the streaming acceleration where the acoustic beams meet, just above the original drop interface. This value, $\approx 60\,\mathrm{m/s^2}$, obtained by independent theoretical means, approximately agrees with the value, $\approx 40\,\mathrm{m/s^2}$, obtained from eqn. (2.1) with the same parameter set: $40\,\mathrm{MHz}$, $0.74\,\mathrm{m/s}$, $0.65\,\mathrm{ms}$, and water. This agreement is remarkable for such dissimilar approaches given the system's complexity.

The simplicity of our approach, considering its accuracy and the insight it provides into the phenomenon, is an advantage over resource-intensive alternatives. For example, one could consider streaming as a force vector field evolving in time and iterate its effect on interface
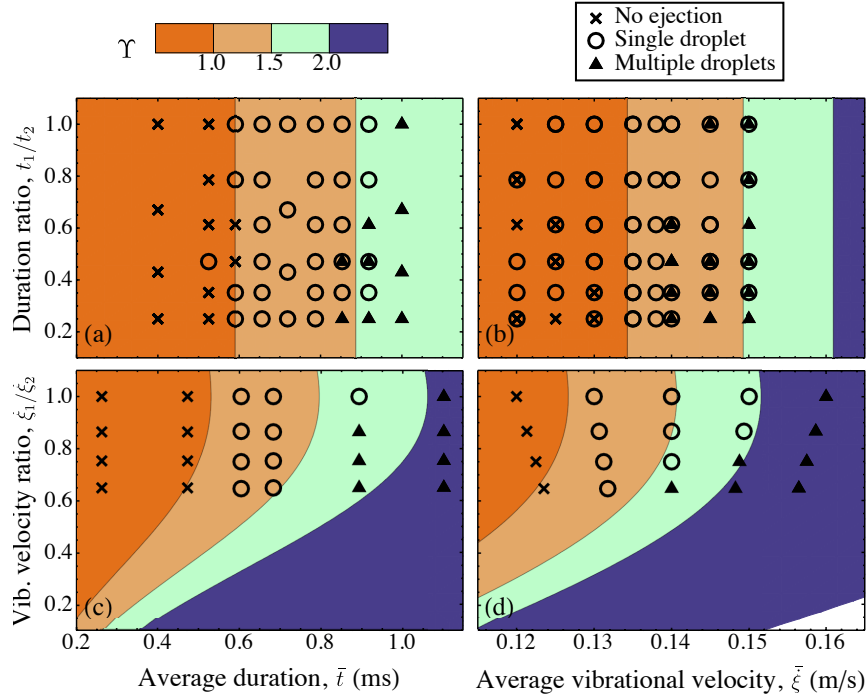
Figure 2.6: Adjusting both the vibrational velocity and the burst duration from each FIDT produces a four-dimensional space; (a), (b), (c), and (d) represent four different cross-sections of this parameter space. Experiments reveal the single droplet regime in these sectional plots as circles amid either zero or multiple droplet ejections. Equation (2.6) generates the contours in the background. In all four spaces, the emboldened line indicating $\Upsilon = 1$ coincides with the onset of single droplet events in the experiments.

shape taking into account surface tension at each point via curvature, a much more difficult and time-consuming problem. In other settings, one might also include acoustic radiation pressure, which deforms liquid interfaces [248]. However, the deformations are typically much smaller than those produced here, and moreover they occur as capillary waves, described by Brunet et al. as "trembling" [249], rather than large scale fluid motion. Simulations by Brunet et al. show that standing wave patterns have already formed by the time the fluid interface deforms. Such patterns cannot result in millimeter scale deformation at θ_R, which Brunet et al. submit is caused by directional, "coherent" acoustics. We argue that this is well described mathematically by acoustic streaming. Further, we point out that particle image velocimetry performed by Dentry et al. in the absence of an interface—in which case radiation pressure can have no effect—show that

flow velocities at $\sim 1\ m/s$ are generated using SAW streaming at the vibrational velocities used in our experiments[6]. Close agreement between our proposed model and experiment validates our omission of radiation pressure.

2.1.5 Acknowledgement

This section, in full, is a reprint of the materials as it appears in Physical Review Letters, 2020. William Connacher, Jeremy Orosco, and James Friend, "Droplet Ejection at Controlled Angles via Acoustofluidic Jetting", Physical Review Letters 125.18 (2020): 184504. The dissertation author was the primary investigator and author of this paper.

2.2 Acoustic heating and thrust production with fSAW

2.2.1 Introduction

As spacecraft and satellites grow in number and decrease in size, the need for reliable and lightweight means of attitude control likewise grow. With thousands of launches per year required for advanced telecommunications applications [250], alongside interplanetary missions for tiny "Cubesat" satellites [251], and tourism flights into low earth orbit [252], there has never been so many space-bound platforms in need of thrusters, particularly small thrusters [253]. These craft do not need large thrust, typically on the order of micro to milli Newtons, but thrust application must be tightly controlled to execute maneuvers, and the mass, volume, and power constraints are restrictive. Additionally, unless there is some way to refuel them, their active lifetime is dependent on the specific impulse. There are a large number of candidates being actively researched: chemical thrusters (e.g., butane) [254], cold gas thrusters [255], hall effect and ion thrusters [256], and electrospray thrusters [257] to name a few. A new technology, Film-evaporated MEMS Tunable Array (FEMTA), offers good thrust to power consumption ratios

and is extremely compact and light weight compared to the more mature options above, but at the cost of relatively low absolute thrust and specific impulse [258].

We propose a new approach using ultrasonic atomization that has advantages similar to those in FEMTA for small craft. High frequency surface acoustic wave (SAW) and thickness mode transducers produce droplets from a fluid in contact with the surface of the transducer. The droplets are ejected with a velocity of 1 m/s order and normal to the surface from a stationary bulk liquid [259]. This phenomenon, which is typically used in various other applications [231], can be used to generate thrust dependent on the flow rate and velocity of the sum of droplets. These piezoelectric transducers are low in mass and volume and miniaturized driving electronics have already been developed [260]. The concept is to feed liquid water to a nozzle—a small 100 μm hole in the substrate—and expose it to vacuum, where it will freeze and remain frozen until thrust is required. Ultrasound then melts the ice and atomizes the liquid water to produce thrust.

It is well known that small liquid volumes increase in temperature when they are exposed to SAW upon a substrate [261]. Several recent studies have investigated this phenomenon in more detail. Wang concluded that heat was generated in the liquid itself not at the interface [262]. Two investigations found that increases in the temperature were positively correlated to the viscosity of the liquid [263, 264], suggesting that viscous dissipation is responsible for the observed heating. Alternatively, Das et al. performed a numerical simulation and determined that pressure fluctuations due to SAW performed work on the liquid that dominated the contribution from viscosity [265]. They also pointed out that flow caused by SAW increases convection, thus speeding heat distribution, and that the temperature increases for a given volume as the frequency of the acoustic wave is increased. Regardless of the exact mechanism, SAW directly heats liquid.

SAW devices typically use lithium niobate (LN), a single crystal media that exhibits no hysteresis [266], notably different than the polycrystalline ceramic lead zirconate titanate (PZT), zinc oxide (ZnO), and lead-free alternatives to PZT, such as doped barium titanate media [267]. This reduces its energy loss compared to its hysteretic, polycrystalline alternatives [268] and

prevents heat generation during energy transformation. If a fluid is placed upon LN with SAW being leaked into it, the heat generation is solely within the fluid, and which has even been used for biological and chemical reactions [269, 92, 270].

Acoustofluidics is now a well-developed field with many successful applications [231], including the atomization of liquids to produce sprays traveling in excess of 1 m/s [261, 271, 220, 272]. There is a wealth of knowledge already to draw on while creating a new acoustofluidic micro-thruster technology. It is furthermore possible to continuously and linearly control the direction of droplets ejected from the source [273] to over 50 degrees off-axis, suggesting the potential of a steerable thruster with no moving parts. However, an aspect that has not been explored in detail is the possibility of using the same acoustic device to melt the ice, enabling the subsequent operation of the thruster. While sublimation of water ice in a vacuum is certainly an important matter, the vision here is the elimination of valves and other complexities by using a working fluid that can be allowed to freeze in the nozzle of an acoustofluidic thruster, thus rendering the thruster inert until needed, at which point the integrated heater melts the working fluid and also functions as the electrically-driven thruster element.

Here we specifically consider a focused 55.5 MHz SAW (fSAW) device capable of producing thrust via atomization of water and we show that this same device can rapidly melt frozen water under a range of conditions. Furthermore we propose a simple analytical model for the acoustothermal interaction and show that melting does not occur through resistive heating from the interdigital electrode present on the SAW device's substrate. Atomization and ejection to produce thrust, the next logical steps in such a thruster, have been studied in detail elsewhere [273, 274], but here we demonstrate a proof of concept device where water is continuously atomized through a nozzle in the substrate and calculate the resulting thrust. Through demonstration of these basic capabilities, we suggest that acoustic atomization is suitable for further study as a thrust mechanism for small spacecraft.
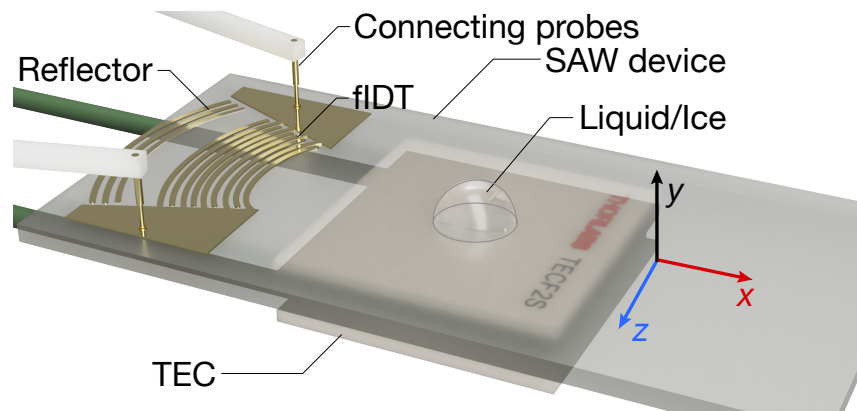
Figure 2.7: The thermodynamic experimental setup consists of a 55.5 MHz fSAW transducer, a Peltier cell (a thermoelectric cooler or TEC, 18 mm square for scale), and a sessile drop of deionized water placed at the focal spot of the fSAW. The bottom, hot side of the TEC is bonded to a heat sink (not shown), in turn immersed in a water ice bath to facilitate low temperatures on the fSAW surface. Ultrasound propagates along the surface of the substrate from the fIDT towards the drop when a signal is applied to the probes in contact with bus bars at either side of the fIDT. The fIDT and reflector pattern and the droplet are not to scale for clarity.
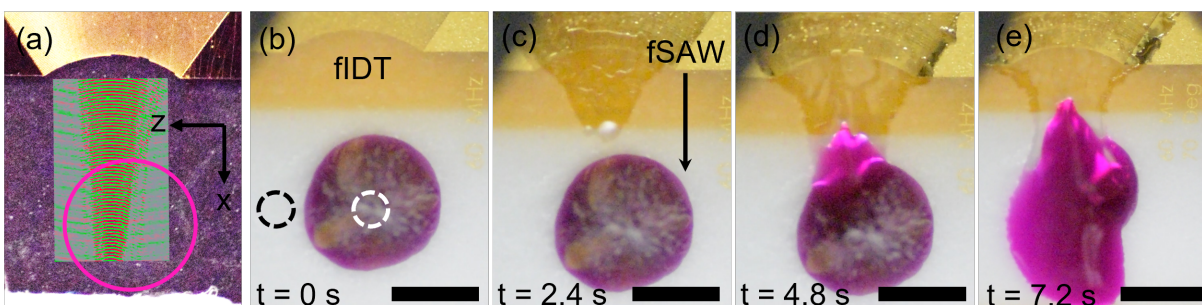
Figure 2.8: A 1 μL frozen DI water droplet is melted by internal acoustic losses. The fIDT can be seen at the top and the sessile drop at the center of each frame. (a) An LDV scan shows the relatively narrow region over which fSAW exists during activation, about one-third of the aperture width and progressively more narrow over the measured region. The sessile water droplet was placed at the pink circle marked in this image. (b) Initially, the droplet was frozen through the action of the TEC and maintained at -13.63$\pm$0.05 °C. The water was dyed with sulforhodamine B to ease visualization. Looking more closely, note the frost appearing across the surface of the device due to condensation. The temperatures were measured at the regions denoted with the dotted circles. (c) Applying 1.10$\pm$0.05 W to the fIDT starts melting the water after 2.4 s. Note that frost remains outside of the fIDT aperture but becomes liquid inside the aperture. (d) After 4.8 s, the frozen droplet is partially melted, principally in the viscous boundary layer in contact with the SAW substrate. (e) The fSAW completely melts the drop after ~7.2 seconds. Scale bar is 2 mm. Please see Supplementary Video 1.

2.2.2 Thermoacoustics

Frozen droplet phase change experiments

We investigated the thermodynamics of our proposed thruster with the system illustrated in Fig. 2.7. We placed a sessile 1.00 ± 0.01 μL drop of deionized (DI) water at the focal spot of a 55.5 MHz fSAW device constructed on 127.68° Y-rotated LN substrate in direct physical contact with a Peltier thermoelectric control module, TEC, (TECF2S, Thorlabs, $\Delta T_{max} = 66.4$ °C, I_{max}=1.9 A) as shown in Fig. 2.7. Details of typicala SAW device fabrication can be found in the literature [275]. Driven with a power supply (DC Power Supply, YH-305D, YiHUA), the TEC was mounted upon a heat sink (ATS-54425D-C1-R0, Advanced Thermal Solutions) that was in turn placed in a water bath. The bottom of the TEC—the "hot" side—was maintained at near freezing, -0.8$\pm$1.3°C, throughout the experiments.

The temperature on the fSAW device surface was measured with a thermocouple probe (TJ1-CAIN-IM15G-600, Omega Engineering Inc, Norwalk, CT, USA) and meter (HH911T, Omega) while the temperature of the sessile drop was measured using an infrared (IR) camera, (FLIR A35 FOV 13, Teledyne FLIR LLC, Wilsonville, OR, USA), calibrated with the thermocouple. The fSAW device was driven with a signal generator (WF1967 multifunction generator, NF Corporation, Yokohama, Japan) and amplifier (5U1000, Amplifier Research Corp., Souderton, Pennsylvania, USA) and the electrical signal was measured using an oscilloscope (InfiniiVision 2000 X-Series, Keysight Technologies, Santa Rosa, CA, USA). The vibrational displacement and velocity of the surface of the fSAW device were measured by laser Doppler vibrometer (LDV, UHF–120, Polytec, Waldbronn, Germany). For visualization, the 1 μL droplet was dyed with 0.005 $\pm10^{-4}$ g of sulforhodamine B (MilliporeSigma, St, Louis, MO, USA).

In order to simulate a reduced temperature environment, we placed the cold face of a thermoelectric cooler (TEC) module in contact with the underside of our fSAW transducer and coupled the hot face to a heat sink in an ice bath. The temperature of the fSAW surface depends

on the current run through the TEC. We pipetted a sessile drop of 1 ± 0.1 μL DI water at the fSAW

focal spot and froze it at several different temperatures below 0°C. After establishing these initial

states, we applied a voltage signal to the fIDT at a range of input powers for each state in order

to determine how easily the droplet could be melted. The purpose was to assess how easily the

approach could be used to melt the thruster's working fluid without requiring other components.

During these experiments we collected video of the system.

Simple model of acoustically-driven melting

Consider the frozen sessile drop as a thermodynamic system in equilibrium at a temper-

ature below freezing, 0°C, as set by the operation of the TEC. Heat influx from the laboratory

environment is balanced with heat flux removed by the TEC. Now consider a new source of

heat is turned on at time $t = 0$—in this case a voltage signal is applied to the fIDT. We assume

some fraction of the input power to the fIDT generates heat in the frozen sessile drop via some

combination of the mechanisms discussed in the introduction. Water ice is known to have an

acoustic loss mechanism that generates heat, but this mechanism is usually considered in the

context of acoustic wave propagation in ice floes [276, 277] and aircraft icing [278]. The frozen

sessile drop will also radiate heat to the laboratory environment and conduct heat to the substrate.

Therefore the energy balance is governed from the first law of thermodynamics as follows:

$$\frac{dE}{dt} = -\dot{Q}_{\text{rad}} - \dot{Q}_{\text{cond}} + P_{\text{IDT}}/N \tag{2.7}$$

where $\frac{dE}{dt}$ is the heat transfer into the system, $\dot{Q}_{\text{rad}}$ is heat flux due to radiation, $\dot{Q}_{\text{cond}}$ is heat flux

due to conduction, P_{IDT} is the input power to the fIDT, and N accounts for any inefficiencies by

which power to the fIDT does not generate heat in the system, e.g., kinetic energy, heat outside

the system, and so on. Integrating Eq. 2.7 from $t = 0$ to the time when the drop has fully melted

yields, on the left hand side, the total energy change required to melt the sessile drop, which

consists of the heat capacity of ice and the latent heat of phase transformation. On the right hand side, we obtain the energy contributions from conduction, radiation, and fIDT input. Dividing the power terms from the time interval yields the following expression for the time required to melt the drop:

$$\Delta t = \frac{cm\Delta T + m\Delta H_{\mathrm{L}}}{-\varepsilon\sigma A_{\mathrm{D/A}}(1/5)\Delta T^4 - kA_{\mathrm{D/S}}(1/2)\Delta T + P_{\mathrm{IDT}}/N}, \tag{2.8}$$

where c is the heat capacity of ice, m is the mass of the drop, ΔT is the difference between $0°\mathrm{C}$ and the initial temperature set by the TEC, ΔH_{L} is the latent heat of transformation from ice to liquid water, Δt is the change in time, ε is the emissivity of ice, σ is the Stefan-Boltzmann constant, $A_{\mathrm{D/E}}$ is the surface area between the drop and the environment, and $A_{\mathrm{D/S}}$ is the surface area between the drop on the substrate. The full derivation of Eq. 2.8 can be found in the Supplementary Information.
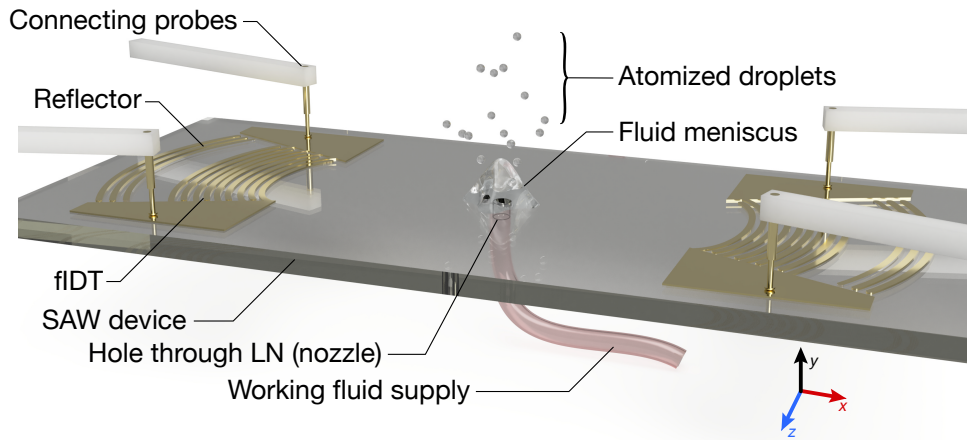
Figure 2.9: The same fSAW device design used for the thermoacoustics experiments, but with a small, 100 μm, through-hole laser cut in the substrate and flexible tubing coupled to the underside to transport water to the nozzle. Water is supplied via a syringe pump at a given mass flow rate and the FSAW power is set such that the atomization rate matches the flow rate. The fIDT and reflector pattern, the fluid meniscus, and the atomized droplets are not to scale for clarity.

Acoustically-driven thrust

An fSAW device nearly identical to the one used for melting frozen water samples in the previous experiment was used to create a prototype thruster, as illustrated in Fig. 2.9. There were two key differences: a pair of fSAW IDTs were used instead of just one, both focused at a central point, and a rudimentary nozzle was cut into the substrate at this location. A small, 100 μm, capillary through-hole was cut using a 1030-nm femtosecond pulsed laser at 9 mJ-cm^{-2} and 60 kHz pulse rate (LightShot, Optec Laser, Frameries, Belgium) into the fSAW substrate. A small silicone tube was attached to the underside of the substrate via a barb nipple glued to the substrate using ultraviolet-cured epoxy (NOA61, Norland Products, Jamesburg, NJ USA). The other end of the tube was connected to a DI water-filled 50 mL syringe that acted as a reservoir.

2.2.3   Results and Discussion

Acoustically-driven melting of water ice

Condensation from the laboratory environment occurs across the fSAW device substrate when the surface temperature is reduced below 0°C via the TEC. The condensed water then freezes, forming a thin layer of ice across the substrate in addition to the frozen sessile drop. If the fIDT were producing significant heat via resistive heating, then we would expect isotropic melting outward from the fIDT and we would expect the bus bars to also heat. A time sequence of images during a melting experiment, Fig.2.8, shows that the thin ice layer melts specifically where SAW is propagating, not in the surrounding regions of the substrate where heat would be easily transmitted. Resistive heating in the fIDT appears to be negligible in comparison to the effect of the SAW.

Once the melting interface propagates to the sessile drop it fully melts the drop in a few seconds, depending on both the initial temperature and the fSAW input power. The time to melt a drop was extracted from the videos of the experiments and is plotted in Fig. 2.10 along with the
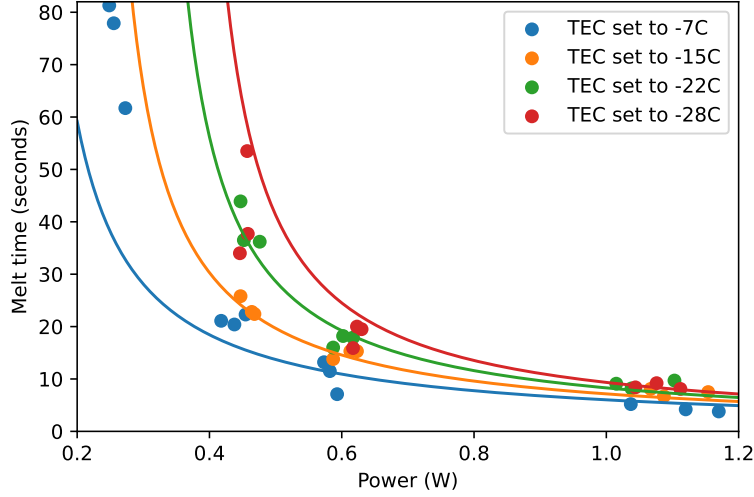
Figure 2.10: The time required to melt a 1 μL frozen droplet of water, starting from the indicated equilibrium temperatures. Experimental data is provided as discrete points; our model is plotted as continuous lines in the corresponding color. Notice that no experimental dots appear in yellow, green, or red below the power at which the corresponding model line becomes asymptotic. Drops actuated at these low powers did not melt when the TEC was set below $-10°$C. The time to melt was consistently 10 s or less regardless of the initial temperature when using 1 W or more for the fSAW.

melting time obtained from Eq. 2.8. We found that if we assume 7% (i.e. $N = 14$) of the fIDT input power produced heat in the drop, then our model roughly matched the data. We also found that an additional term proportional to the TEC current was necessary to properly account for the different equilibrium temperatures. Our modified model, given as follows,

$$\Delta t = \frac{cm\Delta T + m\Delta H_{\mathrm{L}}}{-\varepsilon\sigma A_{\mathrm{D/A}}(1/5)\Delta T^4 - kA_{\mathrm{D/S}}(1/2)\Delta T + P_{\mathrm{IDT}}/14 + I*0.02}, \qquad (2.9)$$

and where I is the current in the TEC, agrees quite well with the data with these two mechanism-based fitting parameters. We may conclude that our model represents the major thermal mechanisms at play in our experiments.

At the lowest input power, the energy barrier in order to melt the drop could not be overcome except in the highest initial temperature set by the TEC. This agrees with our model

since the melt time trends to infinity as the fSAW input power is reduced below about 0.5 W in our system (see Fig.2.10). In cases where the drop did eventually melt, the melting time was greater for lower initial temperatures and lower fSAW input power. However, at high fSAW powers beyond about 1 W, there was little difference between the melt time for any of the four starting temperatures. This likely indicates that conduction and radiation, which depend on the temperature difference between the droplet and its surroundings, play a larger role when the fSAW power is lower. At high fSAW power, there is less time for this temperature difference to have an effect through conduction and radiation. Instead, the energy introduced by the fSAW device is overwhelming.

The temperature on the substrate near the drop, but outside the fSAW path, was recorded via thermocouple at the end of each experiment along with the temperature on the drop via IR camera. These data are plotted in Fig.2.11. Note that the substrate temperature outside the fSAW path remains below freezing except in the case of the lowest TEC current (associated with the highest substraate temperature), while the drop is melted in every case.

Acoustically-driven thruster

In the fSAW device designed to produce thrust from atomization of the working fluid, with two fIDTs and a through hole representing a nozzle, a potential problem is the effects of allowing water to freeze in the machined hole of the fSAW device. The water's expansion could cause failure of the material. We froze two different devices laden with water over ten times and found no failure, cracks, nor other flaws during subsequent operation. During use, the nozzle hole in the LN substrate is subjected to substantial tensile and compressive stresses at 55.5 MHz, or, in other words, over 55 million cycles per second. Consequently, if there were cracks or flaws introduced into the nozzle from the freezing, these would likely lead to failure of the device in a few minutes.

While the system is self-pumping, with capillary pressure at the hole upon the surface
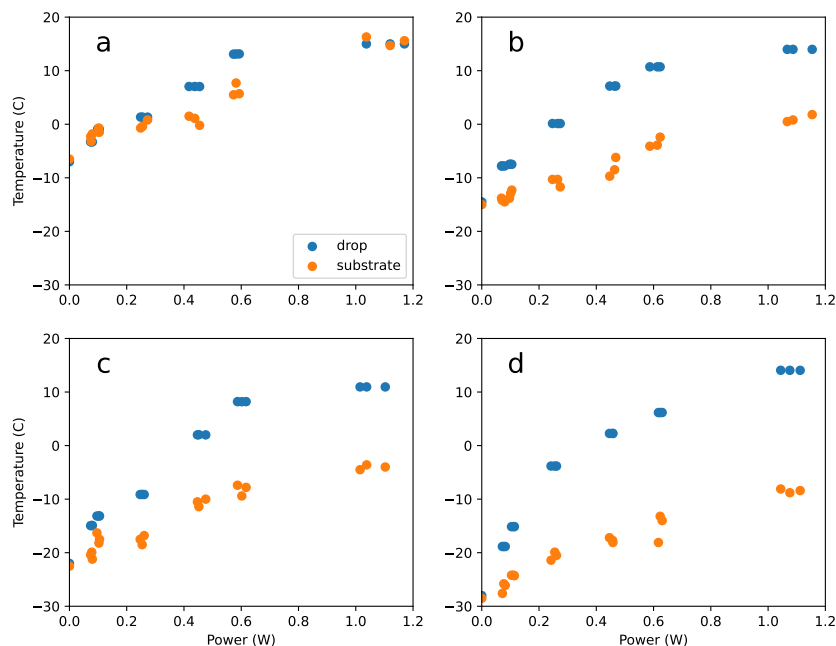
Figure 2.11: The measured temperatures of a spot on the substrate (in orange) and of the drop (in blue), where each location is indicated in Fig.2.8. Each plot represents data taken at a single TEC setting: (a) TEC set to $-7°$ (b) TEC set to $-15°$ (c) TEC set to $-22°$ (d) TEC set to $-28°$. As the power into the fSAW is increased, the droplet's temperature increases well beyond the substrate's temperature, and above freezing for most combinations of fSAW input power and starting equilibrium temperature. Universally, the droplet's temperature during the application of fSAW is greater than the adjacent substrate, indicating that the droplet is the source of heating when exposed to acoustic energy.

of the fSAW device entirely sufficient to replace atomized fluid [273], introducing a pump substantially increases the atomization rate. For this reason, we employed a syringe pump with the syringe. Drive signals were then supplied to both fIDTs on the device. When the fSAW power from each side is equal, water is atomized directly upward at a velocity dependent on the total power [see Supplementary Video 2]. When fSAW power from one side is greater than the other, the direction of atomization changes [see Supplementary Video 3].

Video was taken at 6400 fps, viewing the atomization from the side as it occurred vertically against gravity. At these scales and near the meniscus, gravity has no effect on the droplet ejection.

This information was used to calculate the exit velocity of the atomized droplets for different fSAW power inputs as provided in Table 2.1. The flow rate, defined by the syringe pump, was used with the droplet ejection velocity to calculate the equivalent thrust, $T = v_e \times Q_f$. Here, v_e is the exit velocity of the working fluid and Q_f is the mass flow rate. The flow rate was chosen to match the maximum atomization rate for a given fSAW power. Larger flow rates cause leaking of non-atomized fuel and smaller flow rates needlessly reduce the thrust to power ratio. This fluid supply mechanism will be replaced in future prototypes in favor of a wicking mechanism [279] suited to zero gravity.

Table 2.1: Focused SAW is supplied from both IDTs and impinges on a liquid supplied at a chosen mass flow rate. The power indicated is the sum of the power from two IDTs.

Input power (W)	Flow rate (mL/min)	Exit velocity (m/s)	Thrust (μN)	Specific impulse (sec)
1.00	0.025	1.7	0.706	0.173
2.00	0.1	2.8	4.65	0.286
3.00	0.2	3.7	12.3	0.378

2.2.4 Conclusions

We have introduced a possible method to produce thrust for small spacecraft: continuous acoustic atomization of water from a small piezoelectric, single crystal substrate, and shown that the same transducer can be used to melt ice on the substrate. Water has been heated using SAW previously, but to our knowledge this is the first demonstration of solid-liquid phase change induced using SAW. Moreover, although SAW atomization has been shown many times, continuous SAW atomization through a nozzle—a simple hole in the substrate—has not been reported until now. The device demonstrated here produces melting and atomization of a 1 μL drop with an input power on the order of 1 W, and is capable of producing thrust in the range 1-10 μN, which is large considering the device is $12 \times 20 \times 0.5$ mm^3 in size and 0.6 g mass. A major advantage of this thrust method is that, by simply adjusting the drive signals input into the fIDTs, the direction and amplitude of thrust can be finely tuned with *no moving parts*.

2.2.5 Acknowledgement

Chapter 3

Atomization with a portable thickness mode device

Acoustofluidics has promised to enable lab-on-a-chip and point-of-care devices in ways difficult to achieve using other methods. Piezoelectric ultrasonic transducers—as small as the chips they actuate—provide rapid fluid and suspended object transport. Acoustofluidic lab-on-chip devices offer a vast range of benefits in early disease identification and noninvasive drug delivery. However, their potential has long been undermined by the need for benchtop or rack-mount electronics. The piezoelectric ultrasonic transducers within require these equipment and thus acoustofluidic device implementation in a bedside setting has been limited. Here we detail a general process to enable the reader to produce battery or mains-powered microcircuits ideal for driving 1–300 MHz acoustic devices. We include the general design strategy for the circuit, the blocks that collectively define it, and suitable, specific choices for components to produce these blocks. We furthermore illustrate how to incorporate automated resonance finding and tracking, sensing and feedback, and built-in adjustability to accommodate devices' vastly different operating frequencies and powers in a single driver, including examples of fluid and particle manipulation typical of the needs in our discipline. With this in hand, the many groups active in

lab-on-a-chip acoustofluidics can now finally deliver on the promise of handheld, point-of-care technologies.

3.1 Practical microcircuits for handheld acoustofluidics

3.1.1 Introduction

The challenge to deliver a miniaturized solution to driving acoustofluidics devices has eluded the research community for over twenty-five years. The knowledge and know-how required to design MHz-frequency, high-power driver circuits in a small package is surprisingly rare among the many advancements in microelectronics technologies over the past seventy-five years, and is constraining progress in research and development of acoustofluidics as a potential method for delivering effective lab-on-a-chip devices into commercial and clinical use. The original use of surface acoustic wave (SAW) devices in microfluidics [280] resulted in the formation of a company, Advalytix AG, eventually owned by Becton & Dickinson focused on SAW-driven fluid mixing at small scales, yet the drivers for this commercial product were both mains powered and large. Other, occasional reports of success have been claimed, only to learn that power wires were hidden in a sleeve for a "handheld" driver, or that the circuit fails after only a short time[281]. Several attempts to completely avoid the problem of MHz-order acoustofluifdics have been attempted with lower frequency devices and corresponding driver circuits. Bachman *et al.*[282] produced an acoustofluidic system based on a cell phone and an audio speaker, but this scheme is limited to < 30 kHz. They also developed a system based on an Arduino and a motor controller, but this only increased the upper frequency limit to 65 kHz[283]. While useful, the long wavelengths of these low frequency devices are not suitable for microfluidics that define most lab-on-a-chip technologies, and there is the potential for cell and molecular damage from such low frequency acoustics. While some may contend that the "pull" for acoustofluidics as a technology sufficient to justify investment in developing circuits and other technologies to make

it practical in applications, we suggest that overcoming some of the risk and enabling broader testing and adoption of acoustofluidics can only help its maturation into a beneficial technology.

This paper aims to provide the first comprehensive microcircuit design capable of reliably driving the vast majority of acoustofluidics devices at 1–300 MHz, including the strategy and details necessary to help the reader to build their own driver circuits for lab-on-a-chip acoustofluidics.

Acoustofluidic devices are ideally suited for point-of-care and lab-on-a-chip applications, as they are small and produce ample mechanical power that can be harnessed to transport fluids and suspended objects. When alternating current (AC) signals are applied to piezoelectric transducers used in these devices, the resulting acoustic waves produce direct forces at boundaries with acoustic impedance changes and acoustic streaming from the attenuation of the acoustic wave in the fluid and within the viscous boundary layer. In doing so, acoustofluidics offers the following advantages over other approaches: (i) the forces formed from high frequency acoustic waves overcome surface and viscous-mediated forces that tend to dominate in microfluidics, (ii) acoustic waves enable label-free, non-contact particle manipulation at small scales, and (iii) the AC signals that directly drive these devices offer precise control and simple operation. Fluid mixing, droplet manipulation, particle manipulation, and atomization have all been demonstrated with acoustofluidic technology and helped overcome medical and diagnostic challenges[284, 185, 231]. However, the majority of these solutions have not found practical use because they are unable to be adapted to miniature, portable devices. They still require laboratory equipment including signal generators, amplifiers, and oscilloscopes.

Many point-of-care devices and all drug delivery and disease evaluation technologies must also avoid damaging biological samples. The absence of damage to biological molecules and cells has been shown repeatedly in high frequency acoustic devices[285, 118, 286], but lower frequency acoustic waves, on the order of 10 kHz, are known to cause cavitation[287] that can damage cells, proteins, and antibodies, even—for example—in modulating higher frequency

98

acoustics devices[281].

To highlight the capabilities of our circuit design for enabling lab-on-a-chip concepts and work, we will demonstrate four acoustofluidics devices that utilize our microcircuit. We will first demonstrate quick mixing in a sessile drop using a surface acoustic wave (SAW) device driven by our microcircuit. The Reynolds number, $Re = \rho u D / \mu$, must be large for the turbulent flow that characterizes mixing, and it scales with the length scale of the device, D, so that it is very difficult to generate mixing at the microscale. The earliest broadly known lab-on-a-chip application of SAW devices solved precisely this problem[288]. Very high frequency acoustic waves transmitted into fluids in contact with these SAW devices lead to large accelerations that easily mix a broad range of fluids from glycerol to whole blood [289, 110, 290].

We next demonstrate tunable alignment of 2 μm particles with SAW of 40–80 MHz, another key application of acoustofluidics in lab-on-a-chip applications. The spacing between groupings of particles aligned using standing waves is determined by their frequency[291]. Furthermore, The ability to manipulate small particles with acoustic transducers[292] depends on the wavelength of the acoustic waves they generate.

Similarly, the isolation and manipulation of medically relevant particles—cells, organelles, biomolecules—with acoustofluidic devices[293] requires frequencies beyond 10 MHz. We demonstrate separation of 38 μm and 4 μm diameter particles in a sessile drop as an analog to blood sample separation.

These three SAW based applications are each demonstrated using the same handheld driver circuit, named the *SAW board*, reprogrammed for each case by quickly uploading code from a computer. This board is relatively large—the size of an open hand—and is plugged in to wall power, convenient for prototyping, testing, and saving data.

In the fourth case, we demonstrate a high power application, a nebulizer driven by a handheld, battery powered circuit. This circuit, named the *TM* (thickness mode) *board* is designed using the same principles, but is optimized in parts and layout to be a compact, near-

commercial circuit design. Nebulization is accomplished at practically relevant flow rates from battery power using this circuit and the board comes pre-loaded with a program to run a simple user interface. Acoustofluidic atomization of therapeutic liquids has the potential to replace other forms of nebulization because of the aforementioned biological compatibility and the proven ability to produce droplet sizes in the range for optimal delivery to the lungs[222, 294, 295]. Our circuit enables these benefits in a handheld device.

3.1.2   Circuit design for acoustofluidics

To suit the signal generation needs of acoustofluidics devices while offering the portability required in clinical and commercial applications, a driver circuit must be miniaturized, battery powered, and able to produce signals in the 1–300 MHz frequency range with a power of 50 mW to 2 W, based upon most of the past published work in this discipline[231, 6, 296, 297].

Benchtop equipment—signal generators, DC power supplies, and low-frequency (LF) to radio-frequency (RF) amplifiers—is simply too expensive, bulky, and heavy for use outside of research laboratories. Miniaturized electronics tailored to an application may be achieved using commercially available *off-the-shelf* electronic parts assembled on custom-designed printed circuit boards (PCB). Because of the unique power and frequency requirements of acoustofluidics devices, significant design, programming, and testing efforts are required, but nonetheless can produce compact and user-friendly devices.

We accomplish this by applying electronics design principles to develop two distinct driving circuits, the TM board for 1–25 MHz thickness mode (TM) transducers, and the SAW board for 30–100 MHz SAW transducers. The TM board is compact, as it is intended for battery-driven handheld nebulization. The SAW board was originally developed to drive SAW within prototype lithium batteries[298] on the lab benchtop. Consequently, the SAW board is larger for convenience, requires less power, operates at a higher frequency range, and draws power from a wall outlet. It also has additional circuitry on the board used for charging and other purposes

not relevant to the work reported in this paper. Here, we use the TM board to illustrate how the reader may make practical handheld driver circuits for acoustofluidics sufficient to even drive atomization. Both designs, with minor modifications, may be used for driving acoustofluidic devices from a few kHz to 250 MHz or more. We use the SAW board to demonstrate three other acoustofluidic applications showcasing the adaptability of this circuit design. With some effort, the reader should be able to construct a prototype circuit such as the SAW board for their needs, and once a specific application is identified, a much smaller prototype driver like the TM board may then be produced.

Circuit blocks

Despite the differences in the required stimulus frequencies and power levels, electrical driver systems for acoustofluidic devices incorporate five basic units or *blocks*.

1. **Stimulus generation**: This is accomplished by semiconductor circuits known as *phase locked loops* (PLL), a type of frequency synthesizer. This low-cost solution uses a reference crystal oscillator to produce a highly accurate and stable tone. The frequency is programmable over a specified range with very fine resolution, in this case ¡0.01 MHz. However, unlike the benchtop signal generators or arbitrary waveform generators (AWG) it replaces, the output amplitude is usually fixed; PLLs typically cannot produce the required output power to directly drive the SAW devices. This leads us to the next circuit block.

2. **Amplification**: We employ a chain of amplifiers to connect the output of the PLL to the input of the SAW device, achieving increasingly higher voltage swings as needed. Furthermore, duty cycle control can be added using the enable signals of clock buffers, while attenuators—using dedicated chips or a simple resistor voltage divider—can be used to fine-tune the signal swing, and a power amplifier with a push-pull output stage can be employed to efficiently deliver high current at fixed voltage to the device. The device itself

can be modeled as a low impedance load at the resonance frequency.

3. **Power management**: From a single battery or a wall outlet, the power management unit (PMU) produces all voltage supplies (such as 3.3V, 5V, 24V etc.) as required by various semiconductor chips on the PCB. These circuits are commonly known as *DC-DC converters*. *Boost converters* are used to step-up voltages from input to output, while *low dropout* (LDO) regulators step-down voltages. If higher efficiency is required, a step-down function can also be achieved using a *buck converter*. This block replaces a typical benchtop power supply.

4. **Impedance matching**: In a typical bench-top setup, maximum power transfer is achieved when the load and source impedances match. Signal generators, amplifiers, and cables are typically matched to have 50Ω impedance, for example. If there is an impedance mismatch between two components, some fraction of the power is reflected at the impedance interface. Based on a simple source/load model, the power dissipated by the load is $P_l = V_s^2 R_l / (R_s + R_l)^2$. However, our boards utilize a constant voltage operational amplifier, so there is no defined source impedance with which to match the load impedance. In this case, power transfer, $P_l = V_s^2 / Z_r$, is maximized by minimizing the load impedance, $Z_l = Z_r + iZ_i$, where the real impedance, Z_r, is resistance and the imaginary impedance, Z_i, is capacitive if positive and inductive if negative. At a resonance frequency, $Z_i = 0$ by definition, and we can minimize Z_r by choosing the resonance frequency with the smallest resistance (this is done automatically on our boards as will be explained in the next section). Design choices for the piezoelectric device can aid the reduction in resistance, for example, ensuring the metal electrodes are sufficiently thick whether it is a SAW, flexural, thickness, or some other type of device.

   An impedance matching network is effective at reducing the reflected power in a standard bench-top setup or in a circuit with a source impedance. Such networks do impose a power

loss, so the system must be optimized to account for this trade-off. Qualitative examples and additional tips on electrical design are provided by Winkler et al., who show that impedance matching networks can result in a 30% improvement in acoustic performance (in terms of streaming velocity)[299]. In contrast, the power to the transducer in our circuit could be increased by lowering the effective load resistance. Our boards have designated spots for an impedance network, but they have not been populated because the power transfer was already sufficient for demonstration purposes.

In commercial acoustofluidic products, it will be necessary to measure the impedance of the transducer in the condition it will be used, i.e., within the driver circuit and with realistic mechanical loading with fluids, mounting, wicking, and other attachments. The impedance matching network would be defined from these conditions at the intended frequency. For a transducer used at only one frequency, the simple network designed into our boards or an inductor/capacitor impedance matching network in the case of a more typical set-up is sufficient. Kim et al. utilized an impedance matching network and showed that it leads to more efficient production of acoustic pulses for cell actuation[300]. For multi-frequency applications, more complicated networks are required. Vivek Rathod has covered these and other related topics at length in a recent review[301].

5. **Control and user interface**: A micro-controller unit (MCU), such as the *Arduino Nano* (Arduino LLC, Boston, MA USA), serves as the interface between the electronic driver system and the user. Through general-purpose integrated circuit (I^2C) input-output (IO) expanders, the MCU translates user inputs into low-level digital signals to control all components on the PCB. The MCU can be connected via USB to a laptop for convenient programming and testing flexibility. It may also be pre-programmed with a few options— such as power on/off, frequency up/down—that are selected by onboard push buttons connected to the MCU. As a result, the final SAW-based system may be turned into a completely self-contained and user-friendly device.

6. **Sensing and feedback**: While the electronics described above are already sufficient to drive the SAW device, we can take advantage of modern electronics to offer additional features. For example, one can include thermistors to monitor the board temperature in strategic locations to detect overheating or out-of-design operation. Digitized and read by the MCU, the measured data can be used to simply monitor the operating conditions or to act on the data via a feedback loop, for example, to automatically shut down when a component overheats. As will be discussed below, our systems incorporate current sensors on the SAW device inputs to automatically seek the optimal resonance frequency despite inevitable resonance frequency variations during operation and between devices.
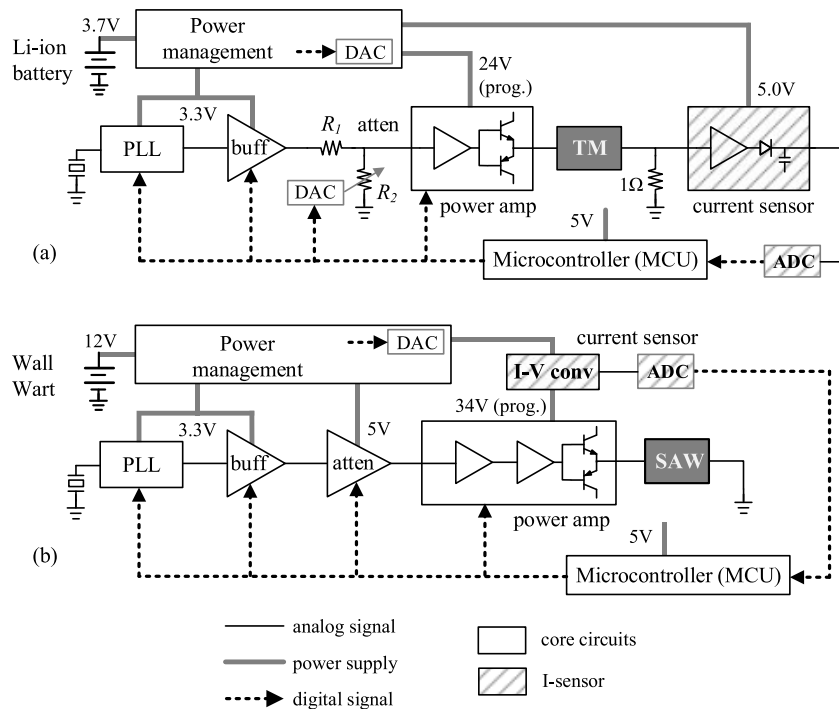
Figure 3.1: Block diagrams of the driving circuits. The (a) TM board is designed to drive a 1–25 MHz thickness mode (TM) transducer in a handheld, battery-powered nebulizer, and the (b) SAW board, designed to drive a 30–100 MHz SAW transducer, originally for enhancing the capacity of a rechargeable lithium metal battery, but useful for a broader range of acoustofluidics applications as illustrated later.

The TM and SAW boards embody these principles. Their block diagrams are shown

in Fig. 3.1, and we will explain their specific implementations, including design choices, parts, layout, testing, and a step-by-step guide in later sections.

Automatic resonance search

In addition to the circuit blocks discussed in the last section that are required for basic functionality, both systems also include blocks to perform a resonance search. The PLL frequency range is swept by the MCU with a frequency step of 1 kHz, and the output current to the SAW device is measured, digitized, and recorded at each frequency step. An initial search range is specified in the algorithm to both minimize the time required to perform the sweep and reduce the risk of a spurious resonance mode's selection. The voltage amplitude, V, at the final stage of the signal chain and in the driver amplifier, is constant by virtue of its resistor feedback architecture. Therefore, the higher the output current amplitude, I, the higher the power, P, delivered to the device since $P = VI$. The frequency at which the measured current amplitude is maximized corresponds to the resonance frequency of the transducer. This feature effectively combats device-to-device differences and accounts for changes in circuit loading conditions, in particular the presence of liquid on the surface of the SAW or TM device. These factors often shift the resonance by 100 kHz or more, which is sufficient to significantly reduce the performance of an acoustic transducer, as most transducers have a quality factor [1] (Q) of ¿100, representing a very narrow bandwidth. Achieved by a straightforward electronics design and controlled by the MCU, this feature ensures all transducers are driven at their optimal frequency, despite any resonance changes. This might arise from the introduction of a new vial for drug atomization, too much fluid introduced in an experiment by accident, using the device at a different temperature, and so on.

The resonance search algorithm is verified against measurements from a vector network

[1] $Q = f_c/\Delta f$, where Q is the quality factor, f_c is the resonant frequency, and Δf is the width in frequency space of the corresponding peak at half the maximum amplitude. Quality factor is also intuitively associated with the energy loss of the oscillation [2].

analyzer (VNA, E5071C Agilent Technologies, Inc., Santa Clara, CA USA) and a laser Doppler vibrometer (LDV, UHF-120SV, Polytec, Irvine, CA USA). A current spectrum resulting from a resonance search on the TM board reveals two peaks (Fig. 3.2(a)) from which the largest is chosen, thus identifying 6.62 MHz as the resonance of the transducer under test. The search is repeated with a drop of water on the transducer, which slightly shifts the resonance. Piezoelectric transducers can be modeled as a series combination of a frequency-dependent resistor, an inductor, and a capacitor. The impedance of such a circuit can be modeled as a complex function of frequency with a zero imaginary component at resonance, i.e., the inductive and capacitive components cancel out, leaving behind the real part: a pure resistance. This is equivalent to the frequency at which the S_{11} parameter, the input port voltage reflection coefficient from the VNA, intersects the real axis on a Smith chart (Fig. 3.2(b)). The closer the intercept point is to the origin, the lower the resistance, so the highest peak in Fig. 3.2(a) should occur at the same frequency as the left-most intercept in the Smith chart (Fig. 3.2(b)). Four thickness mode (TM) transducers intended for the TM board were all tested as shown in Fig. 3.2; each pair of frequencies identified with this technique agreed to within 0.2%. Similarly, a 40 MHz SAW transducer was tested and the VNA and the on-board algorithm were found to agree within 0.2% (Fig. 3.3). In each case, an LDV scan was performed over the region of interest on the transducer, and both the TM and SAW transducers were confirmed to have the largest amplitude at the frequency indicated by the on-board algorithm and the VNA.

Implementation in two examples

Here we elaborate on the circuit design and fabrication principles described in the main article for both the SAW board and the TM board. The thickness-mode (TM) board drives a 6–7 MHz thickness mode transducer to achieve a handheld nebulizer. SAW is impractical at less than 40 MHz because the penetration depth of the SAW is 4–5 wavelengths, exceeding the 500 μm thickness of the widely available piezoelectric lithium niobate wafers used for this purpose. The

106
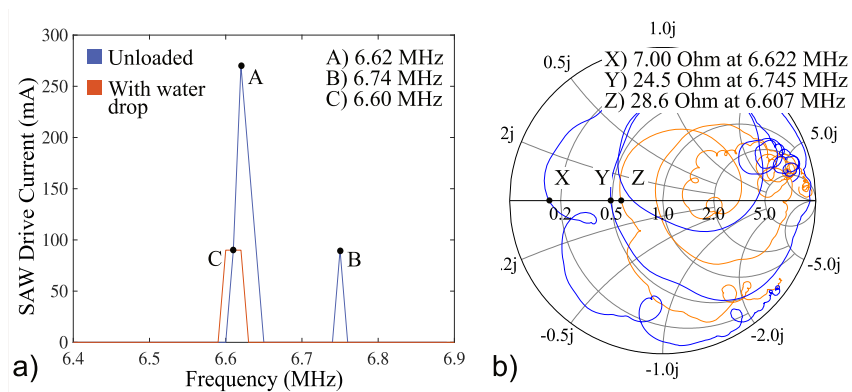
Figure 3.2: A TM transducer was run through a frequency sweep using both the TM board and a VNA. Both a dry transducer (blue plots) and a transducer laden with a ∼5 $\mu\ell$ water drop (orange plots) were considered. (a) The current across the transducer is measured over the frequency range of interest by the MCU. A simple algorithm identifies the largest peak, in this case peak A when dry and peak C with water present. (b) Measured S_{11} of the TM transducer on a VNA. This confirms that the measured current peaks correspond to resonances of the transducer, both with and without liquid present. The messy appearance of the Smith chart is expected for a TM transducer with finite lateral dimensions, since spurious Lamb wave modes exist at similar frequencies. Despite this, the algorithm is still able to identify the desired TM mode for the drive circuit.
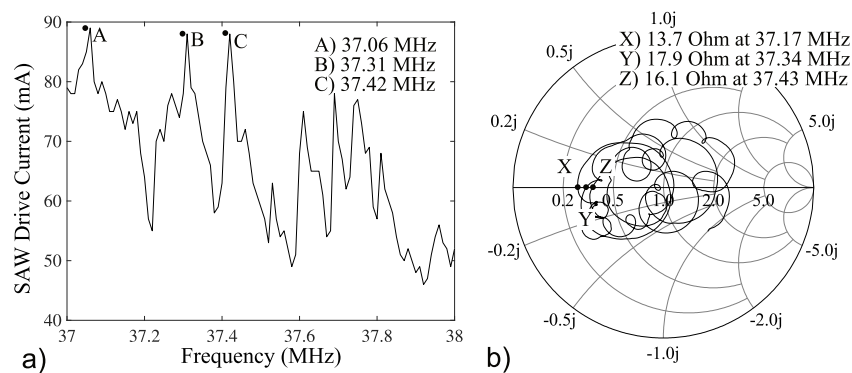
Figure 3.3: A SAW IDT was run through a frequency sweep using both the SAW board and a VNA. (a) The current across the transducer is measured over the frequency range of interest by the MCU. The algorithm simply identifies the largest peak, in this case peak A. (b) Measured S_{11} of the SAW transducer on a VNA. This confirms that the measured current peaks correspond to resonances of the IDT. It is expected that multiple adjacent resonances—*side bands*—exist in an IDT that lacks specific design features, such as apodization, to prevent them.

transducer is driven by 0.5 to 2 W of power. The SAW board has a similar design, but is tailored to drive a 40–120 MHz SAW device used to enhance the capacity of a rechargeable lithium metal battery. The SAW transducer typically demands 0.1 to 1 W of power in this application. The

SAW devices demand as much as 5 W for atomization, the reason for the selection of other vibration modes that are more efficient in that application. However, the designs described in this Electronic Supplementary Information may be readily modified to produce driver circuits appropriate for these greater power requirements.

We will describe our choice of integrated circuits (ICs) for these applications. Since the TM board will be operated by a small 3.7 V battery, the power consumption of the electronics should be minimized. On the other hand, the SAW board operates at much higher frequencies, thus demanding higher-speed electronics. Fortunately, the board is powered by wall-wart supply, so the overall power consumption is of secondary concern. Note that the resulting boards, while fairly optimized, are not unique. Many IC options exist to accomplish the same function, each offering some trade-off in cost, size, performances, ease of assembly and usage. Engineers often start the design process by exploring and comparing ICs from the vast, searchable catalogues on electronic component distributors' web pages.
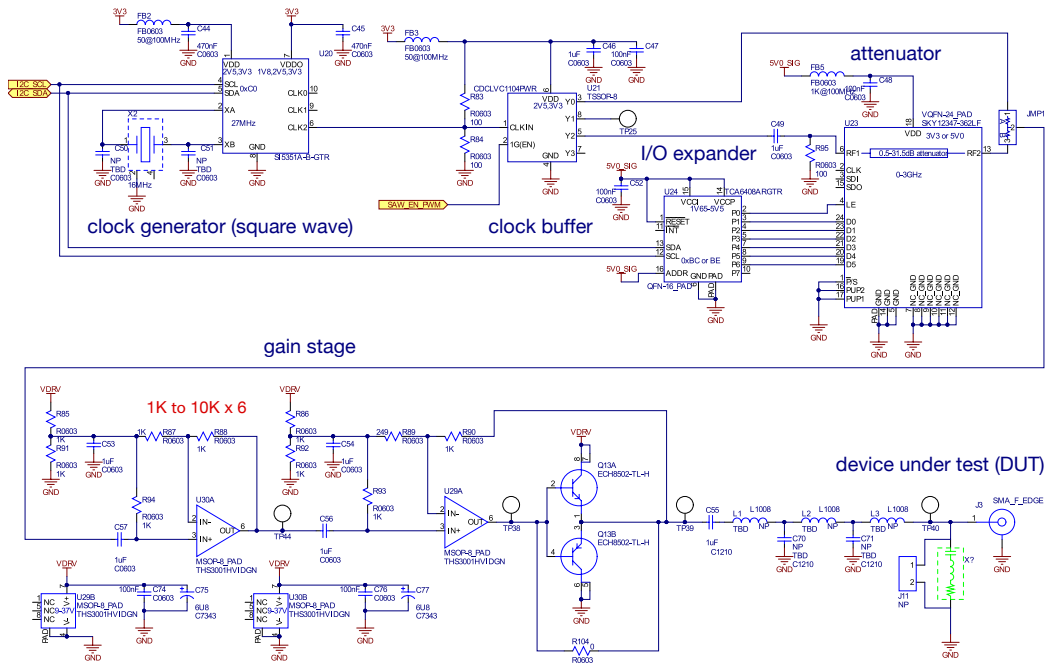
Figure 3.4: Each circuit component is symbolically represented in this schematic organized for conceptual clarity.

The SAW driver signal chain begins with the stimulus source. The complementary metal–oxide–semiconductor (CMOS) Si5351 (from Silicon Laboratories) clock generator (PLL) chip was employed to synthesize a tone with programmable frequency between 2.5 kHz to 300 MHz. It is followed by the CDCLVC1104 clock buffer (Texas Instruments, Dallas, TX USA). At 3.3 V input, it can operate up to 250 MHz. It is used to drive the attenuator that follows, preserve the low-skew clock, and accomplish duty-cycle control for pulse-width modulation. To shorten the development time, identical PLL and buffer circuits are used for both boards. Potential savings in cost and power did not warrant a customized design effort in this case.

Gain control is achieved by a programmable attenuator. The TM board features a "resistor divider" with a variable resistor (R2) achieved by an N-type metal-oxide-semiconductor (NMOS) transistor. Its resistance is digitally adjusted by the gate voltage fed by a voltage DAC (digital-to-analog converter) MCP4726 (from Microchip Technology). While this very simple implementation works well at low frequencies, the parasitic capacitance of the NMOS transistor will form a RC (R for resistance, C for capacitance) low-pass filter (LPF), distorting waveforms at higher frequencies. Therefore, the SAW board employs an active attenuator IC SKY12346 (from Skyworks Solutions). Designed for broadband cellular (up to 3 GHz) operation, the attenuator has no LPF or distortion issues, but at the expense of added direct current (DC) power consumption.

To boost the signal to drive the thickness mode device, the power amplifier section of the TM board employs one stage of a voltage feedback amplifier LM7171 (Texas Instruments). At 6.5 mA bias current, it features a unity-gain bandwidth of 200 MHz, sufficient to handle multiple harmonics of the clock to preserve the sharp, square waveform. On the other hand, the SAW board employs the amplifier THS3001 (also from TI), whose bandwidth reaches 420 MHz at slightly higher (10 mA) bias current. Moreover, gain is distributed into two stages. As the gain of each amplifier is lowered (halved), its stability at high frequencies, formally measured by the "phase margin", also improves. As the last stage of the signal chain, the power amplifier shall deliver high current to the SAW. To achieve that goal, a standard bipolar junction transistor (BJT)

push-pull output driver is employed. Configured as emitter followers, a complementary PNP and NPN BJT pair (ECH8502, from ON semiconductor) can efficiently and rapidly pump and sink currents into and from the load.

The micro-controller (MCU) function is provided by the Arduino nano clone ATmega328P (from Microchip Technology) and the accompanying software. It is pre-loaded with programs to calculate, based on user inputs and component parameters, the control signals for all ICs on the PCB. The input-output (I/O) expander chip TCA6408A (from Texas Instruments) provides eight bits of general-purpose parallel input/output expansion for the two-line bidirectional "I2C" bus protocol, simplifying all IC control and user interfaces.

For the power management unit (PMU), there are literally thousands of boost converter ICs (voltage step-up) and low-dropout (LDO) regulator ICs (voltage step-down) for designers to choose from, targeting different input/output voltage ranges and current ratings. The design process is fairly straightforward. For example, the main input of the TM board comes from a 3.7 V battery, and 3 V, 5 V and 24 V are desired. This is accomplished as follows: (1) a boost converter XCL101C (from Torex Semiconductor) steps up 3.7 V to generate 5 V; (2) an LDO regulator TLV733P (from Texas Instruments) steps down from 5 V to generate 3 V; and (3) a boost converter MP3213 (from Monolithic Power Systems) steps up from 3.7 V to 24 V. On the other hand, the main input of the SAW board comes from a 12 V wall wart supply, and 3.3 V, 5 V and 34 V are required. This is achieved by: (1) two LDO regulators MIC5225 (from Micrel Technology) stepping down 12 V to both 3.3 V and 5 V, and (2) a boost converter LT3489 (from Linear Technology) stepping up from 12 V to 34 V.

The current sensing function in the TM board is achieved by a 1Ω series resistor, directly performing current-to-voltage (I-to-V) conversion on the output sinusoidal current driving the SAW device. The corresponding voltage signal is subsequently amplified and rectified (LT1810, by Linear Technology); a diode (BA891, by NXP) provides peak detection from this signal. The resulting peak DC voltage is digitized by an ADC (analog-to-digital converter) embedded in the

MCU. The MCU automatically sweeps the PLL (stimulus) frequencies over a pre-defined range and records all corresponding ADC values. Resonance is given by the frequency at which the peak ADC value occurs. The current sensing function in the SAW board is indirectly performed. High-frequency current signals vary too quickly for direct rectification and peak detection without disrupting the normal operation of the power amplifier. Instead, a current amplifier chip (LTC6101, by Analog Devices) is employed at the power supply of the driver amplifier.
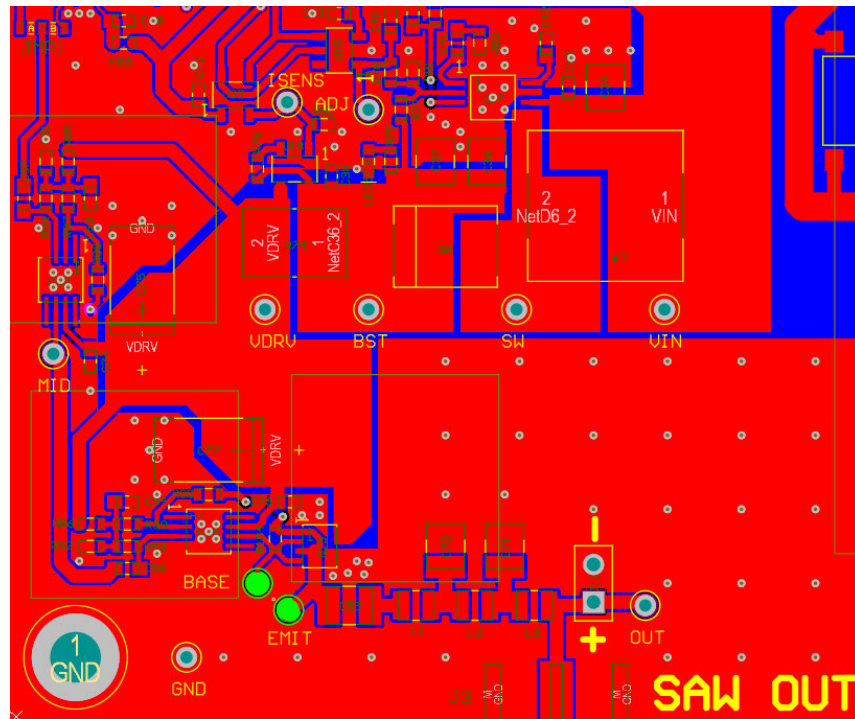
Figure 3.5: The schematic in Fig. 3.4 is transformed into a PCB layout following a standard design procedure using a testing breadboard. This is sent out for fabrication and debugged before designing the final PCB layout with the desired form factor.

Layout and testing

Having chosen the ICs and defined the circuit architecture, the design may be laid out on a custom-made printed circuit board (PCB). There are many commercially available computer-aided drafting (CAD) tools to aid with the PCB development process. Here, Altium Designer was employed. The design process begins by capturing all circuit components schematically (Fig. 3.4).

Symbols representing ICs are connected to all required circuit components. The functions and performances of certain critical parts (e.g. the driver amplifiers) can be verified using circuit simulation software such as LTspice®. All components are laid out according to design rules and manufacturing requirements while maintaining interconnectivity information generated by the schematic (Fig. 3.5). The completed PCB layout, together with the bill of materials, can then be submitted to commercial manufacturing companies for fabrication and assembly (i.e., electronic components and chips are populated and soldered onto the PCB). The finished PCB is then tested, debugged, and verified in the lab.

The above procedure entails a fair amount of design time, cost, and efforts. In order to make the engineering tasks more manageable, especially when new chips or circuit functions were introduced, we adapt the following step-by-step approach. To start, we employ "evaluation boards" offered by chip vendors (e.g., Si535x–B20QFN–EVB for the phase-locked loop (PLL) from Silicon Labs) to test out the circuit functions rapidly. The drawback is the higher cost, and the clumsy interface and size. Next, we integrate all chips onto a relatively large, two-layer PCB, as shown in Fig. 3.5. Routings are done in a straight-forward manner, with all components mounted on only one side of the board, ICs with bigger packages are chosen for easier soldering and probing, and multiple test points and signal breaking points (with a 0ω resistor) are generously incorporated. To avoid signal noise, wide traces and large copper planes for ground and power are used. After this easy to build PCB has been debugged and the functionality verified, the layout is optimized to achieve the desired form factor. Board size is reduced by using double-sided, multi-layer PCBs with dedicated ground and power planes. Testing features, with a few crucial exceptions, are removed. More densely packed components require more carefully planned routings to avoid long traces and signal cross-talk. The resulting boards for Systems 1 and 2 are pictured in Fig. 3.6 and Fig. 3.7 respectively in the nebulizer and particle alignment applications.

Fabrication guide

Taking the handheld nebulizer as an example we show here how to fabricate a complete device from start to finish. With this example, it is our hope that interested groups can recreate this type of circuit for their own application given a month of support or less from a professional circuit designer or an advanced electrical engineering student to fit the design to their application.

1. Follow the design, layout, and testing procedure as described above

2. Assemble a parts list for the PCB along with files required for PCB manufacture (see 'Nebulizer Fabrication/PCB' in the ESI †)

3. Design a transducer holder (see 'Nebulizer Fabrication/Transducer Holder' in the ESI †) and ensure that it will interface with your PCB in the next step

4. Simulate the full integrated design in a CAD software (we used Solidworks, see 'Nebulizer Fabrication/CAD' in the ESI † and Fig. 3.6)

5. Order your PCBs from a manufacturer that will also populate the circuit (we used *PCB Minions*)

6. Order the additional parts for the fully integrated design (see Bill of Materials below)

7. Solder contacts to the Transducer Holder PCBs and assemble the complete device in your lab

Bill of Materials for nebulizer

- Populated driver circuit (manufactured and assembled by PCB minions)

- Transducer holder PCBs (manufactured by OSHpark, see files in the ESI †)

- Lithium Ion Battery - 3.7 V 2000 mAh (Adafruit part)

- Battery charger (Adafruit part)

- JST-PH 2-pin SMT right angle connector (Adafruit part)

- (x4) 15 mm M3 nylon standoffs

- (x4) 8 mm M3 nylon standoffs

- (x5) M3 nylon nuts

- 5 mm M3 nylon screw

- (x4) Spring-clip contact (Digi-key part)

- (x2) vertical, 2-Pos header pins

- 3D printed syringe tip holder parts ('shoe' and 'buckle' in Solidworks files)

- (x4) 0-80 3/8 inch machine screws

- (x4) 0-80 machine nuts

- 12 gauge (ID 0.089, OD 0.109) 0.5-inch syringe tip (Jensen Global part)

- 2 mm diameter, 25 mm long fiber bundle wick

- Luer-Lock syringe reservoir (3 or 10 mL)

3.1.3 Application to handheld acoustofluidics devices

For microcircuit-driven acoustofluidic devices to be viable, they must perform similarly to benchtop devices designed and demonstrated in laboratories. We compare our handheld nebulizer—utilizing the TM board (Fig. 3.18(a)—with acoustofluidic atomization literature and with a benchtop driver setup with an identical transducer. The TM board has a custom program

114
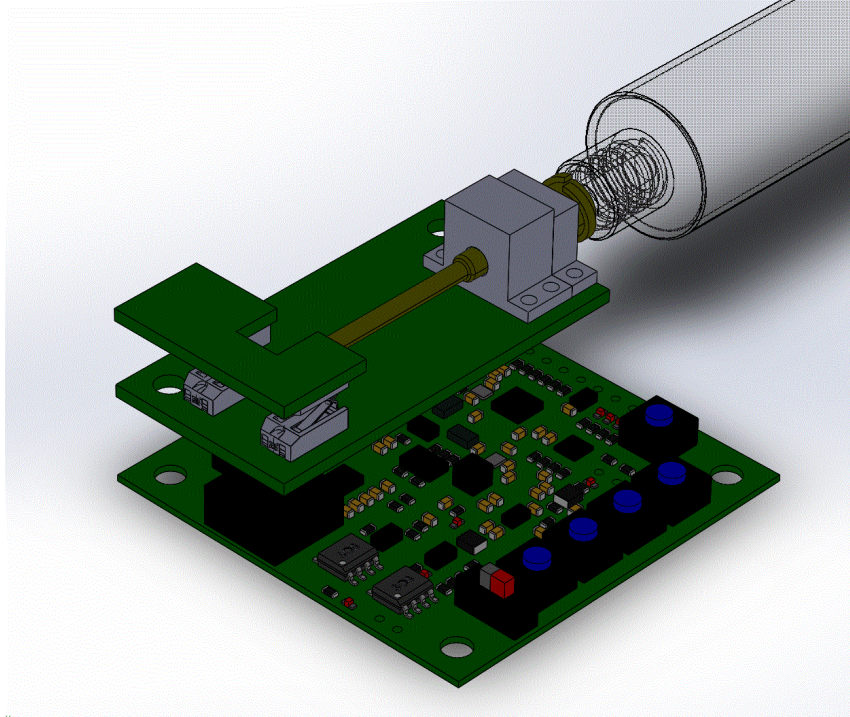
Figure 3.6: The full nebulizer assembly mocked together in computer-aided drafting to confirm the assembly will work with sufficient part clearances and alignment. With careful inspection, this can help prevent tedious iteration and revision of fabricated parts to remedy otherwise easily overlooked dimensional and compatibility mistakes.

pre-loaded to facilitate use without further connection to a computer or other device. Such a pre-programmed board design is especially convenient in a prototype closer to use as a consumer product.

Similarly, we present three implementations of the SAW board and compare these results with benchtop-driven devices from the published literature and a benchtop signal generator and amplifier combination driving these same three devices in our own laboratory. The frequency, power, and duty cycle delivered by the SAW board can be selected by defining these parameters in a custom (MATLAB, Mathwords, Natick, MA USA) script uploaded from a connected PC to the board's MCU. An externally connected PC is required to change these settings with the SAW board, and the PC is convenient for real-time download of the operating state of the SAW board, making it possible to adjust the board's operation and detect the effects from the computer. This

is much more difficult to accomplish with the pre-programmed TM board.

For consistency, during comparisons with benchtop setups, the same equipment is used in all four applications. Acoustic vibrations are produced by applying a sinusoidal voltage signal to the transducers using a signal generator (WF1967 multifunction generator, NF Corporation, Yokohama, Japan) and an amplifier (ZHL–1–2W–S+, Mini-Circuits, Brooklyn, NY USA). The instantaneous voltage and current are measured and used to compute the net power input via an oscilloscope (InfiniVision 2000 X-Series, Keysight Technologies, Santa Rosa, CA USA) as shown in Fig. 3.18(b).

SAW board set up

Here we provide a sample image of the SAW board during its use to perform a typical acoustofluidics-based chip operation. Please also consult the video provided in the ESI † that demonstrates operation of the SAW board during fluid mixing.
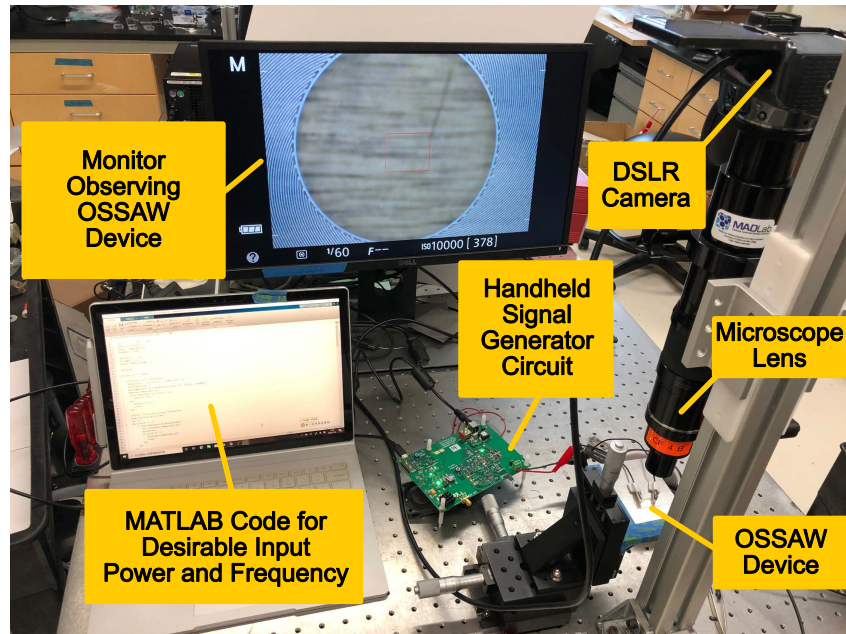
Figure 3.7: An example of the SAW board in use for SAW-induced particle separation.

Mixing in liquid droplets

Rapid and complete mixing in microfludics and nanofludics is needed in time-sensitive chemical reactions and bio-chemical processes [185, 302]. However, diffusion dominates micro scale mixing because the flow is usually laminar. Such diffusion-based mixing is too slow for most lab-on-a-chip applications especially for biological samples. Adopting surface acoustic wave (SAW) induced acoustic streaming to generate chaotic advection is a solution to increase the diffusion rate and decrease the mixing time significantly, as shown by Shilton et al.[152].

We illustrate rapid mixing in a simple experimental setup. A single droplet contains two initially separate liquids—a 1 $\mu\ell$ transparent glycerol drop is first placed on the surface and then a 0.25 $\mu\ell$ blue-color dyed water drop is placed into the glycerol droplet (*see* Fig. 3.8(a)). A 40 MHz SAW device is chosen to produce efficient mixing between the two droplets. Fig. 3.8(b) shows a drop that has been mixed using benchtop equipment for 7 s at 280 mW. Fig. 3.8(c) shows a drop that has been mixed for 6 s at 300 mW using a handheld circuit as illustrate in Fig. 3.7. These results are essentially equivalent and are on par with literature values, for example, Shilton *et al.* report complete mixing of colored dye into a glycerol solution in 8 s at ~1 W (the excess power is because there was a microfluidic well instead of a sessile drop in that case, which increases attenuation).
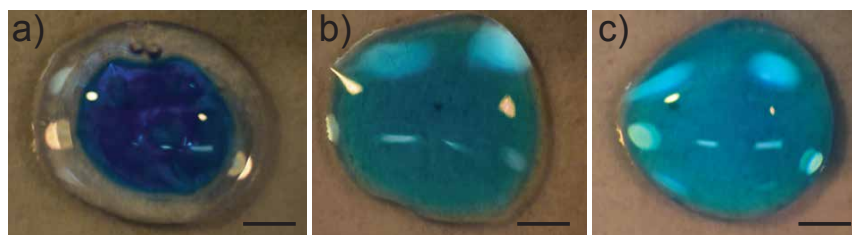
Figure 3.8: Effective droplet mixing via travelling SAW. The water droplet is dyed with blue color (the middle ring), while the glycerol droplet remains transparent. (a) is the pre-mixing stage, (b) and (c) are the post-mixing stage via external driven power caused chaotic mixing with benchtop signal generator with power amplifier and handheld circuit boards, respectively. The scale bar represents 250 μm.

Microparticle separation within a microliter sessile droplet

Particle and cell separation induced by SAW in sessile drops has become a popular platform due to its convenience, rapid response, and biocompatibility. Straight and standard interdigital transducers (IDTs) with a sessile drop located at an offset position from the center of the SAW propagation direction have been used to spin fluid droplets, producing particle concentration and separation due to asymmetric SAW actuation [118, 160, 156]. We have recently produced a novel omnidirectional spiral surface acoustic wave (OSSAW) interdigital transducer design. This spiral design was developed such that the wave propagation direction is always rotationally symmetric and tangent to a circle inside the IDT structure (*see* Fig. 3.9). This allows the production of inward-bound acoustic waves ideal to spin a droplet, but only because we have placed the IDT on a selected cut of lithium niobate that allows the production of SAW in any direction [303]. We further demonstrated accurate particle manipulation and multi-size separation in a microliter ($\mu\ell$) drop with this effort.

Here, we perform microparticle separation with the same OSSAW transducer, but now employ the SAW board instead of a standard benchtop setup. An operating frequency of 40 MHz was chosen to produce a ~8 μm particle/cell separation threshold, taking into account particle compressibility [126, 304, 129]. Polystyrene (PS) particles (Polysciences, Inc., Warrington, PA, USA) with diameters of 4 and 38 μm were selected to show size-selective separation at the microscale. A 1 $\mu\ell$ droplet containing these particles in concentrations of 4×10^9 and 1×10^5 particles/mℓ, respectively, was placed at the center of the transducer. After ~5 s at ~1 W, the smaller particles collected at the periphery and the larger particles concentrated at the center (*see* Fig. 3.10b-d and a video in the ESI †). The same result was obtained with either the SAW board or the benchtop equipment described above and it is reasonably comparable to past work[160] using lab equipment, where 6 μm and 31 μm particles were separated using 20 MHz SAW at 250 mW in ~4 s. Our implementation requires more power for a similarly sized sessile drop because the frequency is much higher, which causes greater attenuation but produces superior

separation selectivity based on particle size.
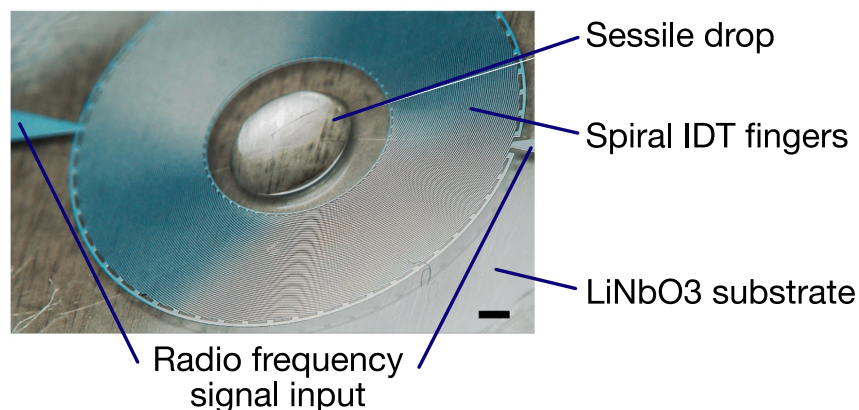
Figure 3.9: A 60-MHz OSSAW device with a microliter sessile drop in the inner circular region, showing the fingers and electrode connection to produce a suitable spiral SAW. Scale bar: 0.5 mm.
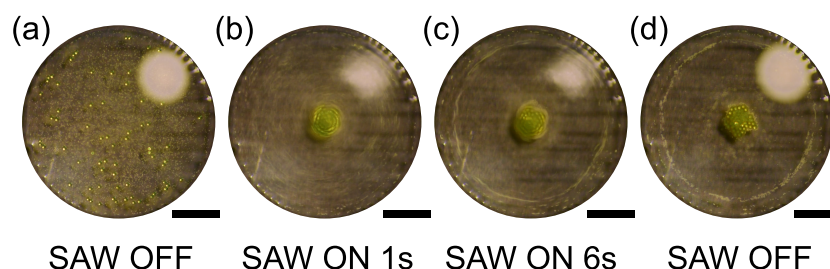
Figure 3.10: Effective particle separation via omnidirectional spiral surface acoustic waves (OSSAW) with size of 38 μm and 4 μm operated at a resonance frequency of 40 MHz. (a) Before SAW actuation, (b) 1 s after SAW is on, (c) 6 s after SAW is on, and (d) after SAW actuation. Scale bar: 0.5 mm. The bright dot at the top right of the droplet is the light reflection from the droplet boundary.

Particle alignment

Particle alignment via collection at nodes of acoustic standing waves has been demonstrated for applications such as tissue engineering[305] and cell characterization[286] and serves as a fundamental tool wherever small particles need to be patterned. Utilizing acoustic forces rather than laser actuation as in optical tweezers prevents damage to cells and does not rely on the magnetic or electric properties of the particles. Standing waves generated by counter propagating

SAWs with the same frequency create stationary pressure nodes, where suspended particles can be trapped by acoustic radiation force. The spacing between adjacent nodes is determined by the wavelength ($\lambda/2$). Chirped IDTs allow for a range of frequencies to be used in the same transducer so that the nodal and anti-nodal positions can be changed at will[292, 306].
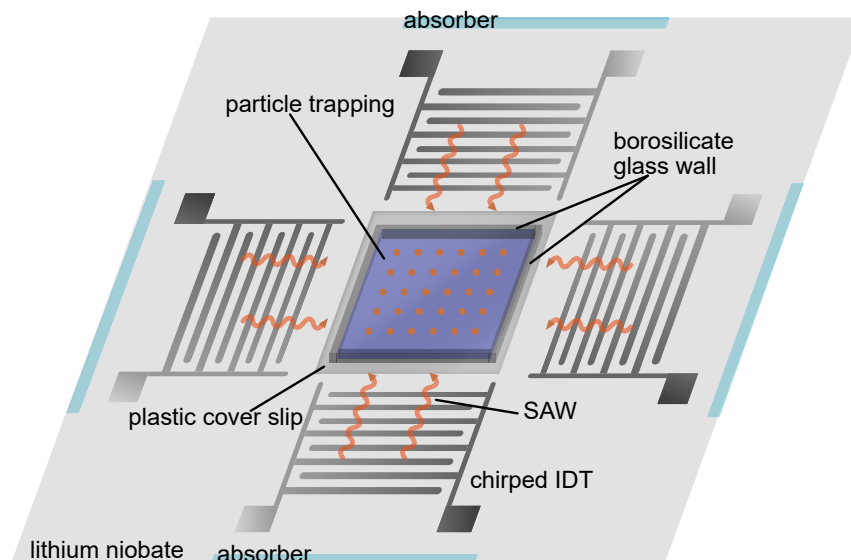
Figure 3.11: A schematic graph of the 2D alignment device. Four-way chirped IDTs create a series of regular pressure nodes where particles are entrapped.

We present particle alignment and patterning with adjustable spacing driven by the SAW board. Two pairs of chirped IDTs with resonance frequencies in the range 40–80 MHz were fabricated around a 6 mm by 6 mm closed glass chamber 100 μm in height (*see* Fig. 3.11). Fluorescent polymer particles 2.1 μm in diameter were aligned in various patterns based on the signals generated with the SAW board. When only one pair of IDTs, as shown in Fig. 3.12(a) and (b), are powered at 40.2 MHz, the particles are aligned in lines with 48.5 μm separation, close to one half the SAW wavelength (49.9 μm); this wavelength is the relevant one as the particles are near the substrate [307]. When all four IDTs are actuated, particles assemble around nodal points to form an equally spaced array. With the chirped IDT, the spacing may be adjusted by changing the frequency. Fig. 3.12(c), (d) and (e) display the arrays at 40.2 MHz, 59.8 MHz and 79.4 MHz, respectively, resulting in 48.3 μm, 34.1 μm and 25.3 μm spacing. A comparison of

results obtained with the SAW board and with the benchtop equipment are given in Table 3.1, which shows nearly identical results. This capability closely mimics that demonstrated by Shi *et al.* where 2 μm particles were aligned to a grid with $\sim$50 μm spacing in a matter of seconds[308].
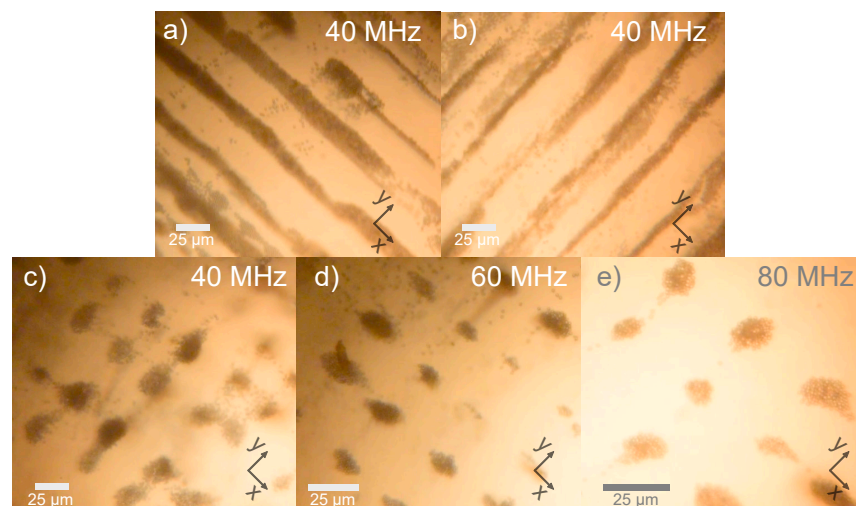
Figure 3.12: When only two IDTs are actuated, particles are aligned in lines along (a) the *x* direction or (b) the *y* direction depending on which pair of IDTs are actuated (in this case at 40.2 MHz). When 4 IDTs are actuated at the same time, particles are aligned in an array with different separations at corresponding frequencies: (c) 40 MHz, (d) 60 MHz and (e) 80 MHz. Scale bar: 25 μm.

Table 3.1: Comparison of handheld device and regular signal generator.

	Handheld device	Signal generator
Frequency (MHz)	40.2	40.2
Voltage output	70%	1.69 V
Oscilloscope read	2.1 V	2.1 V
Response time	7.0 s	6.8 s
Spacing (μm)	48.3	49.1

3.1.4 Conclusions

Acoustofluidics devices have—for far too long—betrayed the ideal of "lab-on-a-chip", bringing instead to mind the tired old joke "chip-in-a-lab" from all the signal generation and monitoring equipment tethering the devices to a lab bench just to get them to function. No

longer. Acoustofluidics may now be used in practical lab-on-a-chip and point-of-care devices with the circuit design information and simple examples provided in this paper. Our aim in this contribution is to enable those trained merely in the basics of electrical circuits to be able to devise and fabricate a design for their needs. Our approach is suitable for providing controlled signals to drive 1–300 MHz acoustic devices from 50 mW to 2 W of power and, with some work by the reader, these ranges may be greatly expanded while maintaining either the mains or battery-powered, handheld format needed in many applications. Using the design principles espoused in Section 3.1.2, we have demonstrated a completely handheld, battery-powered acoustic device driver (the TM board) for a high-power application: atomization. We have also demonstrated a mains-powered design (the SAW board) with a computer interface useful for monitoring and controlling the operation of the driver circuit, including the power and frequency of the signal supplied to the acoustic device. This design was used for acoustic devices to produce liquid mixing, particle separation, and particle alignment exemplifying many of the operations needed in micro to nano-scale fluidics devices.

During these tests, these driver boards delivered signals equivalent to the much larger benchtop or rack-mount laboratory signal generation, amplification, and monitoring equipment in use in many researchers' laboratories. Crucially, these driver boards *also* offer resonance tracking, power management, and signal monitoring features absent in laboratory equipment and necessary in the unpredictable clinical and industrial environments where these devices will be used. Together, these implementations show how almost any embodiment of acoustofluidic research could be miniaturized and rendered conveniently portable.

3.1.5   Acknowledgement

for Handheld Acoustofluidics", Lab on a Chip 21.7 (2020): 1352-1363. The dissertation author was the co-primary investigator and author of this paper.

3.2 Fabrication and Characterization of thickness mode piezoelectric devices

We present a technique to fabricate simple thickness mode piezoelectric devices using lithium niobate (LN). Such devices have been shown to atomize liquid more efficiently, it terms of flow rate per power input, than those that rely on Rayleigh waves and other modes of vibration in LN or PZT. The complete device is composed of a transducer, a transducer holder, and a fluid supply system. The fundamentals of acoustic liquid atomization are not well known, so we also present techniques to characterize the devices and to study the phenomena. Laser Doppler vibrometry (LDV) provides vibration information essential in comparing acoustic transducers and, in this case, indicates whether a device will perform well in thickness vibration. It can also be used to find the resonance frequency of the device, though this information is obtained more quickly via impedance analysis. Continuous fluid atomization requires careful fluid supply and we present such a method. Once the device is characterized and complete, the dynamics involved can be studied with high-speed imaging and the droplet size distribution can be measured with laser scattering. Fabrication of piezoelectric thickness mode transducers via DC sputtering of plate electrodes on lithium niobate is described. Additionally, reliable operation is achieved with a transducer holder and fluid supply system and characterization is demonstrated via impedance analysis, laser doppler vibrometry, high-speed imaging, and droplet size distribution using laser scattering.

3.2.1   Introduction

Ultrasound atomization has been studied for almost a century and although there are many applications, there are limitations in understanding the underlying physics. The first description of the phenomenon was made by Wood and Loomis in 1927 [309], and since then there have been developments in the field for applications ranging from delivering aerosolized pharmaceutical fluids [310] to fuel injection [311]. Although the phenomenon works well in these applications, the underlying physics is not well understood [312, 313, 314].

A key limitation in the field of *ultrasonic* atomization is the choice of material used, lead

zirconate titanate (PZT); a hysteretic material prone to heating [315] and lead contamination with elemental lead available from the inter-grain boundaries [316, 317]. Grain size and mechanical and electronic properties of grain boundaries also limit the frequency at which PZT can operate [318]. By contrast, lithium niobate is both lead-free and exhibits no hysteresis [319], and can be used to atomize fluids an order of magnitude more efficiently than commercial atomizers [320]. The traditional cut of lithium niobate used for operation in the thickness mode is the 36-degree Y-rotated cut, but the 127.86-degree Y-rotated, X-propagating cut (128YX), typically used for surface acoustic wave generation, has been shown to have a higher surface displacement amplitude in comparison with the 36-degree cut [266] when operated in resonance and low loss. It has also been shown that thickness-mode operation offers an order of magnitude improvement in atomizer efficiency over other modes of vibration [266], even when using LN.

The resonance frequency of a piezoelectric device operating in the thickness mode is governed

by its thickness, t: the wavelength $\lambda = 2t/n$ where $n = 1, 2, \ldots$ is the number of anti-nodes. For a 500 μm thick substrate, this corresponds to a wavelength of 1 mm for the fundamental mode, which can then be used to calculate the fundamental resonance frequency, $f = v/\lambda$ if the wave speed, v, is known. The speed of sound through the thickness of 128YX LN is approximately 7000 m/s, and so $f = 7$ MHz. Unlike other forms of vibration, particularly surface-bound

modes, it is straightforward to excite higher-order thickness-mode harmonics to much higher frequencies, here to 250 MHz or more, though only the odd-numbered modes may be excited by uniform electric fields [321]. Consequently, the first harmonic ($n = 2$) near 14 MHz cannot be excited, but the second harmonic at 21 MHz ($n = 3$) can. Fabrication of efficient thickness mode devices requires depositing electrodes onto opposing faces of the transducer. We use *direct current* (DC) sputtering to accomplish this, but electron-beam deposition and other methods could be used. Impedance analysis is useful to characterize the devices, particularly in finding the resonance frequencies and electromechanical coupling at these frequencies. Laser Doppler vibrometry (LDV) is useful to determine the output vibration amplitude and velocity without contact or calibration [322], and, via scanning, the LDV provides the spatial distribution of surface deformation, revealing the mode of vibration associated with a given frequency. Finally, for the purposes of studying atomization and fluid dynamics, high-speed imaging can be employed as a technique to study the development of capillary waves on the surface of a sessile drop [323, 324]. In atomization, small droplets are produced at a rapid rate, over 1 kHz in a given location, too quickly for high-speed cameras to observe with sufficient fidelity and field of view to provide useful information over a sufficiently large droplet sample size. Laser scattering may be used for this purpose, passing the droplets through an expanded laser beam to (Mie) scatter some of the light in reflection and refraction to produce a characteristic signal that may be used to statistically estimate the droplet size distribution.

It is straightforward to fabricate piezoelectric thickness-mode transducers, but the techniques required in device and atomization characterization have not been clearly stated in the literature to date, hampering progress in the discipline. In order for a thickness-mode transducer to be effective in an atomization device, it must be mechanically isolated so that its vibration is not damped and it must have a continuous fluid supply with a flow rate equal to the atomization rate so that neither dryout nor flooding occur. These two practical considerations have not been thoroughly covered in the literature because their solutions are the result of engineering techniques rather

than pure scientific novelty, but they are nonetheless critical to studying the phenomenon. We present a transducer holder assembly and a liquid wicking system as solutions. Our protocol offers a systematic approach to atomizer fabrication and characterization for facilitating further research in fundamental physics and myriad applications.

3.2.2   Protocol

1.   Thickness-mode device fabrication via DC sputtering

1.1   Wafer preparation

1.1.1   Place a 100 mm 128YX LN wafer in a clean PYREX dish of at least 125 mm diameter. Sonicate the wafer in at least 200 mL of acetone for 5 minutes.

1.1.2   Repeat sonication with isopropyl alcohol and again with de-ionized water for 5 minutes each.

1.1.3   Remove visible water from the surface using dry nitrogen.

1.1.4   Completely remove water from the surface by placing the wafer on a hotplate at 100° for 5 minutes. Ensure that there is a sheet of aluminum foil on the hotplate as this helps in dissipation of charge build up on the wafer.

1.2   Electrode deposition

1.2.1   Place the wafer in the vacuum chamber of the sputter deposition system and pump down the chamber to 5×10^{-6} mtorr. Set the argon pressure to 2.3 mTorr and the rotation speed to 13 rpm.
        NOTE: If parameters for the specific instrument being used have been established that result in high quality films, then use those instead.

1.2.2   Deposit 5–10 nm of titanium at 1.2-1.6 A/s.

NOTE: Before beginning this process with the intended wafer, test the deposition rate with the plasma power set to 200 W and depositing for 1 minute. Then measure the height of the layer with a profilometer. Do this separately for each metal. Set the power according to this test in order to achieve the stated deposition rate.

1.2.3 Deposit 1 μm of gold at 7-9 A/s.

NOTE: Deposition at a higher rate due to increased plasma power or increased argon partial pressure may reduce film quality.

1.2.4 Remove the wafer and repeat steps 1.2.1–1.2.3 for the second side of the wafer.

1.3 Dicing

1.3.1 Use a dicing saw to dice the entire wafer as needed.

NOTE: A protective resist can be applied on the substrate prior to dicing, and our system uses a UV curable film just before the samples are loaded on the dicing stage. We have found that dicing the samples with an automated dicing saw does not compromise the integrity of the samples. Hand-scribe dicing of LN is possible, though tedious and prone to inconsistencies.

2. Make electrical and mechanical contact with the transducer. We provide several methods below from which to choose. Later in the protocol we highlight which method is most appropriate for each subsequent step.

2.1 Place the transducer flat on a magnetic steel plate. Mount one pogo-probe in contact with the plate and another pogo-probe in contact with the top surface of the transducer. Hereafter this will be referred to as pogo-plate contact.

2.2 Place the transducer between two pogo-probes. Hereafter referred to as pogo-pogo

contact.

2.3   Solder wire to each face of the transducer. Hereafter referred to as solder contact.

2.4   Assemble a custom transducer holder

2.4.1 Order the custom PCBs whose gerber files have been provided.

2.4.2 Solder the contacts to the custom PCBs.

2.4.3 Press fit the spikes into the plated holes on the custom PCBs such that they point away from each other.

2.4.4 Connect the two custom PCBs with board spacers and screws so that the contacts are just in contact with each other. Adjust the spacing with plastic washers if necessary.

2.4.5 Slide a 3x10 mm transducer in between the inner pair of contacts. Clip the outer contacts so they do not short the circuit. Fig. 3.13 shows the entire assembly.

3.   Resonance frequency identification via impedance analysis

3.1   Ensure that a port calibration has been performed according to the manufacturer's instructions for the specific contact method being used.

3.2   Connect a transducer to the open port of the network analyzer with one of the above contact methods.
       NOTE: It can be instructive to repeat this analysis with multiple electrical contact methods and compare the results.

3.3   Select the reflection coefficient parameter, s_{11}, via the user interface and choose the frequency range of interest.
       NOTE: s_{11} is the input reflection coefficient and has a minimum value at the

resonance frequency of operation. For a typical 500 μm thick 128YX LN wafer, the primary resonance frequency will be near 7 MHz and the second harmonic will be near 21 MHz, as illustrated in Fig. 3.14.

3.4 Perform the frequency sweep by selecting the option on the system display.
NOTE: The impedance plot in frequency space displayed on the instrument will exhibit local minima at the resonance frequencies.

3.5 Export the data for closer inspection using data processing software to identify the precise minima locations.

4. Vibration characterization via LDV

4.1 Place a transducer in pogo-plate contact on the LDV stage. Connect the pogo-probe leads to the signal generator. Ensure that the correct objective is selected in the PSV acquisition software and focus the microscope on the surface of the transducer.

4.2 Define the scan points by selecting the 'Define scan points' option or proceed to the following section if performing a continuous scan.

4.3 Select the 'Settings' option and under the 'General' tab, select either the 'FFT' or 'Time' option depending on whether the scan is being performed in frequency or time domain. Select the number of averages in this section.
NOTE: The number of averages affects scan time.

4.4 In the 'Channel' tab, make sure that the 'Active' boxes are checked. These correspond to the reference and reflected signal from the transducer. Adjust the reference and incident channels in order to obtain maximum signal strength from the substrate.

4.5 In the 'Generator' tab, if the measurement is carried out under single frequency signal, select "Sine" from the 'Waveform' pull down list; if it is under a band signal,

select 'MultiCarrierCW'.

4.6 Change the bandwidth and FFT lines in the 'Frequency' tab to adjust the scan resolution for a frequency domain scan. Similarly, change the 'Sample Frequency' in the 'Time' tab when performing time domain measurements.

4.7 The PSV Presentation software can be used to process and analyze the data obtained from the scan. A typical displacement spectrum is provided in Fig. 3.15.

5. Fluid supply

5.1 Obtain a 25 mm long, 1 mm diameter wick composed of a bundle of fibers of a hydrophilic polymer designed to transport aqueous liquid across its length such as those available for plug-in air fresheners.

5.2 Insert the wick into a syringe tip with an inner diameter that provides a snug fit and a length that allows the wick to extend 1-2 mm beyond each end. Lock the tip onto a syringe with the desired capacity—between 1 and 10 milliliters.

5.3 Mount the wick/syringe assembly such that the wick is $10°$-$90°$ from horizontal (depending on the desired atomization rate, which also depends on the applied voltage) and the tip of the wick is just in contact with the edge of the transducer as shown in Fig. 3.13

5.4 Fill the syringe with water and apply a continuous voltage signal at the resonance frequency determined using the impedance analyzer.

5.5 Adjust the voltage level until the liquid is atomized continuously without the device flooding or drying out.

6. Dynamics observation via high-speed imaging

6.1 Rigidly mount a high-speed camera horizontally on an optical table, place a trans-ducer in either pogo-pogo contact or pogo-plate contact on an x-y-z stage near the focal length of the camera, and position a diffuse light source at least one focal length on the opposite side of the transducer from the camera.

6.2 For the case of pogo-pogo contact, position the fluid supply so that it does not block the camera view or the light source. Or, for the case of pogo-plate contact, apply fluid directly to the substrate with a pipette.

6.3 Adjust the camera focus and the x-y-z position to bring the fluid sample into sharp focus.

6.4 Estimate the frequency of the specific phenomenon you wish to study based on your current knowledge of the field. Choose a frame rate at least twice as large as this frequency according to the Nyquist rate in order to avoid aliasing.
NOTE: For example, we are interested in capillary waves that occur on a sessile drop at a range of frequencies. Our camera is limited in its spatial resolution, so that we can only distinguish waves with a minimum amplitude. In this case our minimum amplitude occurs around 4 kHz so we choose 8,000 fps.

6.5 Adjust the light intensity, the camera shutter, or both in order to optimize contrast between the fluid and the background.
NOTE: An opaque dye can be added to the fluid in order to increase the contrast.

6.6 Connect alligator clips from the amplified signal generator to the pogo-probes leads.

6.7 Capture video in the camera software simultaneously with actuation via the voltage signal either by manually triggering both at the same time or by connecting a trigger out-put from your signal generator to your camera.

NOTE: Typical frame rate used is 8,000 frames per second and a CF4 objective.

6.8 Save only the frames containing the phenomenon to avoid wasted storage, which is particularly relevant at large frame rates, to produce a result as shown in Fig. 3.16. NOTE: Make sure to save the file in a format that is compatible with your image processing software of choice so that useful data can be extracted.

7. Droplet size measurement via laser scattering analysis

7.1 The laser scattering system should have a module that transmits the laser and one that receives the scattered laser signal. Position these, along the rail provided with the system, with a 20-25 cm gap between them.

7.2 Rigidly mount a platform in this gap such that, when the transducer and fluid supply assemblies are placed on it, atomized mist will be ejected into the laser beam path. This alignment is facilitated by turning on the laser beam, 'Tools' ¿ 'Laser Control...' ¿ 'Laser on', as a visual indicator.

7.3 Fix the transducer holder to the platform and fix the fluid supply assembly to an articulated arm (such as those made by Fisso). Position the fluid supply assembly so that the tip of the wick is just in contact with the edge of the transducer.

7.4 Create an SOP in the software by clicking the 'New SOP' icon. Configure the SOP with the following settings: template ¿ 'Default continuous', Sampling period (s) ¿ '0.1', under "Data handling" click 'Edit...' and set Spray profile ¿ Path length (mm) to '20.0', 'Alarms' ¿ uncheck 'Use default values' and set 'Min transmission (%)' to '5' and '1' and set 'Min scattering' to '50' and '10'. Leave all other settings as defaults.
NOTE: Consult the software manual that came with the instrument.

7.5   Start the measurement within the software by clicking 'Measure' ¿ 'Start SOP' and selecting the SOP created above and following the onscreen guidelines. Fill the fluid supply reservoir, the syringe, with water up to the desired level and note the volume. Turn on the voltage signal to begin atomizing the fluid after the measurement has started and begin a stopwatch.

7.6   The software generates a size distribution based on the scattered laser signal at the receiver due to Mie theory and a multiple scattering algorithm. Once the desired volume of fluid has been atomized, turn of the voltage signal, end the stopwatch, and record the final volume.

NOTE: The atomization flow rate can simply be calculated by dividing the volume by the time duration.

7.7   In the measurement histogram, select the portion of the data during which the atomization was occurring as expected and the signal at the receiver was strong enough to be statistically significant.

NOTE: All measurements with this technique are statistical averages and thus, if there are too few droplets, then the scattered signal will be weak and the measurement will be statistically insignificant.

7.8   Click the 'Average' icon and click 'Ok' to generate a distribution based on the selected data. Save this by selecting the window and clicking 'Edit' ¿ 'Copy text' then pasting the result in a text file and saving with an appropriate name. This distribution data can now be used with other software, for example to create the plot in Fig. 3.17 via MatLab.
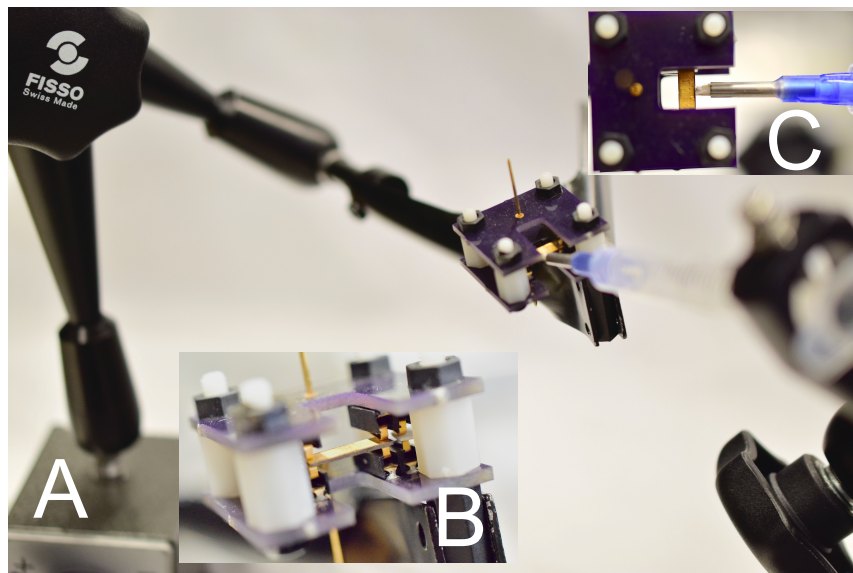
Figure 3.13: The positions of the transducer holder and the fluid supply assembly are each controlled with articulating arms such that the tip of the wick is just in contact with the edge of the transducer(A). Inset (B) reveals nature of the electrical and mechanical contact with the transducer electrodes. Inset (C) reveals the nature of the contact between the transducer edge and the fluid wick.

3.2.3 Representative Results

We fabricated thickness mode piezoelectric devices from 128YX lithium niobate. Fig. 3.13 shows a complete assembly to hold the transducer in place with a custom transducer holder used with the passive fluid delivery system we have developed for continuous atomization. The characterization steps for these devices include determination of the resonant frequency and harmonics using an impedance analyzer Fig. 3.14. The fundamental frequency of the devices was found to be close to 7 MHz using the technique described in this protocol, as predicted by the thickness of the substrate. Further characterization of substrate vibration was performed using non-contact laser doppler vibrometer measurements. These measurements determine the magnitude of displacement of the substrate and is usually in the nm range Fig. 3.15. Continuous atomization is essential to enable practical applications of thickness mode devices, and we have demonstrated this by developing a passive fluid delivery system to the substrate. Finally, we describe two techniques to observe droplet vibration and atomization dynamics by performing
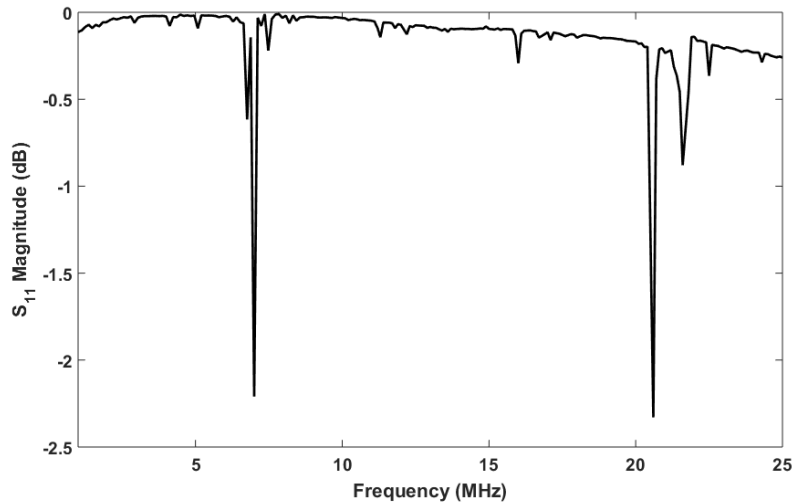
Figure 3.14: The real s_{11} scattering parameter values measured over a range of 1–25 MHz for a 127.86° YX lithium niobate device, indicating the presence of a resonance peak at approximately 7 MHz.

high-speed imaging and by measuring droplet size distribution as shown in Fig. 3.16 and Fig. 3.17.

3.2.4 Discussion

The dimensions and aspect ratio of a transducer affects the vibration modes it produces. Because the lateral dimensions are finite, there are always lateral modes in addition to the desired thickness modes. The above LDV methods can be used to determine dominant modes in the desired frequency range for a given transducer. We have found that a square with dimensions below 10 mm typically gives a close approximation to a thickness mode. Three by ten millimeter rectangles also work well. Supplementary videos SV1 and SV2 show LDV area scans of the square and the 3x10 transducers showing that they're close to thickness mode. These have been empirically determined rather than selected by simulation and design, though such methods could be used to find ideal lateral dimensions.

The method of electrical and mechanical contact with the transducer also affects the vibrations
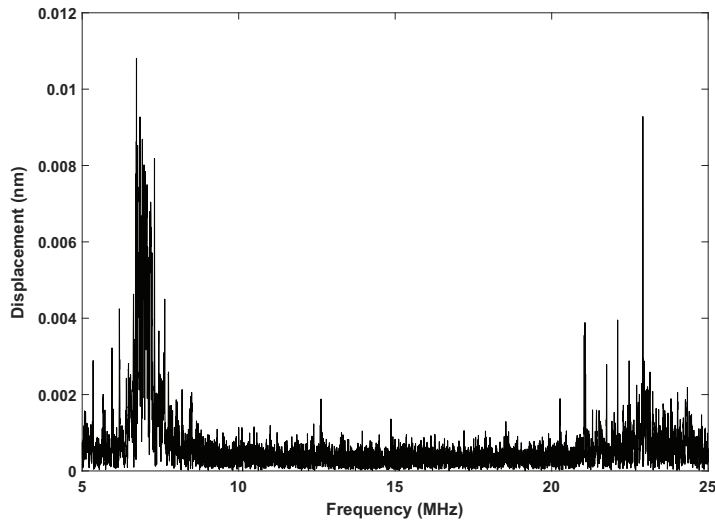
Figure 3.15: A multi-carrier, FFT scan with 5 averages at each point was performed over 9 by 9 scan points defined in a 0.6 by 0.6 mm area in the frequency range 5–25 MHz. The reported displacement is the maximum displacement averaged over all points. The fundamental thickness mode for 0.5 mm thick LN can be seen at 7 MHz, and a weaker second harmonic is present at ≈21 MHz. Notice there are multiple narrow peaks at each resonance due to interference with lateral modes. Multi-carrier scans spread the voltage input, so the displacement here is not an accurate measure of the performance of the device. For such a measurement, it is recommended to perform a single-frequency scan at the resonance frequency and with application relevant voltages. For example, this 10 by 5 mm thickness mode transducer produces a 5 nm max amplitude at 45 Vpp when driven at 6.93 MHz.

it produces since these are the boundary conditions to which the piezoelectric plate is subject. We have performed an impedance spectrum for three measurement techniques - pogo-plate, pogo-pogo, and transducer holder as a comparison and confirmed the resonance peak locations are not changed in this case by our choices of contact. We do note that mechanical contact between the transducer and a plate surface dampens vibrations making atomization less efficient. We use pogo-plate contact in the case of LDV measurements, because this is the simplest way to get a flat, stationary surface on which to focus the laser.

The fluid supply assembly described here relies on capillary action and gravity to passively

resupply the transducer with a thin film of water as it is atomized away. The vibration of the transducer produces a acoustowetting effect that can be enough to create a thin film and avoid

136
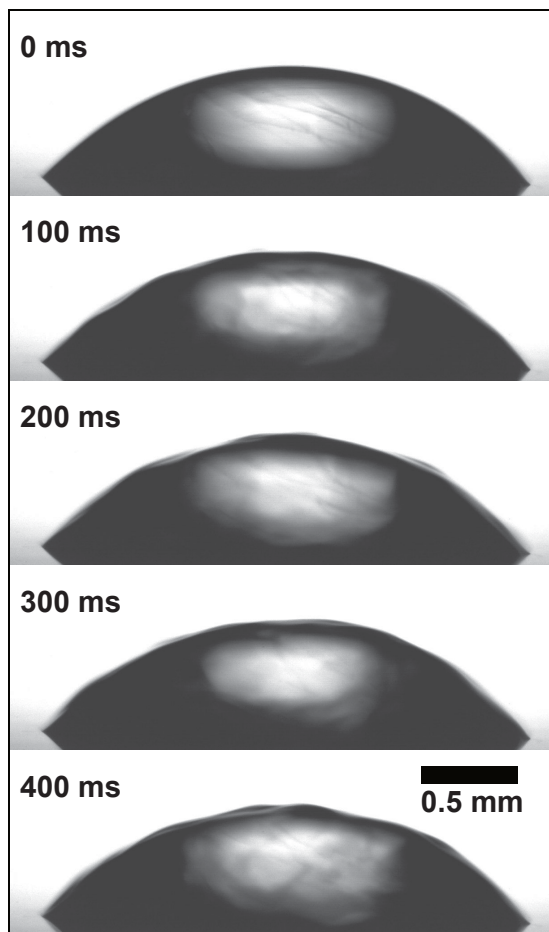
Figure 3.16: Onset of capillary waves on a 2 μL water drop is indicated by an 8000 fps video of the fluid interface; the drop is driven by a thickness mode transducer driven at 6.9 MHz, showing the significant time difference between the hydrodynamic response and the acoustic excitation.
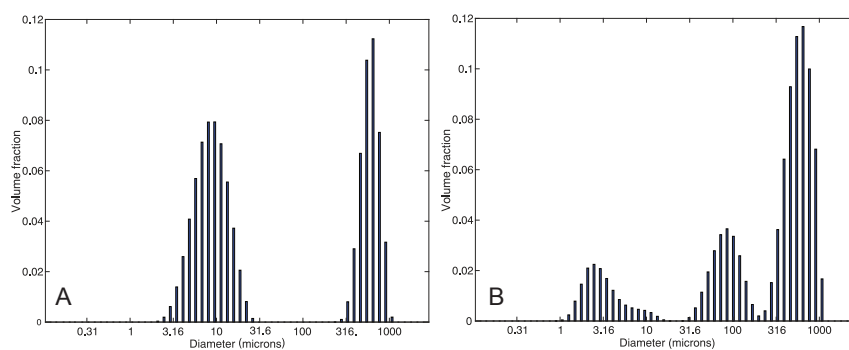
Figure 3.17: Droplet size distribution is typically measured as a volume fraction versus the droplet diameter, here comparing (A) a commercial nebulizer and (B) an LN thickness mode device, both using water.

137

flooding, but in some cases a hydrophilic treatment will be necessary on the transducer surface. If continuous atomization is not achieved, this is the most likely route to resolving the problem.

Measurements were performed with a UHF–120 from Polytec here, but other LDVs may be used. Electrical contact can be made by soldering a wire to each face of the transducer, though the solder can significantly alter the resonance frequencies and modes of the transducer. Another technique is to place the transducer on a metal base and use "pogo" spring contact probes pressed into contact on the top face of the piezoelectric transducer element while it sits flat upon the stage, useful when a large area has to be scanned. Accurate measurement of the resonance frequencies is important to efficiently operate the transducer and maximize energy throughput to mechanical motion at these frequencies. A frequency scan using the LDV provides this information, but requires a long time, on the order of tens of minutes. An impedance analyzer can determine the resonance frequencies much more quickly, often less than a minute. However, unlike the LDV, the impedance based measurement does not provide information on the vibration amplitude at the resonance frequencies, which is important in determining fluid atomization off the surface of the transducer.

Though vibration of the substrate occurs in the 10–100 MHz regime, the dynamics of fluids in contact with the substrate occur at far slower time scales. For example, capillary waves on the surface of a sessile drop are observable at 8,000 fps, assuming that the spatial resolution of the camera can distinguish the amplitude of a wave crest and that the wave frequency of interest is below 2,000 Hz. The camera arrangement described above images transmitted light and thus is good for observing the outline of objects that transmit light differently than air. If insufficient, a reflected or fluorescent light arrangement may be required. The exposure time for each frame decreases as the frame rate is increased so the light intensity must be increased accordingly. The objective lens should be chosen based on the length scale of the phenomenon under study, but the above protocol will work with any commonly available magnification. As an example, Fig. 3.16

138

was obtained with the above high-speed video method. The contrast at the drop interface would allow these frames to be segmented in software (imageJ and MATLAB) so that the interface dynamics may be tracked over time.

In our droplet sizing equipment (Malvern Spraytec), the laser optics and scattering detectors are relatively standard but the software is proprietary and complex. In addition to Mie theory, multiple scattering events make droplet size and enumeration calculations much more difficult. Mie theory assumes that most photons are scattered only one time, but when droplets are densely spaced, i.e. the spacing between droplets is not much larger than the droplets themselves, and the spray plum covers a sufficiently large area, then this assumption fails[325]. As an example of troubleshooting results from this instrument, consider Fig. 3.17. Notice that the 0.5 mm diameter peak appears in both distributions. The commercial nebulizer is known to produce monodisperse droplets near $10\ \mu$m, so the larger peak is likely either a false result due to the large amount of multi-scattering events or agglomeration of smaller droplets within the spray. This implies that the large peak in the thickness mode distribution may also be a false result. This can be directly verified by high-speed video: such large droplets would be readily visible, but we do not observe them in this case.

Laser scattering particle size analysis can also be difficult when the scattering signal becomes weak. This is typically due to a low atomization rate or when part of the spray does not pass through the laser path. A weak vacuum may be used to draw the complete atomized mist through the expanded laser beam of the equipment in cases where it would otherwise escape measurement. For even greater control of spray conditions a humidity chamber can be installed around the laser beam path, but we have not found that to be absolutely necessary.

3.2.5 Acknowledgement

3.3   Portable atomization device design and performance

Megahertz frequency acoustofluidic nebulization offers several advantages over current technology for delivering therapeutic proteins, cells, functionalized nanoparticles, and monoclonal antibodies to the lungs[222, 219, 223]. It is cheaper and less prone to clogging than the current state-of-the-art, ultrasonic mesh nebulizers. These operate at much lower frequencies and in order to generate droplets small enough for optimal lung delivery, and they must rely on 5 μm laser-cut holes in a metal plate through which a drug solution is forced[326, 327]. Mesh nebulizers tend to be tailored to work with a particular solution and have a limited range of fluids that they will nebulize. Mesh nebulizers in general may cause damage to biomolecules due to high shear forces and kHz-order frequency operation[328, 329]. By contrast, acoustofluidic nebulization has been demonstrated for delivery of antibodies[294, 295] and DNA[222]. There is also some evidence— in unpublished work—that the droplet size can be adjustable during device operation. This could be necessary either between patients, for example adults and children, or in compensation for the changing airflow during inhalation and exhalation. These aspects are important in seeking appropriate dose control in pulmonary delivery[222].

However, MHz-frequency nebulization is only competitive with mesh nebulizers if it can be decoupled from benchtop equipment, enabled for the first time with the TM board (Fig. 3.18). A previous attempt at such a circuit[220] did not provide sufficient power for consistent atom-

ization, even with signal modulation intended to reduce the average power consumption[281]. Furthermore, this circuit could drive transducers at only a single, predetermined frequency, and had a short lifetime of a few hours.

We present a handheld nebulizer based on a lithium niobate TM transducer, which has been shown to produce higher efficiency atomization (flow rate per unit power input) than either SAW or other wave types in lithium niobate or TM in lead zirconate titanate (PZT)[266]. We drive the 3x10 mm TM lithium niobate transducers at their primary resonance frequency as indicated in Fig. 3.2, usually 6.6 MHz. The device consists of a transducer holder, a fluid supply system, and the TM board powered by a rechargeable lithium-ion battery (Fig. 3.18). The user interface consists of a power switch and five buttons: resonance frequency algorithm run, switch on or off, amplitude increase, amplitude decrease, and reset. The transducer holder provides electrical contact while minimizing mechanical damping of the acoustic waves. A video provided in the ESI † demonstrates operation of the nebulizer.

Liquid is wicked from a reservoir through a fibrous nib onto the transducer surface. A physically hydrophilic region is ablated onto the surface of the transducer using an excimer laser (LaserShot, Optec, Belgium). This hydrophilic region and the capillary action of the nib help draw liquid out in a thin layer over the transducer. While the transducer is vibrating, acoustowetting provides additional flow forcing[330], leading to a semi-passive liquid supply system that ensures liquid is only drawn out during nebulization, which prevents flooding and drying out of the transducer surface. No active pumping mechanism is required.

We compare the performance of our 6.6 MHz handheld nebulizer to an equivalent atomization set-up with a benchtop signal generator and amplifier. The benchtop set-up can deliver greater power inputs and produces a pure sine wave voltage signal, which often produces a cleaner acoustic wave. The handheld device uses a square wave, which significantly reduces the complexity of the circuit, thus allowing it to fit in a smaller footprint and reducing development time and cost. More frequency modes are generally excited by a square wave, but we show that
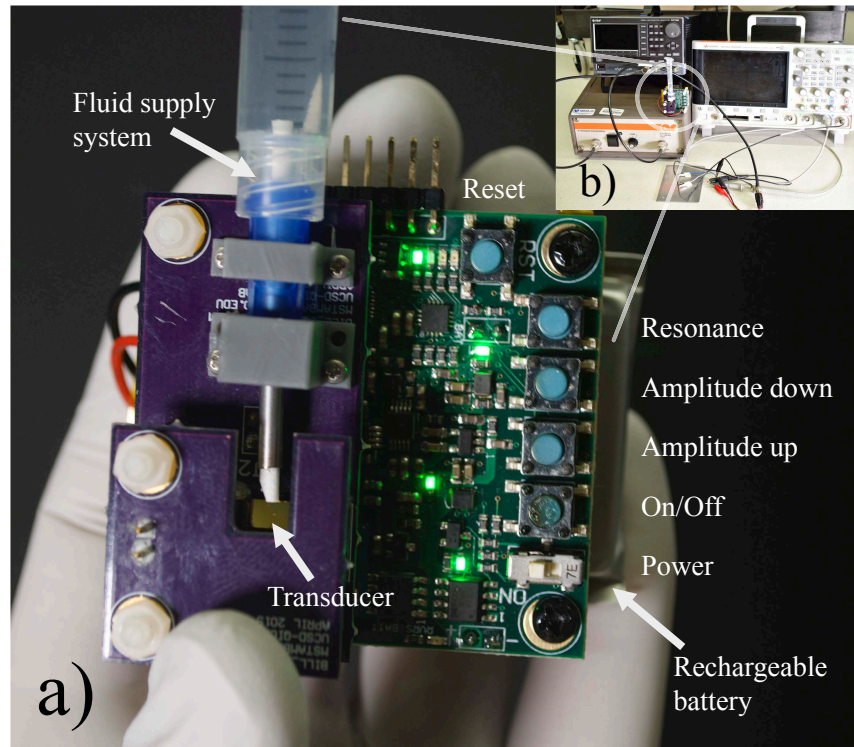
Figure 3.18: (a) Major components of the handheld nebulizer are labeled along with the user interface. (b) Benchtop equipment—including signal generator, amplifier, oscilloscope, cables, and connections—typical of the acoustofluidic device experience—is entirely replaced by our small, inexpensive, and portable circuit.

TM nebulization performance is unaffected. Figure 3.19(a) demonstrates that the droplet size distribution for water is not significantly affected by the voltage signal waveform. The maximum flow rate for a given power input, again, using water, is similar between the handheld and benchtop devices (Fig 3.19(b). These results are the same order of magnitude for maximum flow rate compared with the literature—Winkler *et al.* report 0.2 mℓ/min at 3.5 W for SAW[331] and Collignon *et al.* report 0.3 mℓ/min at 1.4 W for TM[266], all with water (though the latter does report a broader range of fluids). The majority of the atomized water volume occurs in droplets less than 10 μm, ideal for pulmonary drug delivery. The power output of the handheld device is currently limited by a maximum voltage of 22 V (equivalent to ∼2 W in this case), which is sufficient for all but the most demanding acoustofluidics applications. It may be increased, but such an increase must be balanced against the cost and time of further development and any size

or battery constraints.
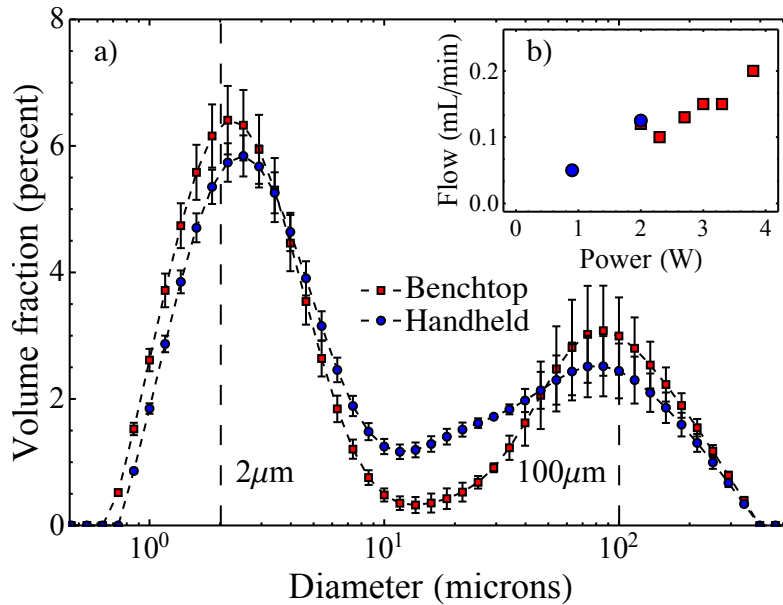
Figure 3.19: (a) Droplet size distributions were obtained using a laser diffraction particle sizer (Spraytec, Malvern). Three measurements were taken for both the benchtop set-up and the handheld device and the mean values and standard errors are reported. Identical electrical/mechanical contact and fluid supply was used in each case and in each case the transducer was driven at 6.6 MHz and 2 W. Notice that the distribution is in terms of volume fraction so that a small number of large droplets produces a relatively large peak—the vast majority of droplets are close to 2 μm. (b) For experiments in this plot alone, for the purpose of accuracy, flow rates were imposed using a syringe pump. The power was adjusted until atomization was sustainable—no sputtering and no flooding. Again the transducer contact and fluid supply were identical in both the benchtop set-up and the handheld device.

3.3.1 Acknowledgement

This section, in part, is a reprint of the materials as it appears in Lab on a Chip, 2020. An Huang and William Connacher, Mark Stambaugh, Naiqing Zhang, Shuai Zhang, Jiyang Mei, Aditi Jain, Sravya Alluri, Vincent Leung, Anushi Rajapaksa, and James Friend, "Practical Microcircuits for Handheld Acoustofluidics", Lab on a Chip 21.7 (2020): 1352-1363. The dissertation author was the co-primary investigator and author of this paper.

Chapter 4

Investigations of capillary wave turbulence with digital holographic microscopy

4.1 Identification of weakly- to strongly-turbulent three-wave processes in a micro-scale system

We study capillary wave turbulence (WT) inherently spanning multiple dynamical regimes and geometries—from weakly to strongly nonlinear WT (SWT) and from shallow to deep domains—all within a $40\,\mu L$ volume. These conditions violate idealizations used in modern WT theories. This study is now viable with recent advances in ultra-high-speed digital holographic microscopy, providing 10-μs time and 10-nm spatial resolutions for images across the entire field of view, encompassing a complete wave system. We derive tractable parameters permitting direct identification of four fundamental WT regimes, all present in this system. A proposed nonlinearity measure permits comparative analysis over varied inputs. Results indicate SWT precedes ultrasonic atomization and promote further SWT study toward improving applications like fuel combustion and ultrasonic nebulization. This work augments current understanding of WT regimes and behaviors, and directly applies to many fields beyond fluid mechanics.

4.1.1 Introduction

A variety of applications, from ink jet printing to fuel combustion, depend on rapid, monodisperse droplet production [332, 333]. Many depend on atomization to produce micron-sized droplets from small fluid volumes [334]. Leveraging extraordinarily large accelerations, high-frequency ultrasound (HFUS) (MHz+) extends atomization's utility to broader ranges of fluid parameters. However, precision lacks due to an incomplete understanding of HFUS-driven atomization. Highly stochastic, generally non-Gaussian turbulent capillary wave fields preceding aerosol dispersal are a key source of theoretical ambiguity.

Classical mechanisms of acoustically-driven interfacial waves are absent in HFUS-driven wave fields [335]. These mechanisms—first described by Faraday long ago [336]—exhibit a fundamental wavemode oscillating at one half the driving frequency and (super)harmonics at frequency-doubled intervals [337]. The power spectral density (PSD) for HFUS-driven waves reveals an isolated peak at the driving frequency and a procession of low-frequency peaks removed from the driving frequency by many orders of magnitude. When forcing magnitudes are increased above a threshold, low-frequency linear mode superpositions give way to energy cascades across essentially continuous distributions of wavenumbers [337, 335]. The hallmark of this turbulent cascade is a well-defined, monotonically decreasing, non-integer linear slope in the log-log PSD.

Wave turbulence (WT) is of great general interest arising in diverse contexts, from brain activity patterns [338] to optical wave propagation within nonlinear media [339]. In pioneering work, Zakharov and Filonenko [340] derive a kinetic equation—at third order in wave amplitudes—governing capillary WT cascades in unbounded basins by expanding the interfacial dynamics Hamiltonian. This equation governs conservative dynamics from the "inertial" range down to the beginning of the viscous "dissipation" range. They show that the stationary collision integral identity is satisfied by $n(k) \propto k^{-\gamma}$, where n is proportional to the square of the wave amplitude at wavenumber k. The system in Ref. [340] has $\gamma = 17/4$. Due to the governing kinetic equation, this is denoted "kinetic" WT (KWT). Strong WT (SWT), by contrast, is WT violating the weak
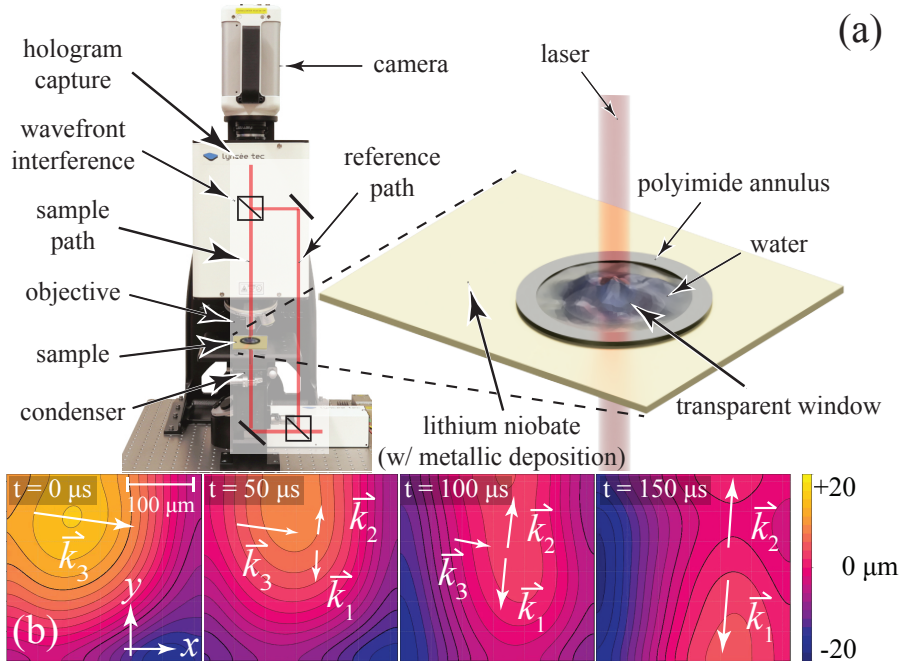
Figure 4.1: High-speed digital holographic microscopy of turbulent microscale capillary waves. (a): An interferometer using a 666 nm laser expanded to occupy the entire field of view of the optics produces phase and intensity patterns that encode 3D surface data recorded at 115.2 kfps. A 25 x 20 x 0.5 mm piezoelectric transducer, with a 6.4 mm window in the electrodes allowing laser passage, is driven at its resonant frequency of 7 MHz, causing vibration below a 725 μm deep fluid volume contained by a 9.5 mm diameter annulus. (b) Four frames from a typical holographic data set of interfacial dynamics depicts a typical three-wave interaction.

nonlinearity assumption.

Within finite geometries, WT behaviors deviate from the above ideal. Wavemodes form a countably infinite set and are designated "discrete" WT (DWT). Kartashova [341] shows that exact three-wave equations satisfied in capillary KWT become Diophantine in DWT and are equivalent to $x^3 + y^3 = z^3$, which has no solutions (*see* Fermat's Last Theorem). In the absence of exact resonances, waves build to finite amplitudes and satisfy nonlinear dispersion relations [342, 343] leading to quasi-resonant three-wave relations [344]:

$$|\omega_{k_1} \pm \omega_{k_2} - \omega_{k_3}| \leq \delta_{\mathrm{NRB}}, \tag{4.1a}$$

$$\mathbf{k}_1 \pm \mathbf{k}_2 - \mathbf{k}_3 = 0, \tag{4.1b}$$

where $\omega_{k_n} \triangleq \omega(\mathbf{k}_n)$. The parameter δ_{NRB} represents nonlinear resonance broadening (NRB) resulting from the finite-amplitude dispersion relation. In unbounded media, $\delta_{\mathrm{NRB}} = 0$ and exact resonances appear as arguments to Dirac combs within a collision integral. In finite media, $\delta_{\mathrm{NRB}} > 0$ and when large enough, the equations are satisfied by groupings of quasiresonances about exact modes. Modal broadening facilitates additional wave interactions and turbulent breakdown.

Small δ_{NRB} values generate arrested cascades called "frozen" turbulence. Pushkarev and Zakharov [343] show that this generates layered "wedding cake" distributions in wavenumber space [343, 344]. Connaughton *et al.* [344] predict a critical NRB value beyond which cascades advance indefinitely. Cascade advancement from larger forcing—called "sandpiling"—has been described by Nazarenko [345].

In real systems, DWT and KWT coexist [346, 347, 343, 348]. The dominance of either mechanism depends on wavenumber and forcing amplitude and can be classified: (i) at low powers and/or small wavenumbers, DWT dominates; (ii) at high powers and/or large wave numbers, KWT dominates; and (iii) at intermediate powers and/or intermediate wavenumbers,

a combination of DWT and KWT contribute to observations. We designate condition (iii) as intermediate WT (IWT).

The majority of liquid WT experiments are devoted to gravity waves; surface tension-dominant systems receive less attention. Work that *has* considered capillary waves generally takes place in deep water environments, often in the presence of gravity waves, and focuses on regimes where kinetic theory is approximately satisfied [349, 350, 351, 352, 353, 337]. Explicit consideration of finite-domain effects has remained mostly theoretical, with Pan and Yue [354] recently providing a framework to account for discreteness by extending earlier work in the kinetic theory of deep-water capillary waves [355, 356].

Here, we study a surface tension-dominated system where spatial scales are much smaller than the capillary length, $k_*^{-1} = \sqrt{\sigma/\rho g}$. The device geometry used in our experiments approximates the dimensions of moderately shallow, surface-wetting "puddles" that form on prototype portable ultrasonic nebulizers developed in our lab [357] (*see* [supplemental materials]). We can access these dynamics due to microsecond-nanometer resolutions provided by our custom ultra high-speed (UHS) digital holographic microscope (DHM). Without this capability, relevant portions of the cascade would be unreachable. The associated data pass through several quantitatively-significant physical regimes due to the range of scales, geometries, and wavenumbers considered: (i) basin depth: shallow, intermediate, and deep; (ii) dominant WT dynamics: discrete, intermediate, and kinetic; and (iii) nonlinearity level: weak and strong. We derive dimensionless quantities from discrete and kinetic theory for analysis and classification of WT dynamics.

4.1.2 Experiment

The experimental configuration is outlined in Fig. 4.1. The device is a 25 mm x 20 mm x 0.5 mm single-crystal lithium niobate piezoelectric transducer with electrodes deposited on each face leaving a 6.35 mm diameter window. In order to produce a repeatable fluid boundary and loca-

tion, a 60 μm thick polyimide annulus with inner diameter 9.5 mm was affixed to the top face, encircling the window. Water (40 μL) was pipetted into the annulus such that a thin circular lens with maximum central depth ≈ 725 μm completely fills the perimeter. A sinusoidal voltage signal was applied at 7.001 MHz, driving thickness-mode resonance. Greater detail regarding materials, fabrication, and characterization is available in [supplemental materials].
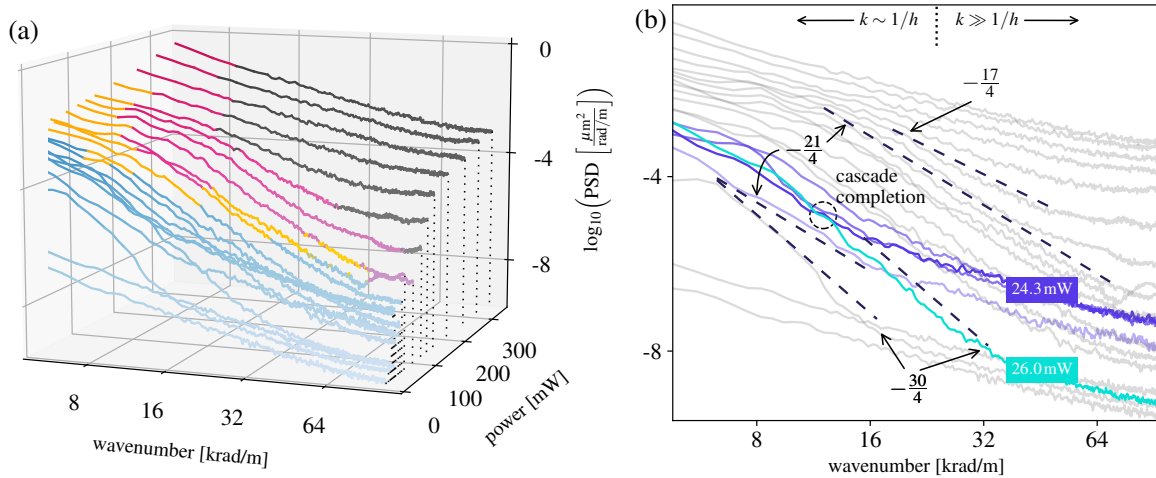
Figure 4.2: Turbulent micro capillary wave power spectral density regime classification. (a) Spectra as functions of increasing power are classified: (blue) discrete, (yellow) intermediate, (pink) kinetic, and (gray) strong. The first three are established in eqns. (4.2) and (4.3). The fourth is discussed later and demonstrated in Fig. 4.3. (b) An input of 24.3 mW leads to an arrested cascade while increasing the power to 26 mW leads to cascade completion, demonstrating a critical NRB value as theorized in Ref. [344]. Also shown (light to dark purple lines) are three input powers preceding 24.3 mW: 15.5 mW, 18.5 mW, and 21.5 mW. Indicated slopes are: 17/4, kinetic capillary wave slope predicted by Zakharov [340]; steepest slope, 21/4, observed in simulations of Ref. [354] and corresponding to an approximately constant slope over the KWT regime here (as discussed further on); and steepest slope, 30/4, observed in our experiments, both at capillary wave onset and immediately after the critical NRB value for a 26 mW input. Spectra in these plots are generated using Welch's method with Hann windowing and fifty percent overlap to average roughly one hundred spectra for all but the lowest two powers (0 and 7 mW). The shallow regime (not shown) exists at wavenumbers ≲ 2 krad/m.

The center of the air-water interface was imaged using an UHS camera (Photron, SA-Z) coupled to a DHM (Lynceé Tec SA, Lausanne, Switzerland). High-intensity coherent light is split with a sample path passing through the sample and a reference path unhindered. Passing

the light through the medium generates a phase delay with respect to the reference. Using the sample refractive index, the phase delay can be associated to a displacement up to a factor of $2\pi\lambda$ (λ is the light source wavelength). Phase jumps exist at integer multiples of $2\pi\lambda$. If the height gradually changes with respect to the viewing plane, phase jumps are uniquely accounted for in phase unwrapping, producing high-fidelity surface measurements. We obtained surface holograms covering a $300\,\mu$m x $300\,\mu$m square central region of the oscillating fluid interface. Holograms were recorded at $115.2\,$kfps and have a $10\,$nm face-normal resolution and a $1.2\,\mu$m image plane resolution. The curated data ($300\,$GB) obtained for this study are freely provided for download [358].

4.1.3 Intra-spectrum regime classification

We derive and apply dimensionless parameters to surface measurements for quantitative WT classification. These parameters also identify the appropriate modeling approach. When DWT dominates, resonance conditions are Diophantine, and number theoretical approaches are necessary [341]. If KWT dominates, resonances are approximate and the kinetic theory is valid [359]. Our expressions draw on the insights of Zakharov [360] and L'vov and Nazarenko [346], comparing NRB to eigenmode grid spacing, δ_k. They are consistent with discrete and kinetic wave theory [361] (*see* [supplemental materials]).

Deepness or shallowness is determined by comparing the wavenumber, inverse capillary length, k_*, and fluid depth, h [361]. Our system progresses from shallow at $O(10^2)\,$rad/m to deep at $O(10^4)\,$rad/m. Intermediate regimes are defined by interpolating between the shallow and deep

conditions (*see* [supplemental materials]). For shallow waves ($k_* \ll k \ll 1/h$):

$$\text{DWT} \quad \text{if} \quad \Delta_s = \tfrac{1}{16\pi} \mathcal{A}_v / \mathcal{A}_w \ll 1, \tag{4.2a}$$

$$\text{KWT} \quad \text{if} \quad \Lambda_s = 2\pi^2 \mathcal{S}_w \Delta_s^2 \gg 1, \tag{4.2b}$$

$$\text{IWT} \quad \text{otherwise.} \tag{4.2c}$$

where $\mathcal{A}_w = 1/k\widehat{\zeta}_k$ is the wave aspect and $\mathcal{A}_v = 1/k_m h$ is the quiescent fluid volume aspect. The Fourier transformed wave amplitude is $\widehat{\zeta}_k$. The grid spacing is $k_m = \pi/D_{\text{inner}}$, with reference to Fig. 4.1. Wave seclusion is $\mathcal{S}_w = k/k_m$, with $\mathcal{S}_w \gg 1$ indicating negligible boundary effects. Thus, the condition for shallow water DWT is that the quiescent fluid geometry should be much less shallow than the wave geometry. And for KWT, the opposite condition is weakly required in concert with waves that are sufficiently isolated from boundary effects. For deep waves ($k \gg 1/h$):

$$\text{DWT} \quad \text{if} \quad \Delta_d = \tfrac{1}{12\pi} \mathcal{S}_w / \mathcal{A}_w \ll 1, \tag{4.3a}$$

$$\text{KWT} \quad \text{if} \quad \Lambda_d = \tfrac{3\pi^2}{2} \mathcal{S}_w \Delta_d^2 \gg 1, \tag{4.3b}$$

$$\text{IWT} \quad \text{otherwise.} \tag{4.3c}$$

Thus, in deep conditions only the lateral dimension is relevant, whereas in shallow waters discreteness depends on both dimensions. For deep waters, finite-basin effects occur when wave steepness is large relative to domain breadth. The kinetic condition has weaker wave seclusion requirements and stronger wave steepness requirements. This qualitatively agrees with expressions found elsewhere [345, 362]. Equations (4.2) and (4.3) are wavenumber dependent and therefore address intra-spectrum characteristics. According to eqns. (4.2) and (4.3) wave turbulence regimes are *fundamentally geometrically determined*.

Figure 4.2 outlines the spectral features of our system. The behavior and significance

of variable-regime bounds can be interpreted by considering their evolving power laws when rewritten as power spectra, S. In shallow regions, $S_{\text{D-I}} \propto k^{-2}$ and $S_{\text{I-K}} \propto k^{-3}$ for the DWT-IWT (D-I) and the IWT-KWT (I-K) PSD bounds, respectively. In deep regions, $S_{\text{D-I}} \propto k^{-4}$ and $S_{\text{I-K}} \propto k^{-5}$. The change is a consequence of the continuously increasing effect of δ_{NRB} within the finite-depth basin as energy is redistributed to larger wavenumbers in the cascade. Thus, the variation in the regime bounds—*i.e.*, proxies for WT character—will smoothly and monotonically vary between these regimes.

Detailed inspection of these spectra reveals order-of-magnitude agreement of regime bounds with expected spectral characteristics. Theoretically, the hallmark of DWT is arrested cascades that are incrementally extended by NRB through sandpiling [345]. The irregular lumpy appearance visible at lower input powers ($P \lesssim 24\,\text{mW}$) in Fig. 4.2 indicates energy confinement due to cascade arrest, "frozen turbulence." This regime is defined primarily by spectral volatility. As power increases towards the DWT-IWT boundary, spectra remain approximately constant in shape and amplitude until NRB overcomes modal separation as theorized by Connaughton *et al.* [344]. At a threshold power ($P \gtrsim 26\,\text{mW}$ here), energy flows freely to small scales, leading to complete cascades, *i.e.*, cascades that extend to the viscous dissipation range near the noise floor.

The IWT regime is brief and characterized by residual irregularities imposed by discreteness and a more easily discernible slope due to KWT onset. At still higher powers, spectral fluctuations are mostly abated and the spectrum has the essentially-continuous appearance associated with KWT. In this regime, we expect Zakharov's kinetic theory [340] to hold to good approximation. Although one finds evidence of a constant spectral slope, the slope value— approximately $-21/4$—is different than the $-17/4$ law theorized by Zakharov. This is true despite the otherwise good agreement between the data and the kinetic theory characteristics in this regime. As demonstrated further on, at higher powers, departure from the constant $-21/4$ slope signals a change in regime from weak KWT to SWT. It is evident in Fig. 2(a) that SWT initializes at higher wavenumbers and spreads toward lower wavenumbers as power is increased.

The steepest spectral slope, $-30/4$, occurs twice over the range of investigated powers. Its first appearance is at onset of continuous capillary wave motion, just beyond a range of powers where dynamics are intermittently interrupted by brief quiescent periods. As power increases beyond this onset value, the cascade remains truncated but its slope gradually increases until a region of constancy is reached where the slope attains a maximum. With a small subsequent increase in input power ($\sim 1.5\,\mathrm{mW}$), the cascade abruptly completes, reinstating the initial slope of $-30/4$. If the power is further increased, the slope gradually increases to $\approx -21/4$. The slope remains relatively constant at this value up to an input power of $125\,\mathrm{mW}$, corresponding to transition to slopes $> -21/4$. For $P > 125\,\mathrm{mW}$, the spectral slope increases, approaching an apparently constant value of ≈ -2 in the SWT regime. This feature, which the authors are unable to compare with other studies from the literature, suggests a power-law type solution within a subset of the SWT regime. We note that the foregoing results differ from those obtained in simulations [354]. The slopes in the latter range from roughly $-21/4$ at lower powers to $-17/4$ at the highest powers and were obtained using Zakharov's kinetic equations modified to account for domain discreteness.

4.1.4   Global nonlinearity analysis

Global assessment of WT behaviors is obtained with a single-value parameter for quantifying nonlinearity as more energy is introduced. We achieve this with:

$$\delta_\mu = \sqrt{\frac{\sum_{n=0}^{N}\sum_{m=0}^{n} \overline{\delta}_n\,\overline{\delta}_m\, b_{n,m}^2}{\sum_{n=0}^{N}\sum_{m=0}^{n} b_{n,m}^2}}. \tag{4.4}$$

Here $\overline{\delta}_n = \delta_{\mathrm{NRB}}(f_n)/\delta_{k_n}$ quantifies nonlinearity at wavenumber k using the ratio of resonance broadening to grid spacing. Root-mean-square summation in (4.4) is weighted by the bicoherence. Since bicoherence is defined over a symmetric frequency grid, we take double summation over

unique pairings. The bicoherence is

$$b_{n,m} = \frac{|\langle \widetilde{\zeta}(t,f_n)\widetilde{\zeta}(t,f_m)\widetilde{\zeta}^*(t,f_n+f_m)\rangle_t|}{\langle |\widetilde{\zeta}(t,f_n)\widetilde{\zeta}(t,f_m)\widetilde{\zeta}^*(t,f_n+f_m)|\rangle_t}. \tag{4.5}$$

The difference between the numerator and denominator is order of operations of the time average $\langle \cdot \rangle_t$ and the modulus $|\cdot|$. The numerator is the bispectrum. In the bispectrum, phase information is removed after time averaging, so that this describes average wave coupling strength at a particular point in frequency space. In the denominator of (4.5), phases are set to zero (*i.e.*, made equivalent) before time averaging, which represents perfect phase coupling. Thus, bicoherence, $b \in [0,1]$, measures the *normalized* three-wave coupling strength, and is relevant for analysis of capillary waves specifically. Equation (4.4) is similar to a metric used by Pan and Yue [354]. The main difference here is that instead of arbitrarily fixing a wavevector within the three wave dependence in order to reduce the dimension of the space, we operate on all three frequencies directly (which themselves represent a dimensional reduction from the wavevectors). This ensures that all dynamics are represented in the computation. Furthermore, since bicoherence obtained from Fourier methods is noisy and insufficient for use with turbulence spectra, we follow van Milligen *et al.* [363] to overcome this obstacle with wavelet-based transforms, $\zeta(t) \mapsto \widetilde{\zeta}(t,f)$, of surface measurements, providing instantaneous spectra needed for computation of (4.5). Details surrounding the wavelet-based implementation are provided in [supplemental materials]. With our definition, one observes non-monotonic structure in the nonlinearity parameter that associates to wave turbulence features (discussed further on).

In Fig. 4.3, we provide a WT regime map. The nonlinearity δ_μ, the terminal cascade wavenumber, and the spectral slope are plotted against input power. Since Zakharov's kinetic theory is based on assumptions of deep water waves and weak nonlinearity, the transition to strong nonlinearity is evident when the observed constant kinetic slope is exceeded ($\gamma > 21/4$) and

154
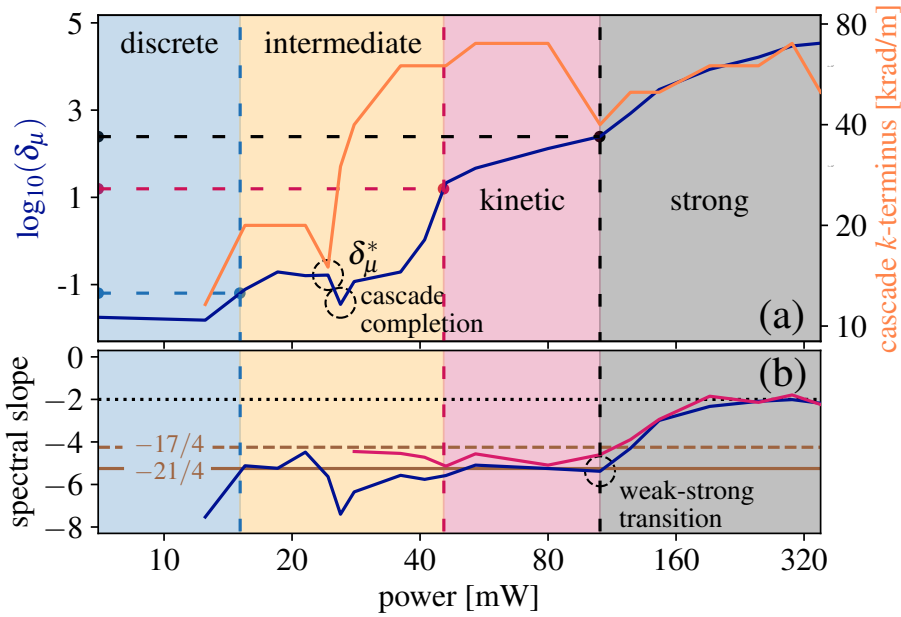
Figure 4.3: Global nonlinearity map of variable-regime capillary WT. (a) Nonlinearity level (4.4) and terminal cascade wavenumber as functions of increasing input power. (b) Inertial regime spectral slope over (blue line) the entire cascade and (red line) the deep water regime. A region of approximate constancy in nonlinearity, cascade length, and slope is observed just before the critical value, $\delta_\mu^* \approx 0.2$, and a recession of all three parameters follows. A sharp increase in cascade length immediately follows $\delta_\mu^* \approx 0.2$. The KWT-SWT bound occurs when the spectral slope exceeds the experimental constant value, $-21/4$, observed within the kinetic regime.

corresponds to $O(\delta_\mu) = 10^2$. This suggests a boundary between weak and strong nonlinearity:

$$\text{SWT} \quad \text{if} \quad \Lambda/10 \gg 1, \qquad\qquad (4.6)$$

where Λ is obtained from (4.2b), (4.3b), or the interpolated region between. Using this criteria, strongly nonlinear wave spectra have been identified in Fig. 1(b) in gray, appearing first at large wavenumbers, and spreading toward smaller wavenumbers as input power is increased.

Figure 4.3 reveals many significant features beyond those already mentioned. At a 16 mW input—corresponding to the DWT-IWT bound—a region of approximately constant nonlinearity level, cascade length, and slope value exists that corresponds to the frozen turbulence region. This immediately precedes a critical value, $\delta_\mu^* \approx 0.2$, that causes cascade completion, as indicated by a very sharp increase in the terminal cascade wavenumber and an abrupt decrease in both δ_μ and slope. The entirety of the critical transitional process occurs within the IWT regime, during which the nonlinearity level "stalls," remaining approximately constant at $\delta_\mu \ll 1$.

The pattern of build-up, plateau, and recession of the cascade k-terminus is initially repeated on entry to the KWT regime. However, the system enters into the SWT regime without a significant recession in slope or nonlinearity level and without a sharp increase in terminal cascade wavenumber. The terminal wavenumber in and beyond the transition region is within $50 - 70$ krad/m, so that the associated Kolmogorov scales are: $\lambda \sim 100\,\mu$m, $\epsilon \sim 0.1$ mW/μL, $\tau \sim 100\,\mu$s, and $u \sim 100$ cm/s. On transition into the SWT regime, the changing slope resembles the pattern of slope change beginning at δ_μ^* and attains a new plateau of -2. This value of the slope may assume the same role in the SWT regime that the Zakharov slope assumes in the KWT regime.

Our analysis has shown that a thinly-wetted surface driven by HFUS is a dynamically rich space. The dynamics traverse several WT regimes and, at sufficient powers, reach the strongly nonlinear regime. In atomizing systems, aerosol dispersal occurs at levels of nonlinearity that

are inaccessible to modern WT theories. Further study of strongly nonlinear WT is therefore essential to a rigorous understanding of the atomization phenomenon.

4.1.5 Acknowledgement

This chapter, in full, has been submitted for publication of the material as it may appear in Chaos, Solitons and Fractals, 2022. Orosco, Jeremy, William Connacher, and James Friend. "Identification of weakly- to strongly turbulent three-wave processes in a micro-scale system", *Chaos, Solitons and Fractals*.

4.2 Modal analysis of deep water capillary waves

4.2.1 Introduction

Nonlinear interactions between a large number of waves with random phase results in wave turbulence that can be modeled with a well developed mathematical theory, 'weak' wave turbulence (WWT) [364]. There has been significant experimental work on wave turbulent systems including liquid surface waves [365, 349], plasmas [366, 367], and solid plates [368], and much of it provides evidence for the predictions of WWT. The primary prediction is the Kolmogorov-Zakharov spectrum of wave height, given here for liquid surface waves dominated by surface tension rather than gravity (capillary waves),

$$S(f) \propto \epsilon^{1/2} \left(\frac{\gamma}{\rho}\right)^{1/6} f^{-17/6} \tag{4.7}$$

where ϵ is mean energy flux, γ is surface tension, f is time frequency of waves, and ρ is liquid density [369, 361]. In what follows, we will refer to the exponent of the frequency as α (i.e. $f^{-\alpha}$). Energy is said to cascade in the system with these scalings according to theory when the following conditions are met i) infinite domain, ii) scale separation between energy injection

and dissipation, iii) weakly nonlinear 3-wave interactions, and iv) local wave interactions (i.e. between waves with similar wavelengths).

Recent work in the field has attempted to reconcile discrepancies between WWT with these idealized conditions and the results of experiments. Connaughton et al. put forward a simple model to explain how quasi-resonances in finite domain capillary wave systems may cause deviation from the predictions of WWT [344]. At low levels of nonlinearity, the discrete resonances are not broad enough to interact and so the energy cascade typical of WWT is stunted. Falcon et al. observed that the frequency scalings in a gravity-capillary wave turbulence system are dependent on the input power [370]. Falcon and Laroche observed that the depth of the liquid also has an impact on the capillary wave spectrum causing it to deviate from a power-law, but the mechanism remains unknown [371]. Deike et al. measure the wave height spectrum with varying viscosity and show that dissipation in real systems occurs in what is theoretically the inertial region, between energy injection and the dissipation zone [372]. They propose a new way to measure energy flux in the system and use it to account for non-ideal dissipation. We have previously investigated the effect of increasing nonlinearity beyond what can be considered weak and also showed experimental evidence of finite domain effects [373]. In the current work we will investigate how energy shifts through length scales in a capillary wave system taking into account much smaller scales than are typically observed.

We are interested in capillary waves at small length and time scales because of their connection to ultrasonic atomization phenomena. Vibration of a surface in contact with liquid in the kHz or MHz range above a threshold amplitude produces many small droplets, on the order of microns, from the liquid surface [374, 375, 376]. In the kHz range, the size of the resulting droplets can be related to Faraday wave theory, where the driving frequency produces capillary waves at half the driving frequency. Lang showed experimentally that using this Faraday wave assumption along with Kelvin's equation relating frequency to wavelength yields a good estimate of the median droplet diameter with a single fitting parameter, $D = 0.34((8\pi\gamma)/(\rho F^2))^{1/3}$, where

γ is surface tension, ρ is density, and *F* is driving frequency [376]. This relationship holds for low atomization rates when *F* is in the kHz range. Lang also verified photographically that the capillary waves appearing on the surface were a uniform lattice of the expected wavelength. Subsequent studies have demonstrated that the droplet size also depends on viscosity, power input, and flow rate and have obtained significantly different values of the fitting parameter [377, 378]. Cavitation seems to play a role in addition to capillary waves, especially at low frequency [379, 377]. Lang was not able to explain the measured variation in diameter about the median.

The above ideas break down in the context of high frequency, high power ultrasonic atomization. A fundamental assumption of Faraday wave theory fails at high frequency (¿5 MHz) and it has been shown experimentally that no peak in the spectrum occurs near half the driving frequency [335]. In fact, a broad band spectrum indicating WWT develops on the surface at powers far below the threshold for atomization. In this context, Lang's simple approach of deducing droplets from wavelengths becomes much more complicated because there is no single frequency at which capillary waves occur—they no longer appear in a uniform lattice. It is also important to mention that cavitation becomes essentially impossible at these frequencies. The actual droplet size distributions measured from high frequency ultrasound have two and sometimes three peaks and often disagree with Lang's equation above [380, 381, 382, 383].

There has been some recent work claiming to solve the problem of determining the droplet size distribution [382]. A Gamma function is fit to the droplet size distributions demonstrating that they obey well studied corrugation and ligamentation processes found in sprays. This helps to explain the variation about the median and the multiple peaks mentioned above. The authors suggest that, because they measure two droplet size peaks, then there must be two sizes of capillary wavelength on the surface of the liquid. This makes intuitive sense based on a paradigm of Faraday waves and, without measuring waves directly, it is difficult to proceed further. It is indeed difficult to gain direct knowledge of the waves in this context because they happen at faster

time scales and smaller length scales than most experimental equipment can handle.

In the current work, we study capillary waves experimentally at very small length and time scales. Our system is a millimeter length, microliter volume of water so we isolate capillary waves from gravity waves and experience significant finite effects. We drive the system using high frequency, high acceleration ultrasound that pushes the wave interactions up to and beyond the weak nonlinearity assumption. We capture the surface displacement field at 115,200 frames per second (fps) using a high speed digital holographic microscope (DHM). We apply standard, single point time-series analysis and obtain amplitude spectra.

In addition to small length and time scales, our experimental technique allows us to examine many points over the surface simultaneously. This opens up spatial analysis techniques rather than only single point time series analysis. Berhanu and Falcon were the first to use this type of data although they were limited to larger length and time scales [384]. They were able to show that linear and nonlinear dispersion relations extracted from data match WWT using spatial and temporal Fourier methods. Another way to utilize spatial data is through modal analysis using eigenfunction decomposition in which the aim is to reveal coherent structures that may not be best represented by sinusoids or wavelets [385]. Proper orthogonal decomposition (POD) produces independent spatial modes optimized by energy with whatever temporal behavior is necessary and has been used extensively in turbulence [386, 387].

Standard modal analysis does not reveal coherent structures in our system, but we are able to quantify energy shifts by length scale. It is well known that isotropic turbulent systems have POD modes that reduce to a Fourier basis [385, 388] and the POD modes of our system are indeed closely related to 2D sinusoidal gratings, but this allows us to attach a definite length scale to each mode and then to track its energy as power is increased.
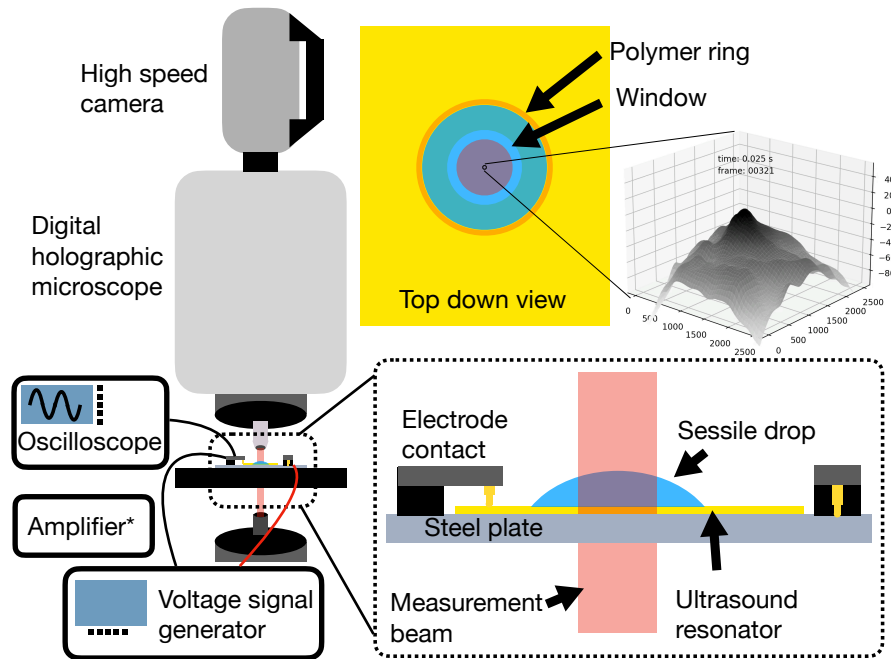
Figure 4.4: DHM with sessile drop on thickness mode

4.2.2 Experimental Setup

Our system consists of a sessile drop of water on a thickness mode piezoelectric resonator (see Fig. 4.4). The resonator has a 6mm diameter circular window in the electrodes that allows light to pass through. We deposit a titanium bonding later followed by 500 nm of gold on a double-side-polished, 0.5mm thick, 128-YX lithium niobate (LN) wafer with a mask in place and then remove the mask to reveal bare LN. This procedure is repeated on the second side to produce a thickness mode resonator with primary resonance at 7 MHz. A circular ring of polymer is adhered to the resonator outside the window area in order to create a repeatable shape and location for the sessile drop and to avoid the drop being displaced during the experiments. We use a pipette to place 66 uL of distilled water on the LN within the ring so that the drop is pinned around the entire perimeter. This volume was chosen so that the surface of the drop would be relatively flat compared with the field of view while not deviating significantly from the inherent contact angle of water on LN, thus ensuring the contact line with the ring remains pinned.

161

This geometry also limits the system to deep water capillary waves as gravity waves [something something something] and shallow capillary waves [something something something].

Very few experiments isolate capillary waves, the leading strategy being experiments performed in low-gravity[365]. Our experiments do so by using a very small fluid volume rather than by reducing gravity but both cause the critical capillary frequency to be lower than the frequencies relevant to the experiments.

The resonator is driven directly with a signal generator (model, maker) except for the largest power data set, which used an amplifier (Amplifer Research). The signal is a single frequency sine wave at the primary resonance frequency and at a constant voltage. The resonator is placed on a steel plate, one pogo probe is placed in contact with the top electrode, and the other is in contact with the plate and thus makes electrical contact with the bottom electrode. The current and voltage are measured with probes connected to an oscilloscope and their product is averaged over 1 million cycles to obtain the net power entering the resonator. The signal is applied to the resonator 0.5 seconds after beginning measurement with the DHM and maintained until after the measurement is completed at six seconds. Experiments are performed at a range of power inputs with all other conditions controlled. We recorded 18 data sets between 0-250 mW. The zero power data set was recorded for only two seconds.

We measure the surface displacement in time using a digital holographic microscope (DHM, Lyncee Tec) coupled to an ultra high speed camera (Photron). Laser light is split into a sample and a reference beam. The sample beam passes through the window in the resonator and the sessile drop and is then combined with the reference beam to form a phase image and an intensity image at the camera. The phase delay caused by passing through varying distances of water produces an instantaneous map of the height of the water surface up to the wavelength of light. If the height change is smooth and gradual enough, then the phase jumps caused by the wavelength of light can be unwrapped to produce a full height map. The height resolution of the system is on the order of 10nm. We refer the reader to Cuche et al for details on DHM technology

[389]. Details on our data processing can be found in Appendix A. We use a 10x objective lens and record at 115,200 frames per second with a 200 by 200 pixel field of view and a pixel size of 1.625 microns. Thus, we expect to observe behavior at frequencies up to 55 kHz and with reasonable amplitude accuracy up to 25 kHz according to Nyquist.

4.2.3 Time-series analysis

In order to obtain the power spectrum we extract the time-series of the central pixel and perform Welch's method[390] with blocks of 2^{15} time steps (see *Fig. 4.5)*. Most studies of wave turbulence inject energy at a range of frequencies lower than the expected dissipation range in order to ensure nonlinear wave interactions and the observation of a turbulent cascade [391, 370]. When these systems are driven parametrically, at a single frequency, it is common to observe Faraday waves indicated by a dominant peak at one half the driving frequency and well ordered patterns in space at low power [365]. At large enough power, however, Faraday wave systems do become turbulent [392]. Our system is fundamentally different, because we drive the system at a frequency five orders of magnitude larger than the frequencies of the beginning of the capillary wave cascade (note that the driving signal cannot be observed in Fig. 4.5 because the frequency is too high). Zhang et al. have proposed a mechanism by which large frequency excitation can stimulate much lower frequency wave behavior in a similar system [393]. This mechanism and/or the geometric resonance of the sessile drop transforms the energy injected at 7 MHz in the bulk to 10s-100s Hz on the surface at which point we obtain nonlinear 3-wave interactions.

As has been seen in numerical simulations by Pushkarev and Zakharov, for this finite domain our system fails to produce a cascade at low power inputs where the nonlinearity is very weak [394]. Based on the model from Connaughton et al. there are multiple thresholds of resonance broadening and therefore of nonlinearity, which is driven by power input. At each of these thresholds, the cascade increases in length towards larger wavenumbers. It seems clear from their work that the specific thresholds for a given system depends on the spacing of the

quasi-resonances and the relationship between forcing and broadening.
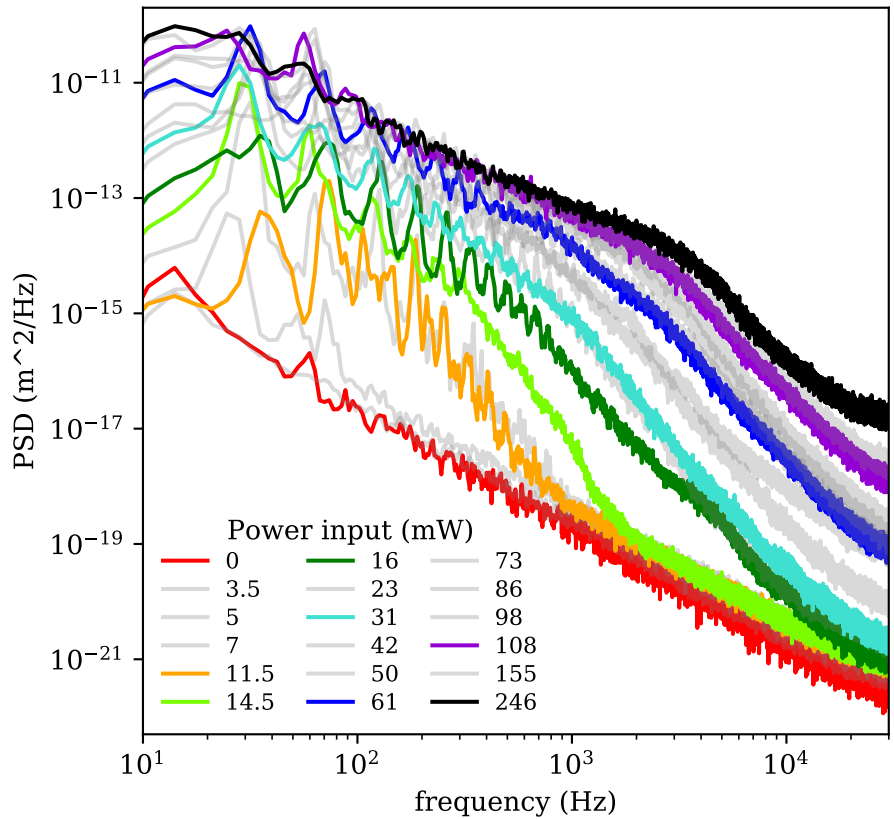
Figure 4.5: FFT spectra combined plot 7 MHz (maybe inset of 21 MHz spectra?)

The amplitude spectra in Fig. 4.5 clearly show a consistent peak at around 30 Hz with harmonics except for the 0 mW line and the 5 mW line. The 0 mW line indicates the noise floor of our measurement system plus thermal excitations. At 3.5, 5, and 7 mW, our system is highly intermittent as can be clearly seen in a short time Fourier transform of each experiment (see Supplementary), which explains why the 5 mW line is not separated from the 0 mW line. More data at these powers would be required to get representative spectra. Up to 11.5 mW the energy remains confined to low frequencies. At 14 mW there is a broadening of the harmonics and the beginnings of a broad band response that extents the cascade to slightly larger frequency. At 16 mW the cascade abruptly extends to much larger frequencies. There appear to be more extensions, but it is difficult to observe here because the cascades reach beyond the frequency resolution of

our measurement system. These characteristics seem to support Connaghton's model of finite domain, "frozen" turbulence.

The predicted value of α occurs only in a specific range of power inputs in a specific frequency range, 0.1-1 kHz at 15-35 mW (see *Fig. 4.6*). The initial jump to large α above the floor (visible as slope in Fig. 4.5) is a direct result of a finite domain. After initial cascade extension, around 20 mW, we find a shoulder separating two regions of constant *alpha* at each power input. Rather than a shift from more negative to less negative slope, as there is typically in systems that contain both gravity and capillary waves[370], we observe a shift towards more negative slopes in the high frequency range. This would seem to indicate a transition to a stronger dissipation mechanism at the frequency where the shoulder occurs, 1 kHz at 23 mW and gradually increasing to 4 kHz at 246 mW. Conversely, the low frequency range shifts from $\alpha = \frac{17}{6}$ just after cascade completion in keeping with WWT towards smaller values of α as power increases. This may indicate a transition from weakly to strongly nonlinear wave interactions.

As power is increased we also observe broadening of the initial low frequency modes while the amplitude of the high frequency portion of the cascade grows more than does the low frequency portion. The broadening of peaks with increased input power again supports Connaghton's finite domain nonlinear resonance broadening model. Increased nonlinear interactions among discrete resonances allow energy to move down the cascade more easily and may explain faster growth at high frequency.

Notably, we do not see any distinct peaks above 100 Hz at the highest power. This power is well below the threshold of atomization onset for this system, so the presence of capillary waves at a certain frequency seems not to foreshadow the peaks of a droplet size distribution in this system as was suggested by Kooij et al.[382]. As further evidence we attempt to produce droplets of a particular size by modulating the ultrasound input signal at a single frequency within the cascade, 5 kHz. At low power, the selected peak is prominent as well as three clear harmonics (see Fig. 4.7) and classical ultrasonic atomization would indicate that, at larger power, droplets
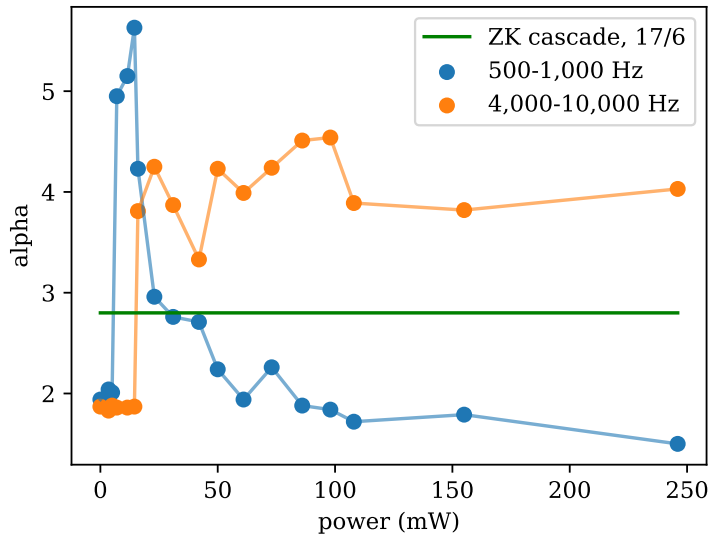
Figure 4.6: Frequency exponent of wave height spectra with increasing power input

would be produced at a size proportional to the corresponding wavelength. However, when we increase the power, the peak is broadened in the same manor as the initial low-frequency modes. Furthermore, the resulting droplet size distribution as measured with a laser particle sizer (Malvern, Spraytec) is no different between a 100% amplitude modulated signal at 5 kHz and an un-modulated signal.
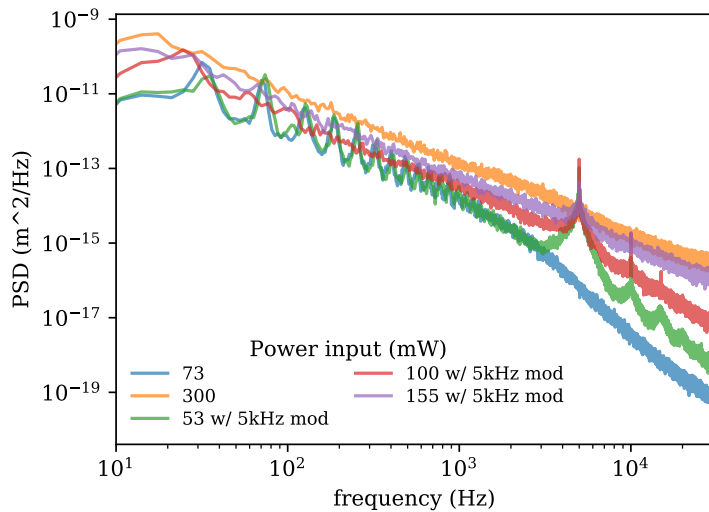
Figure 4.7: Spectra indicating that 5 kHz modulation is dispersed as nonlinearity increases, maybe an inset with droplet size data...

166

4.2.4 Spatial mode analysis

When computing the POD modes and singular values, we select 2^{13} frames from each data set. We transform each frame into a 40,000 element column vector and collect all the frames together into a 40,000 x 8,192 matrix, F. The mean frame is subtracted from each frame to produce a matrix, X. We then perform a singular value decomposition (SVD), which produces a 40,000 x 8,192 matrix that we call 'U', a 8,192 x 8,192 matrix we call 'S', and a third matrix we call 'V'. The matrix U contains 8,192 modes and S, which is diagonal, contains the singular values corresponding to those modes. By virtue of SVD the singular values are in descending order automatically and they are equal to the square root of the eigenvalues, λ, of the classical eigenvalue problem: $R\phi_i = \lambda_i\phi_i$, where R is the covariance between X and itself, ϕ are the modes[385]. When the measurement field is velocity, the the eigenvalues are proportional to the kinetic energy. Therefore, in our case where the measurement field is displacement, the singular values are proportional to the amplitude scaled by the number of time steps. This means that the most important spatial modes in terms of describing the amplitude of the water surface are the first columns of U. The modes after 600 in each data set are cut based on the clear elbow in the singular value distribution (see *Fig. 4.8*).

The first 64 POD modes as well as modes 200-264 are plotted in Fig. 4.8. The length scale clearly decreases with increasing mode number. For the wavelength range where the field of view offers high enough resolution (¡200 microns), it is very clear from 2D FFT (see Supplement) that only one length scale is present in each mode, and even for lower modes it is reasonable to assume by inspection that each mode is roughly composed of sinusoids of a single wavelength. In order to quantify the wavelength of the modes, we perform an in-house algorithm based on two dimensional fast Fourier transforms (2DFFT). For each mode we reshape its column vector into a 200 x 200 image and perform 2DFFT, which produces another 200 x 200 image. Each point in this new image is associated with a wavelength and a strength. For small wavelengths it is accurate to take the wavelength of the pixel with the largest strength as the corresponding mode
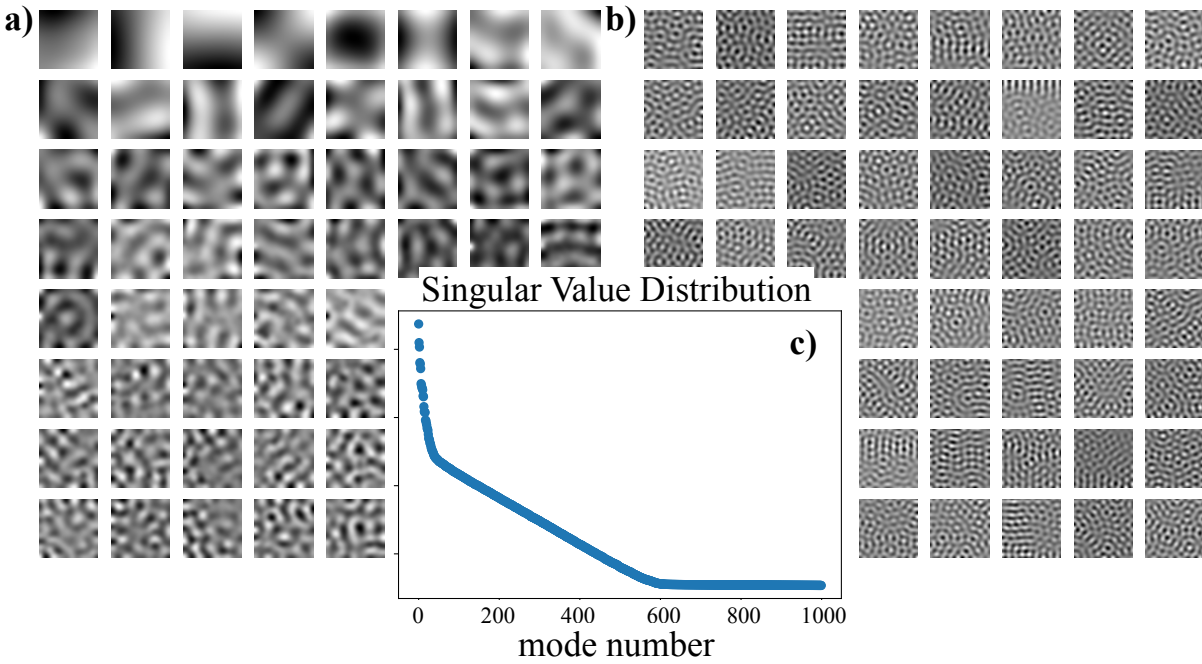
Figure 4.8: PCA modes (0-64, 200-264) from the data set with power set to 16 mW.

length scale. However, for larger wavelengths, poor resolution in wavelength space means we must take the average of some number of the pixels. Based on trial and error we chose to average eight pixels with the largest strengths. Furthermore, in order to account for bias towards modes that are aligned with the square camera window we performed this procedure on 45 different rotations of the mode image and took the average wavelength value.

Thus, we obtain the relationship between wavelength and mode number (see *Fig. 4.9*). This allows us to plot the singular values for each mode, which are equal to wave amplitudes as we described earlier, against their respective length scale (see Fig. 4.10. Energy is clearly restricted to length scales above 500 um until the power reaches 7 mW. There is also a clear transition between 98 and 108 mW where energy shifts towards much smaller length scales. This second transition was not apparent from Fourier analysis (see *Fig. 4.5*). Increasing power in this range abruptly extends the cascade, as we could not see in Fig. 4.5 due to frequency resolution, similar to the cascade extension between 7 and 16 mW that *is observable* in Fig. 4.5. Also, notice

that the proportion of energy at smaller scales is actually increasing relative to the proportion at larger scales—the largest length scale actually has smaller amplitude at 246 mW than it does at 155 mW.
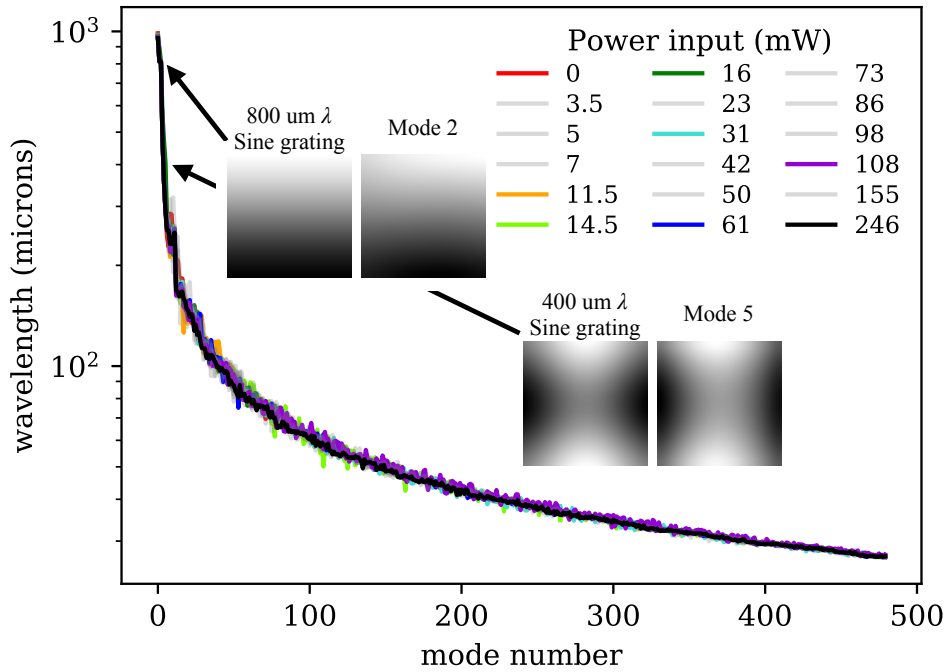
Figure 4.9: Wavelength for each mode of each data set determined using a 2D FFT algorithm.

In order to understand if modes of the same number between data sets are related, we took the covariance between the U matrix for each data set and that of a compiled data set, U_c. The compiled data set is comprised of 1024 frames from each individual data set and we perform the same POD procedure on it to obtain U_c. The covariance reveals how similar each U matrix is to a common basis, U_c. Fig. 4.11 shows the covariance of U_61 with U_c and also highlights cross-sections (horizontal lines) that appear in Fig. 4.12 where they reveal components of the given mode in terms of the basis modes (i.e. the dot product). For a given mode in an individual data set, the distribution of modal components tend to be centered near the corresponding mode in the basis. We can quantify the deviation of this distribution from the corresponding basis mode using weighted moments similar to the center of mass and moment of inertia. The center of mass
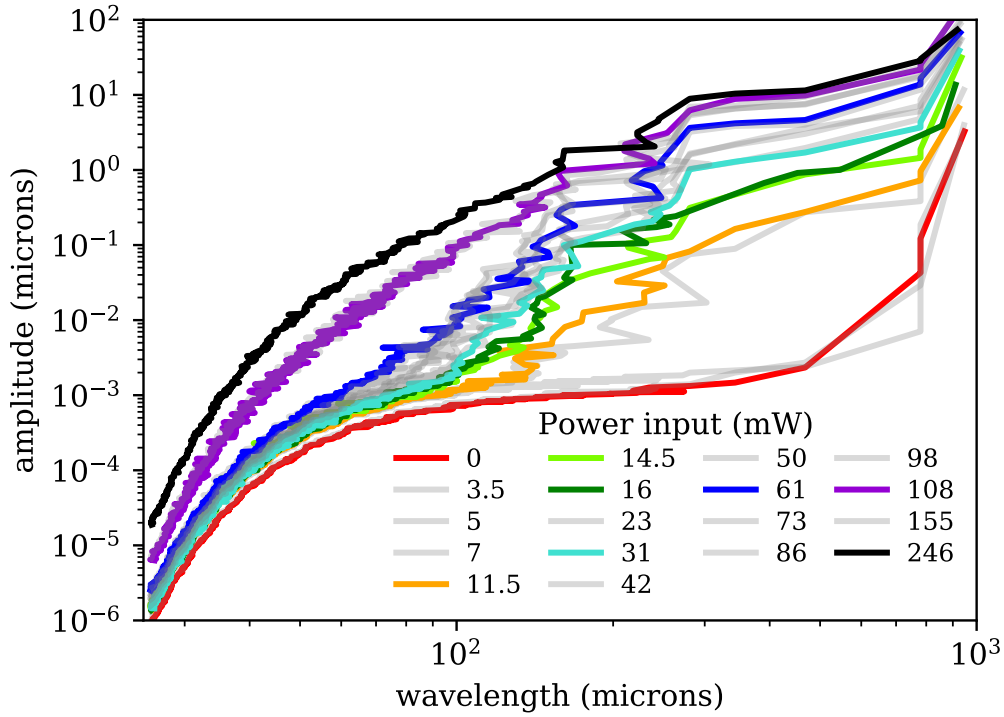
Figure 4.10: Singular values scaled by the number of frames from POD plotted against the wavelength obtained by performing a 2DFFT algorithm on each mode. This is the same plot as Fig. 4.8c), but with the y-axis scaled to be amplitude and with the x-axis transformed from mode to wavelength.

(CM) is given by

$$CM = \frac{1}{M} \sum D(j) * j, \qquad (4.8)$$

where $D(j) = U_c^T * U_i[a]$ is the distribution of components of the ath mode of U_i across the j modes of U_c (e.g. the cross-section) and $M = \sum D(j)$ is the sum of these components (e.g. the total 'mass'). The deviation of the center of mass is then the difference between CM and a. The moment of inertia, I, is given by

$$I = \sum D(j) * (CM - j)^2. \qquad (4.9)$$

The covariance is a convenient way to show that the modes identified by POD are essentially common between different data sets (beyond just their length scale), but they also
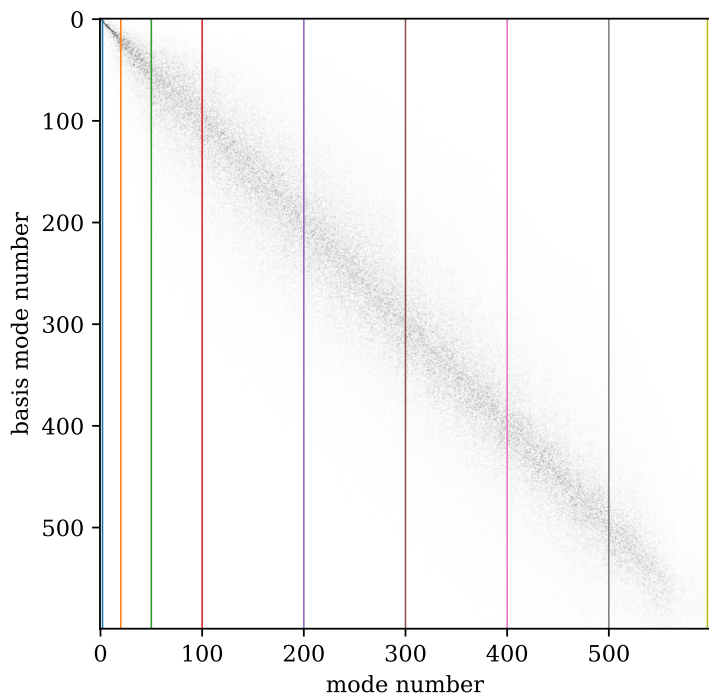
Figure 4.11: Covariance plot for three example data sets
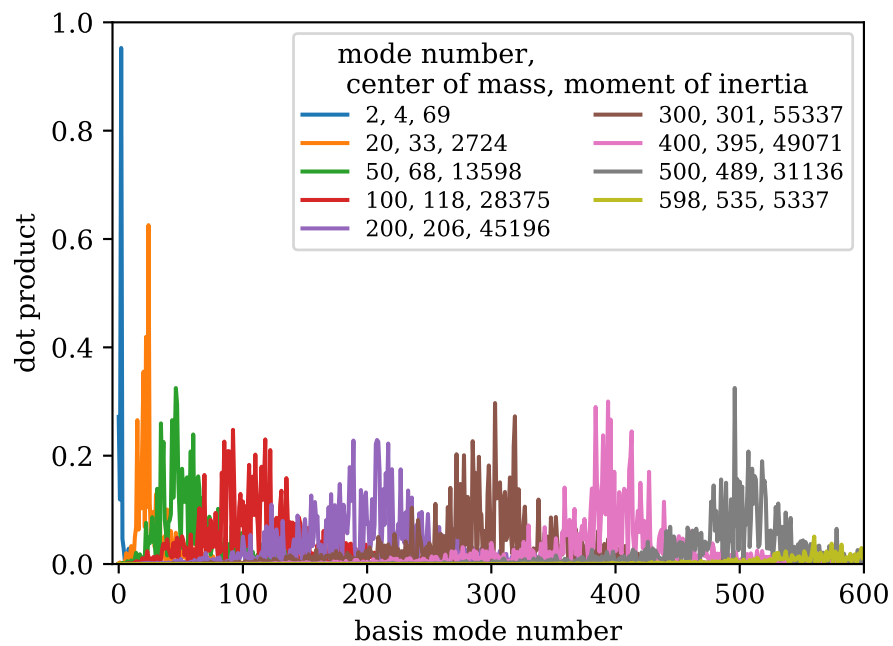
Figure 4.12: Covariance cross-sections (0, 20, 50, 100, 200, 300, 400, 500, 600) from one example data set

quantify how the modes themselves change with power input—setting aside the singular values, which rank the amplitudes of the modes within a data set at a single power. We plot the deviation of the center of mass and the moment of inertia for each mode of every data set in Fig. 4.13. The first three lines (in red) have a similar shape, but then suddenly the 7 mW line is different, which aligns with the sudden changes in both Fig. 4.5 and Fig. 4.10. The way this shape changes indicates that the modes near the 20th mode are interacting with a much larger number of adjacent modes than they were at only a slightly lower power.

The fact that the cross-sections in Fig. 4.12 are distributed generally around their corresponding basis mode is an expression of local wave interaction. When the power crosses some threshold near 6 mW, the modes near 20 suddenly become less localized and interact with modes that are more separated from them in length scale. As power increases from 7 to 42 mW the moment lines gradually move towards the 0 line, which means the modes interact more and more locally and they are more closely described by the corresponding basis modes.

Suddenly at 50 mW the modes beyond mode 45 become de-localized, but again move towards the 0 lines at slightly larger powers. Once again at 86 mW the modes near the 50th mode become de-localized and subsequently move back towards the 0 lines. The final de-localization is centered closer to the 140th mode, which indicates much smaller length scales. This de-localization coincides with the transition identified in Fig. 4.10.

4.2.5 Conclusions

The Fourier analysis standard to wave turbulence provides us with the relationship between wave height and frequency. Finite domain effects result in frozen turbulence and low frequency (relative to our measurement capabilities) abrupt cascade extension. Immediately upon cascade completion we see a small window of theoretical WWT. At larger powers, there is a shoulder separating α into two frequency regions. There is increasingly strong nonlinear wave interaction at low frequencies and increasing dissipation at larger frequencies.
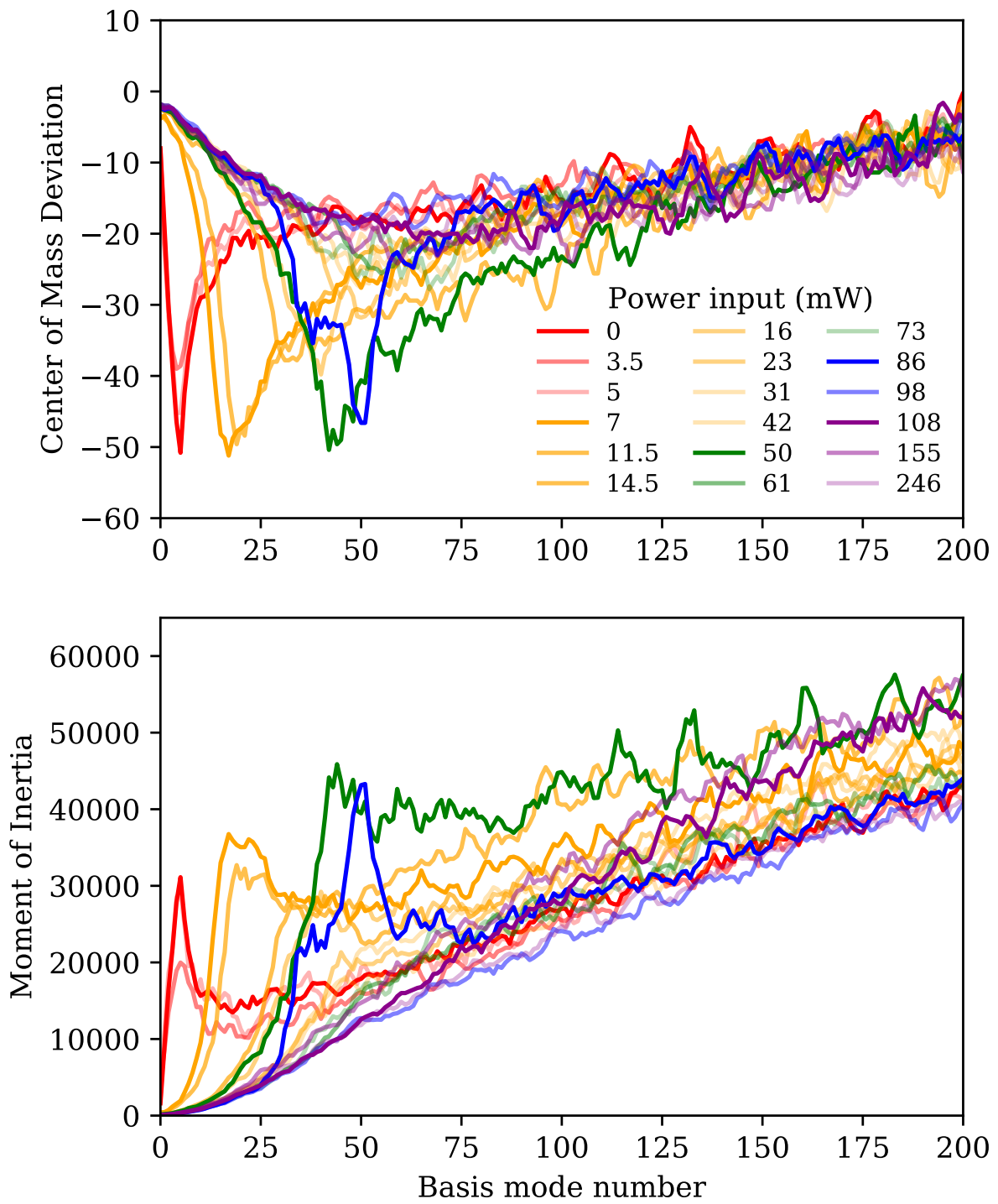
Figure 4.13: Center of mass and moment of inertia versus mode number (wavelength)

Spatial analysis with POD provides us with a direct link between amplitude and wavelength. Energy shifts towards smaller length scales nonlinearly with thresholds at at least power levels. These shifts are analogous to cascade extension and this spatial analysis allows us to identify a small scale, high frequency cascade extension that was not apparent with Fourier analysis. Covariance between each data set and the basis modes provides us with information about how coherent modes change with power input. We are able to identify de-localization events where waves interact with wavelengths more separated from themselves.

Uniform Faraday waves are a poor model for droplet size in this system. Peaks at a specific frequency are quickly flattened at at nonlinearity levels even below the atomization threshold and it remains unclear how to predict which wavelengths will be preferentially amplified if any in order to form droplets at larger power input. A theory of wave turbulence beyond the weak and infinite regimes dictated by WWT are needed to predict which waves will produce droplets in high frequency ultrasound atomization systems.

4.2.6 Acknowledgement

Appendix A

MADVent: A low-cost ventilator

The COVID-19 pandemic has produced critical shortages of ventilators worldwide. There is an unmet need for a rapidly deployable, emergency-use ventilator that retains sufficient functionality to serve patients with severely compromised lung function. Anticipating further waves of COVID-19 infections prior to vaccine development, we have developed and validated a simple, portable, low-cost ventilator that can be rapidly manufactured with minimal susceptibility to supply chain disruptions. This ventilator avoids the safety issues and technical limitations inherent to existing solutions to the current ventilator shortage. Herein, we describe the development and validation of a single-mode continuous, mandatory, closed-loop pressure-controlled time-terminated emergency ventilator. Validation was carried out with certified test lungs at a wide range of compliances, pressures, volumes and resistances to meet U.S. Food and Drug Administration standards of safety and efficacy, and an Emergency Use Authorization is in review for this system. Robust safety controls and alarms complement ventilatory capabilities designed to manage COVID-19 patients with severe Acute Respiratory Distress Syndrome. This novel emergency ventilator design could abrogate the need for rationing ventilators based upon imperfect ethical standards, or resorting to controversial practices such as splitting one ventilator to serve multiple patients. All design and validation information is provided to facilitate ventilator

175

production even in resource-limited settings from parts likely to remain available despite the current public health emergency.

A.1 Introduction

A key challenge in the battle against the disease caused by the novel coronavirus SARS-CoV-2, COVID-19, is a potential worldwide shortage of mechanical ventilators. The required number of ventilators is projected to significantly exceed capacity, based on the number of patients expected to contract the disease in the United States and the percentage of these likely to require assisted ventilation [395, 396, 397, 398]. Adding to this burden is the fact that COVID-19 patients who develop acute respiratory distress syndrome (ARDS) often require prolonged mechanical ventilation [399, 400, 401, 402]. Physicians around the world have been forced to make difficult triage decisions on which patients to treat and which to let go of due to inadequate number of ventilators [403, 404]. Adding to the challenges of increasing number of devices, is the complexity and expense of traditional ICU ventilators further aggravated by the breakdown of regular supply chains as a consequence of the pandemic. [405, 406, 407]

A pandemic caused by a potentially lethal and easily transmissible [408] viral pathogen like SARS-CoV-2 requires rapid, focused effort in either obtaining or manufacturing sufficient medical equipment to save lives despite the disruption of normal supply chains, difficult working conditions, and regulatory restrictions reasonably imposed in normal times that nonetheless jeopardize progress during a state of emergency. In response to the anticipated COVID-19 crisis, we formed the University of California San Diego Acute Ventilation Rapid Response Taskforce (AVERT) to develop a ventilator with functionality sufficient to safely treat COVID-19 patients with ARDS, while simultaneously shortening ventilator production time and cost to make ventilators available when and where they are needed.

The ventilator design focuses on safe operation and reliable production while addressing

the specific needs of COVID-19 patients with ARDS: minimizing part count, cost, and complexity; reducing or eliminating reliance on scarce parts and resources; ensuring viable implementation in different healthcare systems across the world; and seeking simple assembly, testing, and use procedures by healthcare personnel with limited experience in ventilation and no experience with this type of ventilator system [409].

Modern ICU ventilators provide complex control and intricate feedback loops of a wide variety of respiratory parameters and ventilation modalities. Their operation requires highly specialized staff [410]. Regulatory requirements are understandably high, and pandemic crisis-driven emergency orders of ventilators to medical device manufacturers are difficult to fulfill due to the failure of supply lines and the difficulty in rapidly ramping up production of these technically advanced ventilators. In the meantime, lives are at risk. While several emergency ventilators are commercially available, most do not meet the medical requirements of the complex ARDS-like pneumonia associated with COVID-19 which requires pulmonary protective ventilation with careful control of pressure and volume as compliance of the infected lung tissue can rapidly decrease, placing the patient at elevated risk of barotrauma and further lung injury. We are left with an unmet need for COVID-19 pneumonia-appropriate, rapidly deployable, comparatively simple emergency-use ventilators.

Based on published literature and clinical experience, we determined the following ventilation features to be essential for safe use in patients in this crisis: pressure control mode of ventilation, respiratory rate, inspiratory time, and forward-compatibility with external modular components such as adjustable positive end expiratory pressure (PEEP) valves. [411, 412, 413] In addition, basic alarms indicating high and low pressure and volume are necessary to notify the healthcare provider when desired parameters are not being met or if there is a significant problem with the system (e.g. electrical circuit failure). Many modern ventilators can sense and synchronize to patient initiated breaths to provide the most comfortable form of ventilation in a minimally sedated patient. However, we did not include a synchronized mode of ventilation in the

design of this ventilator, recognizing that patients with COVID-19 and severe ARDS will require sedation and possibly pharmacologic paralysis to facilitate optimal ventilation. [414, 415] The advantages of this approach include simplified ventilator settings and simplified troubleshooting with a single-mode continuous, mandatory, closed-loop pressure-controlled time-terminated ventilator (from now on referred to simply as pressure-controlled). This approach provides predictable delivery of ventilated breaths, and streamlined device production. Further design choices were based on the dual goals of safe, effective ventilation and quick production as detailed in the next section.

Ventilators in clinical use are regularly calibrated using lung simulators to comply with U.S. Food and Drug Administration (FDA) standards of safety and efficacy. All devices described in this manuscript were tested and verified with such a lung simulator (Dual Adult Test Lung, ISO 13485 certified; Michigan Instruments, 4717 Talon Court SE Grand Rapids, MI 49512 USA) with the associated data visualization software at the University of California San Diego. Our bedrock of safety is the provision to test every one of our devices using this human ventilation simulator, a physical device designed to emulate human respiration with time-stamped data capture to determine the safety and efficacy of the manufactured ventilators.

All models, print files, simulation data, and all other data obtained have been included either in this manuscript or in the Supplementary Information with the recognition that the situation faced by the medical community is unprecedented and will require a coordinated effort once the design has undergone peer-review by members of the clinical community and Emergency Use Authorization (EUA) by the FDA [416], which we have applied for at the time of writing. Our engineering and clinical teams have closely collaborated to develop a *safe* design that can be quickly manufactured in large numbers in resource-limited settings from parts readily available despite the current public health emergency. We have designed the system to be able to incorporate additional features as necessary, including other mandatory ventilation modes.
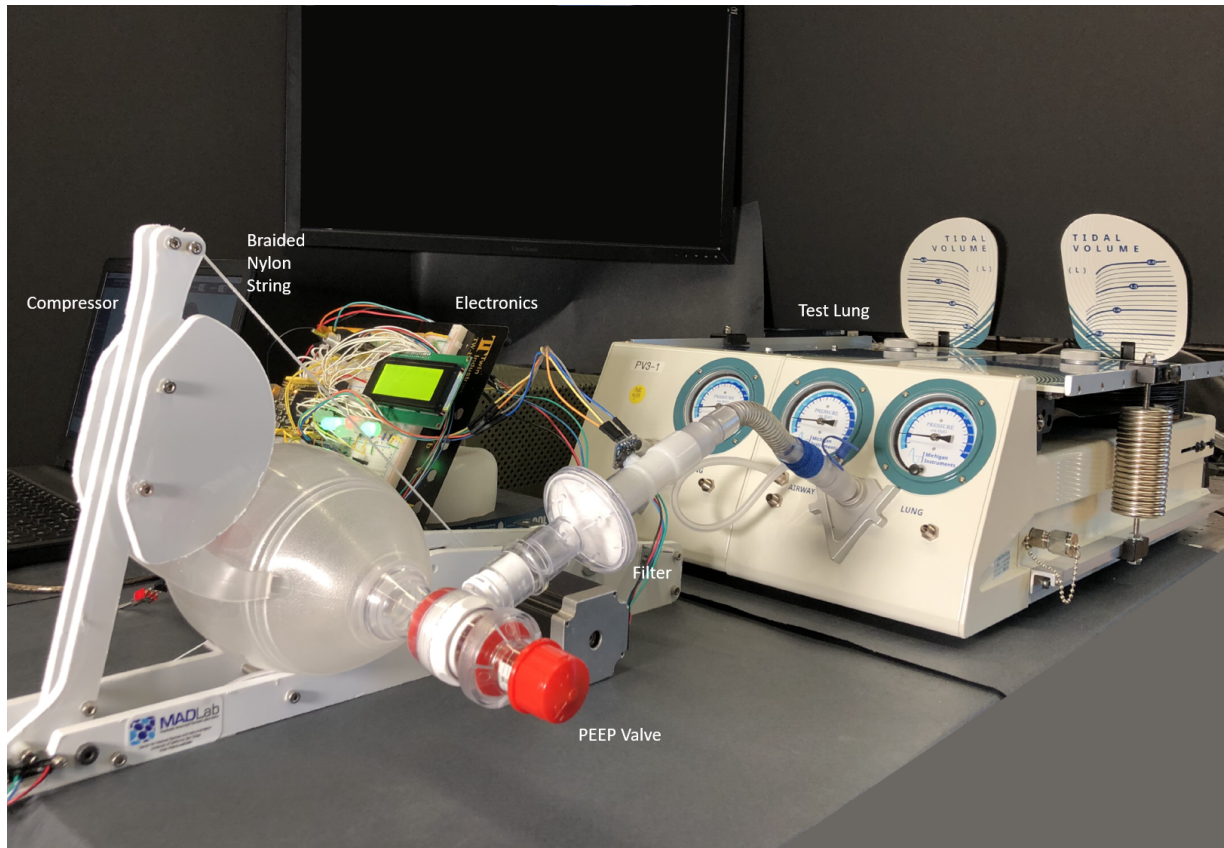
Figure A.1: Testing of the system was performed on the lung simulator. All parameters were tested to their stated limits (over 200 individual experiments) and according to International Standards Organization (ISO) standards for pressure controlled ventilation. Notice that the dead space is kept to a minimum by reducing the length of tube between the bag and the lung simulator; this configuration was reproducible with a full-sized simulator manikin and a standard adjustable overbed hospital bedside table. The system shown here is an early prototype with exposed electronics, but is to be supplied with housings as depicted in Fig. A.2.

A.2 Design of an automated self-inflating bag-based ventilator: MADVent Mark V

Mechanical ventilation typically requires pressure or volume-based control of inspiration at a defined rate [417, 411]. Given the relative ubiquity and simplicity of pressure transducers as compared to flow sensors, the pressure-controlled mode of ventilation was determined to be both safe and best suited to this current project. This has proven fortuitous since, though both volume and pressure limits are included in ARDS recommendations, [413] there are data to support the pressure control mode as being particularly safe in ARDS therapy. [412]

Typically, automatic pressure-controlled ventilation relies on either an impeller motor that pressurizes air within the ventilator or a reticulated, regulated high-pressure source from the healthcare environment. Volume-controlled ventilation relies on the compression of a bag or bellows by a known volume. In order to be truly controlled, each of these methods must measure the pressure or volume—sometimes both—and use this information to appropriately adjust the actuation in a feedback loop. Measuring pressure at the output of the ventilator is far more straightforward, less expensive, and less susceptible to calibration and algorithmic errors than measuring volume. Accurate flow sensors for mechanical ventilation are expensive [418], susceptible to supply chain disruptions, and conversion of their output into volumetric flow rate is difficult [419] with complex algorithms required to deal with the challenges [420]. Air flow is typically integrated over time to estimate the volume of air passed through a ventilator, and the volume-flow relationship is complicated by sensor accuracy [421]; lung compliance [422]; humidity, compression, and temperature [423]; and leaks in the system.

Manual ventilation—and automated ventilators from the past—make use of a bag with valves to ventilate a patient's lungs with mechanical compression and release of the bag. Safe ventilation, however demands care in mechanical compression and release beyond simply compressing a bag. For our ventilator, we adopted a self-inflating bag-based mechanical ventilation

system, combining its intrinsic simplicity with instrumented sensing of the pressure produced by the system to continuously control the ventilator in a closed feedback loop, eschewing air flow sensors in favor of calibrated knowledge of how the bag volume varies with mechanical compression. This allows the ventilator to reach precise pressure targets within a prescribed inspiratory time while setting safety alarmed thresholds on the volume delivered per breath in an inexpensive and rapidly devised design.

Rather than reinventing the bag and valving system, we have elected to utilize a self-inflating manual resuscitator bag (SPUR II, Ambu Inc, Copenhagen, Denmark) already in common worldwide use in hospitals and other emergency care settings. These self-inflating bag systems have been designed to deliver the proper range of tidal volumes with simple manual compression, do not require an pressurized gas source, and have the appropriate valves and standard connections to ventilate patients. Other manual resuscitator bags of similar size are compatible with the MADVent system, but may require calibration for safe use of all ventilatory alarms and features. These resuscitator bags are compatible with external PEEP valves that both add no dead space to the system and are essential for the care of patients with COVID-19 and ARDS. They also have built-in ports for supplemental oxygen administration and pressure monitoring. Two pressure sensors were used to measure ambient and in-line pressure (BMP180, Bosch, Schillerhöhe, Germany) but these can be replaced by a single differential pressure sensor (SSCMRRN060MDSA5, Honeywell Inc, North Carolina, USA) that can be mounted on a printed circuit board (PCB). The differential pressure sensor can be connected to the inspiratory line either at the mouthpiece or at the outlet of the bag. The mouthpiece placement option may be preferable for patients requiring very low tidal volumes or with especially poor gas exchange, for whom reducing dead space is crucial. In either case, the sensor is able to provide pressure measurement for the entire breath cycle: inhalation, exhalation, and the idle time between breaths.

The bag is mounted into a frame under a lever arm that is subsequently used to compress the bag, as shown in Fig. A.2. The entire ventilator structure, including the bag mounting frame
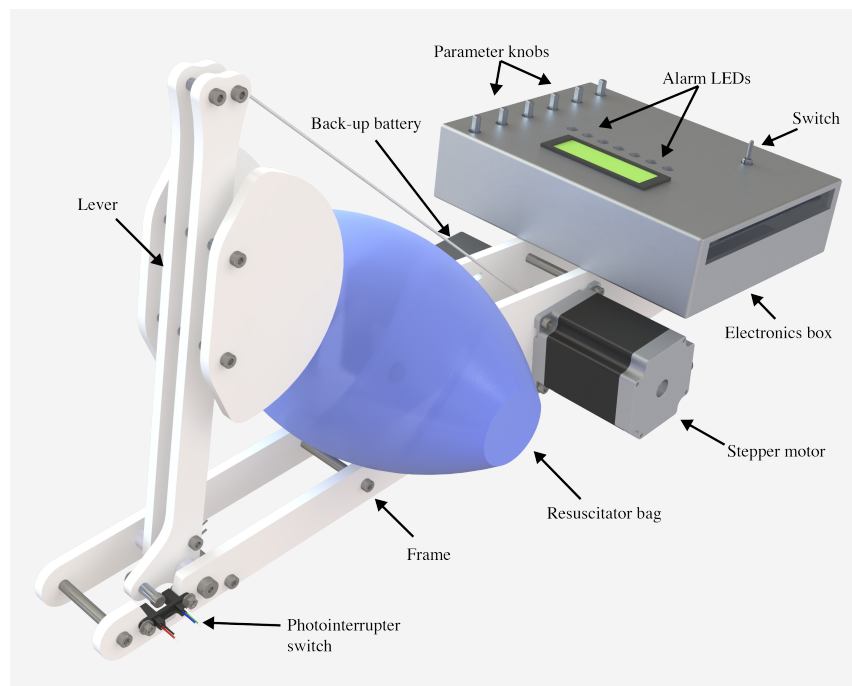
Figure A.2: Render of the final version of MADVent, with an electronics enclosure. The enclosure has an interface for the healthcare provider to adjust various ventilation settings such as target pressure, inspiratory time, respiratory rate and alarm thresholds. An LCD screen displays ventilation parameters in real time. LED's and a built in alarm alert the healthcare provider in the event of an emergency.

and arm, can be rapidly laser cut from polyoxymethylene (acetal) in 15 min, and assembled using readily available hardware. An alternate material choice is polycarbonate, which has superior resistance to commonly used hospital disinfectants such as hydrogen peroxide and sodium hypochlorite (bleach). Complete design files are provided for the reader (see Supplementary Information). Two convex compressor extensions are mounted on the lever arm and press into contact with the bag held in place by corresponding concave surfaces via hook-and-loop (Velcro) fixtures on the fixed frame of the ventilator, ensuring its stability and maximizing the possible compression volume of the bag. The hook-and-loop attachment facilitates quick and simple bag removal in the event the healthcare provider needs to manually ventilate the patient or the bag needs to be exchanged.

Rather than rely on gear or cam mechanisms to translate the rotational motion of a control motor to a rectilinear motion for bag compression [424, 425], we use the bag compression arm as a lever to provide substantial mechanical advantage from the motor. Geared and cam mechanisms are subject to wear, have backlash, add cost and complexity, and tend to be noisy, a significant issue in the critical care setting. Our approach permits simple direct motor drive via a lanyard attached to the top end of the lever arm and wrapped around a spool attached to the motor's shaft. Lengthening the lever arm or placing the bag closer to the pivot point increases the mechanical advantage.

A stepper motor with 1.89 N-m of holding torque and a maximum rotation speed of 180 rpm (QSH5718-76-28-189, NEMA 23, Trinamic Motion Control GmbH, Hamburg, Germany) was chosen (*see* Supplementary Information for details) in order to supply the rotation power and control necessary to implement a pressure control feedback loop and likewise produce sufficient rotation speed to enable rapid breath cycling. A microstepping commutation scheme was chosen for quiet operation, precision, and the avoidance of resonances. Stepper motors are brushless and therefore can fail only by failure of the bearings or the insulation of the electrical wire within. They feature a mean-time-between-failure (MTBF) of at least 10,000 hours, over a year

of continuous operation, and so should not fail in this application for an anticipated four-week lifetime. Supplies of these motors are unlikely to be affected by the pandemic, as they feature in diverse applications from 3D printing to robotics, consumer devices, automobiles, and furniture. The lever arm hinges around a shoulder screw, a type of machine screw characterized by a constant diameter raised portion which is commonly used for simple pivot points, and its lateral movement along this screw is limited by spacers. A torsional spring is mounted at the hinge in order to aid in the return of the lever arm to its zero position at the end of each stroke, as verified for each cycle by a photointerrupter switch (C14D32P-A3, CUI Devices, Lake Oswego, OR USA). An electronics box is secured to the frame opposite the lever hinge. The system is powered by a universal, medical grade (UL/ISO 60601) 12 VDC wall adapter (90–240 VAC input, SWM30-12-NV-P5, CUI Devices), but a rechargeable lead-acid back-up battery (BP1.2-12-T1, B B Battery, Commerce, CA USA) capable of powering the system for at least 20 minutes is also installed and automatically begins supplying power when needed.

The healthcare provider is able to directly set the following six parameters via control knobs on the system: respiratory rate, peak inspiratory pressure (PIP), inspiratory time, high-pressure alarm threshold, low-volume alarm threshold, and high-volume alarm threshold. The system is capable of delivering between 10 and 35 breaths per minute (bpm), peak inspiratory pressures between 10 and 35 cm H_2O, and inspiratory times between 1 s and 3 s. Volume alarms may be set between 200 cc and 1000 cc. The set values of each parameter are displayed on a liquid crystal display (LCD) screen. Seven light emitting diodes (LEDs) are provided to individually indicate to a clinician the nature of an alarm condition. These include alarms for the high and the low-volume thresholds, as already mentioned, and alarms for mechanical failure, overheating, pressure sensor disconnection or failure, wall power disconnection, and low battery. In urgent situations such as a low or high-volume ventilation condition, a loud buzzer will also alert clinicians. If conflicting or otherwise incompatible parameters are entered, then the relevant parameters flash on the screen and the system will begin ventilation and an alarm will sound

immediately. This condition has been programmed to occur in three cases: when the low-volume alarm threshold is higher than the high-volume alarm threshold, when the set peak pressure is higher than the high-pressure alarm threshold and when the user set inspiratory time is more than 75% of the inspiratory time calculated from the user set respiratory rate.

After the parameters have been set, the system waits for activation via a toggle switch before initiating ventilation. During inspiration, the motor rotates an amount proportional to the difference between the intended pressure and the current measured pressure at each time-step. The intended pressure at each time-step is determined by a monotonically increasing function between $p(t = 0) = 0$ and $p(t = t_i) = p_p$, where p is pressure, t is time, p_p is the peak pressure set by the provider, t_i is the inspiratory time set by the provider. Once the peak pressure or the inspiratory time has been reached, the motor reverses direction at a set speed until it reaches the zero position, which is defined by the compressor arm photointerrupter switch and confirmed by the motor encoder. The system then enters a waiting period calculated according to the set respiratory rate and inspiratory time before beginning the next breath cycle.

If, at any point during the control loop, a single breath cycle generates a volume below the low-volume alarm threshold, then that alarm is triggered. The system identifies the volume expelled in each breath via an encoder fixed to the motor shaft that reports exactly how much the shaft has rotated. A low volume may indicate significantly lower compliance in the patient or an endotracheal tube obstruction. Similarly, if a single breath's volume exceeds the high-volume alarm threshold, then that alarm is triggered, and may indicate a patient becoming disconnected from circuit or another source of a leak in the system. Alarms for pressure are triggered directly from the pressure sensor and similarly can identify issues with lung compliance and circuit integrity.
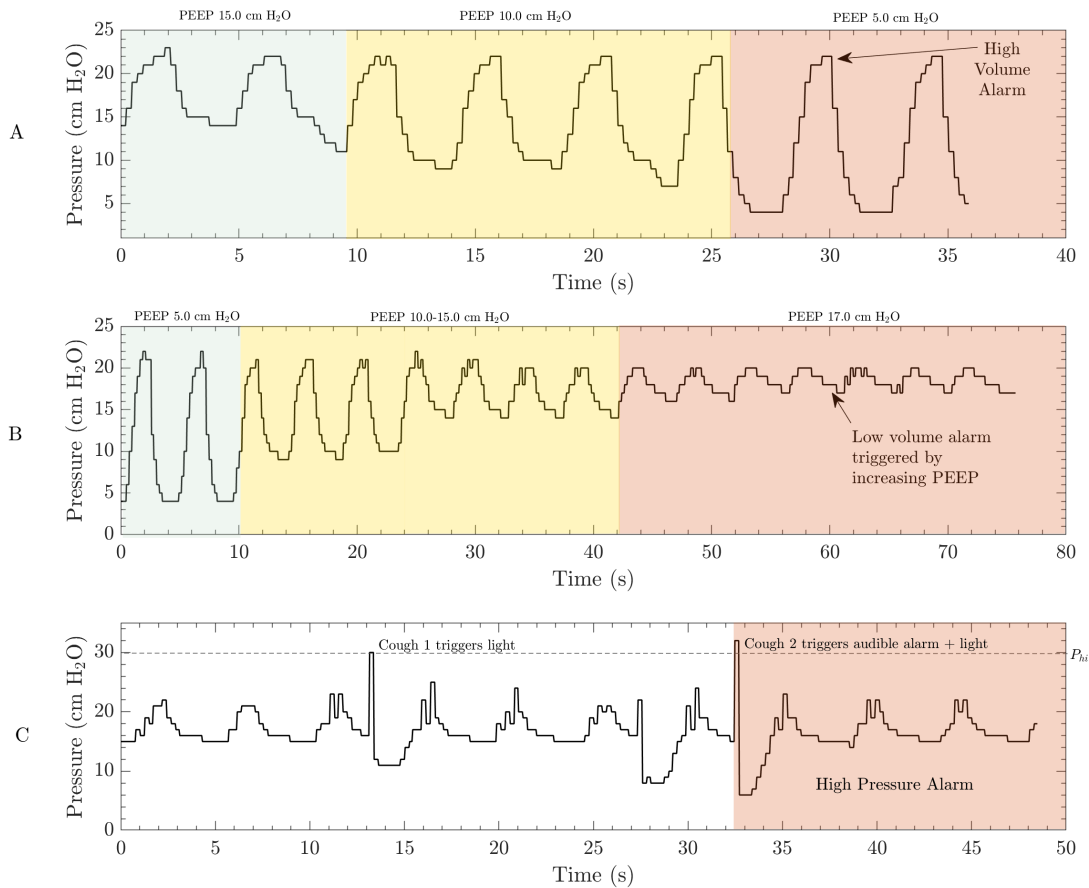
Figure A.3: The MADVent Mark V has alarms for high and low volume that may be set between 200 and 1000 cc. In this example, the system was run at a rate of 13 breaths per minute, a PEEP value of 15 cm H_2O and the compliance on the lung simulator was initially set to 0.03 cc/ cm H_2O. A) The high-volume alarm threshold was set to 500 cc for the first case. PEEP was decreased from 15 cm H_2O to 5 cm H_2O in order to increase the tidal volume delivered to the lung simulator. A high-volume alarm was triggered when the calculated tidal volume exceed the limit set by the healthcare provider. A relevant clinical scenario in this case would be a leak in the inspiratory line leading to an increase in volume delivered without the target pressure being reached. B) The low-volume alarm is triggered once the calculated volume drops below the lower limit set by the healthcare provider. This was simulated by increasing the PEEP up to 17 cm H_2O. A relevant clinical scenario for this case would be the inspiratory line being kinked. C) The high-pressure scenario was simulated by interrupting the expansion of the lung simulator during inspiration to simulate a patient coughing. The high-pressure alarm was set off when the pressure exceeded the set value of 30 cm H_2O.

A.3   Results

To confirm the ventilator's operating and alarm capabilities, it was tested on a lung simulator. Under pressure-control ventilation, the high-volume, low-volume, and high-pressure alarms were all successfully triggered when their alarm set points were crossed, as illustrated in Fig. A.3. For a pressure-controlled system, a high-volume alarm could be triggered by too large of a ΔP (Δpressure = PIP - PEEP), an increase in the patient's compliance, or an accidental disconnect/leak in the inspiratory circuit. This was experimentally demonstrated by slowly increasing the ΔP through PEEP reduction in Fig. A.3A. A low-volume alarm state could be induced by a blockage in the inspiratory circuit, a decrease in the patient's compliance, or too small of a ΔP set by the healthcare provider. This alarm was demonstrated in our system by gradually increasing the PEEP during operation, which gradually lowered the ΔP, and ultimately dropped the tidal volume below the set alarm threshold (Fig. A.3B). The high pressure alarm may be elicited by a patient coughing or "fighting" the ventilator, simulated in our demonstration in Fig. A.3C, potentially indicating insufficient sedation or as a sign of circuit obstruction (along with the low-volume alarm).

In addition to alarms for pressure, the system is equipped with temperature sensors that are mounted on the stepper motor and the motor controller, in order to continually monitor temperature and alert the healthcare provider if the measured motor temperature exceeds 65°C; these mechanical components are far removed from the ventilatory circuit. An encoder mounted on the shaft and an photointerrupter switch attached to the lever arm serve to detect mechanical faults that may occur during operation.

Though we made the decision to omit flow sensors due to their expense [418] and complexity [426], we still require an accurate prediction of the tidal volume in order to safely provide high and low volume alarms. This is achieved by monitoring the compression of the bag. The volume delivered by compressing the bag is directly proportional to the decrease in
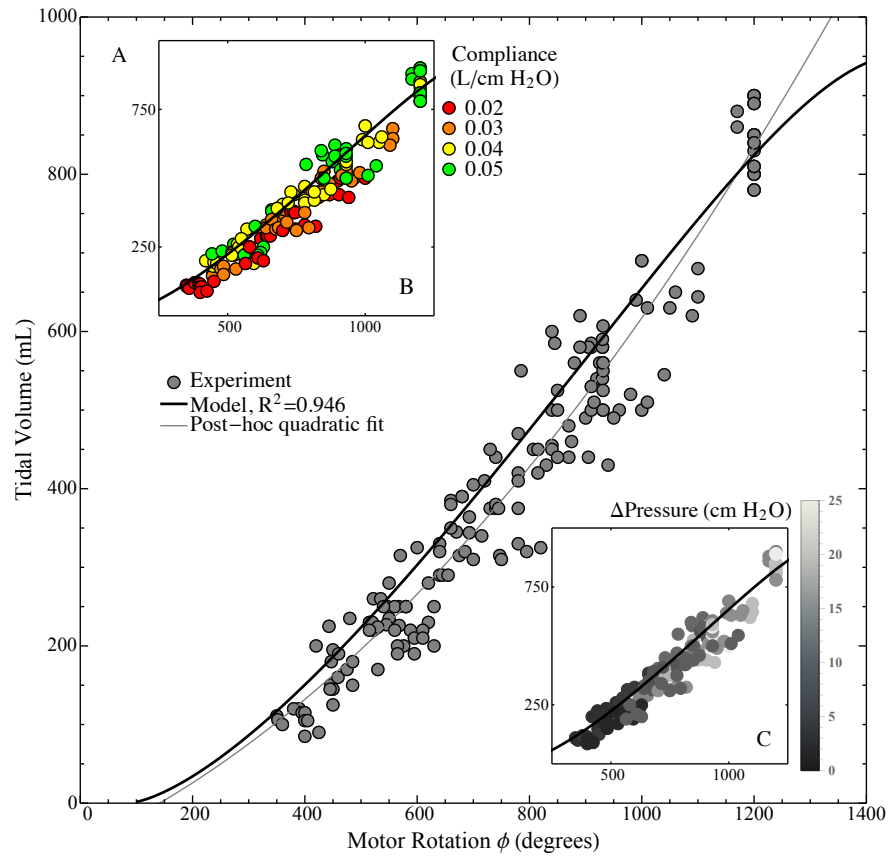
Figure A.4: Tidal volume is related to the rotation of the motor via compression of the bag, as indicated (A) by the experimental results compared with a model $V_{\text{tidal}} = V_{\text{tidal}}(\phi)$ constructed from the geometry (see Supplementary Information for the full derivation). Furthermore, a post-hoc quadratic curve fit ($3.47 \times 10^{-4}\phi^2 + 0.322\phi - 52.5$ with $R^2 = 0.953$) is provided showing a slightly improved fit, indicating that a quadratic function can adequately represent the tidal volume as a function of the angle ϕ. In B, the volume corresponding to a given motor rotation is seen to increase with compliance—accounting for the spread in the data along with experimental error. In C, the difference between peak pressure and PEEP is seen to increase along the model, as expected due to the ideal gas law.

cross sectional area, A_i, of the bag as it is compressed by the lever. Thus, if we can relate A_i to the rotation of the motor, then we can predict the tidal volume, V_{tidal}, since we are controlling the rotation of the motor shaft. An exercise in trigonometry provided in the Supplementary Information reveals the relationship between the rotation of the motor shaft, ϕ and the tidal volume produced by the bag, V_{tidal}. This relationship, $V_{tidal}(\phi)$, is validated in Fig. A.4.

We performed experiments across the full range of ventilation capabilities with four independent parameters, compliance, PEEP, inspiratory time, and peak pressure, and two dependent measurements, tidal volume and motor rotation. Figure A.4 shows that these potentially confounding variables do not have a large effect on the relationship between volume and motor rotation. A quadratic curve was fit to the data (with a coefficient of determination of $R^2 = 0.953$) in order to validate our model. The model generally predicts larger volumes as expected since it does not account for the compliance of the lung and thus should match the higher range of data points. The model assumes two rigid bodies are intersecting, but in reality the lever is rigid while the bag is elastic. As the bag is compressed its shape changes, which accounts for the relative linearity of the fit curve compared with the model.

The volume-rotation relationship described by our model is embedded in the ventilation code so that the volume alarms are triggered correctly without a flow sensor, accurate to a mean value of 5%. It is important to note that manual resuscitation bags with different structure/geometry than the one used in this calibration (Ambu SPUR II, Ambu Inc, Copenhagen, Denmark) will not have identical volume-rotation relationships, $V_{tidal}(\phi)$, and volume-related alarms will therefore be less accurate without another calibration. We expect this effect to be small since adult-sized, self-inflating resuscitation bags have similar geometries and total volumes. Recall these bags are all designed for the same purpose and are interchangeably used by hospital personnel.

The overall range of parameters at which the system is capable of operating is listed in Table A.1, which align with the specifications recommended for ARDS patients [412, 413, 411].

Table A.1: Suitable MADVent Mark V operating parameter ranges

Operating Parameter	Tested Range
Target Inspiratory Pressure	10 – 35 cm H_2O
Tidal Volume (V_T)	200 – 1000 $m\ell$
Respiratory rate (RR)	6 – 35 bpm
Inspiratory time	1 – 3.0 sec
Low-pressure alarm threshold	0 – 20 cm H_2O
High-pressure alarm threshold	30 – 50 cm H_2O
High-volume alarm threshold	200 – 1000 $m\ell$
Low-volume alarm threshold	200 – 1000 $m\ell$

In addition to the testing reported in Fig. A.4, we also performed tests according to ISO standards (see Supplementary Information), which dictate airway resistance values.

The hardware on the system allows for a volume-driven approach to ventilation in addition to pressure-controlled ventilation with continuous feedback. Tests were conducted to characterize the system operating in this mode, but a proper continuous feedback volume-control system would require an in-line flow sensor, adding to the cost and complexity of the system. However, we did test the system as a volume-driven ventilator and the results are included in Fig. A.5. This mode was solely for evaluation purposes and will not be available to the healthcare provider. The volume-driven mode includes user-defined limits for low and high pressure. Baseline conditions were set to 5.0 cm H_2O PEEP, a respiratory rate of 14 breaths per minute, and an initial compliance of 0.03 $\ell/(cm\ H_2O)$. Figure A.5A illustrates a drastic change in compliance resulting in the trigger of a high-pressure alarm. Examples where a high-pressure alarm would be triggered are a blockage in the endotracheal tube, drastic change in patient lung compliance, or bronchospasm. The alarm was programmed to trigger upon two consecutive high pressure events, after which the system will release the bag compression arm and commence a new respiration cycle at lower tidal volumes but increased rate in order to meet the minute ventilation set by the healthcare provider. In the event of an accidental disconnection of the endotracheal tube or other significant leak in the system, a low-pressure alarm will be triggered as illustrated in Fig. A.5B. Kinking of the endotracheal tube or a sudden change in resistance can lead to a high-pressure alarm as plotted in
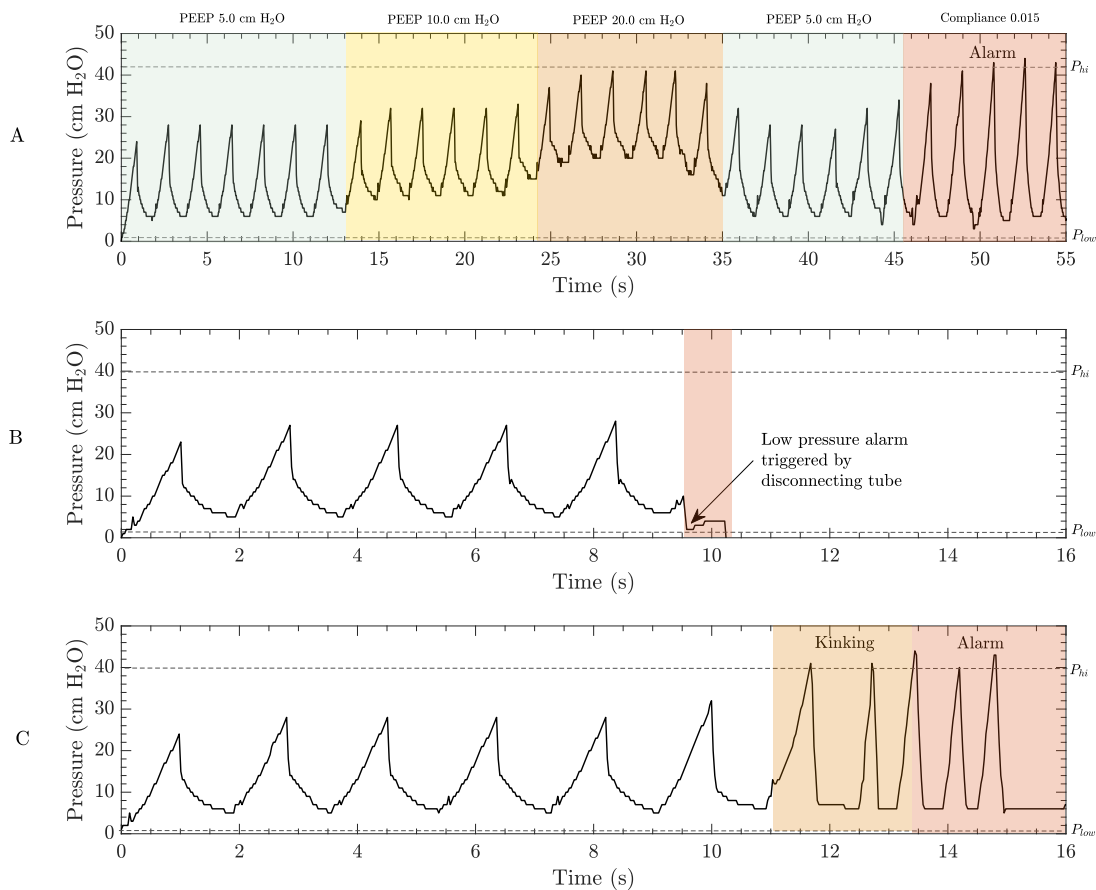
Figure A.5: The volume-driven version of the MADVent comes with alarms for high and low pressure that can be set between 0 and 50 cm H_2O defined by the caregiver. The system was initially set at a rate of 34 breaths per minute, a PEEP value of 5 cm H_2O was chosen and compliance on the lung simulator set to 0.03 $\ell/(cm\ H_2O)$. A) The low and high-pressure alarm thresholds were set to 2 cm H_2O and 42 cm H_2O respectively. PEEP values were increased from 5 cm H_2O to 20 cm H_2O and lowered back down to 5.0 cm H_2O to ensure that the in-line pressure sensor could detect and display changes in pressure values. A high-pressure condition was simulated by decreasing patient lung compliance. The system triggered an alarm once the pressure went above 42 cm H_2O. B) The low-pressure alarm is triggered once the in-line pressure value drops below the lower limit. A low-pressure situation was simulated by disconnecting the endotracheal tube to trigger an alarm which results in the system immediately stopping. C) In the event that the tubing is kinked or there is a blockage in the endotracheal tube, the pressure starts to rise until the upper threshold is reached. This triggers a high-pressure alarm and causes the system to resume ventilation at a lower volume, but at an increased rate according to the set minute ventilation.

191

Fig. A.5C.

A.4 Discussion

A number of solutions have been proposed to address the anticipated shortage of traditional ventilators during the COVID-19 outbreak [427, 428], including other low-cost ventilators [429, 430]. Splitting one ventilator among two or more patients, re-purposing continuous positive airway pressure (CPAP) machines, placing large orders for existing high cost commercial ventilators, and bringing retired ventilators out of storage are some of the proposed solutions to meet the demand for reliable ventilators. Although there have been several cases [427, 431] of healthcare workers around the world splitting ventilators for shared use among two or more patients, this method still requires further testing to better ensure safety of all patients on the shared circuit [428]. Placing large orders for ventilators has put a strain on supply chains, many of which are located in countries that are severely affected by the pandemic. Bringing retired ventilators out of storage and re-purposing CPAP machines could have unintended consequences due to component failures and a lack of testing for off-label use.

There are currently multiple groups working in parallel to develop ventilation solutions with the similar goal of providing care to patients with COVID-19. Notable devices are the Puritan Bennett$^{\text{TM}}$ 560 (PB560) developed by Medtronic and released under a temporary license to the public, the E-Vent in development at the Massachusetts Institute of Technology [424], and the Coventor developed at the University of Minnesota [425]. The PB560 is a fully functioned portable ventilator system, and with its functions come increased cost and increased complexity, both of which are issues when ventilators need to be produced quickly and in great quantity, especially with over-burdened supply lines in times of crisis. The MADVent, E-Vent, and Coventor ventilators are all less expensive and simpler to manufacture than the PB560.

The following information on the MIT E-Vent is representative of the publicly available

information at the time of this publication's writing, but may not remain accurate as their development process continues [424, 425]. The MIT E-Vent is described as a volume-control system with the option of being triggered by spontaneous respirations. The question of calibration is mentioned in the MIT E-Vent's results summary [432], but follow-up data releases do not mention this, although their implementation of a spirometer to measure flow does partially address this. The E-Vent does have the advantage of multiple rounds of testing in a porcine model in addition to a robust team of volunteers working on its development [432].

Although the Coventor [425] recently received FDA Emergency Use Authorization, details on controls, features, patient safety, and clinician controls are not publicly available. It is not clear what degree of patient monitoring is possible with the Coventor, what respiratory parameters can be adjusted, or the presence and function of alarms based on publicly available information. At the time of this publication, it is estimated that the MADVent Mark V will cost around $250. This is likely less than the E-Vent, whose publicly cited costs vary between $150-$500 and lack recent robust citation, and certainly less than the publicly disclosed $1000 cost of the Coventor ($150 advertised component-only cost) [425, 424]. The MIT E-vent and the MADVent have similar alarm and failure mode functions, but little is currently known about the Coventor's function or safety features.

Compared to these other low-resource ventilator examples, the UCSD MADVent Mark V is the only device offering pressure-controlled ventilation. Despite the relative simplicity of our mechanical system, the electronics of the system allow clinicians wide-ranging control over ventilation characteristics and alarms. A conclusion on which device is most appropriate or effective in the current crisis cannot be responsibly made until all devices under consideration have publicly available testing, calibration, and safety monitoring information. Low-cost, scalable ventilator technologies such as this may also have applications for use in rural environments, low-resource environments, natural disaster response, and other mass casualty scenarios.[433, 434]

The MADVent Mark V pressure-controlled ventilator works by compressing a self-

inflating bag-valve resuscitator until a target inspiratory pressure is reached. The peak pressure is set by the healthcare provider. An in-line pressure sensor continually monitors pressure and provides feedback to control a lever arm that compresses the self-inflating bag until the set peak pressure is attained. The system reaches the peak pressure at the inspiratory time per the set respiratory rate, both as selected by the healthcare provider, and serving to define the remaining expiratory time and idle time between breaths. We prefer this pressure-controlled version of the MADVent as it is continually regulated by means of a feedback loop between the pressure sensor and the motor, in order to accommodate changes in lung compliance and enable finer control over the delivery of mechanical ventilation. Though we have chosen the pressure-controlled version for our final configuration, the hardware on the system is also capable of supporting a volume-driven ventilation system that relies on compressing the bag by a specific amount corresponding to the volume set by the healthcare provider (Fig. A.5). This version would also monitor in-line pressure during the breath cycle using the same sensors as the pressure-controlled version. Here, we make the distinction between pressure-controlled and volume-driven approaches by pointing out there is no continuous feedback from any sensed tidal volume delivered to the patient and the compression of the bag, because there is no integrated flow sensor for this purpose. On the other hand, if it is determined that breath triggering is a necessary feature, the MADVent Mark V already has the hardware in place to provide this feature. This would allow the ventilator to be used in patients with lower levels of sedation and who are capable of initiating breaths but require the support of a ventilator.

One well-known limitation of using bipolar stepper motors in any application is the high current they require when operating at low speeds. As the motor pauses for a period of time at each step in order to provide slow rotation, it could theoretically lead to high power consumption and overheating. However, this difficulty was foreseen, and both pulse-width modulation (PWM) and current limiting was programmed into the controller to eliminate it. Pulse-width modulation lowers the effective voltage drop across the motor for longer step times, in turn lowering the

current draw of the motor. A motor controller was chosen that is capable of significantly higher current than the programmed limit current, preventing the motor controller from overheating. The robust motor controller set up and software limiting, combined with a power supply capable of no more than 3 A of constant draw, comprehensively limits possible thermal issues. As an added measure of safety, the temperature of the motor and circuits are continually monitored using temperature sensors and a visual alarm indicator is displayed in the event of the system overheating. The rotational position of the motor and the arm are tracked during operation to ensure mechanical integrity during operation. The limitations of individual ventilator components were identified and thorough testing performed to ensure no mechanical or electrical problems during operation. A full list of all potential errors and the systems we have in place to mitigate these risks are included in the Supplementary Information.

Patients with COVID-19 and ARDS can require mechanical ventilation for over two weeks[435, 436]. All electrical components in the system were chosen to provide reliable continuous operation for such patients over weeks of use. The mechanical components chosen are all capable of withstanding the standard operational load due to the weight of the motor and that of the battery. The components of the ventilator were placed to balance the system across the width and length of the frame, and to provide easy access for maintenance and disinfection. The materials of the ventilator may be sanitized with conventional disinfectants such as 0.5% hydrogen peroxide, 0.5% sodium hypochlorite (bleach), and 70% ethanol. As part of the design we attempted to integrate as many standard hospital items as possible. These items, such as the bag-valve resuscitator and PEEP valve, are staples of the hospital environment and have already undergone rigorous testing for safety, longevity, and compatibility with conventional disinfectants.

A.5 Conclusions

The lack of adequate ventilatory support has already caused preventable deaths in the first few months of the COVID-19 pandemic and more can be expected unless ventilators can quickly be provided to areas overburdened with COVID-19 patients. The MADVent is capable of safely meeting the diverse ventilation requirements of COVID-19 patients because its parameters are adjustable over the broad ranges necessary for ARDS patients. The combination of off-the-shelf components and laser cut parts in addition to our choice of mechanically driven pressure control makes our design both low cost and rapidly manufacturable. The essential qualities of safety, effectiveness, low cost, and rapid manufacturablity make it a feasible option for scaled production and use in current and future health crises.

The MADVent Mark V ventilator generates a pressure curve up to a set level in a prescribed rise time. A widely available resuscitator bag is used to drive flow with a simple mechanical system controlled by a widely available stepper motor, controller, and system-on-a-chip computer. Standard control of PEEP is provided with a disposable off-the-shelf valve. Volume and pressure alarms are provided for safety and additional alarms provided for electronics temperature and device failure detection ensure that healthcare providers will be informed if this life support system shows signs of failure. Tidal volumes and pressure waveforms were tested and verified on a lung simulator, confirming the prototype is effective over the intended operating range.

As we continue to refine the design of the MADVent, we intend to add additional features to bring our low-cost ventilator even closer to the expansive capabilities of standard ICU mechanical ventilators, though still at a reduced cost, to facilitate broader adoption. Much of the high cost associated with modern ventilators is a consequence of thorough adherence to safety regulations and ensuring the manufacturer is responsive to patient outcomes per FDA requirements. Our ventilator is not a substitute for these well-designed and produced systems. Instead, our system—like many other recent low-cost ventilators arising in this emergency—is
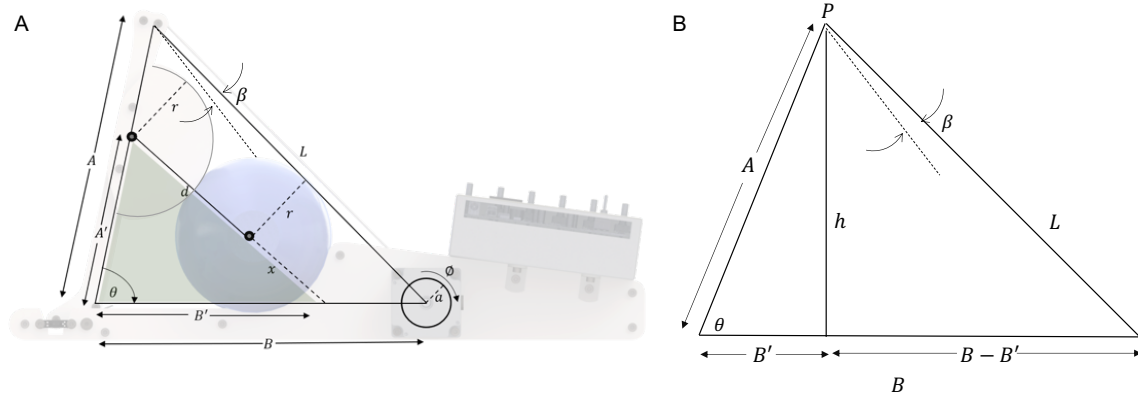
Figure A.6: The side view of the MADVent ventilator, to scale, including geometry sufficient to determine the relationship between the angle of rotation of the spool and the delivered tidal volume(A) and estimated torque to compress the bag(B) (V_{tidal}).

a ventilator of last resort during a pandemic or mass casualty event. The design focuses upon patient safety, simplicity of manufacturing, and modularity. The system, in its current state of development, can easily accommodate new modules that enable more sophisticated features, such as flow monitoring, which can enable additional ventilation modes and provide healthcare operators more information regarding a patient's breathing.

A.6 Supplementary

Torque Estimation

Referring to Supplementary Fig. A.6, there is a force, $F_b = p_b \times A_b + F_s$, on the lever due to contact with a pressurized bag, where p_b is the pressure in the bag, A_b is the contact area between the bag and the lever, and F_s is the inherent force of the self-inflating bag.

We assume the pressure in the bag is 40 cm H_2O, the largest pressure anticipated to be used during normal operation. The contact area in the most compressed state can be approximated by the radius of the circular portions of the lever and the distance between these two, $A_b = 6.5 \times 3 = 19.5\,\text{cm}^2$. The force produced by the self-inflating bag estimated by applying an

increasing amount of static weight to the bag until the force of gravity on the weight overcomes F_s, ≈ 10 N. The torque required about the hinge is estimated by $T_{arm} = A'F_b$, presuming the force is perpendicular to the arm. But given that the string is not always perpendicular to the arm depending on the angle of rotation, the force produced due to motor rotation is given by $\frac{F_b}{cos(\beta)}$, where β is the angle between the lanyard and the normal direction to the arm and F is the perpendicular component of tension from the string. Using the law of of cosines and referring to Fig.A.6 B, the relationship between θ, the angle between the lever and the base, and β can be solved by the equation:

$$\frac{2AB\sin^2(\theta)\cos(\theta+\beta)}{\cos(\beta)} + (B - A\cos(\theta))^2 = A^2\sin^2(\theta) + \frac{B^2\sin^2(\theta)}{\cos^2(\beta)} \tag{A.1}$$

A and B in the above equation are known lengths, and the system operates over $37° \leq \theta \leq 78°$ based on the geometry of the device. This equation allows us to solve for $\cos(\beta)$ and hence, find the torque required to compress the bag.

$$T_{\text{motor}} = \frac{aF_b}{\cos(\beta)} \tag{A.2}$$

The above expression produces a torque ranging from $140\ mN - m$ to $180\ mN - m$ as represented in Supplementary Fig. A.7. The expression does not take into account the changing contact area of the bag or the increasing force during short inspiration times. The force for a particular inspiration time can vary by as much as a factor of 3, given the range of inspiration times that the system allows. An additional factor in the system that can limit the torque delivered to the bag include the torsion spring, which always acts to restore the arm to its original position. Consequently, a factor of safety of 2 was taken into account while choosing a motor, which produces an estimate for the required motor torque to be 1.8 N-m. This is the rated torque of the selected motor.
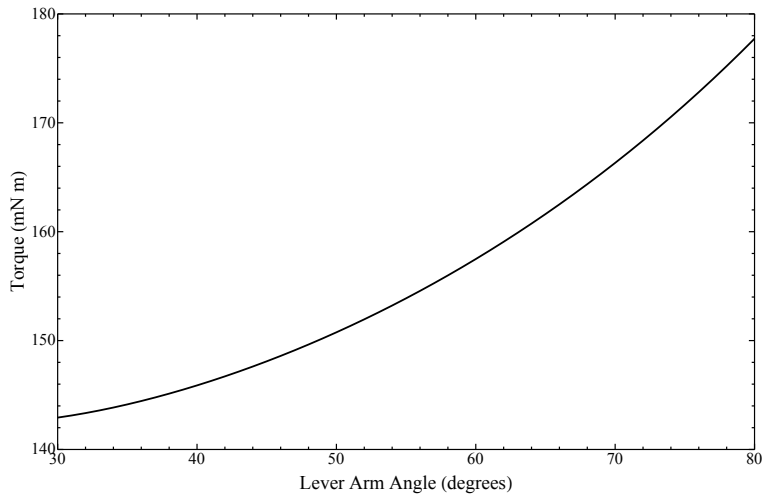
Figure A.7: Motor torque as a function of θ, the angle between the lever arm and the base of the ventilator.

Volume derivation

When the motor rotates by an angle ϕ in Supplemental Fig. A.6, the distance between the tip of the lever arm and the motor shaft, L, is reduced by the amount $a\phi$. The rotation furthermore reduces both the length, d, between the center of the bag and the center of the circular portion of the lever, and the angle θ. The tidal volume is the cross-sectional area A_i multiplied by a length scale, b_d, dependent upon the bag's length in a somewhat complex manner as detailed below.

The equation for the area of intersection, A_i of two circles of equal radius, r whose centers are separated by a distance, d is

$$A_i(d) = 2r^2 \arccos \frac{d}{2r} - \frac{d}{2}\sqrt{4r^2 - d^2}. \tag{A.3}$$

The law of cosines determines the length of string between lever and motor shaft,

$$l(\theta) = \sqrt{A^2 + B^2 - 2AB\cos\theta}. \tag{A.4}$$

Knowledge of the coordinates of the centers of the circular objects leads to an expression for the

center separation distance,

$$d(\theta) = \sqrt{(x - y\cos\theta)^2 + (r - y\sin\theta)^2}. \qquad (A.5)$$

The arc-length formula gives the amount by which l decreases when the motor shaft rotates by ϕ,

$$\alpha(\phi) = a\phi. \qquad (A.6)$$

The total length of the lanyard is assumed to be constant,

$$L = l - \alpha, \qquad (A.7)$$

where l is the portion wound around the spool and α is the portion between the shaft and the lever.

Rearranging eqn. A.7, we can solve for l and set the result equal to eqn. A.4. Solving for θ and substituting into eqn. A.5 and then eqn. A.3 produces $A_i(\phi)$, the area of intersection as a function of the motor rotation. To find the volume change in compression, $V_{\text{tidal}}(\phi)$, we then

multiply the area $A_i(\phi)$ by a constant b_d related to the length of the bag,

$$V_{\text{tidal}}(\phi) = b_d \left(2r^2 \cos^{-1}\left(\frac{\sqrt{\left(r - A'\sqrt{1 - \frac{\left(-(L-(a\phi))^2 + A^2 + B^2\right)^2}{4A^2B^2}}\right)^2 + \left(B' - \frac{A'\left(-(L-(a\phi))^2 + A^2 + B^2\right)}{2AB}\right)^2}}{2r} \right) \right.$$

$$-\frac{1}{2}\sqrt{\left(-\left(r - A'\sqrt{1 - \frac{\left(-(L-(a\phi))^2 + A^2 + B^2\right)^2}{4A^2B^2}}\right)^2 - \left(B' - \frac{A'\left(-(L-(a\phi))^2 + A^2 + B^2\right)}{2AB}\right)^2 + 4r^2}\right)}$$

$$\left.\sqrt{\left(\left(r - A'\sqrt{1 - \frac{\left(-(L-(a\phi))^2 + A^2 + B^2\right)^2}{4A^2B^2}}\right)^2 + \left(B' - \frac{A'\left(-(L-(a\phi))^2 + A^2 + B^2\right)}{2AB}\right)^2\right)} \right).$$

$$(A.8)$$

The bag length-dependent factor, b_d, is obtained by noting the maximum total volume expelled from the bag when fully compressed within the prototype, 1175 mℓ, and calculating the equivalent length of a cylinder with this volume and a radius equal to that of the bag. To improve the result, the maximum volume determined in this way should further be adjusted for the lanyard's elastic stretch during operation, accomplished by finding the y-intercept of the experimentally obtained tidal volume to rotor angle data, giving 1225 mℓ. Setting this volume equal to the equation for the volume of a cylinder, $1225 = (b_d)(\pi r^2)$, in which the length of the equivalent cylinder is b_d, we find $b_l = 9.23$ cm. All other constants are directly measured from the prototype as provided in Supplementary Fig. A.6.

ISO Test Results

Table A.2 corresponds to the clinically relevant portion of Table 201.105 from ISO 80602-2-12 [437] for pressure-controlled mechanical ventilators. The resulting tidal volumes, as mea-

Table A.2: Test results according to ISO 80601-2-12:2020(E) Table 201.105. All tests were performed using a one second inspiratory time.

Rate (bpm)	Inspiratory Pressure (cmH$_2$O)	PEEP (cmH$_2$O)	Compliance $\left(\frac{\text{L}}{\text{cmH}_2\text{O}}\right)$	Airway Resistance $\left(\frac{\text{cmH}_2\text{O s}}{\text{L}}\right)$	Tidal Volume (mL)
20	10	5	0.05	5	236
12	15	10	0.05	20	212
20	25	5	0.02	5	384
20	25	10	0.02	20	292
20	15	5	0.02	20	166
12	25	10	0.02	50	187
20	30	5	0.01	50	203
20	25	10	0.01	10	167

sured by the lung simulator, are reported for a range of inspiratory pressure, PEEP, compliance, rate, and airway resistance values. These volume values do not match the expected values outlined by ISO 80602-2-12 Table 201.105 [437]. We instead find good agreement between the volume reported by the lung simulator and the volume calculated using inspiratory pressure and compliance at lower airway resistances (eqn. A.9).

$$V_{\text{tidal}} = C\big(\text{PIP} - \text{PEEP}\big) \tag{A.9}$$

A.7 Acknowledgement

Bibliography

[1] K. Shibayama, K. Yamanouchi, H. Sato, and T. Meguro, "Optimum cut for rotated y-cut linbo 3 crystal used as the substrate of acoustic-surface-wave filters," *Proceedings of the IEEE*, vol. 64, no. 5, pp. 595–597, 1976.

[2] C. K. Campbell, "Applications of surface acoustic and shallow bulk acoustic wave devices," *Proceedings of the IEEE*, vol. 77, no. 10, pp. 1453–1484, 1989.

[3] D. Ciplys and R. Rimeika, "Measurements of electromechanical coupling coefficient for surface acoustic waves in proton-exchanged lithium niobate," *Ultrasound*, vol. 33, no. 3, pp. 14–20, 2014.

[4] V. Soluch and M. Lysakowska, "Surface acoustic waves on x-cut linbo/sub 3," *IEEE transactions on ultrasonics, ferroelectrics, and frequency control*, vol. 52, no. 1, pp. 145–147, 2005.

[5] F. S. Hickernell, "Surface acoustic wave technology macrosuccess through microseisms," *Physical Acoustics*, vol. 24, pp. 135–207, 1999.

[6] M. B. Dentry, L. Y. Yeo, and J. R. Friend, "Frequency effects on the scale and behavior of acoustic streaming," *Physical Review E*, vol. 89, no. 1, p. 013203, 2014.

[7] G. M. Whitesides, "The origins and the future of microfluidics," *Nature*, vol. 442, no. 7101, p. 368, 2006.

[8] E. K. Sackmann, A. L. Fulton, and D. J. Beebe, "The present and future role of microfluidics in biomedical research," *Nature*, vol. 507, no. 7491, p. 181, 2014.

[9] H. Becker, "Hype, hope and hubris: the quest for the killer application in microfluidics," *Lab on a Chip*, vol. 9, no. 15, pp. 2119–2122, 2009.

[10] H. Becker and C. Gärtner, "Microfluidics-enabled diagnostic systems: Markets, challenges, and examples," *Microchip Diagnostics: Methods and Protocols*, pp. 3–21, 2017.

[11] C.-Y. Lee, W.-T. Wang, C.-C. Liu, and L.-M. Fu, "Passive mixers in microfluidic systems: A review," *Chemical Engineering Journal*, vol. 288, pp. 146–160, 2016.

[12] D. J. Collins, T. Alan, K. Helmerson, and A. Neild, "Surface acoustic waves for on-demand production of picoliter droplets and particle encapsulation," *Lab on a Chip*, vol. 13, no. 16, pp. 3225–3231, 2013.

[13] L. Van Valen, "A new evolutionary law," *Evol Theory*, vol. 1, pp. 1–30, 1973.

[14] E. F. F. Chladni, *Discoveries on the theory of sound*. Weidmanns, Erben und Reich, 1787.

[15] M. Faraday, "On the forms and states assumed by fluids in contact with vibrating elastic surfaces," *Philos. Trans. R. Soc. London*, vol. 121, no. 319, p. 1831, 1831.

[16] A. Kundt, "On a new kind of acoustic dust figures and on the application of the same for determining sound velocity in solid bodies and gases," *Annals of Physics*, vol. 203, no. 4, pp. 497–523, 1866.

[17] J. Friend and L. Y. Yeo, "Microscale acoustofluidics: Microfluidics driven via acoustics and ultrasonics," *Reviews of Modern Physics*, vol. 83, no. 2, p. 647, 2011.

[18] X. Ding, P. Li, S.-C. S. Lin, Z. S. Stratton, N. Nama, F. Guo, D. Slotcavage, X. Mao, J. Shi, F. Costanzo, *et al.*, "Surface acoustic wave microfluidics," *Lab on a Chip*, vol. 13, no. 18, pp. 3626–3649, 2013.

[19] L. Y. Yeo and J. R. Friend, "Surface acoustic wave microfluidics," *Annual Review of Fluid Mechanics*, vol. 46, pp. 379–406, 2014.

[20] G. Destgeer and H. J. Sung, "Recent advances in microfluidic actuation and micro-object manipulation via surface acoustic waves," *Lab on a Chip*, vol. 15, no. 13, pp. 2722–2738, 2015.

[21] C. Eckart, "Vortices and streams caused by sound waves," *Physical review*, vol. 73, no. 1, p. 68, 1948.

[22] L. Rayleigh, "On waves propagated along the plane surface of an elastic solid," *Proceedings of the London Mathematical Society*, vol. 1, no. 1, pp. 4–11, 1885.

[23] R. White and F. Voltmer, "Direct piezoelectric coupling to surface elastic waves," *Applied Physics Letters*, vol. 7, no. 12, pp. 314–316, 1965.

[24] B. Jaffe, *Piezoelectric ceramics*, vol. 3. Elsevier, 2012.

[25] H. Birol, D. Damjanovic, and N. Setter, "Preparation and characterization of (k 0.5 na 0.5) nbo 3 ceramics," *Journal of the European Ceramic Society*, vol. 26, no. 6, pp. 861–866, 2006.

[26] X. Y. Kong and Z. L. Wang, "Spontaneous polarization-induced nanohelixes, nanosprings, and nanorings of piezoelectric nanobelts," *Nano Letters*, vol. 3, no. 12, pp. 1625–1631, 2003.

[27] A. J. Lovinger, "Ferroelectric polymers," *Science*, vol. 220, no. 4602, pp. 1115–1121, 1983.

[28] S. M. Nakhmanson, M. B. Nardelli, and J. Bernholc, "Collective polarization effects in β-polyvinylidene fluoride and its copolymers with tri- and tetrafluoroethylene," *Phys. Rev. B*, vol. 72, p. 115210, Sep 2005.

[29] J. Curie and P. Curie, "Contractions and dilatations produced by electric voltages in crystals," *Compt. Makes*, vol. 93, pp. 1137–1140, 1881.

[30] X.-h. Du, J. Zheng, U. Belegundu, and K. Uchino, "Crystal orientation dependence of piezoelectric properties of lead zirconate titanate near the morphotropic phase boundary," *Applied physics letters*, vol. 72, no. 19, pp. 2421–2423, 1998.

[31] S. Huang, J. Chang, L. Lu, F. Liu, Z. Ye, and X. Cheng, "Preparation and polarization of 0–3 cement based piezoelectric composites," *Materials Research Bulletin*, vol. 41, no. 2, pp. 291–297, 2006.

[32] M. Ozgul, K. Takemura, S. Trolier-McKinstry, and C. A. Randall, "Polarization fatigue in pb (zn 1/3 nb 2/3) o 3–pbtio 3 ferroelectric single crystals," *Journal of Applied Physics*, vol. 89, no. 9, pp. 5100–5106, 2001.

[33] W. P. Mason, "Piezoelectricity, its history and applications," *The Journal of the Acoustical Society of America*, vol. 70, no. 6, pp. 1561–1566, 1981.

[34] I. Donald, "Sonar the story of an experiment," *Ultrasound in medicine & biology*, vol. 1, no. 2, pp. 109–117, 1974.

[35] A. Manbachi and R. S. Cobbold, "Development and application of piezoelectric materials for ultrasound generation and detection," *Ultrasound*, vol. 19, no. 4, pp. 187–196, 2011.

[36] W. B. Robertson, "The ultrasonic cleaner in the laboratory," *J. Chem. Educ*, vol. 44, no. 8, p. 460, 1967.

[37] L. Rozenberg, "Efficiency of ultrasonic cleaning," in *Physical Principles of Ultrasonic Technology*, pp. 270–318, Springer, 1973.

[38] N. Dam, "Non-contact ultrasonic micromeasurement system," Mar. 9 1999. US Patent 5,880,364.

[39] D. Yang, "Ultrasonic range finder," Feb. 12 2008. US Patent 7,330,398.

[40] S. Saadon and O. Sidek, "A review of vibration based mems piezoelectric energy harvesters," *Energy Conversion and Management*, vol. 52, no. 1, pp. 500–504, 2011.

[41] M. K. Kurosawa, O. Kodaira, Y. Tsuchitoi, and T. Higuchi, "Transducer for high speed and large thrust ultrasonic linear motor using two sandwich-type vibrators," *IEEE transactions on ultrasonics, ferroelectrics, and frequency control*, vol. 45, no. 5, pp. 1188–1195, 1998.

[42] B. Watson, J. Friend, and L. Yeo, "Piezoelectric ultrasonic micro/milli-scale actuators," *Sensors and Actuators A: Physical*, vol. 152, no. 2, pp. 219–233, 2009.

[43] J. Friend, K. Nakamura, and S. Ueha, "A piezoelectric micromotor using in-plane shearing of pzt elements," *IEEE/ASME Transactions on Mechatronics*, vol. 9, no. 3, pp. 467–473, 2004.

[44] S. Tonami, A. Nishikata, and Y. Shimizu, "Characteristics of leaky surface acoustic waves propagating on linbo 3 and litao 3 substrates," *Japanese journal of applied physics*, vol. 34, no. 5S, p. 2664, 1995.

[45] Y. V. Gulyaev, "Review of shear surface acoustic waves in solids," *IEEE transactions on ultrasonics, ferroelectrics, and frequency control*, vol. 45, no. 4, pp. 935–938, 1998.

[46] F. Martin, "Propagation characteristics of harmonic surface skimming bulk waves on st quartz," *Electronics Letters*, vol. 38, no. 16, pp. 941–942, 2002.

[47] V. L. Strashilov and V. M. Yantchev, "Surface transverse waves: properties, devices, and analysis," *IEEE transactions on ultrasonics, ferroelectrics, and frequency control*, vol. 52, no. 5, pp. 812–821, 2005.

[48] S. Collingon, O. Manor, and J. Friend, "Improving and predicting fluid atomization via hysteresis-free thickness vibration of lithium niobate," *Advanced Functional Materials*, 2017.

[49] B. Jaffe, R. Roth, and S. Marzullo, "Piezoelectric properties of lead zirconate-lead titanate solid-solution ceramics," *Journal of Applied Physics*, vol. 25, no. 6, pp. 809–810, 1954.

[50] I. Bretos, R. Jiménez, J. Garcïa-López, L. Pardo, and M. L. Calzada, "Photochemical solution deposition of lead-based ferroelectric films: Avoiding the pbo-excess addition at last," *Chemistry of Materials*, vol. 20, no. 18, pp. 5731–5733, 2008.

[51] "95/ec of the european parliament and of the council of 27 january 2003 on the restriction of the use of certain hazardous substances in electrical and electronic equipment." Directive, EU, 2002.

[52] Y. Saito, H. Takao, T. Tani, T. Nonoyama, K. Takatori, T. Homma, T. Nagaya, and M. Nakamura, "Lead-free piezoceramics," *Nature*, vol. 432, pp. 84–87, 11 2004.

[53] K. Uchino and S. Hirose, "Loss mechanisms in piezoelectrics: how to measure different losses separately," *IEEE Transactions on Ultrasonics, ferroelectrics, and frequency control*, vol. 48, no. 1, pp. 307–321, 2001.

[54] S. Jyomura, K. Nagatsuma, and H. Takeuchi, "Saw propagation loss mechanism in piezo-electric ceramics," *Journal of Applied Physics*, vol. 52, no. 7, pp. 4472–4478, 1981.

[55] R. N. Thurston, A. D. Pierce, and E. P. Papadakis, *Reference for Modern Instrumentation, Techniques, and Technology: Ultrasonic Instruments and Devices I: Ultrasonic Instruments and Devices I*, vol. 23. Academic Press, 1998.

[56] R. Williamson, "Case studies of successful surface-acoustic-wave devices," in *Ultrasonics Symposium, 1977*, pp. 460–468, IEEE, 1977.

[57] C. Hartmann, "Systems impact of modern rayleigh wave technology," in *Rayleigh-Wave Theory and Application*, pp. 238–253, Springer, 1985.

[58] I. M. Mason and E. A. Ash, "Acoustic surface-wave beam diffraction on anisotropic substrates," *Journal of Applied Physics*, vol. 42, no. 13, pp. 5343–5351, 1971.

[59] A. Takayanagi, K. Yamanouchi, and K. Shibayama, "Piezoelectric leaky surface wave in linbo3," *Applied Physics Letters*, vol. 17, no. 5, pp. 225–227, 1970.

[60] A. Slobodnik and E. Conway, "New high-frequency high-coupling low-beam-steering cut for acoustic surface waves on linbo3," *Electronics Letters*, vol. 6, no. 6, pp. 171–173, 1970.

[61] C. K. Campbell, "Longitudinal-mode leaky saw resonator filters on 64/spl deg/yx lithium niobate," *IEEE transactions on ultrasonics, ferroelectrics, and frequency control*, vol. 42, no. 5, pp. 883–888, 1995.

[62] J. Hechner and W. Soluch, "Pseudo surface acoustic wave dual delay line on 41 yx linbo 3 for liquid sensors," *Sensors and Actuators B: Chemical*, vol. 111, pp. 436–440, 2005.

[63] A. Riaud, J.-L. Thomas, E. Charron, A. Bussonnière, O. B. Matar, and M. Baudoin, "Anisotropic swirling surface acoustic waves from inverse filtering for on-chip generation of acoustic vortices," *Physical Review Applied*, vol. 4, no. 3, p. 034004, 2015.

[64] M. Kurosawa, M. Takahashi, and T. Higuchi, "Ultrasonic linear motor using surface acoustic waves," *IEEE Transactions on Ultrasonics, Ferroelectrics, and Frequency Control*, vol. 43, no. 5, pp. 901–906, 1996.

[65] F. Guo, P. Li, J. B. French, Z. Mao, H. Zhao, S. Li, N. Nama, J. R. Fick, S. J. Benkovic, and T. J. Huang, "Controlling cell–cell interactions using surface acoustic waves," *Proceedings of the National Academy of Sciences*, vol. 112, no. 1, pp. 43–48, 2015.

[66] C. Devendran, N. R. Gunasekara, D. J. Collins, and A. Neild, "Batch process particle separation using surface acoustic waves (saw): integration of travelling and standing saw," *RSC Advances*, vol. 6, no. 7, pp. 5856–5864, 2016.

[67] M. Gasparetti, G. M. Revel, and E. P. Tomasini, "Theoretical modeling and experimental evaluation of an in-plane laser doppler vibrometer in different working conditions," in *Third International Conference on Vibration Measurements by Laser Techniques: Advances and Applications*, pp. 317–327, International Society for Optics and Photonics, 1998.

[68] P. Castellini, M. Martarelli, and E. Tomasini, "Laser doppler vibrometry: Development of advanced solutions answering to technology's needs," *Mechanical Systems and Signal Processing*, vol. 20, no. 6, pp. 1265–1285, 2006.

[69] S. Rothberg, M. Allen, P. Castellini, D. Di Maio, J. Dirckx, D. Ewins, B. J. Halkon, P. Muyshondt, N. Paone, T. Ryan, *et al.*, "An international review of laser doppler vibrometry: Making light work of vibration measurement," *Optics and Lasers in Engineering*, 2016.

[70] P. Castellini and C. Santolini, "Vibration measurements on blades of naval propeller rotating in water," in *Second International Conference on Vibration Measurements by Laser Techniques: Advances and Applications*, pp. 186–194, International Society for Optics and Photonics, 1996.

[71] A. Barker, P. Jaeger, and D. E. Oliver, "Non-contacting vibration measurement: role in design and industrial applications," *Stress and Vibration: Recent Developments in Industrial Measurement and Analysis*, vol. 1084, pp. 293–299, 1989.

[72] L. Zhu, K. Hallamasek, and D. Bogy, "Measurement of head/disk spacing with a laser interferometer," *IEEE Transactions on Magnetics*, vol. 24, no. 6, pp. 2739–2741, 1988.

[73] J. M. Sabatier and N. Xiang, "Laser-doppler-based acoustic-to-seismic detection of buried mines," in *AeroSense'99*, pp. 215–222, International Society for Optics and Photonics, 1999.

[74] R. White, "Acoustic and vibration transducers and measurement techniques," *Journal of Physics E: Scientific Instruments*, vol. 18, no. 9, p. 790, 1985.

[75] R. Herdier, D. Jenkins, E. Dogheche, D. Rèmiens, and M. Sulc, "Laser doppler vibrometry for evaluating the piezoelectric coefficient d 33 on thin film," *Review of scientific instruments*, vol. 77, no. 9, p. 093905, 2006.

[76] M. Miansari and J. R. Friend, "Acoustic nanofluidics via room-temperature lithium niobate bonding: A platform for actuation and manipulation of nanoconfined fluids and particles," *Advanced Functional Materials*, vol. 26, no. 43, pp. 7861–7872, 2016.

[77] J. E. Sader and J. R. Friend, "Note: Calibration of atomic force microscope cantilevers using only their resonant frequency and quality factor," *Review of Scientific Instruments*, vol. 85, no. 11, p. 116101, 2014.

[78] J. Friend and L. Yeo, "Using laser doppler vibrometry to measure capillary surface waves on fluid-fluid interfaces," *Biomicrofluidics*, vol. 4, no. 2, p. 026501, 2010.

[79] J. Vanherzeele, M. Brouns, P. Castellini, P. Guillaume, M. Martarelli, D. Ragni, E. P. Tomasini, and S. Vanlanduit, "Flow characterization using a laser doppler vibrometer," *Optics and lasers in engineering*, vol. 45, no. 1, pp. 19–26, 2007.

[80] J. Blamey, L. Y. Yeo, and J. R. Friend, "Microscale capillary wave turbulence excited by high frequency vibration," *Langmuir*, vol. 29, no. 11, pp. 3835–3845, 2013.

[81] T. Tachizaki, T. Muroya, O. Matsuda, Y. Sugawara, D. H. Hurley, and O. B. Wright, "Scanning ultrafast sagnac interferometry for imaging two-dimensional surface wave propagation," *Review of Scientific Instruments*, vol. 77, no. 4, p. 043713, 2006.

[82] G. Siegmund, "Sources of measurement error in laser doppler vibrometers and proposal for unified specifications," in *Proc. SPIE*, vol. 7098, pp. 70980Y–1, 2008.

[83] L. Yarovoi and G. Siegmund, "The effect of three-wave interference in laser doppler vibrometry," *Measurement Science and Technology*, vol. 15, no. 10, p. 2150, 2004.

[84] B. J. Halkon and S. Rothberg, "Vibration measurements using continuous scanning laser doppler vibrometry: theoretical velocity sensitivity analysis with applications," *Measurement science and technology*, vol. 14, no. 3, p. 382, 2003.

[85] J. Poittevin, F. Gautier, C. Pézerat, and P. Picart, "High-speed holographic metrology: principle, limitations, and application to vibroacoustics of structures," *Optical Engineering*, vol. 55, no. 12, pp. 121717–121717, 2016.

[86] M. Leclercq, P. Picart, G. Penelet, and V. Tournat, "Investigation of 3d surface acoustic waves in granular media with 3-color digital holography," *Journal of Applied Physics*, vol. 121, no. 4, p. 045112, 2017.

[87] T. Cacace, M. Paturzo, P. Memmolo, M. Vassalli, P. Ferraro, M. Fraldi, and G. Mensitieri, "Digital holography as 3d tracking tool for assessing acoustophoretic particle manipulation," *Optics Express*, vol. 25, no. 15, pp. 17746–17752, 2017.

[88] A. R. Rezk, J. R. Friend, and L. Y. Yeo, "Simple, low cost MHz-order acoustomicrofluidics using aluminium foil electrodes.," *Lab on a chip*, vol. 14, no. 11, pp. 1802–5, 2014.

[89] J. Nam and C. S. Lim, "A conductive liquid-based surface acoustic wave device," *Lab on a Chip*, vol. 16, no. 19, pp. 3750–3755, 2016.

[90] A. Winkler, P. Bergelt, L. Hillemann, and S. Menzel, "Influence of Viscosity in Fluid Atomization with Surface Acoustic Waves," *Open Journal of Acoustics*, vol. 6, pp. 23–33, 2016.

[91] A. Winkler, S. Harazim, D. Collins, R. Brünig, H. Schmidt, and S. Menzel, "Compact SAW aerosol generator," *Biomedical Microdevices*, vol. 19, no. 1, p. 9, 2017.

[92] R. J. Shilton, V. Mattoli, M. Travagliati, M. Agostini, A. Desii, F. Beltram, and M. Cecchini, "Rapid and controllable digital microfluidic heating by surface acoustic waves," *Advanced Functional Materials*, vol. 25, no. 37, pp. 5895–5901, 2015.

[93] M. J. Madou, *Fundamentals of microfabrication: the science of miniaturization*. CRC press, 2002.

[94] M. Pekarcikova, M. Hofmann, S. Menzel, H. Schrnidt, T. Gemming, and K. Wetzig, "Investigation of high power effects on Ti/Al and Ta-Si-N/Cu/Ta-Si-N electrodes for SAW devices," *IEEE Transactions on Ultrasonics, Ferroelectrics, and Frequency Control*, vol. 52, pp. 911–917, May 2005.

[95] D. Morgan, *Surface acoustic wave filters: With applications to electronic communications and signal processing*. Academic Press, 2010.

[96] H. Wohltjen, "Mechanism of operation and design considerations for surface acoustic wave device vapour sensors," *Sensors and Actuators*, vol. 5, no. 4, pp. 307–325, 1984.

[97] Z. Ma, A. J. Teo, S. H. Tan, Y. Ai, and N.-T. Nguyen, "Self-aligned interdigitated transducers for acoustofluidics," *Micromachines*, vol. 7, no. 12, p. 216, 2016.

[98] D. Morgan, "Surface acoustic wave filters," *Amsterdam: Elsevier*, 2007.

[99] J. Green and G. Kino, "Saw convolvers using focused interdigital transducers," *IEEE Transactions on Sonics Ultrasonics*, vol. 30, pp. 43–50, 1983.

[100] Y. Nakagawa, "A new saw convolver using multichannel waveguide," in *Ultrasonics Symposium, 1991. Proceedings., IEEE 1991*, pp. 255–258, IEEE, 1991.

[101] T. Marynowski, "Focusing transducer for saw beamwidth compression on yz lithium niobate," in *1982 Ultrasonics Symposium*, pp. 160–165, IEEE, 1982.

[102] J. Green, G. Kino, and B. Khuri-Yakub, "Focused surface wave transducers on anisotropic substrates: a theory developed for the waveguided storage correlator," in *1980 Ultrasonics Symposium*, pp. 69–73, IEEE, 1980.

[103] J. Z. Wilcox and R. E. Brooks, "Time-fourier transform by a focusing array of phased surface acoustic wave transducers," *Journal of applied physics*, vol. 58, no. 3, pp. 1148–1159, 1985.

[104] M. de Lima Jr, R. Hey, J. Stotz, and P. Santos, "Acoustic manipulation of electron–hole pairs in gaas at room temperature," *Applied physics letters*, vol. 84, no. 14, pp. 2569–2571, 2004.

[105] M. S. Kharusi and G. W. Farnell, "On diffraction and focusing in anisotropic crystals," *Proceedings of the IEEE*, vol. 60, no. 8, pp. 945–956, 1972.

[106] M. Cohen, "Optical study of ultrasonic diffraction and focusing in anisotropic media," *Journal of Applied Physics*, vol. 38, no. 10, pp. 3821–3828, 1967.

[107] S. R. Fang, S. Zhang, and Z. F. Lu, "Saw focusing by circular-arc interdigital transducers on yz-linbo/sub 3," *IEEE transactions on ultrasonics, ferroelectrics, and frequency control*, vol. 36, no. 2, pp. 178–184, 1989.

[108] T.-T. Wu, H.-T. Tang, and Y.-Y. Chen, "Frequency response of a focused saw device based on concentric wave surfaces: simulation and experiment," *Journal of Physics D: Applied Physics*, vol. 38, no. 16, p. 2986, 2005.

[109] T.-T. Wu, H.-T. Tang, Y.-Y. Chen, and P.-L. Liu, "Analysis and design of focused interdigital transducers," *IEEE transactions on ultrasonics, ferroelectrics, and frequency control*, vol. 52, no. 8, pp. 1384–1392, 2005.

[110] R. Shilton, M. K. Tan, L. Y. Yeo, and J. R. Friend, "Particle concentration and mixing in microdrops driven by focused surface acoustic waves," *Journal of Applied Physics*, vol. 104, no. 1, p. 014910, 2008.

[111] V. Laude, D. Gérard, N. Khelfaoui, C. F. Jerez-Hanckes, S. Benchabane, and A. Khelif, "Subwavelength focusing of surface acoustic waves generated by an annular interdigital transducer," *Applied Physics Letters*, vol. 92, no. 9, p. 094104, 2008.

[112] A. Riaud, M. Baudoin, J.-L. Thomas, and O. B. Matar, "Saw synthesis with idts array and the inverse filter: toward a versatile saw toolbox for microfluidics and biological applications," *IEEE Transactions on Ultrasonics, Ferroelectrics, and Frequency Control*, vol. 63, no. 10, pp. 1601–1607, 2016.

[113] M. Tanter, J.-L. Thomas, and M. Fink, "Time reversal and the inverse filter," *The Journal of the Acoustical Society of America*, vol. 108, no. 1, pp. 223–234, 2000.

[114] A. Riaud, M. Baudoin, O. B. Matar, L. Becerra, and J.-L. Thomas, "Selective manipulation of microscopic particles with precursor swirling rayleigh waves," *Physical Review Applied*, vol. 7, no. 2, p. 024007, 2017.

[115] M. K. Tan, J. R. Friend, and L. Y. Yeo, "Direct visualization of surface acoustic waves along substrates using smoke particles," *Applied Physics Letters*, vol. 91, no. 22, p. 224101, 2007.

[116] R. Rambach, J. Taiber, C. Scheck, C. Meyer, J. Reboud, J. Cooper, and T. Franke, "Visualization of surface acoustic waves in thin liquid films," *Scientific reports*, vol. 6, 2016.

[117] M. K. Tan, J. R. Friend, and L. Y. Yeo, "Microparticle collection and concentration via a miniature surface acoustic wave device," *Lab on a Chip*, vol. 7, no. 5, p. 618, 2007.

[118] H. Li, J. R. Friend, and L. Y. Yeo, "Surface acoustic wave concentration of particle and bioparticle suspensions," *Biomedical microdevices*, vol. 9, no. 5, pp. 647–656, 2007.

[119] R. Arzt, E. Salzmann, and K. Dransfeld, "Elastic surface waves in quartz at 316 mhz," *Applied Physics Letters*, vol. 10, no. 5, pp. 165–167, 1967.

[120] R. P. Hodgson, M. Tan, L. Yeo, and J. Friend, "Transmitting high power RF acoustic radiation via fluid couplants into superstrates for microfluidics," *Applied Physics Letters*, vol. 94, no. 2, p. 024102, 2009.

[121] S. M. Langelier, L. Y. Yeo, and J. Friend, "Uv epoxy bonding for enhanced saw transmission and microscale acoustofluidic integration," *Lab on a Chip*, vol. 12, no. 16, pp. 2970–2976, 2012.

[122] J. Lighthill, "Acoustic streaming," *Journal of sound and vibration*, vol. 61, no. 3, pp. 391–418, 1978.

[123] S. Shiokawa, Y. Matsui, and T. Moriizumi, "Experimental study on liquid streaming by saw," *Japanese Journal of Applied Physics*, vol. 28, no. S1, p. 126, 1989.

[124] H. Schlichting, "Berechnung ebener periodischer grenzschichtströmungen," *Phys. Z*, vol. 33, no. 1932, pp. 327–335, 1932.

[125] A. R. Rezk, O. Manor, L. Y. Yeo, and J. R. Friend, "Double flow reversal in thin liquid films driven by megahertz-order surface vibration," in *Proc. R. Soc. A*, vol. 470, p. 20130765, The Royal Society, 2014.

[126] L. V. King, "On the acoustic radiation pressure on spheres," in *Proceedings of the Royal Society of London A: Mathematical, Physical and Engineering Sciences*, vol. 147, pp. 212–240, The Royal Society, 1934.

[127] K. Yosioka and Y. Kawasima, "Acoustic radiation pressure on a compressible sphere," *Acta Acustica united with Acustica*, vol. 5, no. 3, pp. 167–173, 1955.

[128] H. Bruus, "Acoustofluidics 7: The acoustic radiation force on small particles," *Lab on a Chip*, vol. 12, no. 6, pp. 1014–1021, 2012.

[129] F. Nadal and E. Lauga, "Asymmetric steady streaming as a mechanism for acoustic propulsion of rigid bodies," *Physics of Fluids*, vol. 26, no. 8, p. 082001, 2014.

[130] P. L. Marston, "Phase-shift expansions for approximate radiation forces on solid spheres in inviscid-acoustic standing waves," *The Journal of the Acoustical Society of America*, vol. 142, no. 6, pp. 3358–3361, 2017.

[131] B.-T. Chu and R. E. Apfel, "Acoustic radiation pressure produced by a beam of sound," *The Journal of the Acoustical Society of America*, vol. 72, no. 6, pp. 1673–1687, 1982.

[132] L. A. Crum, "Bjerknes forces on bubbles in a stationary sound field," *The Journal of the Acoustical Society of America*, vol. 57, no. 6, pp. 1363–1370, 1975.

[133] M. Weiser, R. Apfel, and E. Neppiras, "Interparticle forces on red cells in a standing wave field," *Acta Acustica united with Acustica*, vol. 56, no. 2, pp. 114–119, 1984.

[134] B. Hammarström, T. Laurell, and J. Nilsson, "Seed particle-enabled acoustic trapping of bacteria and nanoparticles in continuous flow systems," *Lab on a Chip*, vol. 12, no. 21, pp. 4296–4304, 2012.

[135] P. Rogers and A. Neild, "Selective particle trapping using an oscillating microbubble," *Lab on a Chip*, vol. 11, no. 21, pp. 3710–3715, 2011.

[136] A. Huang, M. Miansari, and J. Friend, "Driving morphological changes in magnetic nanoparticle structures through the application of acoustic waves and magnetic fields," in *APS Meeting Abstracts*, 2017.

[137] G. Kwon, D. Panchanathan, S. R. Mahmoudi, M. A. Gondal, G. H. McKinley, and K. K. Varanasi, "Visible light guided manipulation of liquid wettability on photoresponsive surfaces," *Nature Communications*, vol. 8, 2017.

[138] Y.-H. Lin and G.-B. Lee, "Optically induced flow cytometry for continuous microparticle counting and sorting," *Biosensors and Bioelectronics*, vol. 24, no. 4, pp. 572–578, 2008.

[139] S.-B. Huang, M.-H. Wu, Y.-H. Lin, C.-H. Hsieh, C.-L. Yang, H.-C. Lin, C.-P. Tseng, and G.-B. Lee, "High-purity and label-free isolation of circulating tumor cells (ctcs) in a microfluidic platform by using optically-induced-dielectrophoretic (odep) force," *Lab on a Chip*, vol. 13, no. 7, pp. 1371–1383, 2013.

[140] S. Haeberle and R. Zengerle, "Microfluidic platforms for lab-on-a-chip applications," *Lab on a Chip*, vol. 7, no. 9, pp. 1094–1110, 2007.

[141] A. Wixforth, C. Strobl, C. Gauer, A. Toegl, J. Scriba, and Z. v. Guttenberg, "Acoustic manipulation of small droplets," *Analytical and bioanalytical chemistry*, vol. 379, no. 7-8, pp. 982–991, 2004.

[142] R. Raghavan, J. R. Friend, and L. Y. Yeo, "Particle concentration via acoustically driven microcentrifugation: microPIV flow visualization and numerical modelling studies," *Microfluidics and Nanofluidics*, vol. 8, pp. 73–84, 2010.

[143] W. L. M. Nyborg, *Physical Acoustics*, vol. 2B of *5*, ch. Acoustic Streaming, pp. 265–331. New York, NY: Academic Press, 1965. ed. W. P. Mason.

[144] S. Shiokawa, Y. Matsui, and T. Ueda, "Study on saw streaming and its application to fluid devices," *Japanese journal of applied physics*, vol. 29, no. S1, p. 137, 1990.

[145] M. Alghane, B. Chen, Y. Q. Fu, Y. Li, J. Luo, and A. Walton, "Experimental and numerical investigation of acoustic streaming excited by using a surface acoustic wave device on a $128°$ yx-linbo3 substrate," *Journal of micromechanics and Microengineering*, vol. 21, no. 1, p. 015005, 2010.

[146] J. Vanneste and O. Bühler, "Streaming by leaky surface acoustic waves," in *Proceedings of the Royal Society of London A: Mathematical, Physical and Engineering Sciences*, p. rspa20100457, The Royal Society, 2010.

[147] A. R. Rezk, L. Y. Yeo, and J. R. Friend, "Poloidal flow and toroidal particle ring formation in a sessile drop driven by megahertz order vibration," *Langmuir*, vol. 30, no. 37, pp. 11243–11247, 2014.

[148] A. Riaud, M. Baudoin, J.-L. Thomas, and O. Bou Matar, "Cyclones and attractive streaming generated by acoustical vortices," *Physical Review*, vol. 90, no. 013008, p. 8, 2014.

[149] R. Shilton, M. Tan, L. Yeo, and J. Friend, "Concentration and mixing of particles in microdrops driven by focused surface acoustic waves," *Proceedings - IEEE Ultrasonics Symposium*, pp. 930–933, 2008.

[150] A. Riaud, M. Baudoin, O. B. Matar, L. Becerra, and J.-L. Thomas, "Selective manipulation of microscopic particles with precursor swirling rayleigh waves," *Physical Review Applied*, vol. 7, no. 2, 2017.

[151] A. Riaud, M. Baudoin, O. Bou Matar, J.-L. Thomas, and P. Brunet, "On the influence of viscosity and caustics on acoustic streaming in sessile droplets: an experimental and a numerical study with a cost-effective method," *Journal of Fluid Mechanics*, vol. Not yet pu, 2017.

[152] R. J. Shilton, L. Y. Yeo, and J. R. Friend, "Quantification of surface acoustic wave induced chaotic mixing-flows in microfluidic wells," *Sensors and Actuators B: Chemical*, vol. 160, no. 1, pp. 1565–1572, 2011.

[153] R. J. Shilton, M. Travagliati, F. Beltram, and M. Cecchini, "Nanoliter-droplet acoustic streaming via ultra high frequency surface acoustic waves," *Advanced Materials*, vol. 26, no. 29, pp. 4941–4946, 2014.

[154] C.-M. Ho, "Fluidics-the link between micro and nano sciences and technologies," in *Micro Electro Mechanical Systems, 2001. MEMS 2001. The 14th IEEE International Conference on*, pp. 375–384, IEEE, 2001.

[155] A. Kundt and O. Lehmann, "Ueber longitudinale schwingungen und klangfiguren in cylindrischen flüssigkeitssäulen," *Annalen der Physik*, vol. 229, no. 9, pp. 1–12, 1874.

[156] G. Destgeer, H. Cho, B. H. Ha, J. H. Jung, J. Park, and H. J. Sung, "Acoustofluidic particle manipulation inside a sessile droplet: four distinct regimes of particle concentration," *Lab on a Chip*, vol. 16, no. 4, pp. 660–667, 2016.

[157] R. Wilson, J. Reboud, Y. Bourquin, S. L. Neale, Y. Zhang, and J. M. Cooper, "Phononic crystal structures for acoustically driven microfluidic manipulations," *Lab on a Chip*, vol. 11, no. 2, pp. 323–328, 2011.

[158] G. Destgeer, B. Ha, J. Park, and H. J. Sung, "Lamb wave-based acoustic radiation force-driven particle ring formation inside a sessile droplet," *Analytical chemistry*, vol. 88, no. 7, pp. 3976–3981, 2016.

[159] C. Wood, S. Evans, J. Cunningham, R. O'Rorke, C. Wälti, and A. Davies, "Alignment of particles in microfluidic systems using standing surface acoustic waves," *Applied Physics Letters*, vol. 92, no. 4, p. 044104, 2008.

[160] P. R. Rogers, J. R. Friend, and L. Y. Yeo, "Exploitation of surface acoustic waves to drive size-dependent microparticle concentration within a droplet," *Lab on a Chip*, vol. 10, no. 21, pp. 2979–2985, 2010.

[161] Y. Bourquin, J. Reboud, R. Wilson, and J. M. Cooper, "Tuneable surface acoustic waves for fluid and particle manipulations on disposable chips," *Lab on a chip*, vol. 10, no. 15, pp. 1898–1901, 2010.

[162] Y. Bourquin, A. Syed, J. Reboud, L. C. Ranford-Cartwright, M. P. Barrett, and J. M. Cooper, "Rare-cell enrichment by a rapid, label-free, ultrasonic isopycnic technique for medical diagnostics," *Angewandte Chemie*, vol. 126, no. 22, pp. 5693–5696, 2014.

[163] J. L. Garcia-Cordero and Z. H. Fan, "Sessile droplets for chemical and biological assays," *Lab on a Chip*, 2017.

[164] D. Mampallil, J. Reboud, R. Wilson, D. Wylie, D. R. Klug, and J. M. Cooper, "Acoustic suppression of the coffee-ring effect," *Soft Matter*, vol. 11, no. 36, pp. 7207–7213, 2015.

[165] R.-Z. Lin and H.-Y. Chang, "Recent advances in three-dimensional multicellular spheroid culture for biomedical research," *Biotechnology journal*, vol. 3, no. 9-10, pp. 1172–1184, 2008.

[166] L. Alhasan, A. Qi, A. Al-Abboodi, A. Rezk, P. P. Chan, C. Iliescu, and L. Y. Yeo, "Rapid enhancement of cellular spheroid assembly by acoustically driven microcentrifugation," *ACS Biomaterials Science & Engineering*, vol. 2, no. 6, pp. 1013–1022, 2016.

[167] Y. Kurashina, K. Takemura, and J. Friend, "Cell agglomeration in the wells of a 24-well plate using acoustic streaming," *Lab on a Chip*, vol. 17, no. 5, pp. 876–886, 2017.

[168] F. G. Strobl, D. Breyer, P. Link, A. A. Torrano, C. Bräuchle, M. F. Schneider, and A. Wixforth, "A surface acoustic wave-driven micropump for particle uptake investigation under physiological flow conditions in very small volumes," *Beilstein journal of nanotechnology*, vol. 6, no. 1, pp. 414–419, 2015.

[169] N. Sivanantha, C. Ma, D. J. Collins, M. Sesen, J. Brenker, R. L. Coppel, A. Neild, and T. Alan, "Characterization of adhesive properties of red blood cells using surface acoustic wave induced flows for rapid diagnostics," *Applied Physics Letters*, vol. 105, no. 10, p. 103704, 2014.

[170] A. Bussonnière, Y. Miron, M. Baudoin, O. B. Matar, M. Grandbois, P. Charette, and A. Renaudin, "Cell detachment and label-free cell sorting using modulated surface acoustic waves (saws) in droplet-based microfluidics," *Lab on a Chip*, vol. 14, no. 18, pp. 3556–3563, 2014.

[171] D. Taller, K. Richards, Z. Slouka, S. Senapati, R. Hill, D. B. Go, and H.-C. Chang, "On-chip surface acoustic wave lysis and ion-exchange nanomembrane detection of exosomal rna

for pancreatic cancer study and diagnosis," *Lab on a Chip*, vol. 15, no. 7, pp. 1656–1666, 2015.

[172] Z. Guttenberg, H. Müller, H. Habermüller, A. Geisbauer, J. Pipper, J. Felbel, M. Kielpinski, J. Scriba, and A. Wixforth, "Planar chip device for pcr and hybridization with surface acoustic wave pump," *Lab on a Chip*, vol. 5, no. 3, pp. 308–317, 2005.

[173] L. Gao and T. J. McCarthy, "Wetting 101°," *Langmuir*, vol. 25, no. 24, pp. 14105–14115, 2009.

[174] A. Wixforth, "Acoustically driven planar microfluidics," *Superlattices and Microstructures*, vol. 33, no. 5, pp. 389–396, 2003.

[175] A. Renaudin, P. Tabourier, V. Zhang, J. C. Camart, and C. Druon, "SAW nanopump for handling droplets in view of biological applications," *Sensors and Actuators, B: Chemical*, vol. 113, no. 1, pp. 389–397, 2006.

[176] M. Baudoin, P. Brunet, O. Bou Matar, and E. Herth, "Low power sessile droplets actuation via modulated surface acoustic waves," *Applied Physics Letters*, vol. 100, no. 15, p. 154102, 2012.

[177] P. Brunet, M. Baudoin, O. B. Matar, and F. Zoueshtiagh, "Droplet displacements and oscillations induced by ultrasonic surface acoustic waves: A quantitative study," *Physical Review E - Statistical, Nonlinear, and Soft Matter Physics*, vol. 81, no. 3, pp. 1–8, 2010.

[178] A. R. Rezk, O. Manor, J. R. Friend, and L. Y. Yeo, "Unique fingering instabilities and soliton-like wave propagation in thin acoustowetting films," *Nature communications*, vol. 3, p. 1167, 2012.

[179] M. Morozov and O. Manor, "An extended Landau – Levich model for the dragging of a thin liquid film with a propagating surface acoustic wave," *Journal of fluid mechanics*, vol. 810, pp. 307–322, 2017.

[180] M. Travagliati, G. D. Simoni, M. Lazzarini, and V. Piazza, "Interaction-free, automatic, on-chip fluid routing by surface acoustic waves," *Lab on a chip*, vol. 12, pp. 2621–2624, 2012.

[181] Y. Ai and B. L. Marrone, "Droplet translocation by focused surface acoustic waves," *Microfluidics and Nanofluidics*, vol. 13, pp. 715–722, 2012.

[182] S. Collignon, J. Friend, and L. Yeo, "Planar microfluidic drop splitting and merging," *Lab on a chip*, vol. 15, no. 8, pp. 1942–1951, 2015.

[183] A. Bussonniere, M. Baudoin, P. Brunet, and O. B. Matar, "Dynamics of sessile and pendant drops excited by surface acoustic waves: Gravity effects and correlation between oscillatory and translational motions," *Physical Review E*, vol. 93, no. 5, p. 053106, 2016.

[184] K. Mullis, F. Faloona, S. Scharf, R. Saiki, G. Horn, and H. Erlich, "Specific enzymatic amplification of dna in vitro: the polymerase chain reaction," in *Cold Spring Harbor symposia on quantitative biology*, vol. 51, pp. 263–273, Cold Spring Harbor Laboratory Press, 1986.

[185] L. Y. Yeo, H.-C. Chang, P. P. Chan, and J. R. Friend, "Microfluidic devices for bioapplications," *small*, vol. 7, no. 1, pp. 12–48, 2011.

[186] J. Dong, T. Uemura, Y. Shirasaki, and T. Tateishi, "Promotion of bone formation using highly pure porous β-tcp combined with bone marrow-derived osteoprogenitor cells," *Biomaterials*, vol. 23, no. 23, pp. 4493–4502, 2002.

[187] V. Maquet, D. Martin, B. Malgrange, R. Franzen, J. Schoenen, G. Moonen, and R. Jérôme, "Peripheral nerve regeneration using bioresorbable macroporous polylactide scaffolds," *Journal of Biomedical Materials Research Part A*, vol. 52, no. 4, pp. 639–651, 2000.

[188] H. Li, J. R. Friend, and L. Y. Yeo, "A scaffold cell seeding method driven by surface acoustic waves," *Biomaterials*, vol. 28, no. 28, pp. 4098–4104, 2007.

[189] M. Bok, H. Li, L. Y. Yeo, and J. R. Friend, "The dynamics of surface acoustic wave-driven scaffold cell seeding," *Biotechnology and bioengineering*, vol. 103, no. 2, pp. 387–401, 2009.

[190] J. Eggers, "Nonlinear dynamics and breakup of free-surface flows," *Reviews of modern physics*, vol. 69, no. 3, p. 865, 1997.

[191] M. K. Tan, J. R. Friend, and L. Y. Yeo, "Interfacial jetting phenomena induced by focused surface vibrations," *Physical Review Letters*, vol. 103, no. 2, 2009.

[192] J. Wang, H. Hu, A. Ye, J. Chen, and P. Zhang, "Experimental investigation of surface acoustic wave atomization," *Sensors and Actuators, A: Physical*, vol. 238, pp. 1–7, 2016.

[193] T. Tuladhar and M. Mackley, "Filament stretching rheometry and break-up behaviour of low viscosity polymer solutions and inkjet fluids," *Journal of Non-Newtonian Fluid Mechanics*, vol. 148, no. 1, pp. 97–108, 2008.

[194] L. E. Rodd, T. P. Scott, J. J. Cooper-White, and G. H. McKinley, "Capillary break-up rheometry of low-viscosity elastic fluids," *Applied Rheology*, 2004.

[195] P. Bhattacharjee, A. McDonnell, R. Prabhakar, L. Yeo, and J. Friend, "Extensional flow of low-viscosity fluids in capillary bridges formed by pulsed surface acoustic wave jetting," *New Journal of Physics*, vol. 13, no. 2, p. 023005, 2011.

[196] A. G. McDonnell, T. C. Gopesh, J. Lo, M. O'Bryan, L. Y. Yeo, J. R. Friend, and R. Prabhakar, "Motility induced changes in viscosity of suspensions of swimming microbes in extensional flows," *Soft Matter*, vol. 11, no. 23, pp. 4658–4668, 2015.

[197] A. G. McDonnell, N. N. Jason, L. Y. Yeo, J. R. Friend, W. Cheng, and R. Prabhakar, "Extensional viscosity of copper nanowire suspensions in an aqueous polymer solution," *Soft matter*, vol. 11, no. 41, pp. 8076–8082, 2015.

[198] R. J. Lang, "Ultrasonic Atomization of Liquids," *The Journal of the Acoustical Society of America*, vol. 34, pp. 6–8, 1962.

[199] W. Eisenmenger, "Dynamic properties of the surface tension of water and aqueous solutions of surface active agents with standing capillary waves in the frequency range from 10 kc/s to 1.5 mc/s," *Acta Acustica united with Acustica*, vol. 9, no. 4, pp. 327–340, 1959.

[200] T. B. Benjamin and F. Ursell, "The stability of the plane free surface of a liquid in vertical periodic motion," in *Proceedings of the Royal Society of London A: Mathematical, Physical and Engineering Sciences*, vol. 225, pp. 505–515, The Royal Society, 1954.

[201] M. Faraday, "On a peculiar class of acoustical figures; and on certain forms assumed by groups of particles upon vibrating elastic surfaces," *Philosophical transactions of the Royal Society of London*, vol. 121, pp. 299–340, 1831.

[202] M. Kurosawa, T. Watanabe, A. Hutami, and T. Higuchi, "Surface Acoustic Wave Atomizer with Pumping Effect," *IEEE*, pp. 25–30, 1995.

[203] M. Kurosawa, A. Futami, and T. Higuchi, "Characteristics of liquids atomization using surface acoustic wave," in *Solid State Sensors and Actuators, 1997. TRANSDUCERS'97 Chicago., 1997 International Conference on*, vol. 2, pp. 801–804, IEEE, 1997.

[204] A. Qi, L. Y. Yeo, and J. R. Friend, "Interfacial destabilization and atomization driven by surface acoustic waves," *Physics of Fluids*, vol. 20, no. 7, p. 074103, 2008.

[205] M. K. Tan, J. R. Friend, O. K. Matar, and L. Y. Yeo, "Capillary wave motion excited by high frequency surface acoustic waves," *Physics of Fluids*, vol. 22, no. 11, pp. 1–22, 2010.

[206] D. J. Collins, O. Manor, A. Winkler, H. Schmidt, J. R. Friend, and L. Y. Yeo, "Atomization off thin water films generated by high-frequency substrate wave vibrations," *Physical Review E - Statistical, Nonlinear, and Soft Matter Physics*, vol. 86, no. 5, pp. 1–9, 2012.

[207] A. Rajapaksa, A. Qi, L. Y. Yeo, R. Coppel, and J. R. Friend, "Enabling practical surface acoustic wave nebulizer drug delivery via amplitude modulation," *Lab Chip*, vol. 14, no. 11, pp. 1858–1865, 2014.

[208] A. R. Rezk, J. K. Tan, and L. Y. Yeo, "HYbriD Resonant Acoustics (HYDRA)," *Advanced Materials Communication*, vol. 28, pp. 1970–1975, 2016.

[209] A. Winkler, S. Harazim, S. Menzel, and H. Schmidt, "Saw-based fluid atomization using mass-producible chip devices," *Lab on a Chip*, vol. 15, no. 18, pp. 3793–3799, 2015.

[210] A. Winkler, R. Brünig, C. Faust, R. Weser, and H. Schmidt, "Towards efficient surface acoustic wave (SAW)-based microfluidic actuators," *Sensors & Actuators A*, vol. 247, pp. 259–268, 2016.

[211] C. J. Brinker, Y. Lu, A. Sellinger, H. Fan, *et al.*, "Evaporation-induced self-assembly: nanostructures made easy," *Advanced materials*, vol. 11, no. 7, pp. 579–585, 1999.

[212] J. R. Friend, L. Y. Yeo, D. R. Arifin, and A. Mechler, "Evaporative self-assembly assisted synthesis of polymeric nanoparticles by surface acoustic wave atomization," *Nanotechnology*, vol. 19, pp. 145301–6, 2008.

[213] M. Bognitzki, W. Czado, T. Frese, A. Schaper, M. Hellwig, M. Steinhart, A. Greiner, J. H. Wendorff, *et al.*, "Nanostructured fibers via electrospinning," *Advanced Materials*, vol. 13, no. 1, pp. 70–72, 2001.

[214] S. Megelski, J. S. Stephens, D. B. Chase, and J. F. Rabolt, "Micro-and nanostructured surface morphology on electrospun polymer fibers," *Macromolecules*, vol. 35, no. 22, pp. 8456–8466, 2002.

[215] K. H. Choi, H. B. Kim, K. Ali, M. Sajid, G. U. Siddiqui, D. E. Chang, H. C. Kim, J. B. Ko, H. W. Dang, and Y. H. Doh, "Hybrid surface acoustic wave-electrohydrodynamic atomization (saw-ehda) for the development of functional thin films," *Scientific reports*, vol. 5, 2015.

[216] A. Kirchner, A. Winkler, S. M. Menzel, B. Holzapfel, and R. Huhne, "Surface Acoustic Waves—A New Thin-Film Deposition Approach for Coated Conductors," *IEEE Transactions on Applied Superconductivity*, vol. 26, no. 3, pp. 1–4, 2016.

[217] T. Vuong, A. Qi, M. Muradoglu, B.-P. Cheong, O. Liew, C. Ang, J. Fu, L. Yeo, J. Friend, and T. Ng, "Precise drop dispensation on superhydrophobic surfaces using acoustic nebulization," *Soft Matter*, vol. 9, no. 13, pp. 3631–3639, 2013.

[218] K. M. Ang, L. Y. Yeo, J. R. Friend, Y. M. Hung, and M. K. Tan, "Nozzleless spray cooling using surface acoustic waves," *Journal of Aerosol Science*, vol. 79, pp. 48–60, 2015.

[219] M. Alvarez, J. Friend, and L. Y. Yeo, "Rapid generation of protein aerosols and nanoparticles via surface acoustic wave atomization," *Nanotechnology*, vol. 19, no. 45, p. 455103, 2008.

[220] A. Qi, J. R. Friend, L. Y. Yeo, D. A. Morton, M. P. McIntosh, and L. Spiccia, "Miniature inhalation therapy platform using surface acoustic wave microfluidic atomization," *Lab on a Chip*, vol. 9, no. 15, pp. 2184–2193, 2009.

[221] C. Cortez-Jugo, A. Qi, A. Rajapaksa, J. R. Friend, and L. Y. Yeo, "Pulmonary monoclonal antibody delivery via a portable microfluidic nebulization platform," *Biomicrofluidics*, vol. 9, no. 5, p. 052603, 2015.

[222] A. E. Rajapaksa, J. J. Ho, A. Qi, R. Bischof, T.-H. Nguyen, M. Tate, D. Piedrafita, M. P. McIntosh, L. Y. Yeo, E. Meeusen, C. L. Ross, and J. R. Friend, "Effective pulmonary delivery of an aerosolized plasmid dna vaccine via surface acoustic wave nebulization," *Respiratory research*, vol. 15, no. 1, p. 60, 2014.

[223] A. Qi, L. Yeo, J. Friend, and J. Ho, "The extraction of liquid, protein molecules and yeast cells from paper through surface acoustic wave atomization," *Lab on a Chip*, vol. 10, no. 4, pp. 470–476, 2010.

[224] S. R. Heron, R. Wilson, S. A. Shaffer, D. R. Goodlett, and J. M. Cooper, "Surface acoustic wave nebulization of peptides as a microfluidic interface for mass spectrometry," *Analytical chemistry*, vol. 82, no. 10, pp. 3985–3989, 2010.

[225] J. Ho, M. K. Tan, D. B. Go, L. Y. Yeo, J. R. Friend, and H.-C. Chang, "based microfluidic surface acoustic wave sample delivery and ionization source for rapid and sensitive ambient mass spectrometry," *Analytical chemistry*, vol. 83, no. 9, pp. 3260–3266, 2011.

[226] Y. Huang, S. H. Yoon, S. R. Heron, C. D. Masselon, J. S. Edgar, F. Tureček, and D. R. Goodlett, "Surface acoustic wave nebulization produces ions with lower internal energy than electrospray ionization," *Journal of The American Society for Mass Spectrometry*, vol. 23, no. 6, pp. 1062–1070, 2012.

[227] Y. Huang, S. R. Heron, A. M. Clark, J. S. Edgar, S. H. Yoon, D. Kilgour, F. Turecek, A. Aliseda, and D. R. Goodlett, "Surface acoustic wave nebulization device with dual interdigitated transducers improves sawn-ms performance," *Journal of Mass Spectrometry*, vol. 51, no. 6, pp. 424–429, 2016.

[228] J. C. Brenker, C. Devendran, A. Neild, and T. Alan, "On-demand sample injection: combining acoustic actuation with a tear-drop shaped nozzle to generate droplets with precise spatial and temporal control," *Lab on a Chip*, 2020.

[229] P. Bhattacharjee, A. McDonnell, R. Prabhakar, L. Yeo, and J. Friend, "Extensional flow of low-viscosity fluids in capillary bridges formed by pulsed surface acoustic wave jetting," *New Journal of Physics*, vol. 13, no. 2, p. 023005, 2011.

[230] J. O. Castro, S. R. Ramesan, H. D. Dang, A. R. Rezk, and L. Y. Yeo, "Acoustopipetting: Tunable nanoliter sample dispensing using surface acoustic waves," *Analytical Chemistry*, vol. 91, no. 9, pp. 5621–5628, 2019.

[231] W. Connacher, N. Zhang, A. Huang, J. Mei, S. Zhang, T. Gopesh, and J. Friend, "Micro/nano acoustofluidics: materials, phenomena, design, devices, and applications," *Lab on a Chip*, vol. 18, no. 14, pp. 1952–1996, 2018.

[232] S. Shiokawa, Y. Matsui, and T. Ueda, "Liquid streaming and droplet formation caused by leaky rayleigh waves," in *Proceedings., IEEE Ultrasonics Symposium,*, pp. 643–646, IEEE, 1989.

[233] P.-G. De Gennes, F. Brochard-Wyart, and D. Quéré, *Capillarity and wetting phenomena: drops, bubbles, pearls, waves*. Springer Science & Business Media, 2013.

[234] J. O. Castro, S. Ramesan, A. R. Rezk, and L. Y. Yeo, "Continuous tuneable droplet ejection via pulsed surface acoustic wave jetting," *Soft Matter*, vol. 14, no. 28, pp. 5721–5727, 2018.

[235] J. Eggers, "Nonlinear dynamics and breakup of free-surface flows," *Reviews of Modern Physics*, vol. 69, no. 3, p. 865, 1997.

[236] J. Eggers and E. Villermaux, "Physics of liquid jets," *Reports on Progress in Physics*, vol. 71, no. 3, p. 036601, 2008.

[237] See Supplemental Material at [URL will be inserted by publisher] for video of droplet ejection at a range of angles.

[238] *V* and *r* are related via the equation for a spherical cap with height, h: $V = \frac{1}{6}\pi h(3r^2 + h^2)$.

[239] See Supplemental Material at [URL will be inserted by publisher] for a plot of ejection angles for different sessile drop contact angles, comparison of the time averaged radius calculation to experimental data, plots of ejection angle for different frequency devices, LDV measurements of vibrational velocity and net power as a function of Vpp, fluid parameter information, and the procedure used to obtain data from high speed imaging.

[240] See Supplemental Material at [URL will be inserted by publisher] for imageJ and MatLab code.

[241] See Supplemental Material at [URL will be inserted by publisher] for video comparing effects of contact angle and volume.

[242] M. F. Hamilton, D. T. Blackstock, *et al.*, *Nonlinear acoustics*, vol. 237. Academic Press, San Diego, 1998.

[243] r_s is given by the solution of the following system of equations: an offset circle representing the interface, $x^2 + (y + R - h)^2 = R^2$ and a line representing the jet, $y = \cot\theta_R(x + r - \alpha_r^{-1}/4)$. The solution can be put in terms of the sessile drop volume and contact angle via the following equations: $\cos\theta_c = \frac{R-h}{R}$, $V = \frac{\pi h^2}{3}(3R - h)$.

[244] $\theta_s = \tan^{-1}\left[\frac{dy}{dx}\right]_{x=r_s}$.

[245] H. Bertoni and T. Tamir, "Unified theory of rayleigh-angle phenomena for acoustic beams at liquid-solid interfaces," *Applied Physics*, vol. 2, no. 4, pp. 157–172, 1973.

[246] See Supplemental Material at [URL will be inserted by publisher] for ejection angle and acceleration ratio models in Mathematica code.

[247] $\frac{1}{t_{df}}\int_0^{t_{df}} r\left(\frac{t_{df}-t}{t_{df}}\right)^3 dt = \frac{r}{4}$.

[248] P. L. Marston and R. E. Apfel, "Quadrupole resonance of drops driven by modulated acoustic radiation pressure—experimental properties," *The Journal of the Acoustical Society of America*, vol. 67, no. 1, pp. 27–37, 1980.

[249] P. Brunet, M. Baudoin, O. B. Matar, and F. Zoueshtiagh, "Droplet displacements and oscillations induced by ultrasonic surface acoustic waves: A quantitative study," *Physical Review E*, vol. 81, no. 3, p. 036315, 2010.

[250] J. C. McDowell, "The low earth orbit satellite population and impacts of the spacex starlink constellation," *The Astrophysical Journal Letters*, vol. 892, no. 2, p. L36, 2020.

[251] A. Freeman, "Exploring our solar system with cubesats and smallsats: the dawn of a new era," *CEAS Space Journal*, vol. 12, pp. 491–502, 2020.

[252] E. Y.-W. Chang, "From aviation tourism to suborbital space tourism: A study on passenger screening and business opportunities," *Acta Astronautica*, vol. 177, pp. 410–420, 2020.

[253] S. Miller, M. L. Walker, J. Agolli, and J. Dankanich, "Survey and performance evaluation of small-satellite propulsion technologies," *Journal of Spacecraft and Rockets*, vol. 58, no. 1, pp. 222–231, 2021.

[254] J. Mueller, R. Hofer, and J. Ziemer, "Survey of propulsion technologies applicable to cubesats," Tech. Rep. 10-1646, Jet Propulsion Laboratory, Pasadena, CA USA, 2010.

[255] M. Sorgenfrei, T. Stevenson, and G. Lightsey, "Performance characterization of a cold gas propulsion system for a deep space cubesat," in *40th Annual AAS Guidance and Control Conference, Breckenridge, CO*, 2017.

[256] A. Bapat, P. B. Salunkhe, and A. V. Patil, "Hall-effect thrusters for deep-space missions: A review," *IEEE Transactions on Plasma Science*, vol. 50, pp. 189–202, 2022.

[257] D. Krejci and P. Lozano, "Space propulsion technology for small spacecraft," *Proceedings of the IEEE*, vol. 106, no. 3, pp. 362–378, 2018.

[258] S. Pugia, A. Cofer, and A. Alexeenko, "Characterization of film-evaporating microcapillaries for water-based microthrusters," *Acta Astronautica*, vol. 196, pp. 442–458, 2022.

[259] D. J. Collins, O. Manor, A. Winkler, H. Schmidt, J. R. Friend, and L. Y. Yeo, "Atomization off thin water films generated by high-frequency substrate wave vibrations," *Physical Review E*, vol. 86, no. 5, p. 056312, 2012.

[260] A. Huang, W. Connacher, M. Stambaugh, N. Zhang, S. Zhang, J. Mei, A. Jain, S. Alluri, V. Leung, A. E. Rajapaksa, *et al.*, "Practical microcircuits for handheld acoustofluidics," *Lab on a Chip*, vol. 21, no. 7, pp. 1352–1363, 2021.

[261] J. Kondoh, N. Shimizu, Y. Matsui, and S. Shiokawa, "Liquid heating effects by SAW streaming on the piezoelectric substrate," *IEEE Transactions on Ultrasonics, Ferroelectrics, and Frequency Control*, vol. 52, no. 10, pp. 1881–1883, 2005.

[262] Y. Wang, Q. Zhang, R. Tao, D. Chen, J. Xie, H. Torun, L. E. Dodd, J. Luo, C. Fu, J. Vernon, *et al.*, "A rapid and controllable acoustothermal microheater using thin film surface acoustic waves," *Sensors and Actuators A: Physical*, vol. 318, p. 112508, 2021.

[263] J. Kondoh, N. Shimizu, Y. Matsui, M. Sugimoto, and S. Shiokawa, "Development of temperature-control system for liquid droplet using surface acoustic wave devices," *Sensors and Actuators A: Physical*, vol. 149, no. 2, pp. 292–297, 2009.

[264] D. Beyssen, L. Le Brizoual, O. Elmazria, P. Alnot, I. Perry, and D. Maillet, "Droplet heating system based on SAW/liquid interaction," *2006 IEEE Ultrasonics Symposium*, pp. 949–952, 2006.

[265] P. K. Das, A. D. Snider, and V. R. Bhethanabotla, "Acoustothermal heating in surface acoustic wave driven microchannel flow," *Physics of Fluids*, vol. 31, no. 10, p. 106106, 2019.

[266] S. Collignon, O. Manor, and J. Friend, "Improving and predicting fluid atomization via hysteresis-free thickness vibration of lithium niobate," *Advanced Functional Materials*, vol. 28, no. 8, p. 1704359, 2018.

[267] H. Nagata, M. Yoshida, Y. Makiuchi, and T. Takenaka, "Large piezoelectric constant and high Curie temperature of lead-free piezoelectric ceramic ternary system based on bismuth sodium titanate-bismuth potassium titanate-barium titanate near the morphotropic phase boundary," *Japanese Journal of Applied Physics*, vol. 42, no. 12R, p. 7401, 2003.

[268] M. Senousy, R. Rajapakse, D. Mumford, and M. Gadala, "Self-heat generation in piezo-electric stack actuators used in fuel injectors," *Smart Materials and Structures*, vol. 18, no. 4, p. 045008, 2009.

[269] K. Kulkarni, L. Y. Yeo, J. R. Friend, and P. Perlmutter, "An emerging reactor technology for chemical synthesis: Surface acoustic wave-assisted closed-vessel suzuki coupling reactions," *Ultrasonics Sonochemistry*, vol. 21, no. 4, pp. 1305–1309, 2014.

[270] T. Roux-Marchand, D. Beyssen, F. Sarry, and O. Elmazria, "Rayleigh surface acoustic wave as an efficient heating system for biological reactions: Investigation of microdroplet temperature uniformity," *IEEE Transactions on Ultrasonics, Ferroelectrics, and Frequency Control*, vol. 62, no. 4, pp. 729–735, 2015.

[271] Q.-Y. Huang, Q. Sun, H. Hu, J.-L. Han, and Y.-L. Lei, "Thermal effect in the process of surface acoustic wave atomization," *Experimental Thermal and Fluid Science*, vol. 120, p. 110257, 2021.

[272] M. Kurosawa, T. Watanabe, A. Futami, and T. Higuchi, "Surface acoustic wave atomizer," *Sensors and Actuators-A-Physical Sensors*, vol. 50, no. 1, pp. 69–74, 1995.

[273] W. Connacher, J. Orosco, and J. Friend, "Droplet ejection at controlled angles via acoustofluidic jetting," *Physical Review Letters*, vol. 125, no. 18, p. 184504, 2020.

[274] N. Zhang, Y. Wen, and J. Friend, "MHz-order surface acoustic wave thruster for underwater silent propulsion," *Micromachines*, vol. 11, no. 4, 2020.

[275] J. Mei, N. Zhang, and J. Friend, "Fabrication of surface acoustic wave devices on lithium niobate," *Journal of Visualized Experiments*, vol. 160, p. e61013, 2020.

[276] A. Meyer, D. Eliseev, D. Heinen, P. Linder, F. Scholz, L. S. Weinstock, C. Wiebusch, and S. Zierke, "Attenuation of sound in glacier ice from 2 to 35 kHz," *The Cryosphere*, vol. 13, no. 4, pp. 1381–1394, 2019.

[277] P. Price, "Attenuation of acoustic waves in glacial ice and salt domes," *Journal of Geophysical Research: Solid Earth*, vol. 111, no. B2, 2006.

[278] Y. Liu, L. J. Bond, and H. Hu, "Ultrasonic-attenuation-based technique for ice characterization pertinent to aircraft icing phenomena," *AIAA Journal*, vol. 55, no. 5, pp. 1602–1609, 2017.

[279] W. Unterberg and J. Congelliere, "Zero gravity problems in space powerplants: A status survey," *ARS (American Rocket Society) Journal*, vol. 32, no. 6, pp. 862–872, 1962.

[280] A. Wixforth, "Acoustically driven planar microfluidics," *Superlattices and Microstructures*, vol. 33, no. 5-6, pp. 389–396, 2003.

[281] A. Rajapaksa, A. Qi, L. Y. Yeo, R. Coppel, and J. R. Friend, "Enabling practical surface acoustic wave nebulizer drug delivery via amplitude modulation," *Lab on a Chip*, vol. 14, no. 11, pp. 1858–1865, 2014.

[282] H. Bachman *et al.*, "Acoustofluidic devices controlled by cell phones," *Lab on a Chip*, vol. 18, no. 3, pp. 433–441, 2018.

[283] H. Bachman, H. Fu, P.-H. Huang, Z. Tian, J. Embry-Seckler, J. Rufo, Z. Xie, J. H. Hartman, S. Zhao, S. Yang, *et al.*, "Open source acoustofluidics," *Lab on a Chip*, vol. 19, no. 14, pp. 2404–2414, 2019.

[284] X. Ding, P. Li, S.-C. S. Lin, Z. S. Stratton, N. Nama, F. Guo, D. Slotcavage, X. Mao, J. Shi, F. Costanzo, *et al.*, "Surface acoustic wave microfluidics," *Lab on a Chip*, vol. 13, no. 18, pp. 3626–3649, 2013.

[285] H. Li, J. Friend, L. Yeo, A. Dasvarma, and K. Traianedes, "Effect of surface acoustic waves on the viability, proliferation and differentiation of primary osteoblast-like cells," *Biomicrofluidics*, vol. 3, no. 3, p. 034102, 2009.

[286] Y. Chen, S. Li, Y. Gu, P. Li, X. Ding, L. Wang, J. P. McCoy, S. J. Levine, and T. J. Huang, "Continuous enrichment of low-abundance cell samples using standing surface acoustic waves (ssaw)," *Lab on a Chip*, vol. 14, no. 5, pp. 924–930, 2014.

[287] M. N. Topp, "Ultrasonic atomization-a photographic study of the mechanism of disintegration," *Journal of Aerosol Science*, vol. 4, no. 1, pp. 17–25, 1973.

[288] T. Frommelt, M. Kostur, M. Wenzel-Schäfer, P. Talkner, P. Hänggi, and A. Wixforth, "Microfluidic mixing via acoustically driven chaotic advection," *Physical Review Letters*, vol. 100, no. 3, p. 034502, 2008.

[289] K. Sritharan, C. Strobl, M. Schneider, A. Wixforth, and Z. v. Guttenberg, "Acoustic mixing at low reynolds numbers," *Applied Physics Letters*, vol. 88, no. 5, p. 054102, 2006.

[290] S. Meyer dos Santos, A. Zorn, Z. Guttenberg, B. Picard-Willems, C. Kläffling, K. Nelson, U. Klinkhardt, and S. Harder, "A novel μ-fluidic whole blood coagulation assay based on rayleigh surface-acoustic waves as a point-of-care method to detect anticoagulants," *Biomicrofluidics*, vol. 7, no. 5, p. 056502, 2013.

[291] L. Tian, N. Martin, P. G. Bassindale, A. J. Patil, M. Li, A. Barnes, B. W. Drinkwater, and S. Mann, "Spontaneous assembly of chemically encoded two-dimensional coacervate droplet arrays by acoustic wave patterning," *Nature communications*, vol. 7, 2016.

[292] X. Ding, S.-C. S. Lin, B. Kiraly, H. Yue, S. Li, I.-K. Chiang, J. Shi, S. J. Benkovic, and T. J. Huang, "On-chip manipulation of single microparticles, cells, and organisms using surface acoustic waves," *Proceedings of the National Academy of Sciences*, vol. 109, no. 28, pp. 11105–11109, 2012.

[293] M. Wu, Y. Ouyang, Z. Wang, R. Zhang, P.-H. Huang, C. Chen, H. Li, P. Li, D. Quinn, M. Dao, *et al.*, "Isolation of exosomes from whole blood by integrating acoustics and microfluidics," *Proceedings of the National Academy of Sciences*, p. 201709210, 2017.

[294] C. Cortez-Jugo, A. Qi, A. Rajapaksa, J. R. Friend, and L. Y. Yeo, "Pulmonary monoclonal antibody delivery via a portable microfluidic nebulization platform," *Biomicrofluidics*, vol. 9, no. 5, p. 052603, 2015.

[295] A. E. Rajapaksa, L. A. H. Do, D. Suryawijaya Ong, M. Sourial, D. Veysey, R. Beare, W. Hughes, W. Yang, R. J. Bischof, A. McDonnell, *et al.*, "Pulmonary deposition of radionucleotide-labeled palivizumab: Proof-of-concept study," *Frontiers in Pharmacology*, vol. 11, p. 1291, 2020.

[296] A. Ozcelik, J. Rufo, F. Guo, Y. Gu, P. Li, J. Lata, and T. J. Huang, "Acoustic tweezers for the life sciences," *Nature Methods*, vol. 15, no. 12, pp. 1021–1028, 2018.

[297] G. Destgeer and H. J. Sung, "Recent advances in microfluidic actuation and micro-object manipulation via surface acoustic waves," *Lab on a Chip*, vol. 15, no. 13, pp. 2722–2738, 2015.

[298] A. Huang, H. Liu, O. Manor, P. Liu, and J. Friend, "Enabling rapid charging lithium metal batteries via surface acoustic wave driven electrolyte flow," *Advanced Materials*, vol. 32, no. 14, p. 1907516, 2020.

[299] A. Winkler, R. Brünig, C. Faust, R. Weser, and H. Schmidt, "Towards efficient surface acoustic wave (saw)-based microfluidic actuators," *Sensors and Actuators A: Physical*, vol. 247, pp. 259–268, 2016.

[300] M. G. Kim, S. Yoon, H. H. Kim, and K. K. Shung, "Impedance matching network for high frequency ultrasonic transducer for cellular applications," *Ultrasonics*, vol. 65, pp. 258–267, 2016.

[301] V. T. Rathod, "A review of electric impedance matching techniques for piezoelectric sensors, actuators and transducers," *Electronics*, vol. 8, no. 2, p. 169, 2019.

[302] G. Whitesides, "The lab finally comes to the chip!," *Lab on a Chip*, vol. 14, no. 17, pp. 3125–3126, 2014.

[303] N. Zhang, J. Mei, T. Gopesh, and J. Friend, "Optimized, omnidirectional surface acoustic wave source: 152 degree y-rotated cut of lithium niobate for acoustofluidics," *IEEE Transactions on Ultrasonics, Ferroelectrics, and Frequency Control*, pp. 2176–2186, 2020.

[304] A. Doinikov, "Acoustic radiation pressure on a rigid sphere in a viscous fluid," *Proceedings of the Royal Society of London. Series A: Mathematical and Physical Sciences*, vol. 447, no. 1931, pp. 447–466, 1994.

[305] J. P. Lata, F. Guo, J. Guo, P.-H. Huang, J. Yang, and T. J. Huang, "Surface acoustic waves grant superior spatial control of cells embedded in hydrogel fibers," *Advanced Materials*, vol. 28, no. 39, pp. 8632–8638, 2016.

[306] K. Chen, M. Wu, F. Guo, P. Li, C. Y. Chan, Z. Mao, S. Li, L. Ren, R. Zhang, and T. J. Huang, "Rapid formation of size-controllable multicellular spheroids via 3d acoustic tweezers," *Lab on a Chip*, vol. 16, no. 14, pp. 2636–2643, 2016.

[307] O. Manor, L. Y. Yeo, and J. R. Friend, "The appearance of boundary layers and drift flows due to high frequency surface waves," *Journal of Fluid Mechanics*, vol. 707, pp. 482–495, 2012.

[308] J. Shi, D. Ahmed, X. Mao, S.-C. S. Lin, A. Lawit, and T. J. Huang, "Acoustic tweezers: patterning cells and microparticles using standing surface acoustic waves (ssaw)," *Lab on a Chip*, vol. 9, no. 20, pp. 2890–2895, 2009.

[309] R. W. Wood and A. L. Loomis, "{XXXVIII}.\ The physical and biological effects of high-frequency sound-waves of great intensity," *The London, Edinburgh, and Dublin Philosophical Magazine and Journal of Science*, vol. 4, no. 22, pp. 417–436, 1927.

[310] A. Dalmoro, A. A. Barba, G. Lamberti, and M. D'Amore, "Intensifying the microencapsulation process: Ultrasonic atomization as an innovative approach," *European Journal of Pharmaceutics and Biopharmaceutics*, vol. 80, no. 3, pp. 471–477, 2012.

[311] K. Namiyama, H. Nakamura, K. Kokubo, and D. Hosogai, "Development of ultrasonic atomizer and its application to SI engines," *SAE Transactions*, pp. 701–711, 1989.

[312] A. Qi, L. Y. Yeo, and J. R. Friend, "Interfacial destabilization and atomization driven by surface acoustic waves," *Physics of Fluids*, vol. 20, no. 7, p. 74103, 2008.

[313] J. Wang, H. Hu, A. Ye, J. Chen, and P. Zhang, "Experimental investigation of surface acoustic wave atomization," *Sensors and Actuators A: Physical*, vol. 238, pp. 1–7, 2016.

[314] A. James, B. Vukasinovic, M. K. Smith, and A. Glezer, "Vibration-induced drop atomization and bursting," *Journal of Fluid Mechanics*, vol. 476, pp. 1–28, 2003.

[315] C. A. Randall, N. Kim, J.-P. Kucera, W. Cao, and T. R. Shrout, "Intrinsic and extrinsic size effects in fine-grained morphotropic-phase-boundary lead zirconate titanate ceramics," *Journal of the American Ceramic Society*, vol. 81, no. 3, pp. 677–688, 1998.

[316] S. C. Tsai, S. K. Lin, R. W. Mao, and C. S. Tsai, "Ejection of uniform micrometer-sized droplets from {Faraday} waves on a millimeter-sized water drop," *Physical Review Letters*, vol. 108, no. 15, p. 154501, 2012.

[317] Y.-R. Jeng, C.-C. Su, G.-H. Feng, Y.-Y. Peng, and G.-P. Chien, "A PZT-driven atomizer based on a vibrating flexible membrane and a micro-machined trumpet-shaped nozzle array," *Microsystem Technologies*, vol. 15, no. 6, pp. 865–873, 2009.

[318] D. Lupascu and J. Rödel, "Fatigue in bulk lead zirconate titanate actuator materials," *Advanced Engineering Materials*, vol. 7, no. 10, pp. 882–898, 2005.

[319] A. Kawamata, H. Hosaka, and T. Morita, "Non-hysteresis and perfect linear piezoelectric performance of a multilayered lithium niobate actuator," *Sensors and Actuators A: Physical*, vol. 135, no. 2, pp. 782–786, 2007.

[320] A. Qi, L. Yeo, J. Friend, and J. Ho, "The Extraction Of Liquid, Protein Molecules and Yeast Cells From Paper Through Surface Acoustic Wave Atomization," *Lab on a Chip*, vol. 10, no. 4, pp. 470–476, 2010.

[321] A. W. Lawson, "The vibration of piezoelectric plates," *Physical Review*, vol. 62, no. 1-2, p. 71, 1942.

[322] Y. Fukushima, O. Nishizawa, and H. Sato, "A performance study of a laser doppler vibrometer for measuring waveforms from piezoelectric transducers," *IEEE Transactions on Ultrasonics, Ferroelectrics, and Frequency Control*, vol. 56, no. 7, pp. 1442–1450, 2009.

[323] S. T. Thoroddsen, T. G. Etoh, and K. Takehara, "High-speed imaging of drops and bubbles," *Annual Reviews in Fluid Mechanics*, vol. 40, pp. 257–285, 2008.

[324] A. J. Yule and Y. Al-Suleimani, "On droplet formation from capillary waves on a vibrating surface," *Proceedings of the Royal Society of London. Series A: Mathematical, Physical and Engineering Sciences*, vol. 456, no. 1997, pp. 1069–1085, 2000.

[325] E. D. Hirleman, "Modeling of multiple scattering effects in Fraunhofer diffraction particle size analysis," in *Optical Particle Sizing*, pp. 159–175, Springer, 1988.

[326] J. Waldrep and R. Dhand, "Advanced nebulizer designs employing vibrating mesh/aperture plate technologies for aerosol generation," *Current Drug Delivery*, vol. 5, no. 2, pp. 114–119, 2008.

[327] K. H. Chang, S.-H. Moon, J. Y. Oh, Y.-S. Yoon, N. Gu, C.-Y. Lim, B. J. Park, and K. C. Nam, "Comparison of salbutamol delivery efficiency for jet versus mesh nebulizer using mice," *Pharmaceutics*, vol. 11, no. 4, p. 192, 2019.

[328] A. Aver'yanov, A. Konoplyannikov, N. Antonov, G. Osipova, O. Vasil'eva, M. Sakharova, A. Tatarskii, and V. Kobylyansky, "Survival of mesenchymal stem cells in different methods of nebulization," *Bulletin of Experimental Biology and Medicine*, vol. 164, no. 4, pp. 576–578, 2018.

[329] A. Astudillo, S. S. Y. Leung, E. Kutter, S. Morales, and H.-K. Chan, "Nebulization effects on structural stability of bacteriophage pev 44," *European Journal of Pharmaceutics and Biopharmaceutics*, vol. 125, pp. 124–130, 2018.

[330] G. Altshuler and O. Manor, "Spreading dynamics of a partially wetting water film atop a mhz substrate vibration," *Physics of Fluids*, vol. 27, no. 10, p. 102103, 2015.

[331] A. Winkler, S. Harazim, D. Collins, R. Brünig, H. Schmidt, and S. Menzel, "Compact saw aerosol generator," *Biomedical Microdevices*, vol. 19, no. 1, p. 9, 2017.

[332] J. Friend and L. Y. Yeo, "Microscale acoustofluidics: Microfluidics driven via acoustics and ultrasonics," *Rev. Mod. Phys.*, vol. 83, pp. 647–704, 2011.

[333] W. Connacher, J. Orosco, and J. Friend, "Droplet Ejection at Controlled Angles via Acoustofluidic Jetting," *Phys. Rev. Lett.*, vol. 125, p. 184504, 2020.

[334] W. Connacher, N. Zhang, A. Huang, J. Mei, S. Zhang, T. Gopesh, and J. Friend, "Micro/nano acoustofluidics: Materials, phenomena, design, devices, and applications," *Lab Chip*, vol. 18, pp. 1952–1996, 2018.

[335] J. Blamey, L. Y. Yeo, and J. R. Friend, "Microscale Capillary Wave Turbulence Excited by High Frequency Vibration," *Langmuir*, vol. 29, pp. 3835–3845, Mar. 2013.

[336] M. Faraday, "XVII. On a peculiar class of acoustical figures; and on certain forms assumed by groups of particles upon vibrating elastic surfaces," *Phil. Trans. R. Soc. Lond.*, vol. 121, pp. 299–340, 1831.

[337] H. Xia, M. Shats, and H. Punzmann, "Modulation instability and capillary wave turbulence," *Europhys. Lett.*, vol. 91, p. 14002, 2010.

[338] A. Sheremet, Y. Qin, J. P. Kennedy, Y. Zhou, and A. P. Maurer, "Wave Turbulence and Energy Cascade in the Hippocampus," *Front. Sys. Neuro.*, vol. 12, p. 00062, 2019.

[339] A. Picozzi, J. Garnier, T. Hansson, P. Suret, S. Randoux, G. Millot, and D. N. Christodoulides, "Optical wave turbulence: Towards a unified nonequilibrium thermodynamic formulation of statistical nonlinear optics," *Phys. Rep.*, vol. 542, pp. 1–132, 2014.

[340] V. E. Zakharov and N. N. Filonenko, "Weak turbulence of capillary waves," *J Appl Mech Tech Phys*, vol. 8, pp. 37–40, 1967.

[341] E. Kartashova, *Nonlinear Resonance Analysis: Theory, Computation, Applications*. Cambridge University Press, first ed., 2010.

[342] L. Debnath, *Nonlinear Water Waves*. Academic Press, first ed., 1994.

[343] A. Pushkarev and V. Zakharov, "Turbulence of capillary waves — theory and numerical simulation," *Physica D: Nonlinear Phenomena*, vol. 135, pp. 98–116, Jan. 2000.

[344] C. Connaughton, S. Nazarenko, and A. Pushkarev, "Discreteness and quasiresonances in weak turbulence of capillary waves," *Physical Review E*, vol. 63, p. 046306, Mar. 2001. ZSCC: 0000043.

[345] S. Nazarenko, "Sandpile behaviour in discrete water-wave turbulence," *J. Stat. Mech.*, vol. 2006, p. L02002, 2006.

[346] V. S. L'vov and S. Nazarenko, "Discrete and mesoscopic regimes of finite-size wave turbulence," *Phys. Rev. E*, vol. 82, p. 056322, 2010.

[347] E. Kartashova, "Model of laminated wave turbulence," *Jetp Lett.*, vol. 83, pp. 283–287, 2006.

[348] V. E. Zakharov, A. O. Korotkevich, A. N. Pushkarev, and A. I. Dyachenko, "Mesoscopic wave turbulence," *Jetp Lett.*, vol. 82, pp. 487–491, 2005.

[349] M. Y. Brazhnikov, G. V. Kolmakov, A. A. Levchenko, and L. P. Mezhov-Deglin, "Observation of capillary turbulence on the water surface in a wide range of frequencies," *Europhysics Letters (EPL)*, vol. 58, pp. 510–516, May 2002.

[350] É. Falcon, C. Laroche, and S. Fauve, "Observation of Gravity-Capillary Wave Turbulence," *Phys. Rev. Lett.*, vol. 98, p. 094503, 2007.

[351] E. Herbert, N. Mordant, and E. Falcon, "Observation of the Nonlinear Dispersion Relation and Spatial Statistics of Wave Turbulence on the Surface of a Fluid," *Physical Review Letters*, vol. 105, p. 144502, Sept. 2010.

[352] M. Kharbedia, N. Caselli, D. Herráez-Aguilar, H. López-Menéndez, E. Enciso, J. A. Santiago, and F. Monroy, "Moulding hydrodynamic 2D-crystals upon parametric Faraday waves in shear-functionalized water surfaces," *Nat. Comm.*, vol. 12, p. 1130, 2021.

[353] D. Snouck, M.-T. Westra, and W. van de Water, "Turbulent parametric surface waves," *Phys. Fluids*, vol. 21, p. 025102, 2009.

[354] Y. Pan and D. K. P. Yue, "Understanding discrete capillary-wave turbulence using a quasi-resonant kinetic equation," *J. Fluid Mech.*, vol. 816, p. R1, 2017.

[355] Y. Pan and D. K. P. Yue, "Direct Numerical Investigation of Turbulence of Capillary Waves," *Phys. Rev. Lett.*, vol. 113, p. 094501, 2014.

[356] Y. Pan and D. K. P. Yue, "Decaying capillary wave turbulence under broad-scale dissipation," *J. Fluid Mech.*, vol. 780, p. R1, 2015.

[357] A. Huang, W. Connacher, M. Stambaugh, N. Zhang, S. Zhang, J. Mei, A. Jain, S. Alluri, V. Leung, A. E. Rajapaksa, and J. Friend, "Practical microcircuits for handheld acoustofluidics," *Lab Chip*, vol. 21, pp. 1352–1363, 2021.

[358] J. Orosco, W. Connacher, and J. Friend, "Data from: Identification of weakly- to strongly-turbulent three-wave processes in a micro-scale system," 2022.

[359] E. Kartashova, "Discrete wave turbulence," *Europhys. Lett.*, vol. 87, p. 44001, 2009.

[360] V. Zakharov, "Statistical theory of gravity and capillary waves on the surface of a finite-depth fluid," *Eur. J. Mech. B-Fluids*, vol. 18, pp. 327–344, 1999.

[361] V. E. Zakharov, V. S. L'vov, and G. Falkovich, *Kolmogorov Spectra of Turbulence I.* Springer Series in Nonlinear Dynamics, Berlin, Heidelberg: Springer Berlin Heidelberg, 1992. ZSCC: NoCitationData[s0].

[362] P. Denissenko, S. Lukaschuk, and S. Nazarenko, "Gravity Wave Turbulence in a Laboratory Flume," *Phys. Rev. Lett.*, vol. 99, p. 014501, 2007.

[363] B. P. van Milligen, C. Hidalgo, and E. Sánchez, "Nonlinear Phenomena and Intermittency in Plasma Turbulence," *Phys. Rev. Lett.*, vol. 74, pp. 395–398, 1995.

[364] A. C. Newell and B. Rumpf, "Wave Turbulence," *Annual Review of Fluid Mechanics*, vol. 43, pp. 59–78, Jan. 2011.

[365] C. Falcón, E. Falcon, U. Bortolozzo, and S. Fauve, "Capillary wave turbulence on a spherical fluid surface in low gravity," *European Physics Letters*, vol. 86, Apr. 2009.

[366] P. A. Robinson, "Scalings, spectra, and statistics of strong wave turbulence," *Physics of Plasmas*, vol. 3, pp. 192–201, Jan. 1996.

[367] P. H. Yoon, "Generalized weak turbulence theory," *Phys. Plasmas*, vol. 7, no. 12, p. 15, 2000.

[368] A. Boudaoud, O. Cadot, B. Odille, and C. Touzé, "Observation of Wave Turbulence in Vibrating Plates," *Physical Review Letters*, vol. 100, p. 234504, June 2008.

[369] V. E. Zakharov and N. N. Filonenko, "Weak turbulence of capillary waves," *Journal of Applied Mechanics and Technical Physics*, vol. 8, no. 5, pp. 37–40, 1971.

[370] E. Falcon, C. Laroche, and S. Fauve, "Observation of gravity-capillary wave turbulence," *Physical Review Letters*, vol. 98, p. 094503, Mar. 2007. ZSCC: 0000201.

[371] E. Falcon and C. Laroche, "Observation of depth-induced properties in wave turbulence on the surface of a fluid," *EPL (Europhysics Letters)*, vol. 95, p. 34003, Aug. 2011. arXiv: 1106.3246.

[372] L. Deike, M. Berhanu, and E. Falcon, "Energy flux measurement from the dissipated energy in capillary wave turbulence," *Physical Review E*, vol. 89, p. 023003, Feb. 2014.

[373] J. Orosco, W. Connacher, and J. Friend, "Identification of weakly- to strongly-turbulent three-wave processes in a micro-scale system," May 2022. arXiv:2205.01803 [physics].

[374] M. Kurosawa, T. Watanabe, A. Futami, and T. Higuchi, "Surface acoustic wave atomizer.pdf," *Sensors and Actuators A: Physical*, vol. 50, pp. 69–74, 1995.

[375] S. Collignon, O. Manor, and J. Friend, "Improving and Predicting Fluid Atomization via Hysteresis-Free Thickness Vibration of Lithium Niobate," *Advanced Functional Materials*, vol. 28, p. 1704359, Feb. 2018.

[376] R. J. Lang, "Ultrasonic Atomization of Liquids," *The Journal of the Acoustical Society of America*, vol. 34, p. 4, 1962.

[377] K. A. Ramisetty, A. B. Pandit, and P. R. Gogate, "Investigations into ultrasound induced atomization," *Ultrasonics Sonochemistry*, vol. 20, pp. 254–264, Jan. 2013.

[378] A. Qi, L. Y. Yeo, and J. R. Friend, "Interfacial destabilization and atomization driven by surface acoustic waves," *Physics of Fluids*, vol. 20, p. 074103, July 2008. ZSCC: 0000242.

[379] J. M. Mir, "Cavitation-induced capillary waves in ultrasonic atomization," *The Journal of the Acoustical Society of America*, vol. 67, pp. 201–205, Jan. 1980.

[380] D. J. Collins, O. Manor, A. Winkler, H. Schmidt, J. R. Friend, and L. Y. Yeo, "Atomization off thin water films generated by high-frequency substrate wave vibrations," *Physical Review E*, vol. 86, p. 056312, Nov. 2012.

[381] F. Barreras, H. Amaveda, and A. Lozano, "Transient high-frequency ultrasonic water atomization," *Experiments in Fluids*, vol. 33, pp. 405–413, Sept. 2002. ZSCC: 0000175.

[382] S. Kooij, A. Astefanei, G. L. Corthals, and D. Bonn, "Size distributions of droplets produced by ultrasonic nebulizers," *Scientific Reports*, vol. 9, p. 6128, Dec. 2019.

[383] A. Winkler, S. M. Harazim, S. B. Menzel, and H. Schmidt, "SAW-based fluid atomization using mass-producible chip devices," *Lab on a Chip*, vol. 15, no. 18, pp. 3793–3799, 2015.

[384] M. Berhanu and E. Falcon, "Space-time-resolved capillary wave turbulence," *Physical Review E*, vol. 87, p. 033003, Mar. 2013.

[385] K. Taira, S. L. Brunton, S. T. M. Dawson, C. W. Rowley, T. Colonius, B. J. McKeon, O. T. Schmidt, S. Gordeyev, V. Theofilis, and L. S. Ukeiley, "Modal Analysis of Fluid Flows: An Overview," *AIAA Journal*, vol. 55, pp. 4013–4041, Dec. 2017.

[386] G. Berkooz, P. Holmes, and J. L. Lumley, "The Proper Orthogonal Decomposition in the Analysis of Turbulent Flows," *Annual Review of Fluid Mechanics*, vol. 25, pp. 539–575, 1993.

[387] M. Rovira, K. Engvall, and C. Duwig, "Proper orthogonal decomposition analysis of the large-scale dynamics of a round turbulent jet in counterflow," *Physical Review Fluids*, vol. 6, p. 014701, Jan. 2021.

[388] O. T. Schmidt and T. Colonius, "Guide to Spectral Proper Orthogonal Decomposition," *AIAA Journal*, vol. 58, pp. 1023–1033, Mar. 2020.

[389] E. Cuche, P. Marquet, and C. Depeursinge, "Simultaneous amplitude-contrast and quantitative phase-contrast microscopy by numerical reconstruction of Fresnel off-axis holograms," *Applied Optics*, vol. 38, p. 6994, Dec. 1999.

[390] P. Welch, "The use of fast Fourier transform for the estimation of power spectra: A method based on time averaging over short, modified periodograms," *IEEE Transactions on Audio and Electroacoustics*, vol. 15, pp. 70–73, June 1967.

[391] Q. Aubourg and N. Mordant, "Investigation of resonances in gravity-capillary wave turbulence," *Physical Review Fluids*, vol. 1, p. 023701, June 2016.

[392] W. B. Wright, R. Budakian, and S. J. Putterman, "Diffusing Light Photography of Fully Developed Isotropic Ripple Turbulence," *Physical Review Letters*, vol. 76, pp. 4528–4531, June 1996. ZSCC: 0000124.

[393] S. Zhang, J. Orosco, and J. Friend, "Onset of low-frequency capillary waves driven by high-frequency ultrasound," Aug. 2021. arXiv:2108.09579 [physics].

[394] A. N. Pushkarev and V. E. Zakharov, "Turbulence of Capillary Waves," *Physical Review Letters*, vol. 76, pp. 3320–3323, Apr. 1996.

[395] D. Wang, B. Hu, C. Hu, F. Zhu, X. Liu, J. Zhang, B. Wang, H. Xiang, Z. Cheng, Y. Xiong, Y. Zhao, Y. Li, X. Wang, and Z. Peng, "Clinical characteristics of 138 hospitalized patients with 2019 novel coronavirus–infected pneumonia in wuhan, china," *Journal of the American Medical Association*, vol. 323, pp. 1061–1069, February 2020.

[396] G. E. Weissman, A. Crane-Droesch, C. Chivers, T. Luong, A. Hanish, M. Z. Levy, J. Lubken, M. Becker, M. E. Draugelis, G. L. Anesi, *et al.*, "Locally informed simulation to predict hospital capacity needs during the covid-19 pandemic," *Annals of Internal Medicine*, 2020.

[397] M. L. Ranney, V. Griffeth, and A. K. Jha, "Critical supply shortages — the need for ventilators and personal protective equipment during the covid-19 pandemic.," *New England Journal of Medicine*, March 2020.

[398] A. S. Fauci, H. C. Lane, and R. R. Redfield, "Covid-19 — navigating the uncharted.," *New England Journal of Medicine*, vol. 382, pp. 1268–1269, March 2020.

[399] M. Cascella, M. Rajnik, A. Cuomo, S. C. Dulebohn, and R. Di Napoli, "Features, evaluation and treatment coronavirus (covid-19)," in *StatPearls [Internet]*, StatPearls Publishing, 2020.

[400] J. Phua, L. Weng, L. Ling, M. Egi, C.-M. Lim, J. V. Divatia, B. R. Shrestha, Y. M. Arabi, J. Ng, C. D. Gomersall, *et al.*, "Intensive care management of coronavirus disease 2019 (covid-19): challenges and recommendations," *The Lancet Respiratory Medicine*, 2020.

[401] P. K. Bhatraju, B. J. Ghassemieh, M. Nichols, R. Kim, K. R. Jerome, A. K. Nalla, A. L. Greninger, S. Pipavath, M. M. Wurfel, L. Evans, *et al.*, "Covid-19 in critically ill patients in the seattle region—case series," *New England Journal of Medicine*, 2020.

[402] X. Yang, Y. Yu, J. Xu, H. Shu, J. Xia, H. Liu, Y. Wu, L. Zhang, Z. Yu, M. Fang, T. Yu, Y. Wang, S. Pan, X. Zou, S. Yuan, and Y. Shang, "Clinical course and outcomes of critically ill patients with sars-cov-2 pneumonia in wuhan, china: a single-centered, retrospective, observational study," *The Lancet Respiratory Medicine*, 04 2020.

[403] L. Rosenbaum, "Facing covid-19 in italy—ethics, logistics, and therapeutics on the epidemic's front line," *New England Journal of Medicine*, 2020.

[404] J. Xie, Z. Tong, X. Guan, B. Du, H. Qiu, and A. S. Slutsky, "Critical care crisis and some recommendations during the covid-19 epidemic in china," *Intensive Care Medicine*, March 2020.

[405] T. Netland, "A better answer to the ventilator shortage as the pandemic rages on." https://www.weforum.org/agenda/2020/04/covid-19-ventilator-shortage-manufacturing-solution/, April 2020.

[406] H.-C. Huang1, O. M. Araz, D. P. Morton, G. P. Johnson, P. Damien, B. Clements, and L. A. Meyers, "Stockpiling ventilators for influenza pandemics," *Emerging Infectious Diseases*, vol. 23, pp. 914–921, June 2017.

[407] A. Woodyatt, "The world is scrambling to buy ventilators in the covid-19 pandemic. one country has only four of them – for 12 million people." https://www.cnn.com/2020/04/18/africa/covid-19-ventilator-shortage-intl-scli/index.html, April 2020.

[408] S. Sanche, Y. T. Lin, C. Xu, E. Romero-Severson, N. Hengartner, and R. Ke, "High contagiousness and rapid spread of severe acute respiratory syndrome coronavirus 2," *Emerging Infectious Diseases*, vol. 26, no. 7, 2020.

[409] V. Krishnamoorthy, M. S. Vavilala, and C. N. Mock, "The need for ventilators in the developing world: An opportunity to improve care and save lives," *Journal of global health*, vol. 4, no. 1, 2014.

[410] S. Morrison, "Ford and gm are making tens of thousands of ventilators. it may already be too late.," Apr 2020.

[411] C. H. Weiss, D. W. Baker, S. Weiner, M. Bechel, M. Ragland, A. Rademaker, B. B. Weitner, A. Agrawal, R. G. Wunderink, and S. D. Persell, "Low tidal volume ventilation use in acute respiratory distress syndrome," *Critical care medicine*, vol. 44, no. 8, p. 1515, 2016.

[412] M. B. Amato, M. O. Meade, A. S. Slutsky, L. Brochard, E. L. Costa, D. A. Schoenfeld, T. E. Stewart, M. Briel, D. Talmor, A. Mercat, J.-C. M. Richard, C. R. Carvalho, and R. G. Brower, "Driving pressure and survival in the acute respiratory distress syndrome," *New England Journal of Medicine*, vol. 372, pp. 747–755, February 2015.

[413] E. Fan, L. Del Sorbo, E. C. Goligher, C. L. Hodgson, L. Munshi, A. J. Walkey, N. K. J. Adhikari, M. B. P. Amato, R. Branson, R. G. Brower, N. D. Ferguson, O. Gajic, L. Gattinoni, D. Hess, J. Mancebo, M. O. Meade, D. F. McAuley, A. Pesenti, V. M. Ranieri, G. D. Rubenfeld, E. Rubin, M. Seckel, A. S. Slutsky, D. Talmor, B. T. Thompson, H. Wunsch, E. Uleryk, J. Brozek, L. J. Brochard, and American Thoracic Society, European Society of Intensive Care Medicine, and Society of Critical Care Medicine, "An official american thoracic society/european society of intensive care medicine/society of critical care medicine clinical practice guideline: Mechanical ventilation in adult patients with acute respiratory distress syndrome," *American Journal Respiratory Critical Care Medicine*, vol. 195, pp. 1253–1263, 05 2017.

[414] J. Bourenne, S. Hraiech, A. Roch, M. Gainnier, L. Papazian, and J.-M. Forel, "Sedation and neuromuscular blocking agents in acute respiratory distress syndrome," *Annals of Translational Medicine*, vol. 5, pp. 291–303, July 2017.

[415] Prevention and E. T. of Acute Lung Injury (PETAL) network, "Early neuromuscular blockade in the acute respiratory distress syndrome," *New England Journal of Medicine*, vol. 380, pp. 1997–2008, May 2019.

[416] D. Hinton, "Emergency use authorization for ventilators," Mar 2020.

[417] R. L. Dellaca', C. Veneroni, and R. Farre', "Trends in mechanical ventilation: are we ventilating our patients in the best possible way?," *Breathe*, vol. 13, no. 2, pp. 84–98, 2017.

[418] S. Corp, "Flow sensor." https://www.sensirion.com/en/about-us/newsroom/sensirion-specialist-articles/flow-sensor-solutions-in-modern-medical-ventilators/, March 2020.

[419] P. J. C. Biselli, R. S. Nóbrega, and F. G. Soriano, "Nonlinear flow sensor calibration with an accurate syringe," *Sensors*, vol. 18, no. 7, 2018.

[420] P. R. Bachiller, J. M. McDonough, and J. M. Feldman, "Do new anesthesia ventilators deliver small tidal volumes accurately during volume-controlled ventilation?," *Anesthesia & Analgesia*, vol. 106, no. 5, 2008.

[421] M. J. Heulitt, S. J. Holt, and T. L. Thurman, "Accuracy of small tidal volume measurement comparing two ventilator airway sensors," *Journal of Pediatric Intensive Care*, vol. 2, pp. 33–38, 2013.

[422] R. S. Harris, "Pressure-volume curves of the respiratory system," *Respiratory care*, vol. 50, no. 1, pp. 78–99, 2005.

[423] A. Lyazidi, A. W. Thille, G. Carteaux, F. Galia, L. Brochard, and J.-C. M. Richard, "Bench test evaluation of volume delivered by modern icu ventilators during volume-controlled ventilation," *Intensive Care Medicine*, vol. 36, no. 12, pp. 2074–2080, 2010.

[424] MIT, "Mit emergency ventilator (e-vent) project." https://e-vent.mit.edu/, April 2020.

[425] U. of Minnesota, "Covid-19 ventilator." https://med.umn.edu/covid19Ventilator, April 2020.

[426] Sensirion, "Cmosens® technology for gas flow and differential pressure." https://www.sensirion.com/en/about-us/company/technology/cmosens-technology-for-gas-flow/, 2020.

[427] M. Abir, C. Nelson, E. W. Chan, H. Al-Ibrahim, C. Cutter, K. Patel, and A. Bogart, "Critical care surge response strategies for the 2020 covid-19 outbreak in the united states," tech. rep., RAND Corporation, 2020.

[428] S. for critical care in medicine, "Consensus statement on multiple patients per ventilator." https://www.sccm.org/Disaster/Joint-Statement-on-Multiple-Patients-Per-Ventilato, March 2020.

[429] A. Darwood, J. McCanny, R. Kwasnicki, B. Martin, and P. Jones, "The design and evaluation of a novel low-cost portable ventilator," *Anaesthesia*, vol. 74, no. 11, pp. 1406–1415, 2019.

[430] A. M. Al Husseini, H. J. Lee, J. Negrete, S. Powelson, A. T. Servi, A. H. Slocum, and J. Saukkonen, "Design and prototyping of a low-cost portable mechanical ventilator," *Transactions of the ASME-W-Journal of Medical Devices*, vol. 4, no. 2, p. 027514, 2010.

[431] B. M. Rosenthal, J. Pinkowski, and J. Goldstein, "'the other option is death': New york starts sharing of ventilators." https://www.nytimes.com/2020/03/26/health/coronavirus-ventilator-sharing.html, March 2020.

[432] M. E-Vent, "Testing." https://e-vent.mit.edu/testing-results/, 04 2020.

[433] R. D. Branson, J. A. Johannigman, E. L. Daugherty, and L. Rubinson, "Surge capacity mechanical ventilation," *Respiratory Care*, vol. 53, pp. 78–88, January 2008.

[434] H. S. R. Inc., "Bioterrorism and other public health emergencies: Altered standards of care in mass casualty events." https://archive.ahrq.gov/research/altstand/altstand.pdf, April 2005.

[435] A. Anzueto, F. Frutos-Vivar, A. Esteban, I. Alía, L. Brochard, T. Stewart, S. Benito, M. J. Tobin, J. Elizalde, F. Palizas, *et al.*, "Incidence, risk factors and outcome of barotrauma in mechanically ventilated patients," *Intensive care medicine*, vol. 30, no. 4, pp. 612–619, 2004.

[436] G. L. Anesi, S. Manaker, G. Finlay, and A. Bloom, "Coronavirus disease 2019 (covid-19): Critical care issues," *UpToDate*, April 2020.

[437] I. S. Organization, "Medical electrical equipment — part 2-12: Particular requirements for basic safety and essential performance of critical care ventilators." https://www.iso.org/standard/72069.html, March 2020.